Multilayer coatings based on aluminum nitride coatings for receivers in concentrated solar power technology

Danying Chen

Communauté
UNIVERSITÉ Grenoble Alpes

THÈSE

Pour obtenir le grade de

DOCTEUR DE LA COMMUNAUTE UNIVERSITE GRENOBLE ALPES

Spécialité : **Matériaux, Mécanique, Génie Civil, Electrochimie**

Arrêté ministériel : 25 mai 2016

Présentée par

Danying CHEN

Thèse dirigée par **Michel PONS,** Directeur de recherche CNRS, SIMaP,
Codirigée par **Frédéric MERCIER** Chargé de recherche CNRS, SIMaP

Préparée au sein du **Laboratoire SIMaP**
dans **l'École Doctorale I-MEP²,** *« Ingénierie – Matériaux, Mécanique, Environnement, Energétique, Procédé, Production »*

Revêtements multicouches à base de nitrure d'aluminium pour les récepteurs solaires

Thèse soutenue publiquement le **15 novembre 2019**,
devant le jury composé de :

Madame Angeline POULON
Maître de Conférences, Université de Bordeaux, rapportrice
Monsieur Francis MAURY
Directeur de recherche CNRS émérite, Toulouse-CIRIMAT, rapporteur
Monsieur Frédéric SANCHETTE
Professeur Université de Technologie de Troyes, examinateur
Monsieur Yves WOUTERS
Professeur Université de Grenoble Alpes, Président
Monsieur Michel PONS
Directeur de recherche CNRS, Grenoble-SIMaP, directeur de thèse
Monsieur Frédéric MERCIER
Chargé de recherche CNRS, Grenoble-SIMaP, Co-encadrant
Madame Elisabeth BLANQUET
Directrice de recherche CNRS, Grenoble-SIMaP, invitée
Monsieur Ludovic CHARPENTIER
Chargé de recherche CNRS, PROMES-CNRS, invité
Monsieur Didier PIQUE
Docteur Ingénieur, Sil'Tronix, invité

General introduction

The demand for renewable energy resources has led to the development of concentrating solar power (CSP) technologies. The central receiver system, one of the main CSP technologies, is now moving to the forefront and becoming an emerging option for large-scale electricity production. This design uses a large number of sun-tracking mirrors to focus sunlight onto a receiver at the top of a tall tower. A heat transfer fluid, heated in the receiver by thermal convection, then flows through the receiver and passes to a conventional turbine to produce electricity. The challenge for a central receiver system is related to ensuring the longevity of the receiver and demonstrating that the receiver material can handle high temperature fluxes across the 30-year lifetime of a plant. A further research step for this technology is to reach even higher temperatures ($\geq$ 1000 °C) and therefore higher efficiencies. The question of which material is the most suitable for different temperatures is still under study. Nickel-based alloys with high chromium contents, coated with a commercial absorbing material (Pyromark 2500) are the state-of-the-art solar receiver materials. But their operating temperature are limited to around 800 °C. Dense or foam ceramics are the most suitable materials for temperatures higher than 800 °C. Temperatures as high as 1200 °C can be reached with SiSiC ceramics and 1500 °C with SiC ceramics. However, the brittleness of ceramics is the main concern for their use in solar receivers. Indeed, to reach a high efficiency, a solar receiver material should have a high thermal conductivity, a high solar absorptivity, and a high resistance to thermal fatigue. Characterization of thermal losses and incident fluxes for a thermal receiver will lead to optimized receiver designs. To achieve outlet temperatures of higher than 1000 °C new developments are necessary.

In this thesis, the research route is to develop ceramic coatings deposited on high temperature alloys. The metallic substrate is selected for its thermal and mechanical properties while the coating should exhibit good surface properties like high absorptivity and good oxidation resistance to protect the substrate against aggressive oxidizing environment. Aluminum nitride (AlN) and silicon carbide (SiC) are selected as coating materials due to their high thermal conductivity, low thermal expansion coefficient, high temperature stability and their ability to develop stable oxide scales at high temperature. Two kinds of metallic alloys are selected as substrate materials. Refractory-based alloys have excellent thermal and mechanical properties but poor oxidation resistance. The alumina-forming iron-based alloys are selected as alternative substrates for their ability to develop stable oxides at high temperature and to simplify the characterization of the lifetime of the coatings. The comparison of coated and uncoated systems allows

the quality of the coating to be studied. In addition, the thermal fatigue of these systems can be evaluated during cyclic oxidation tests of the coatings deposited on the two alloy classes. Accelerated cyclic oxidation tests and emissivity measurements are made in solar furnace facilities to study the potential of AlN coatings as materials for high temperature solar receivers. The methodology followed in this thesis involves (1) coating deposition using high temperature chemical vapor deposition (HTCVD), (2) characterizations of microstructure, oxidation resistance, durability and optical properties of the coating(s) and (3) investigations of stress evolution within the coating(s)/substrate system during the daily operation. The depositions, characterizations and simulations of stress evolution performed for the selected coating(s)/substrate systems are described in the following chapters.

The introductory ***Chapter 1*** starts with a brief introduction to the concentrating solar power technologies. A detailed description of the central receiver system and its plant efficiency is then presented, followed by a summary of current solar receiver materials and solar selective coatings. The chapter ends with an introduction of fundamental properties of solar receiver materials for high temperature operation ($\geq$ 1000 °C), which is dedicated to a better understanding of the selection of materials in the next chapter.

The methodology for a complete design of the coating(s)/substrate systems as solar receiver materials is fully explained in ***Chapter 2***. The design process starts with the selection of the coating and substrate materials. The HTCVD process is then described. The film growth mechanisms involving film growth process and the evolution of microstructure and stress during the deposition of a polycrystalline film is detailed. Afterwards, a description of the experimental set-up is presented. Finally, all the characterization techniques used in this study are briefly described.

In ***Chapter 3***, the details of the deposition of AlN coatings on molybdenum-based alloy (TZM) and iron-based alloys (Fecralloy and APMT) by HTCVD are firstly presented. The microstructure and residual stress of the coatings are extensively characterized. The relationship between process parameters and microstructure are discussed. Cyclic oxidation of AlN coated samples in the high temperature range (800-1100 °C) are carried out to study the lifetime of AlN coatings

Chapter 4 is dedicated to exploring the thermomechanical behavior of the coating(s)/substrate systems during thermal cycling. An analytical model is developed in the first step. Therein, the model is validated by the comparison with a finite element analysis. The effect of various factors involving thermal conditions in solar receivers, intrinsic growth stress in the coatings, oxidation kinetics and creep properties of materials are thoroughly analyzed to further investigate the durability of AlN coating for its use in solar receivers. A comparison with experimental results is performed.

Chapter 5 firstly studies the optical properties of the AlN coatings. Then, the potential of SiC as a coating material for solar receivers is also investigated. The microstructure, oxidation resistance and optical properties of SiC deposited

on different substrates coated with an AlN accommodation layer are discussed. The SiC/AlN coatings are worth investigating for receivers able to meet the requirements of the future CSP power plants for durability and performance.

The general conclusions of this thesis and perspective for future research are discussed at the end.

Acknowledgement

During these three years of my PhD, I have been extremely fortunate to have had the support of the SIMaP Laboratory, colleagues, friends and family. Without this support, this thesis would not have possible.

First, and most importantly, I would like to thank Michel Pons and Frédéric Mercier, my supervisors, for their help, encouragement and countless hours that they dedicated to this thesis. Their understanding and expertise greatly improved the contents of this thesis, and I feel grateful to have the opportunity to work with such carrying and inspiring people. Words are not enough to describe their support in all situations: from common daily issues, up to the preparation for oral conference presentations and scientific papers. The interesting discussions and meetings with Michel, are always helpful to move things forward. I would like to appreciate the time and energy you spent on this project, your pertinent remarks and suggestions, as well as your patience throughout these three years. Fred, thanks for your detailed training, which not only help me to grow as a young researcher, but as a person as well. I have been always felt trust, encouraged and supported by you.

This project is also supported by Johann Colas, Ludovic Charpentier and Marianne Balat-Pichelin in PROMES Laboratory for the optical measurements. Moreover, I would like to appreciate the CMTC team for materials characterization. Thanks to Rachel Martin, Frédéric Charlot, Francine Roussel and Joelle Calabro for SEM observations and FIB preparation; Thierry Encinas and Stephane Coindeau for XRD analyses; Florence Robaut for EBSD analyses; and Alexandre Crisci for Raman and PL analyses.

I would like to thank all the professors, engineers, researchers and technicians in the group TOP where I spent three exciting years. I would like to appreciate Elisabeth Blanquet, Ionana Nuta, Raphael Boichot, Roman Rebout, Laurent Artaud, Stéphane Massucci, Gaël Guist, Alexandre Crisci for their technical and scientific support and suggestions. Thanks to all the PhD students and post-doctoral researchers for all their help, support, advices, as well as moments and interesting conversations that we share in the experimental platform, at the coffee break and out of the laboratory: Solène Iruela, Erwan Gicquel, Juan Su, Adrien Moll and all the others. And thanks to Damien Tresallet and Mohammed Ali Lakhdari for sharing all their 'magic' techniques for polishing. Without your kind advices and help, the EBSD images in this thesis would have never existed. Fatma Trabelsi, I promise to do sport with you this year. Manoel Jacquemin, thanks for pushing me to practice my French and for your patience to improve my

pronunciation and oral speaking. We started our PhD journey together and we finally made it.

The support of my friends has been wonderful. I would like to thank Yifu Guo, Fengyang Quan, Zikun Zhao and Zhiying Xu for the moments we spent outside work, skiing in the Deux Alpes ski sation and having tasteful asian diners. Thanks to Shuting Wu and Jiayu Chen for the sincere talks on the research, future, stars and ourselves. That encourage me and make me brave. Thanks to friends from IFCEN, Weifeng Zhou, Yanjun Wang and Yang Li, for all the trips we have taken together, the beautiful scenery and the precious memories. I should also give special thanks to my dear friend, Beilin Hu, for always being there so that I can share all the moments of anxiety and happiness.

These last lines are dedicated to my parents for all of their support and understanding, not only during my PhD and the years I stay far away with them, but for always being with me, in all of my life. Last but not least, I would like to thank my boyfriend, Fanshi, for being so supportive while I was doing my PhD. Thanks for taking time to proofread the drafts of my thesis and for your constructive suggestions. I am grateful that you are always there in the difficult moments and also the happy ones. Quatorze, our precious cat, thanks for your emotional meow everyday. You make my daily life filled with smiles (and/or some yells).

Table of Contents

General introduction **i**

1 Introduction and overview **1**
1.1 Central receiver systems . . . 3
1.2 Plant efficiency of central receiver systems . . . 7
1.3 Current solar receiver materials . . . 10
1.3.1 High temperature metallic alloy based receivers . . . 10
1.3.2 Ceramics . . . 13
1.3.3 Solar selective coatings . . . 15
1.4 Guidelines for selection of receiver materials . . . 18

2 Methodologies for a complete design for solar receiver materials **21**
2.1 Selection of materials . . . 22
2.1.1 Coating materials . . . 22
2.1.2 Metallic substrates . . . 26
2.2 Processing . . . 30
2.2.1 Overview of CVD . . . 31
2.2.2 Film growth mechanisms . . . 33
2.2.3 Experimental set-up . . . 40
2.3 Characterization methods . . . 42
2.3.1 X-ray diffraction . . . 42
2.3.2 Scanning Electron Microscopy . . . 42
2.3.3 Electron Back Scatter Diffraction . . . 43
2.3.4 XRD-$\sin^2\psi$ method . . . 45
2.3.5 Raman spectroscopy . . . 45
2.3.6 Photoluminescence piezospectroscopy . . . 46

3 Deposition and high temperature oxidation of AlN coatings **49**
3.1 HTCVD deposition conditions . . . 49
3.2 Chemical stability between substrates and AlN . . . 51
3.3 AlN deposition on TZM . . . 53
3.3.1 Microstructure of AlN coatings . . . 53
3.3.2 Residual stress . . . 55
3.4 Oxidation of AlN coatings on TZM . . . 57
3.4.1 Oxidation conditions . . . 57
3.4.2 Microstructure . . . 58
3.5 AlN deposition on FeCrAl alloys . . . 61

3.5.1 Microstructure of AlN coatings on Fecralloy 61
3.5.2 Microstructure of AlN coatings on pre-oxidized APMT . . . 69
3.6 Oxidation of AlN coatings on Fecralloy and APMT 71
3.6.1 Oxidation conditions 71
3.6.2 Oxidation of uncoated Fecralloy and APMT 71
3.6.3 Oxidation of AlN coatings 74
3.6.4 Residual stress evolution during cyclic oxidation 80
3.6.5 Lifetime evaluation for AlN coatings 82

4 Thermomechanical model of multilayer coating systems 85
4.1 Synopsis of the model 86
4.1.1 Concepts of stress evolution 86
4.1.2 Model construction 88
4.2 Verification of the model: comparison with finite element analysis . 100
4.2.1 Finite element model 100
4.2.2 Comparison between FEA and analytical model calculations 101
4.3 Time evolution of stress and creep strain in the multilayer system . 104
4.3.1 Simplified model: without oxidation 104
4.3.2 Complete model: growing oxide scales 112
4.4 Effects of individual factors 117
4.4.1 Effect of heat flux 118
4.4.2 Effect of temperature at the bottom surface of the system . 121
4.4.3 Effect of intrinsic growth stress in the AlN coating 124
4.4.4 Effect of creep deformation 126
4.4.5 Effect of oxide scale growth kinetics 130
4.5 Assessment of the creep properties used in the simulation 132
4.6 Limitation of the model 133

5 Potential of AlN and SiC coatings for their use in solar receivers 137
5.1 Optical properties of AlN coatings 137
5.2 SiC coatings for solar receivers 140
5.2.1 HTCVD deposition conditions 140
5.2.2 Stack SiC/AlN/TZM 140
5.2.3 Stack SiC/AlN/FeCrAl alloys 142

General conclusion 147

Perspectives 151

Résumé 153

References 160

Annex 1: Material properties for the selection of substrates 183

Annex 2: Pole figure analysis 189

Annex 3: Material properties for modeling 191

Annex 4: Finite element model **193**

List of Figures

1 Introduction and overview

1.1 Typical concentrated solar power technologies: parabolic trough, linear Fresnel reflector, central receiver system, and parabolic dish stirling [43]. . . . 2
1.2 Schematic illustration of a Central Receiver System. . . . 3
1.3 Concept of hybrid pressurized air receiver integrated Combined-Cyble in the framework of PEGASE [1]. . . . 7
1.4 Power cycle efficiencies for different CSP technologies [2, 3]. . . . 7
1.5 Optical, thermal and global efficiency as a function of receiver temperature with varying concentration ratio: (a) optical (solar-to-thermal), $\eta_{optical}$, and thermal conversion efficiency, $\eta_{thermal}$, versus receiver temperature and (b) Optimum operating temperature for each concentration ratio; with α=0.95, ε = 0.85, h=10 W·m^{-2}·K^{-1}), η_{field}=0.6, E_{DNI}=1000 W·m^{-2} and T_{amb}=T_c=20 °C. . . . 9
1.6 Creep rupture strength and allowable stress as a function of operating temperature for various nickel-based alloys and stainless steels: (a) 100,000 hour creep rupture strength [4] and (b) allowable stress [5, 6]. . . . 11
1.7 Spectral emissivity of an idealized solar selective coating, accompanied with solar spectral irradiation and the black-body radiation spectrum at two different temperatures (1000 K and 1500 K) for a better understanding. . . . 16
1.8 Current temperature in commerical CRS and the targeted temperature in the present work; the global efficiency with respect to receiver temperature for different concentration ratios has been presented in Figure 1.5(b). . . . 18

2 Methodologies for a complete design for solar receiver materials

2.1 Schematic representation of coating-substrate system. . . . 21
2.2 Thermal conductivities of Al_2O_3, high purity AlN and SiC single crystals versus temperature [7, 8]. . . . 23
2.3 Instantaneous thermal expansion coefficient of 3C-SiC, polycrystalline 6H-SiC, AlN and Al_2O_3 calculated by the first principle theory [9]. . . . 23
2.4 Transport and physicochemical mechanisms in a CVD process. . . . 32

2.5 Schematic of logarithmic growth rate as a function of deposition temperature in a conventional CVD process. 32
2.6 Arrhenius plot of growth rate of TiN by CVD as a function of 1/T [10]. 33
2.7 Schematic representation showing (a) the events in a typical vapor-phase thin film growth process and (b) three primary growth modes. 34
2.8 Effect of deposition temperature and supersaturation on the deposit morphology. 35
2.9 Overview of microstructural evolution during growth of a polycrystalline film: (a) nucleation and growth, (b) coalescence of islands leading to the formation of grain boundaries. The subsequent film thickening results in two different microstructures: (c) columnar (at low deposition temperature) and (d) equiaxed (at high deposition temperature). Transformation from columnar microstructure to equiaxed microstructure can be achieved by annealing [11]. 37
2.10 Fastest growing directions (double arrows) of a number of free-growing single crystals. Crystals having their fastest direction nearly normal to the substrate envelop the other crystals and gradually determine the preferred orientation of the film [12]. 38
2.11 Schematic of the two-dimensional growth of randomly distributed (10)-bounded grains on a substrate; Δ t is the shortest time required for two neighbouring grains to meet each other. The selection of orientation proceeds and permits only crystals with their vertical growth rate nearly normal to the substrate surface to grow further [12]. 38
2.12 General behavior of the volume-average stress in a thin film as a function of mean thickness. The three stages correspond to the surface and/or interface stress, island coalescence and growth of a continuous film respectively [11]. 39
2.13 Schematic representation of crystallites prior to coalescence [13]. . . 40
2.14 The evolution of intrinsic growth stresses during the vapor deposition of type 1 and type 2 materials (Figure 2.9(c) and (d) respectively) as a function of film thickness. 41
2.15 Schematic representation of experimental set-up for HTCVD growth of AlN. 41
2.16 Schematic representation of mounted sample and detector for EBSD analysis; A1, A2 and A3 are the rolling direction (ND), transverse direction (TD) and normal direction (ND), respectively, with respect to the cross-sectional surface of mounted sample. . . . 44
2.17 (a) Energy emitted from chromium-doped alumina resulting in (b) the R-lines in the spectrum of α-alumina [14]. 46

3 Deposition and high temperature oxidation of AlN coatings

3.1 Interrupted growth mode used for AlN deposition in this study . . . 51
3.2 Calculated ternary phase diagrams at (a, b) 1100 °C and (c) at 1200 °C of the systems: (a) Al-N-Fe, (b) Al-N-Cr, and (c) Al-N-Mo. 52

3.3 Surface morphology and microstructure of AlN coating deposited on TZM substrate at 1200 °C: (a) surface morphology, (b) cross-sectional microstructure and (c) a high magnification of (b) at the AlN/TZM interface 53

3.4 θ-2θ X-ray diffraction spectrum of AlN coating grown on TZM at 1200 °C. 54

3.5 Preferred orientations changed from $(11\bar{2}2)$ to $(21\bar{3}1)$, and finally to $(11\bar{2}0)$ with increasing deposition temperature in the work of Claudel et al. [15]. 55

3.6 Macroscopic images of AlN coated TZM sample (a,c) before and (b,d) after oxidation: (a,b) front-side and (c,d) backside. 58

3.7 Two different surface morphologies of AlN coated TZM sample after 8 min of oxidation at 1327 °C: (a) at the edge and (b) at the center. 58

3.8 Microstructure of AlN coated TZM sample after 8 min of oxidation at 1327 °C: (a) at the center, (b) at the edge, (c) at the Al_2O_3/AlN interface and (d) at the AlN/TZM interface. 59

3.9 Loss of adhesion of AlN coating during oxidation resulting in: (a) formation of MoO_3 and (b) competitive oxidation of AlN and Mo. . 60

3.10 'Laminated' defect located on the lateral side of the substrate: (a) SEM cross-section image after deposition of AlN with a macroscopic image of TZM substrate before deposition and (b) a high magnification of the 'laminated' defect shown in (a). 60

3.11 (a)-(e) Surface morphologies and (f)-(j) cross-sections of AlN coatings processed on Fecralloy at T=1100 °C, P=2000 Pa, Cl_2 flow rate of 20 sccm, NH_3 flow rate varying from 40 to 600 sccm, N/Al ratio estimated by $NH_3/AlCl_3$ inlet flow rate ratio assuming that $AlCl_3$ is the predominant $AlCl_x$ specie. 63

3.12 Effect of N/Al ratio on preferred orientation(s) of AlN deposited at 1100 °C on Fecralloy. 64

3.13 EBSD orientation mappings of coated systems shown in Figure 3.11: (a) N/Al=3 and (b) N/Al=11.25; the A1 axis is perpendicular to the substrate surface. 66

3.14 EBSD orientation mappings of coated systems shown in Figure 3.11 along selected directions: (a) N/Al=3 and (b) N/Al=11.25. For each map, reference directions are selected and the color assignment is presented at the right side; the A1 axis is perpendicular to the substrate surface. 67

3.15 XRD θ-2θ patterns of AlN coatings deposited at 1100 °C with thickness of (a) 12 μm and (b) 45 μm. 68

3.16 (a) Surface morphology and (b) XRD θ-2θ patterns of AlN coating deposited at 1200 °C with a N/Al ratio of 3. Its thickness is around 45 μm. 69

3.17 Surface morphology and microstructure of AlN coating deposited on pre-oxidized APMT at 1100 °C: (a) surface morphology, (b) cross-sectional microstructure and (c) a high magnification of (b) at the AlN/Al_2O_3 interface. The thermally grown Al_2O_3 on APMT is used to accommodate large difference of CTE between AlN and APMT. 70
3.18 θ-2θ X-ray diffraction spectrum of AlN coating grown on pre-oxidized APMT at 1100 °C with a N/Al ratio of 3. 70
3.19 Oxidation kinetics of uncoated Fecralloy and APMT at 1100 °C in this study. 72
3.20 Surface morphology of (a) Fecralloy and (b) APMT after 25 h of oxidation. 73
3.21 Oxidation curve of a typical commercial Fecralloy (2 mm thick) at 1200 °C [16]. 74
3.22 Oxidation kinetics of AlN coatings in the temperature range of 800-1100 °C. 75
3.23 Oxidation kinetics of Fecralloy and pre-oxidized APMT coated with AlN (45 μm) at 1100 °C. 76
3.24 Surface morphology of AlN coated samples after 120 h of oxidation: (a) Fecralloy coated with 45 μm of AlN and (b) Pre-oxidized APMT coated with 15 μm of AlN) 77
3.25 SEM cross-section images after 94 h of oxidation at 1100 °C of Fecralloy: (a) coated with 10 μm AlN (N/Al=11.25) and (b) uncoated. 78
3.26 Simulated crystals for various orientations: (a) surface morphology and (b) view at 90°. [17] 78
3.27 Cross-section after 1470 h of oxidation at 1100 °C of pre-oxidized APMT coated with 15 μm AlN ('standard' processing conditions). . 80
3.28 Schematic representation of the pre-oxidized APMT coated with AlN coatings for cyclic oxidation. 80
3.29 Residual stress in (a) AlN and (b) Al_2O_3 top layers, dashed lines are used for eye guidance and dotted lines represent the compressive strength of AlN and Al_2O_3. 81

4 Thermomechanical model of multilayer coating systems

4.1 Schematic representation of the multilayer coating system: (a) a typical stress-free multilayer coating system; and (b) bending of the system induced by asymmetric stresses, leading to a convex curvature. 89
4.2 Schematic representation of thermal cycling conditions and the corresponding bending behavior of the multilayer coating system; q is the absolute value of imposed heat flux, T_t(t) and T_b(t) are the time-dependent temperatures at the top and bottom surfaces respectively. 91
4.3 Basic creep strain curve including primary, secondary, and tertiary creep stages. 92

4.4 Dependence of creep strain on stress and temperature: (a) creep strain versus time at a constant temperature with different stress levels; and (b) creep strain versus time at a constant engineering stress and different temperatures [18]. 93
4.5 Possible locations to form new oxide scales, where J_o and J_m are diffusion fluxes of oxygen and metal ions respectively [19]. 95
4.6 Flow chart of the model. 99
4.7 Schematic representation of thermal loading history for FEA. 100
4.8 Comparison between FEA and the present model for the temperature distribution along the thickness direction. 101
4.9 Comparison between FEA and the present model: (a) normal stress and (b) creep strain distribution at high temperature. 102
4.10 Evolution of (a, c, e) normal stress and (b, d, f) creep strain at the center position of (a, b) top coating, (c, d) bottom coating and (e, f) substrate. 103
4.11 Time-dependent curvature of the system predicted by the analytical model; triangles represent the curvature at ambient temperature. . . 105
4.12 Effect of growth stress in AlN coatings: evolution of (a, c, e) normal stress and (b, d, f) creep strain at the center position of (a, b) top coating, (c, d) bottom coating and (e, f) substrate; circles and triangles represent the thermoelastic stresses ($\sigma_{0,HT}$) and stresses at ambient temperature respectively. 109
4.13 Evolution of the curvature of the system calculated (a) with and (b) without consideration of intrinsic CVD growth stress in the AlN coating; triangles represent the curvature at ambient temperature. . 110
4.14 Evolution of distribution of (a, c, e) normal stress and (b, d, f) creep strain fields at the center of (a, b) top coating, (c, d) bottom coating and (e, f) substrate. 111
4.15 Evolution of (a) normal stress and (b) creep strain at the coating/substrate interfaces; triangles represent stresses at ambient temperature. 112
4.16 Thickness of the oxide scales and AlN coatings during thermal cycling on the top and bottom surfaces of the system. 113
4.17 Temperature redistribution due to the oxidation of AlN coatings. . 113
4.18 Curvature evolution of the system taking into account the high temperature oxidation of AlN coatings; the curvature evolution without consideration of oxidation (orange curve) has been already presented in Figure 4.13(a). Triangles represent the curvature at ambient temperature. 114
4.19 Effect of high temperature oxidation: evolution of (a, c, e, g) normal stress and (b, d, f, h) creep strain in (a, b) oxide scales at oxide/AlN coating interface, (c, d, e, f) AlN coatings at (c, d) AlN top coating/substrate and (e, f) AlN bottom coating/substrate interfaces; and (g, h) the substrate; triangles represent stresses at ambient temperature. 116
4.20 Temperature distribution along the z direction when the system is initially subjected to a thermal load. 118

4.21 Schematic representation showing the curvature variation due to temperature change from high temperature to ambient temperature; red dashed line represents the structure of the system prior to cooling in i cycle; (1), (2) and (3) indicate the three representative positions mentioned above. 119

4.22 Effect of heat fluxes on (a) evolutions of the curvature, and stress evolutions at (b) oxide/AlN top coating interface (on oxide side), (c) AlN top coating/substrate interface (on coating side) and (d) the center of substrate; triangles represent the curvature and/or stresses at ambient temperature. 120

4.23 Effect of temperature at the bottom surface on (a) evolutions of the curvature of the system, and stress evolutions at (b) oxide/AlN top coating interface (on oxide side), (c) AlN top coating/substrate interface (on coating side) and (d) the center of substrate; triangles represent the curvature and/or stresses at ambient temperature. . . 123

4.24 Effect of intrinsic CVD growth stress in AlN coatings on (a) evolutions of the curvature of the system, and stress evolutions at (b) oxide/AlN top coating interface (on oxide side), (c) AlN top coating/substrate interface (on coating side) and (d) the center of substrate; triangles represent the curvature and/or stresses at ambient temperature. 125

4.25 Schematic representation showing the curvature variation due to creep mismatches between the oxide scales and the {coatings+substrate}; red dashed line represent the structure of the system at time t. . . . 126

4.26 Effect of creep properties of the oxide scale on (a) evolutions of the curvature of the system, and stress evolutions at (b) oxide/AlN top coating interface (on oxide side), (c) AlN top coating/substrate interface (on coating side) and (d) the center of substrate; triangles represent the curvature and/or stresses at ambient temperature. . . 127

4.27 Effect of creep properties of the substrate on (a) evolutions of the curvature of the system, and stress evolutions at (b) oxide/AlN top coating interface (on oxide side), (c) AlN top coating/substrate interface (on coating side) and (d) the center of substrate; triangles represent the curvature and/or stresses at ambient temperature. . . 128

4.28 Effect of creep properties of the AlN coatings on (a) evolutions of the curvature of the system, and stress evolutions at (b) oxide/AlN top coating interface (on oxide side), (c) AlN top coating/substrate interface (on coating side) and (d) the center of substrate; triangles represent the curvature and/or stresses at ambient temperature. . . 130

4.29 Effect of oxidation kinetics of AlN on (a) evolutions of the curvature of the system, and stress evolutions at (b) oxide/AlN top coating interface (on oxide side), (c) AlN top coating/substrate interface (on coating side) and (d) the center of substrate; triangles represent the curvature and/or stresses at ambient temperature. 131

4.30 Measured (blue points and curves) and calculated (orange and green curves) stresses at ambient temperature in (a) the top oxide and (b) AlN top coating; the residual stresses in top oxide and AlN top coating are measured by photoluminescence and Raman spectroscopy respectively (section 3.6.4). 133

5 Potential of AlN and SiC coatings for their use in solar receivers

5.1 Hemispherical spectral emissivity of uncoated Fecralloy, AlN coated Fecralloy before and after 4 fast oxidation cycles (25-1225 °C in the REHTPS set-up; the thickness of the 'standard' AlN layer is around 45 μm. 138
5.2 Hemispherical spectral emissivity of uncoated APMT, AlN coated APMT before and after 4 fast oxidation cycles (25-1225 °C in the REHTPS set-up, and after 100 h of oxidation in a conventional furnace at 1100 ∘C; the thickness of the 'standard' AlN layer is around 45 μm. 139
5.3 (a) surface morphology and (b) cross-section of SiC coating grown on TZM substrate coated with an AlN layer (15μm). 140
5.4 (a) Mass change of SiC/AlN coated TZM sample during cyclic oxidation at 1100 °C and (b) macroscopic image showing the failure of the sample after 5.5 h of oxidation. 141
5.5 (a) Surface morphology and (b) cross-section of SiC coating grown on TZM substrate coated with an AlN layer (15μm). 141
5.6 XRD θ-2θ patterns of the SiC/AlN coated TZM sample after cyclic oxidation. 142
5.7 Surface morphology of SiC coatings grown on (a) AlN coated Fecralloy and (b) pre-oxidized APMT coated with an AlN layer. . . 143
5.8 Cross-sections of the SiC coatings grown on (a) AlN coated Fecralloy and (b) pre-oxidized APMT. 143
5.9 Hemispherical spectral emissivity of uncoated Fecralloy and SiC/AlN coated Fecralloy before and after 3 fast oxidation cycles (25-1225 °C in the REHTPS set-up; the thickness of the 'standard' AlN layer is around 15 μm. 144
5.10 Hemispherical spectral emissivity of uncoated and SiC/AlN coated APMT; the thickness of the 'standard' AlN layer is around 15 μm. . 145

R.1 Schéma des technologies solaires à concentration. 154
R.2 Schéma des empilements de matériaux pour les récepteurs solaires. . 154
R.3 (a) Exemple de texture sur les revêtements déposés sur TZM et (b) une grande magnification de (a) à l'interface AlN/TZM. 155
R.4 Exemple de texture sur les revêtements déposés sur acier: (a) la morphologie de surface et (b) la microstructure. 155
R.5 Cinétique d'oxydation d'une couche de 45 μm d'AlN sur Fecralloy (ou APMT). 156
R.6 Mise en évidence de la porosité de la couche d'alumine formée au cours de l'oxydation. 156

R.7 Mise en évidence des contraintes dans le système revêtement/substrat: (a) évolution de courbure du système, et évolution des contraintes (b) à l'interface oxyde/AlN (dans l'oxyde), (c) à l'interface AlN/substrat (dans la couche d'AlN) et (d) dans le substrat; les triangles représentent la courbure et/ou les contraintes à température ambiante. 157
R.8 Emissivité hémisphérique spectrale à 300 K des échantillons d'APMT revêtu d'AlN (45 μm) et oxydé. 158

A.1.1 Property map showing the resistance of materials to fracture versus its resistance to creep. 187
A.1.2 Property map showing the resistance of materials to the spallation of AlN coating versus its resistance to creep. 188

A.2.1 Pole figures of coated system deposited at N/Al=3 (Figure 3.11(e) and (j)) for $(10\bar{1}2)$, $(10\bar{1}3)$ and $(20\bar{1}3)$) orientations; the A1 axis is perpendicular to the substrate surface. 189
A.2.2 Pole figures of coated system deposited at N/Al=11.25 (Figure 3.11(d) and (i)) for $(10\bar{1}2)$, $(10\bar{1}3)$, $(20\bar{1}3)$, and $(11\bar{2}2)$) orientations; the A1 axis is perpendicular to the substrate surface. . 190

A.4.1 Schematic representation of a part of the system; boundary conditions are employed in the finite element model: violet triangles represent symmetric boundary condition and the cyan one show the constraint of vertical displacement; MPC conditions applied at the righ edge to force nodes move along a straight line. 193
A.4.2 Normal stress field calculated by FEA after deposition at T_{amb}: (a) with MPC boundary condition applied at the right edge; (b) without the use of MPC boundary condition and (c) a high magnification of (b) at the right edge. 194

List of Tables

1 Introduction and overview

1.1 Central receiver systems build in the 20th century [20, 21]. 4
1.2 Central receiver systems in operation in 2018 [20–26]. 4
1.3 Comparaison of conventional Heat transfer fluids (HTFs) [1, 2, 24, 27–32]. 6
1.4 Chemical compositions in weight percent (wt%) of some nickel-based alloys. 12
1.5 Commercialized available solar selective coatings for temperatures higher than 400 °C. 17

2 Methodologies for a complete design for solar receiver materials

2.1 Main physical, mechanical and optical properties of AlN and SiC. . 24
2.2 Coefficients of fifth-order polynomial fit for the thermal expansion coefficient of polycrystalline AlN, Al_2O_3, 6H-SiC and 3C-SiC [9]. . . 24
2.3 Oxidation kinetics of AlN reported in the literature. 25
2.4 Piezospectroscopic coefficients for R-lines determined by He and Clarke [33]. 46

3 Deposition and high temperature oxidation of AlN coatings

3.1 Conditions for the deposition of AlN on Fecralloy to study the influence of N/Al ratio 61
3.2 Texture coefficients for AlN deposited with different N/Al ratio . . 64
3.3 Kinetic parameters for the oxidation of Fecralloy and APMT at 1100 °C 72
3.4 Oxidation kinetic parameter, k_p, for AlN in the temperature range of 800-1100 °C. 77

4 Thermomechanical model of multilayer coating systems

4.1 Stresses in AlN coatings and TZM substrate after deposition calculated by FEA with MPC boundary condition and the analytical model. 101
4.2 Calculated thermal strains at high temperature and accumulated creep strains after ten thermal cycles at the center of the AlN top coating, substrate and AlN bottom coating. 106

4.3 Coefficients of fifth-order polynomial fit for the thermal expansion coefficients of AlN and pure molybdenum (used for the calculation of thermal strain of TZM in the following analysis) [9, 34]. 107
4.4 Thermoelastic stresses and creep strains after 10 thermal cycles at the center of the AlN coatings and substrate calculated using constant and instantaneous thermal expansion coefficients. 107
4.5 'Standard' modeling conditions used. 118
4.6 Thickness of the top oxide scales after 100 h of thermal cycling. . . 119
4.7 Temperature at the top surface of the system and the thickness of the top and bottom oxide scales after 10 thermal cycles. 122

5 Potential of AlN and SiC coatings for their use in solar receivers

5.1 Calculated values (Eqs. (2.26) and (2.27)) of the solar absorptivity, total emissivity and α/ε ratio for uncoated Fecralloy and Fecralloy coated with AlN (40-50 μm) before and after cyclic oxidation. . . . 138
5.2 Calculated values (Eqs. (2.26) and (2.27)) of the solar absorptivity, total emissivity and α/ε ratio for the uncoated APMT, AlN (40-50 μm) coated APMT before and after cyclic oxidation in the REHTPS set-up, and after 100 h of oxidation in a furnace. 138
5.3 Calculated values (Eqs. (2.26) and (2.27)) of the solar absorptivity, total emissivity and α/ε ratio for uncoated Fecralloy and Fecralloy coated with SiC/AlN bilayer before and after cyclic oxidation. . . . 144
5.4 Calculated values (Eqs. (2.26) and (2.27)) of the solar absorptivity, total emissivity and α/ε ratio for uncoated and SiC/AlN coated pre-oxidized APMT. 145

A.1.1 Thermal, elastic and mechanical parameters used in determination of Fracture Resistance (FR), Creep Resistance (CR) and thermal shock resistance (ΔT) for a wide range of high temperature materials. 184

A.3.1 Material properties of AlN and TZM for the benchmark with FEA [7, 35–41]. 191
A.3.2 Input parameters for the benchmark with FEA. 191
A.3.3 Material properties of Al_2O_3 used in the complete model. 192
A.3.4 Material properties of APMT used in the model. 192

Abbreviations and nomenclature

Abbreviations

APMT	Oxide dispersion strengthened FeCrAl alloy, Kanthal, Sandivk
CSP	Concentraing solar power
CR	Creep resistance
CRS	Central receiver system
CVD	Chemical vapor deposition
EBSD	Electron backscatter diffraction
FR	Fracture resistance
HTCVD	High temperature chemical vapor deposition
HTF	Heat transfer fluid
MOCVD	Metal-organic chemical vapor deposition
ODS	Oxide dispersion strngthened
PECVD	Plasma-enhanced chemical vapor deposition
PLPS	Photoluminescence piezospectroscopy
PVD	Physical vapor deposition
PVT	Physical vapor transport
s-CO_2	Supercritical carbon dioxide
sccm	strandard cubic centimeters per minute
SEM	Scanning electron microscopy
TZM	Molybdenum-based alloy, 99 wt% Mo, 0.5 wt% Ti, 0.1 wt Zr% and C, Goodfellow Metal
XRD	X-ray diffraction

Symbols

D	diffusion coefficient
E	Young's modulus
E_a	Activation energy
k	Thermal conductivity
K_c	Fracture toughness
M	Molecular mass
$\overrightarrow{q}$	Heat flux
Q_{cr}	Creep activation energy

R_{total}	Total thermal resistance of system
T	Temperature
T_{amb}	Ambient temperature
T_b	Temperature at the backside of system
T_{growth}	Deposition temperature
T_m	Melting point
T_R	Receiver temperature
T_t	Temperature at the front-side of system

Greek symbols

α	Absorptivity
α_{th}	Thermal expansion coefficient
β	Supersaturation degree
δ	Boundary layer thickness
ϵ	Strain
ϵ_{cr}	Creep strain
ϵ_g	Growth strain in coating
ϵ_l	Lateral strain in oxide
ϵ_{th}	Thermal strain
ε	Emissivity
ν	Poisson's ratio
σ	Stress
σ_{cr}	Creep strength
σ_f	Failure strength
σ_g	Intrinsic growth stress
σ_{th}	Thermal stress
σ_{res}	Residual stress
ξ	Reacte fraction of oxidation
Ω	Volume per Al ion

Subscriptions

c	coating
o	oxide
s	substrate

Chapter 1

Introduction and overview

Introduction

The greatly expanding energy demand worldwide has led to the development of a sustainable energy supply. The application of sunlight as high temperature heat source for electricity production has been examined for several years. Numerous solar thermal power plants using solar concentration technology, namely concentrated solar power (CSP) plants, have been developed at the beginning of 1980s in the world (USA, Spain, France, ...). The first commercial CSP plant has operated in the Mojave Desert (California, USA) from 1984 by Luz Industries, combined with eight separated CSP plants constructed in the following years, providing a combined net capacity of 354 MW. These CSP plants, named solar energy generating systems, still operate today. Even though the development of solar thermal technologies has been slowed down due to the oil price shock in the early 1990s, nowadays, there is a renewed growing interest in CSP plants, to improve the security of energy supply and reduce greenhouse gas emissions from fossil fuels. Currently, CSP technology is considered as a clean and renewable alternative to fulfill electrical demands. Figure 1.1 shows the four main technologies used in CSP plants as described below:

- Parabolic trough: the most mature of the CSP technologies. This technology has been developed since 1980s and forms the bulk of current commercial plants. It is made up of parallel rows of curved mirrors concentrating solar radiations to an absorber tube located along the focus line of mirrors. The tube is filled with a heat transfer fluid (HTF) that might be oil or water/steam. The operating temperature is around 300-450 °C depending on the working HTF.

- Linear Fresnel reflector: its sunlight reflectors are similar to that of parabolic trough systems, but are flat or slightly curved mirrors to redirect sunlight onto a downward-facing tubular receiver. Linear Fresnel collector has lower cost, but it is less effective.

- Parabolic dish stirling system: it consists of a dish and generally a stirling engine or a micro-turbine placed at the focal point of the dish. Dish stirling systems are modular, meaning that each system could be used to produce

electricity independently or linked to increase capacity. The capacity of a dish stirling system is usually 5-25 kW [42].

- Central receiver system (CRS, sometimes referred to as solar power tower): this design uses a field of sun-tracking mirrors (heliostats) to concentrate sunlight on the receiver fixed at the top of a tower. Due to the usage of large numbers of mirrors and the high level of concentration, very high temperature heat could be generated. The CRS is generally quite large, with an optimum size of 50-400 MW [42].

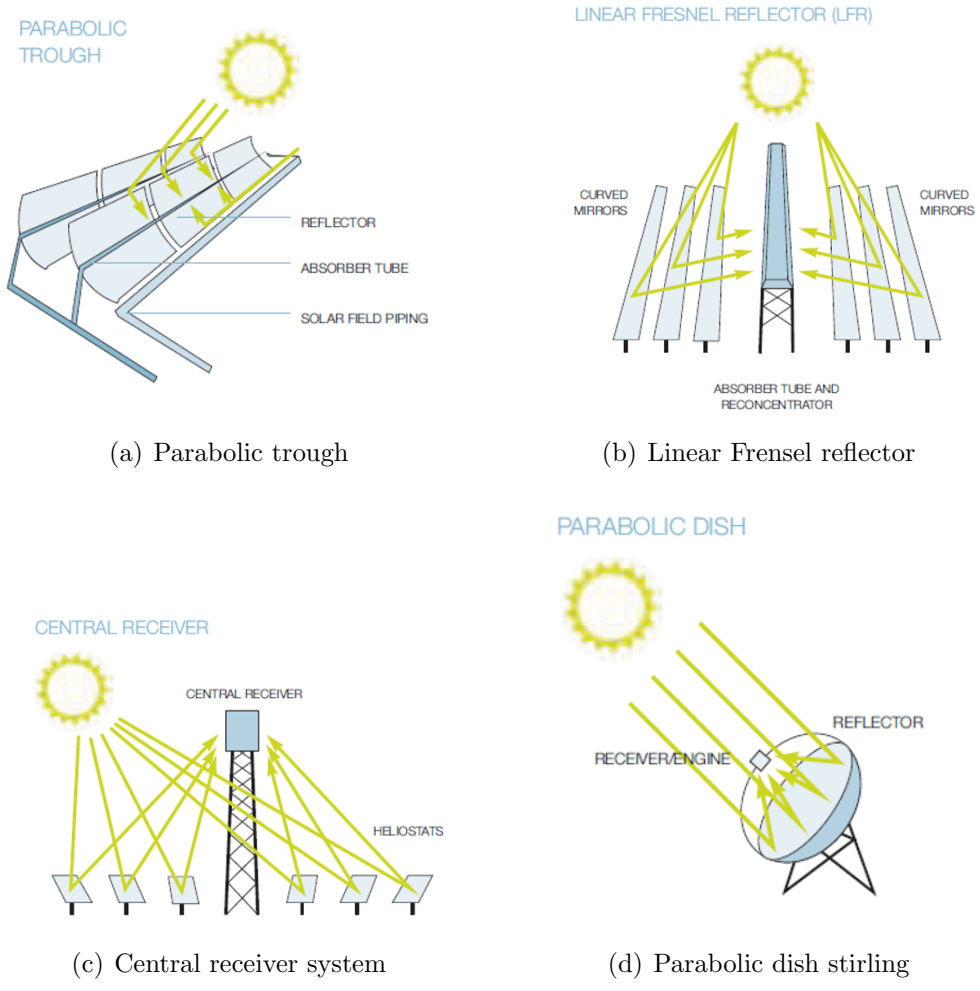

(a) Parabolic trough

(b) Linear Frensel reflector

(c) Central receiver system

(d) Parabolic dish stirling

Figure 1.1 Typical concentrated solar power technologies: parabolic trough, linear Fresnel reflector, central receiver system, and parabolic dish stirling [43].

These four CSP technologies are usually divided into two categories [43]:

(1) parabolic trough and linear Fresnel reflector are line-concentrating systems as their mirror reflectors concentrate sunlight onto a focal line (Figures 1.1(a) and 1.1(b)).

(2) sunlight is concentrated onto a focal point by heliostats in the central receiver

system (Figure 1.1(c)) and by a parabolic dish collector in the dish stirling (Figure 1.1(d)). They are also referred to as point-focusing systems.

1.1 Central receiver systems

Of all CSP technologies, CRS is moving to the forefront and becoming an emerging option for large-scale electricity production. The first CRS was built in 1981 in Spain with capacity of 0.5 MW. After that, various CRS projects have been carried out in the 1980s and 1990s. Although it is less mature than parabolic trough, the possibility for CRSs to provide higher plant efficiency leads to the improvement of this technology in the past decades. Another advantage is that CRS could easily and steadily employ thermal energy storage. To date, the total capacity of CRS worldwide is more than 3 GW_e, with a total gross capacity of 620 MW_e for operating plants [24, 25]. Table 1.1 and Table 1.2 summarize central receiver systems build in the 20th century and in operation around the world respectively.

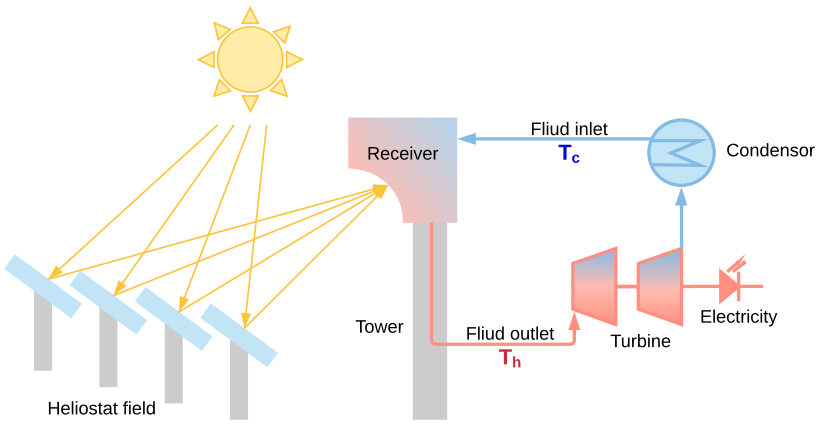

Figure 1.2 Schematic illustration of a Central Receiver System.

The basic design of this technology, as shown in Figure 1.2, is to collect and concentrate incident sunlight to a receiver placed at the top of a tower, by using a large field of flat, sun-tracking mirrors, known as heliostats, to produce high temperature heat by radiation. This heat is absorbed and then diffused by conduction within the internal part of receiver. A HTF, heated by thermal convection, then flows through the receiver and passes to a power cycle system which converts the thermal energy into electricity. The optimum shape of a CRS is a function of a wide variety of parameters, including solar radiations intercepted and absorbed, thermal loss, cost, and design of the heliostat field [42]. Receivers, coupled with Rankine cycle engines, operating at temperatures of less than 600 °C have been adopted in current commercial CRS using water/steam or molten salts as HTFs [27–29]. As shown in Table 1.2, water/steam is used as HTF in more than half of current operating CRS. However, high cost and difficulty of direct storage of high temperature and pressure steam in large storage systems limit its applications [1, 24, 27, 44]. Molten salts are available to be stored, and could

Table 1.1 Central receiver systems build in the 20th century [20, 21].

Project	**Country**	**Capacity (MW)**	**Heat transfer fluid**	**Beginning operation**
SSPS	Spain	0.5	Liquid sodium	1981
EURELIOS	Italy	1	Water/Steam	1981
SUNSHINE	Japan	1	Water/Steam	1981
Solar One	USA	10	Water/Steam	1982
CESA-1	Spain	1	Water/Steam	1983
MSEE/Cat B	USA	1	Molten salt	1984
THEMIS	France	2.5	Molten salt	1984
SPP-5	Russia	5	Water/Steam	1986
TSA	Spain	1	Air	1993
Solar two	USA	10	Molten salt	1996

Table 1.2 Central receiver systems in operation in 2018 [20–26].

Project	**Country**	**Capacity (MW)**	**Heat transfer fluid**	**Thermal energy storage**	**Beginning operation**
PS10	Spain	11	Water/Steam	1 h	2007
Jülich	Germany	1.5	Air	1.5 h	2008
PS20	Spain	20	Water/Steam	1 h	2009
Gemasolar	Spain	19.9	Molten salt	15 h	2011
ACME	India	2.5	Water/Steam	No storage	2011
Dahan	China	1	Water/Steam	1 h	2012
Greenway	Turkey	1.4	Water/Steam	4 MW/h	2012
Ivanpah	USA	392	Water/Steam	No storage	2014
Crescent Dunes	USA	110	Molten Salt	10 h	2015
SunCan	China	10	Molten salt	15 h	2016
Khi Solar One	South Africa	50	Molten salt	2 h	2016
Sundrop	Astralia	1.5	Water/Steam	No storage	2016
Jemalong	Australia	1.1	Liquid sodium	3 h	2017

be heated to temperatures of 565-600 °C for nitrate salts [30, 45, 46]. The most common liquid metals used in CRS such as liquid sodium, lead-bismuth and tin, have been studied at temperatures higher than 700 °C. Liquid metals are stable at high temperature with very high thermal conductivity, allowing higher radiation flux on the receiver, greater efficiencies as well as lower thermal stresses on tube walls [28]. However, corrosion and high cost (2-20 times more than molten salts) may be the main drawbacks and challenges for liquid metals as HTFs [29].

To minimize thermal loss, many new concepts are developed for high temperature service. Some new central receiver designs such as volumetric or external gas receivers using pressurized air, supercritical CO_2 (s-CO_2) or other gases as HTF are capable of integrating solar thermal energy in more efficient high temperature power cycles like Brayton cycle [46]. Another option to achieve high plant efficiency is particle-based receivers that heat solid particles by concentrated solar radiation. The advantage of particles as HTF is that they could be irradiated and heated directly to temperatures above 1000 °C, eliminating the heat transfer loss associated with indirect heating in traditional heat exchangers. Another advantage is that particle-based receivers could be associated with different options like high temperature and high efficient power cycle, or thermal storage integration using same particles as HTF and thermal storage medium [28, 29]. Table 1.3 provides a summary of limitations and advantages of different HTFs used in CRS.

Central receivers can be easily hybridized in a wide variety of options. Apart from thermal energy storage, hybridization with an additional combustion chamber using biomass or conventional fossil fuel allows to heat the HTF at higher temperature, which makes the power cycle more efficient. A second Rankine cycle with a vapor turbine is implanted to reuse excess heat after the gas turbine. This concept is developed in most recent research works [47–50]. Pressurized-air based solar receivers have been considered to be options for hybrid operation [51]. This design has been developed by the PROMES/CNRS laboratory, France, within the frame of PEGASE project (Production of Electricity by GAs turbine and Solar Energy) [52].

As Figure 1.3 shows, pressurized air (pressure of 8 bar and mass flow rate of 8 kg/s [53]) firstly heated through irradiated solar receiver, at a temperature exceeding 800 °C, is then sent to a combustion chamber using fossil fuel or biomass for a complete heating to reach higher temperatures (900-1300 °C). This hybridization step leads to the capacity to power Brayton cycle at a higher thermal efficiency. Hot exhaust out of the gas turbine could be then sent to a steam generator following a secondary Rankine cycle. This is called a Combined-Cycle, and can improve the overall solar to electricity efficiency to 30% or even higher [1, 53]. Moreover, in such Combined-Cycle modes, the costs of electricity are expected to be significantly reduced. Another advantage of Combined-Cycle is its capacity to economize cooling water. The consumption of cooling water for a Combined-Cycle is reduced by a factor of 2-4 compared to a single vapor cycle [53]. Together with these advantages, hybrid pressurized air receivers integrated Combined-Cycle have attracted increasing interest in the past few years and are expected to be options in the utility-scale electric power market.

Table 1.3 Comparaison of conventional Heat transfer fluids (HTFs) [1, 2, 24, 27–32].

HTF	**Advantages**	**Limitations**
Pressurized air	• Extensive operating temperature range • Compatible with high efficient cycles • Economic, environmentally friendly	• Low heat transfer coefficient • Indirect storage required • High pressure in receiver
Water/Steam	• Compatible with direct power cycles • Economic, environmentally friendly	• Operating temperature limited (<∼600 °C) • Difficult and high cost for direct storage at large scale • High pressure in receiver for efficient power cycle
Molten salt	• Compatible with direct storage, high storage capacity • Low cost, reduced inventory, high heat transfer coefficient • Low vapor pressure at operating temperature	• Operating temperature limited by its chemical stability • Freezing risks • Corrosive
Liquid metal	• High operating temperature • High thermal conductivity	• High cost • Corrosive and/or toxic
Solid Particles	• Stable at high temperature • Compatible with direct storage • Low cost • Available for direct solar irradiation • Able to be hybridized with high efficient air- or s-CO_2 Brayton power cycle	• Efficient air-solid heat exchangers required • Complex mass flow control
s-CO_2	• Extensive operating temperature range • Compatible with high efficient Brayton cycle • Able to integrate with molten salt direct storage • Low cost due to turbomachinery size and simple cycle designs	• High pressure in receiver • May be corrosive to several alloys at high temperature • Not commercial available

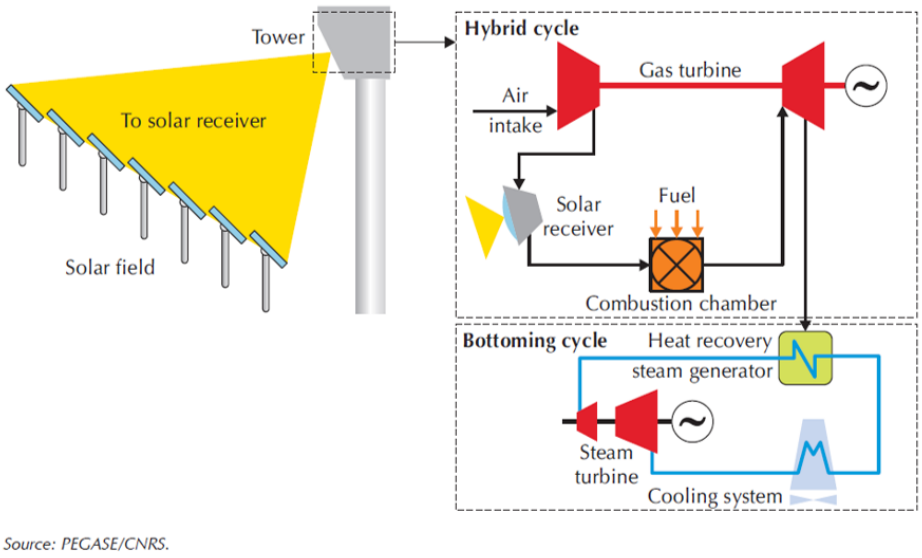

Figure 1.3 Concept of hybrid pressurized air receiver integrated Combined-Cyble in the framework of PEGASE [1].

1.2 Plant efficiency of central receiver systems

According to Carnot's theorem, increasing the efficiencies of any thermal system (nuclear, fossil fuel, or solar thermal) generally means to increase the operating temperature in hot sections. Based on the review in previous sections, CSP plants are compatible with high temperature power cycles and thus available to achieve high thermal efficiencies. Figure 1.4 shows major compatible power cycles for CSP plants and the benefits of increasing temperature of HTFs.

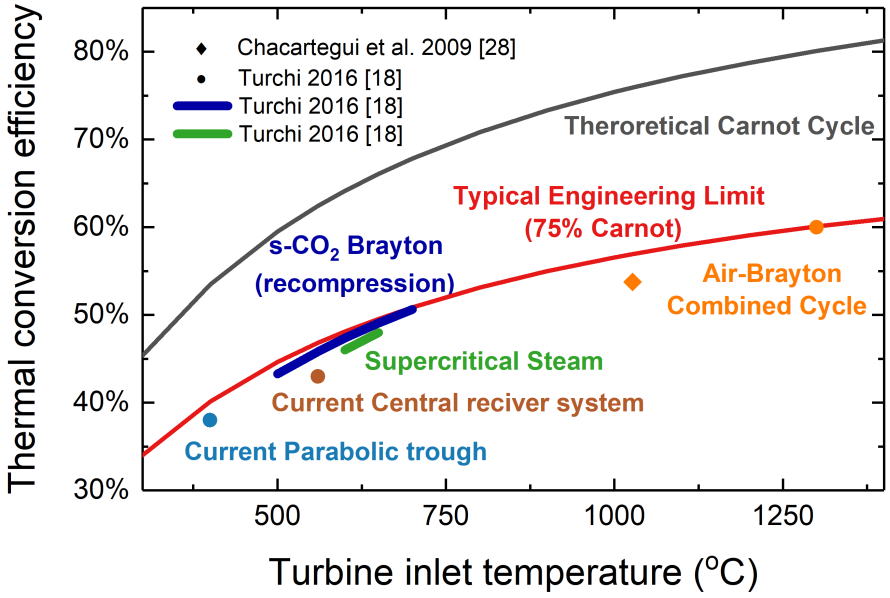

Figure 1.4 Power cycle efficiencies for different CSP technologies [2, 3].

The s-CO_2 recompression Brayton power cycle provides the potential to be operated at temperatures higher than 700 °C ($\sim$ 750 °C) and outlines the path to achieve high thermal efficiencies approaching or even exceeding 50% [31]. Air-Brayton Combined-Cycle is being considered to be the candidate not only for its ability to reach elevated operating temperature (of about 1300 °C) and corresponding very high thermal efficiency ($\sim$ 60 %) but also for its capacity of ensuring a continuous production of electricity throughout the day [47].

However, the plant efficiency of CSP plants is a complex combination of solar-to-thermal efficiency and thermal conversion efficiency in receivers. The solar-to-thermal efficiency of the receiver is a function of the incoming concentrated solar radiations and energy losses. When the operating temperature is increased, reflective, radiative and convection heat loss increase correspondingly.

Kretzchmar and Gauché [54] reported that radiative and convection heat losses are predominant over reflection losses within a high temperature range (>600 °C). The effect of reflection can be therefore neglected. Conduction losses are also neglected to simplify the calculation. Based on these assumptions, the solar-to-thermal (optical) efficiency, $\eta_{optical}$, could be expressed as follow [29]:

$$\begin{aligned} \eta_{optical} &= \frac{\alpha Q_{in} - Q_{loss}}{Q_{in}} \\ &= \alpha - \frac{\varepsilon \sigma T_R^4 + h(T_R - T_{amb})}{\eta_{field} E_{DNI} C} \end{aligned} \tag{1.1}$$

where Q_{in} and Q_{loss} are the incident irradiance on the receiver as well as the radiative and convection heat losses ($W{\cdot}m^{-2}$) respectively, α is the solar absorptivity (sometimes referred to as absorptance) of receiver, ε is its hemispherical emissivity (sometimes referred to as emittance) value, σ is the Stefan-Boltzmann constant (5.67×10^{-8} $W{\cdot}m^{-2}{\cdot}K^{-4}$), h is the convective heat transfer coefficient of air ($W{\cdot}m^{-2}{\cdot}K^{-1}$), T_R and T_{amb} are the receiver and ambient temperatures (K) respectively, η_{field} is the efficiency of heliostat field, E_{DNI} is the direct normal irradiance ($W{\cdot}m^{-2}$) and C is the concentration ratio defined as the ratio of concentrated solar flux on receiver to the incident solar flux. The concentration ratio is a dimensionless parameter, sometimes referred in unit of 'suns': ten suns means a concentration of a factor of ten. The concentration ratio represents the capacity of the sun-tracking systems of tracking the diurnal (daily) sunlight movement and keeping the receiver in the focus of reflectors. Generally, for line-focusing systems, their concentration ratios usually range from 40 to 100 suns. Higher concentration ratios (100-2000 suns) can be achieved by point-focusing systems [1].

The thermal conversion efficiency $\eta_{thermal}$ for a typical heat engine is 75% of theoretical Carnot efficiency:

$$\begin{aligned} \eta_{thermal} &= 0.75 \cdot \eta_{carnot} \\ &= 0.75 \cdot (1 - \frac{T_c}{T_h}) \end{aligned} \tag{1.2}$$

with T_c and T_h the temperatures of HTF in cold tank and hot tank of the power cycle respectively, as indicated in Figure 1.2.

Therefore, the solar-to-electricity plant efficiency of a typical CRS, η_{global}, is given by:

$$\begin{aligned}\eta_{global} &= \eta_{thermal} \cdot \eta_{optical} \\ &= 0.75 \cdot (1 - \frac{T_c}{T_h}) \cdot (\alpha - \frac{\varepsilon\sigma T_R^4 + h(T_R - T_{amb})}{\eta_{field} E_{DNI} C})\end{aligned} \tag{1.3}$$

To simplify the study, the heat losses by convective heat transfer from receiver to HTF are neglected, i.e., T_R=T_h. Figure 1.5(a) plots the solar-to-thermal efficiencies $\eta_{optical}$ and thermal conversion efficiency $\eta_{thermal}$ as a function of temperature for different concentration ratios. It is worth noting that the increase of concentration ratio reduces energy losses, improving the solar-to-thermal efficiencies. Therefore, a high concentration ratio is one of the critical points to maintain a high plant efficiency. To obtain a temperature of 1000 °C at the outlet, at least 1000 suns are required. However, as temperature increases, the solar-to-thermal efficiency decreases whereas the thermal conversion efficiency increases. The competition of energy losses and gains in power cycle versus the receiver temperature leads to an increase of efficiency in lower temperature ranges at which gains in power cycle predominates, and a decrease while energy losses exceed the gains. For each concentration ratio, it exists an optimum temperature at which the maximum plant efficiency could be obtained, as plotted in Figure 1.5(b).

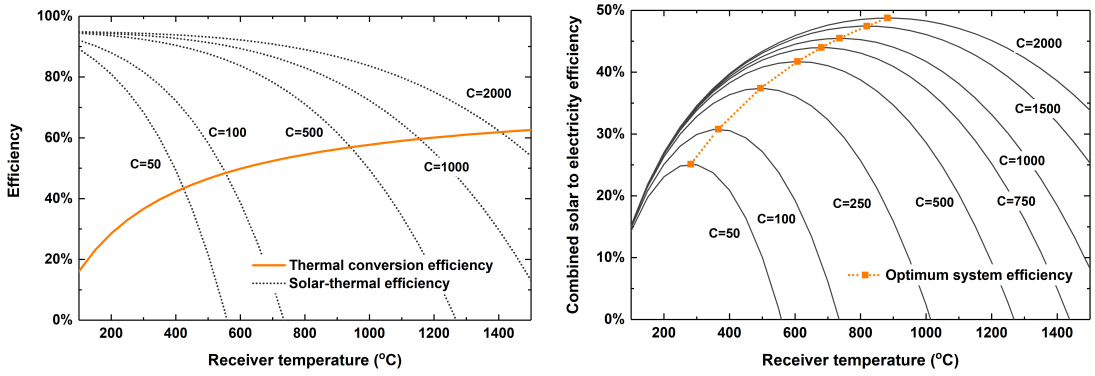

(a) (b)

Figure 1.5 Optical, thermal and global efficiency as a function of receiver temperature with varying concentration ratio: (a) optical (solar-to-thermal), $\eta_{optical}$, and thermal conversion efficiency, $\eta_{thermal}$, versus receiver temperature and (b) Optimum operating temperature for each concentration ratio; with α=0.95, ε = 0.85, h=10 W·m^{-2}·K^{-1}), η_{field}=0.6, E_{DNI}=1000 W·m^{-2} and T_{amb}=T_c=20 °C.

CRSs are capable of achieving concentration ratios up to several thousand suns, so the improvement in efficiencies in CRSs partially means the increase of operating temperatures in solar receiver. Moreover, the increase of temperature would require improved receiver materials. The aging of receiver materials during operation and their service lifetime would be the critical issue to evaluate the viability of CRSs operated at temperatures higher than 1000 °C in competitive electricity markets.

1.3 Current solar receiver materials

Different from conventional fossil fuel or nuclear power plants at which the heat supply is continuous, CSP plants operate under daily extreme thermal cycling. One of the most critical elements is the solar receiver. It is rapidly heated from zero to the peak power when exposed to concentrated sunlight and cooled down when a cloud passes between the sun and heliostats. Such thermal shocks lead to high thermal stresses and/or thus thermal-mechanical fatigue and failure of materials. Therefore, solar receiver materials must be able to resist to thermal cycling at fast heating (or cooling) rates and mechanical loads for high temperature operations. The question of which material is the most suitable for different temperatures is still under studied. The prediction of outlet temperatures of over 1000 °C for a variety of current solar receiver materials has not been fulfilled. In the following sections, an overview of currently used and potential receiver materials, as well as their allowable working conditions is provided.

1.3.1 High temperature metallic alloy based receivers

In general, metal-based alloys are suitable for solar receivers at temperatures below 800 °C due to their high mechanical strength and capacity for efficient heat transfer. A commercialized silicone-based paint coating, Pyromark 2500, developed by Tempil, USA, is generally used to increase the solar absorptivity [55].

Stainless steels are well known as structural materials in hot section of gas turbine. However, their maximum service temperatures are usually limited to 700 °C, due to their rapid degradation. Generally, with 9%-12% of Cr (ferritic and martensitic steels), the operating temperature is limited to 620 °C due to the breakaway oxidation and the degradation of creep strength [56, 57]. When the Cr content is higher than 12% (austenitic steels), the steels are capable of operating at temperatures of around 700 °C [57]. But the inherent high thermal expansion coefficient and low thermal conductivity of austenitic steels may cause large deformations and temperature gradients within the thin section, leading to high thermal mechanical fatigue. When thermal cycling is considered with creep, the combined effect can significantly affect the lifetime of the receiver. For example, the austenitic stainless steel 316H was used as a receiver tube material at Solar Two molten salt facility [58], but it was found to be susceptible to stress-corrosion cracking and thus it was not recommended for the next generation of high temperature CRS [59].

Refractory metals like tungsten (W) or molybdenum (Mo) have elevated melting points (>2200 °C), as well as adequate thermal and mechanical properties at high temperature. However, the main challenge is their low oxidation resistance.

Therefore, the capacity to develop a protective oxide layer, with excellent mechanical properties such as high creep rupture strength, thermal fatigue resistance and microstructure stability are important criteria for solar receiver materials that must operate under severe environment. Nickel-based alloys would be a compromise for these conflicting required properties.

1.3.1.1 Nickel-based alloys

Nickel based-alloys with high Cr content (>20%) are widely used as high temperature and high strength materials. Studies showed that advanced nickel-based alloys exhibit high creep rupture strength and are able to work with higher external load compared to conventional commercial stainless steels [4, 5, 60]. The commercial nickel-based alloy Inconel 625 has been studied as a receiver material in several solar projects since it displays high allowable stress in the temperature range of 600-800 °C [61–67]. Inconel 740H, one of enhanced age-hardenable nickel based alloys, is demonstrated to be suitable for solar receivers operating up to 800 °C for next generation of high temperature CRS due to its excellent high temperature creep strength and corrosion resistance [4, 68].

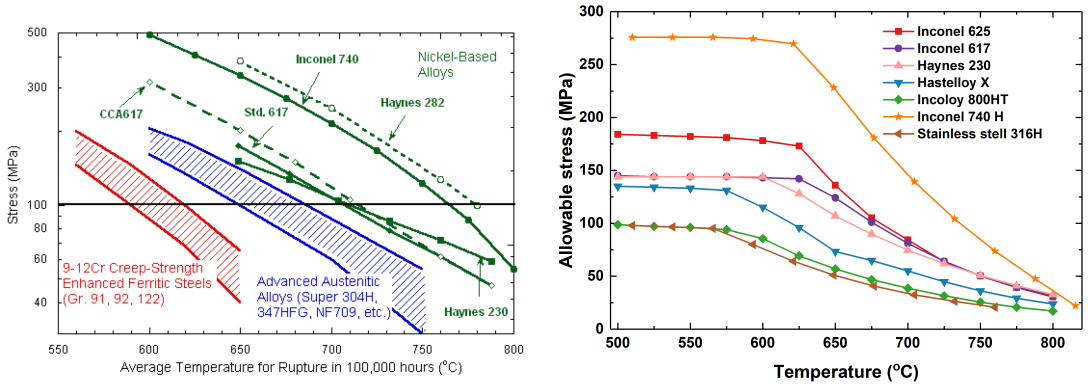

(a) (b)

Figure 1.6 Creep rupture strength and allowable stress as a function of operating temperature for various nickel-based alloys and stainless steels: (a) 100,000 hour creep rupture strength [4] and (b) allowable stress [5, 6].

In general, 100,000 hours creep rupture strength and allowable stress under creep conditions (determined as 80% of the minimum creep rupture stress at 100,000 h) are usually the design criteria for high temperature components. Figure 1.6 provides a comparison of 100,000 hours creep rupture strength and allowable stress for various nickel-based alloys and stainless steels. Chemical composition of some nickel-based alloys are given in Table 1.4. In Figure 1.6(a), no stainless steels have creep rupture strength exceeding 100 MPa at 700 °C, while nickel-based alloys such as Inconel 740 and Haynes 282 satisfies the target of 100 MPa throughout the temperature range of 600-760 °C. However, the allowable stress of such alloys degrades rapidly when the operating temperature is higher than 625 °C (Figure 1.6(b)).

Another challenge is the thermal fatigue damage caused by rapid heating and cooling process, as well as transient variations in daily operational conditions. Therefore, materials must be able to resist to the thermal fatigue throughout the lifetime of the receiver (>30 years [45, 59]). Klob [59] has studied the low-cycle fatigue (LCF) behavior at Solar Two for three different nickel-based alloys: Incoloy 800H (I-800H), Inconel 625-LCF, and Haynes 230. I-800H is one of high temperature materials and has been used in the Solar One steam receiver [73].

Table 1.4 Chemical compositions in weight percent (wt%) of some nickel-based alloys.

Materials	**Haynes 230**	**Haynes 282**	**Hastelloy X**	**Inconel 617**	**Inconel 625**	**Inconel 625-LCF**	**Inconel 740**	**Inconel 740H**	**Incoloy 800H**	**Incoloy 800HT**
C	0.10	0.06	0.07	0.10*	0.10*	0.03*	0.03	0.03	0.10*	0.10*
Cr	22	20	21.27	22	21	23*	25	24.5	23*	23*
Mo	2.0	8.0	8.59	9.0	9.02	10.0*	0.5	0.1	...	...
Co	5*	10	1.55	12	1*	1.0*	20	20	...	...
Al	0.3	1.5	0.12	1	0.4*	0.40*	0.9	1.35	0.60*	0.60
Ti	...	2.1	0.01	0.50	0.4*	0.40*	1.8	1.35	0.60*	0.60*
Mn	0.5	0.3*	0.51	1.0*	0.1*	0.50*	0.3	1.0*	...	...
Si	0.4	0.15*	0.24	1.0*	0.5*	0.15*	0.5	0.15	...	...
Ni	Bal	Bal	Bal	Bal	Bal	Bal	Bal	Bal	Bal	Bal
Others	W 14	Fe 1.5*	W 0.59	Fe 3.0*	Fe 5	Fe 5.0*	Fe 0.7	Fe 3.0*	Fe 39.5	Fe 39.5
	Fe 3*	B 0.005	Fe 18.63	B 0.006*	Nb 3.7	Nb 4.15*	Nb 2.0	Nb 1.5		
	La 0.02		B 0.002			P 0.0115*				
	B 0.015*					S 0.015*				
Reference	[56]	[56]	[69]	[56]	[56]	[70]	[56]	[71]	[72]	[72]

* Maximum

Inconel 625-LCF has been studied by Sandia National Laboratories (SNL) and industry after Solar Two, and was proposed as a potential material for the next generation of high temperature molten-salt power towers [59]. Haynes 230 was found to be more thermally stable than the two other studied nickel-based alloys [59]. It has already been identified as high temperature material adopted by ASME Boiler and Pressure Vessel Code (BPVC) [74]. The low-cycle fatigue data for these alloys for temperatures of 565 °C, 600 °C and 650 °C demonstrated the high performance of Haynes 230 in this temperature range. This alloy is also identified as the most suitable receiver material for temperatures in the range of 600-800 °C.

However, for temperatures above 800 °C, thermal fatigue may cause the failure of nickel-based alloys. Generally, their maximum operating temperature may be limited to 900 °C. Rojas-Morín and Fernández-Reche [75] proved that Inconel 625-LCF plates exposed to a solar radiation flux of 800 $kW \cdot cm^{-2}$ could reach a maximum operating temperature of 908 °C. But when temperature exceeds 800 °C, the thermal stresses may approach the tensile strength of Inconel 625-LCF, which could lead to its failure.

Olivares et al. [76] have tested three nickel-based alloys with greater than 20% Cr content (Haynes HR160, Hastelloy X and Haynes 230) in the temperature range of 900-1050 °C for a duration of 10 h. Although Haynes 230 shows the best oxidation resistance in dry air and dry CO_2, the linear breakaway oxidation in air at temperatures higher than 1000 °C and scale spallation in CO_2 at 1050 °C were observed.

1.3.2 Ceramics

Reaching outlet temperatures of 1000 °C or even higher could be achieved by using ceramic materials. Ávila-Marín [77] has presented a detailed review of refractory ceramic materials used in volumetric receivers, including alumina (Al_2O_3), silicon infiltrated silicon carbide (SiSiC), and silicon carbide (SiC). Alumina, which has an elevated melting point of 2000 °C, is one of promising materials because of its low price and good oxidation properties. SNL has tested a volumetric air receiver made up of 92% alumina with 80% porosity (reticulated foam from Hi-Tech Ceramics) [78]. The absorber is coated with Pyromark 2500 paint coating to increase the absorptivity. The maximum average air outlet temperature has reached 730 °C, showing an efficiency of 54%. The efficiency in this case is defined as the power gained by air divided by incident power, with a material temperature of 1350 °C. It has also been demonstrated that this type of porous ceramic receiver can operate at elevated temperature (>1000 °C).

The Weiwmann Institute of Science (WIS) and Rotem Industries developed the first Directly Irradiated Annular Pressurized Receiver (DIAPR) using alumina-silica (60% Al_2O_3) tubes as receiver materials [79, 80]. The most encouraging result is that the air outlet temperature reached 1204 °C with a working pressure of 18 bar in 250 h of operation [79]. Karni et al. [79] also experimentally demonstrated the capability of DIAPR to operate at temperatures up to 1300 °C. Despite its high service temperature and oxidation resistance, the absorptivity of bulk alumina and

its low thermal conductivity at high temperature are still the main drawbacks to be overcome.

SiSiC ceramics have been tested as receiver materials in different projects due to their good thermal properties. However, the maximum outlet temperature did not achieve temperatures over 800 °C [77]. Silicon carbide is another attractive material due to its elevated operating temperature, high strength, high thermal conductivity, low thermal expansion and good resistance to oxidation at high temperature [29]. Moreover, its naturally black color enhances its solar absorptivity, enabling the effective solar absorption and heat transfer in the receiver [81, 82]. PROMES laboratory has designed and constructed a pilot-scale plate solar absorber module with SiC ceramics (BOOSTEC®SiC) at Themis solar central receiver facility [83, 84]. Leray et al. [84] proved that with an incident solar power of 54 kW, the temperature at the back side of the module reached 840 °C, while the pressurized air is heated at around 650 °C at the outlet. This demonstrated the viability of the design of the module. However, the brittleness of SiC may lead to the failure of material when subjected to high mechanical load [85].

Sani et al. [86] have investigated the use of zirconium carbide (ZrC) as solar receiver material. The high temperature emissivity of ZrC is markedly lower than that of SiC in the temperature range of 827-1127 °C. Caccia et al. [87] developed a cost-effective composite of ZrC and W as a receiver material used at temperatures above 750 °C. The ZrC/W-based composite has a high rupture strength ($\geq$350 MPa) at 750 °C without and after thermal cycling and high thermal conductivity ($66.0 \pm 4.6\ W \cdot m^{-2} \cdot K^{-1}$), which is 2.5-3 times greater than that of nickel-based alloys at the same temperature). However, the poor oxidation resistance of both ZrC and W requires a novel strategy that utilizes s-CO_2 with the addition of more than 20 parts per million (p.p.m.) of carbon monoxide (CO) as HTF to prevent the oxidation of copper (Cu) coated ZrC/W-based composites [87].

Other ultra-high temperature carbides such as hafnium and tantalum carbides (HfC and TaC) have also been investigated due to their high melting point (>3900 °C), good chemical stability and thermomechanical properties [88]. These carbides are also considered to be promising materials for extremely high temperature applications, i.e., aerospace industry, nuclear fusion reactors and scramjet engines [89]. Recently, HfC and TaC are found to be useful as intrinsic solar selective materials [89, 90], but the knowledge of their optical properties is still missing [88, 89]. Sani et al. [88, 89] measured the emissivity of HfC and TaC in the temperature range of 827-1227 °C. Results show that the HfC and TaC based ceramics have higher reflectivity in the medium-infrared region than SiC, and thus considerable lower emissivity ranged from 0.2 to 0.6.

As described in 1.2, the radiative losses are predominant at high temperatures. The decrease in thermal emissivity of solar materials helps in reducing the energy loss and thus improving the plant efficiency. However, the poor oxidation resistance of these carbides make them impossible to be used in an open atmosphere, which implies their use under vacuum or inert environment [88]. Therefore, the high cost would be an important concern.

Diborides of transition metals such as zirconium, hafnium and tantalum diborides (ZrB_2, HfB_2, and TaB_2), have been widely considered as potential materials in the ultra-high temperature environments due to their elevated melting points (>3000 °C) [91]. However, the application of pure borides is limited by the formation of non-protective boron trioxide (B_2O_3) in temperatures higher than 1100 °C. The evaporation of B_2O_3 leads to the formation of porous metal oxides at the temperature range of 1100-1400 °C, and the rapid, linear oxidation kinetics later for temperatures above 1400 °C. [92]. The addition of a secondary phase (silicon carbide or transition metal silicides) is mandatory to improve the oxidation resistance of these diborides to at least 1600 °C [93], and to increase their flexure strength to more than 800 MPa in the temperature range of 1500-2100 °C [94]. These transition metal diborides-based ceramics also exhibit comparable high thermal conductivity to refractory metal-based alloys (80-110 $W{\cdot}m^{-1}{\cdot}K^{-1}$) up to 2000 °C [95]). Therefore, ongoing researches study their potential for use as receiver materials in CRSs [88, 96–101].

Reported emissivities of the diborides-based materials are ranged from 0.25 to around 0.4 in the wavelength range of 0.6-40 μm for temperatures in the range of 1100-1450 K, which are remarkably lower than that of SiC (0.6-0.8) [96–98, 100]. However, the absorptivity in the visible wavelengths is lower (0.44-0.52 depending on the processing and the secondary phase) [101]. It is also worth noting that the emissivity is a surface property. The oxidation of diborides could significantly change the optical properties due to the formation of a thin silica (SiO_2) scale. The oxidized diborides have a similar emissivity as oxidized SiC [101].

MAX phase materials are a family of carbides and nitrides. Their general chemical formula are $M_{n+1}AX_n$ (n=1, 2 or 3), where M is an early transition metal, A is an element from groups 13-16, and N is carbon, nitrogen or both. MAX phase materials are proposed as possible solar receiver materials for high temperature operations since they combine both ceramic- and metal-like properties as well as excellent oxidation resistance at high temperature [102]. Sarwar et al. [102] studied the absorptivity of MAX phase materials (Cr_2AlC and Ti_2AlC) as a function of exposure time for a maximum duration of 24000 s. Results show that the absorptivity (measured at temperature of 60±5 °C) of both materials increases over time, from 0.639 to 0.671 for Cr_2AlC and from 0.717 to 0.828 for Ti_2AlC, independent upon incident solar flux. However, the data of high temperature emissivity of MAX phase materials in the infrared spectrum is still missing.

1.3.3 Solar selective coatings

Currently, the commercial paint coating Pyromark 2500 has been used on central receivers to enhance solar absorption. It could be easily applied on different material, like steel, alloys and ceramics. However, its emissivity (> 0.9 at 1000 °C) is similar to its absorptivity (~ 0.96) [55]. Nevertheless, its absorptivity degrades when exposed to a temperature of around 750 °C or higher within a few days [55]. Therefore, solar selective coatings (sometimes referred to as solar absorber coatings) have been studied for decades to achieve higher solar absorption efficiency. An ideal solar selective coating should have a high solar absorptivity α

(ideally 1 in the visible wavelength region) to absorb most of sunlight and a low emissivity ε (ideally 0) to minimize the thermal radiations. The above conditions could be expressed by Eq.(1.4) and schematically represented in Figure 1.7:

$$\begin{cases} \alpha(\lambda) = 1 & 0.3\ \mu m < \lambda < \lambda_c \\ \varepsilon(\lambda) = 0 & \lambda_c < \lambda < 30\ \mu m \end{cases} \tag{1.4}$$

where λ_c is the critical wavelength (between 2 and 3 μm) depending on the operating temperature [103].

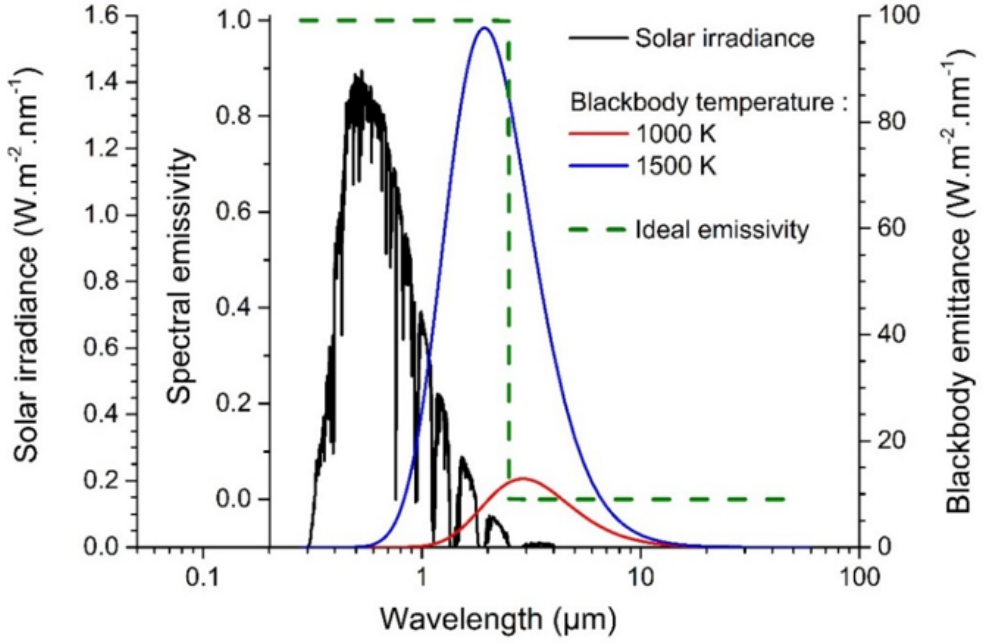

Figure 1.7 Spectral emissivity of an idealized solar selective coating, accompanied with solar spectral irradiation and the black-body radiation spectrum at two different temperatures (1000 K and 1500 K) for a better understanding.

Many novel selective coatings have been developed with various techniques and some of them have already been commercialized [104, 105]. Table 1.5 provides a list of some commercial selective coatings capable of working at temperatures high than 400 °C and their optical properties. However, for instance, there is no commercial selective coatings that could be used in the oxidizing environment [104]. Nevertheless, the operating temperature of solar selective coatings are generally limited by their thermal stability and oxidation resistance. There is also a degradation of absorptivity and an increase of emissivity at high temperature. Most of the developed selective coatings have been successfully applied at mid-temperatures ($\sim$ 600 °C), but the selective coatings with high performance and long durability at high temperature (>800 °C) are still lacking. Gray et al. [106] reported that $TiSi_2$-based coating could achieve the target of withstanding high temperature operation with high solar absorption efficiency ($\sim$ 0.9), but its durability in air is not yet studied.

Table 1.5 Commercialized available solar selective coatings for temperatures higher than 400 °C.

Company	**Coatings**	**Absorptivity**	**Emissivity**	**Thermal stability**	**Reference**
Almeco-TINOX,	TiNOX energy	0.95	0.04 at 100 °C	400 °C in vacuum	[105, 107]
Germany	TINOX Nano	0.90	0.05	400 °C in vacuum	[105, 107]
	TINOX artline	0.90	0.05	400 °C in vacuum	[105, 107]
Schott, Germany	*	$\geq$0.95	$\leq$0.095 at 350 °C	500 °C in vacuum	[105]
Angelantoni-ENEA,	Mo-SiO_2	0.94	<0.13 at 580 °C	580 °C in vacuum	[108]
Italy	W-SiO_2	0.93	<0.14 at 550 °C	580 °C in vacuum	[109]
Simens, Germany	Al_2O_3 based cermet	0.6	0.10 at 400 °C	400 °C in vacuum	[105, 107]
	Mo-Al_2O_3	0.96	0.16 at 350 °C	350-500 °C in vacuum	[105, 107]
	W-Al_2O_3	0.96	0.16 at 350 °C	350-500 °C in vacuum	[105, 107]
GRINM, China	GRIST70/90/42	0.96	<0.09 at 400 °C	400 °C in vacuum, 350 °C in air	[105]
	GRIST70A	0.95	<0.09 at 400 °C	400 °C in vacuum, 350 °C in air	[105]
TurboSun, China	W-AlN	0.92-0.94	0.08-0.10 at 350 °C	330-500 °C in vacuum	[110]
	SS-AlN	0.94-0.95	0.12-0.14 at 350 °C	500 °C in vacuum	[111]

* for PTR®70Premium receiver

1.4 Guidelines for selection of receiver materials

Actually, receivers in commercial CRS are built with metal-based alloys, the operating temperatures in commercial CRS are generally limited to an average maximum temperature of 600 °C [112], partially due to the degradation problems of the receiver materials at high temperature when exposed to air. The present study, based on the concept of Combined-Cycle hydride pressurized air receiver (Figure 1.3), aims to develop suitable and reliable material which is capable of operating at high temperature, in order to meet the high plant efficiency target. As one of the most important elements in CRS, the receiver undergoes extremely high solar flux and high temperature. Its performances consequently greatly affect the efficiency, the viability, and the lifetime of CRS. Therefore, selection of suitable and compatible receiver materials is one important key to highlight the path for the development of the next generation CRS. The present work aims to develop materials hat could withstand temperatures close or ever higher than 1000 °C (Figure 1.8) in a solar receiver to reach higher efficiency. According to Morris et al. [112], ideal candidate materials should possess a combination of properties such as:

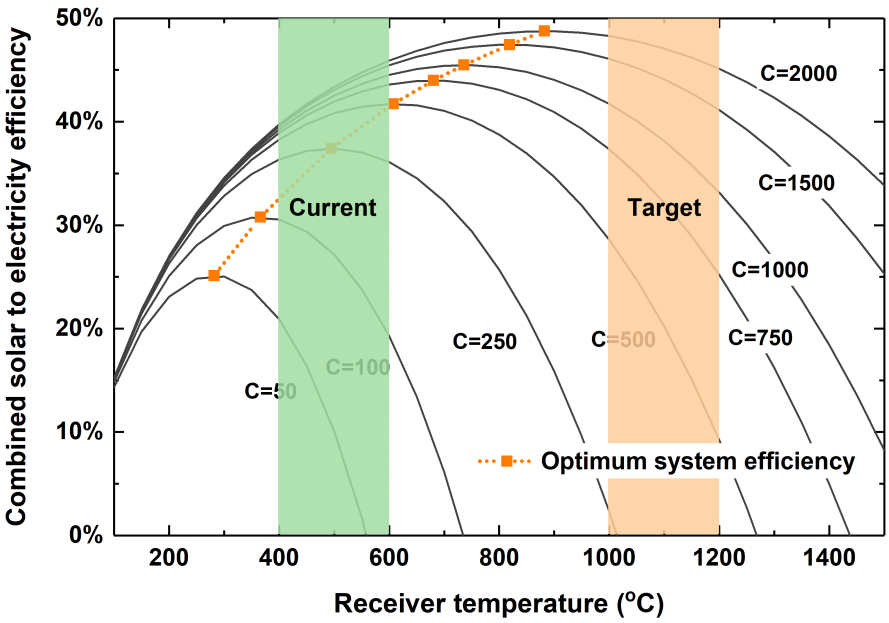

Figure 1.8 Current temperature in commerical CRS and the targeted temperature in the present work; the global efficiency with respect to receiver temperature for different concentration ratios has been presented in Figure 1.5(b).

- High solar absorption of solar radiations and reduced emissivity at high temperature;
- High temperature stability;
- High thermal conductivity;
- Sufficient low thermal expansion coefficient;

- Low creep during thermal cycling ;
- Resistance to high temperature oxidation and/or corrosion.

Solar Selectivity As mentioned in previous sections, an ideal non-transparent solar absorber material should have a total absorption in the visible region and zero emission in the infrared region. But it is evident that this ideal case will never be reached. Therefore, it is common to use the absorptivity to emissivity ratio (α/ε) as an important parameter for evaluating the solar selectivity of materials [101]. Moreover, Burlafinger et al. [113] investigated the influence of solar absorptivity on the overall plant efficiency and pointed out the importance of a high absorptivity value at low wavelengths. It is also reported that the effect of low emissivity at longer wavelengths is less important [113]. Furthermore, the corresponding optimal operation temperature increases when the system has a higher concentration ratio. Therefore, the radiation losses are getting merged with the incident solar radiation. It is difficult to separate these effects and thus, for concentration ratios exceeding 1200 suns (optimal operation temperatures higher than 1000 °C), materials with higher absorptivity yield higher plant efficiency [113]. The solar selective absorbers are reported to be more suitable for lower concentration ratios (especially <100 suns) [113].

High Temperature Stability It is important to identify the ability of materials to retain their functionality at high temperature. Materials should have as high melting point as possible and the ability to work at high temperature, i.e. higher than 1000 °C in the present study. No phase transformation and significant microstructure evolution throughout the operation period should be observed.

Thermal Conductivity High thermal conductivity of materials is required for efficient heat transfer from the incident solar radiation to the HTFs, and reduction of thermal gradient as well. It allows also to increase solar flux densities on the material surface.

Thermal Expansion Coefficient The material should have a low thermal expansion coefficient, which should be compatible with surrounding supporting components. A low thermal expansion coefficient is important for solar receiver materials to reduce thermal deformation and limits the stresses when subjected to thermal shock [112]. Moreover, low thermal expansion coefficient, coupled with high thermal conductivity could avoid thermal mechanical fatigue during thermal cycling, especially for thin components [4].

Creep strength As discussed in the section 1.3.1, creep behavior at high temperature is one of key design factors for high temperature components. Creep rupture strength (see Section 1.3.1) is usually used to evaluate the lifetime of materials withstanding external loads. However, it is reported that for those high temperature components, the damage comes mainly from the creep deformation during steady-state operation [32, 114]. Thus, in the present study, the deflection of materials is considered as the design-limiting factor rather than fracture. The limiting creep strength is therefore determined by a minimum creep strain rate or a specified amount of creep deformation in a given time [115, 116]. This will be pursed in detail in Chapter 2 and Chapter 4.

Oxidation Resistance The outer-surface of receiver materials is exposed to oxidizing environment, while the internal part is in contact with the HTFs. Therefore, the candidate materials should be resistant to oxidation and/or corrosion depending on the HTF. Moreover, the damage from cyclic oxidation might be more significant than that caused by isothermal oxidation due to severe heating/cooling [112]. It is worth noting that the protective oxide scale developed on receiver materials (normally Al_2O_3, SiO_2, Cr_2O_3, and etc.) usually have lower thermal expansion coefficients than metallic alloys. The thermal expansion mismatch of oxide scale and material substrates may cause cracking of the oxide during thermal cycling, leading to the lack of protection at high temperature.

It is difficult or impossible to fulfill all these conflicting properties with a single material. The overall objective of this study is to develop solar receiver materials compatible with temperatures of over 1000 °C. The basic concept is to develop an optimal multilayer coating system consisting of a high temperature metallic alloy and additional protective ceramic coating(s). The methodology for a complete design is described in Chapter 2. The selection of materials, basic theories for deposition, and the characterizations will be discussed in detail.

Conclusions

There is a growing interest in concentrated solar power systems as alternative solutions for power generation at the utility level. Efficiency optimization means increasing the operating temperature of solar receivers. One of the challenges is therefore to build solar receivers that can operate at high temperatures for a lifetime of 30 years. The building materials of the receiver must have properties against accelerated ageing due to mechanical loads, severe thermal cycles, oxidation at high temperature, etc. Temperatures in receivers currently in use are generally limited to 600 °C. The choice and improvement of suitable materials are therefore necessary to achieve operating temperatures above 1000 °C with a lifetime of at least 10 years. The objective of this work is to develop multilayer coatings for solar receivers operating at temperatures above 1000 °C.

Chapter 2

Methodologies for a complete design for solar receiver materials

Introduction

As discussed in Chapter 1, one of the challenges for central receiver systems is the selection of solar receiver materials compatible with operating temperatures of over 1000 °C. The aggressive high temperature environments not only accelerate the aging of materials but degrade their thermal, mechanical and optical properties as well [66]. Thus, the high temperature behaviors of materials play important roles on the overall efficiency, the reliability and the lifetime of CRS. In such case, the selection of materials is dependent upon a wide range of optical, physical, mechanical and chemical properties, which may not be fulfilled with one particular material. For example, the poor oxidation resistance at elevated temperatures limits the application of high strength metallic materials. However, the inherent brittleness of ceramics might lead to the fracture and failure at the early stage of their service life.

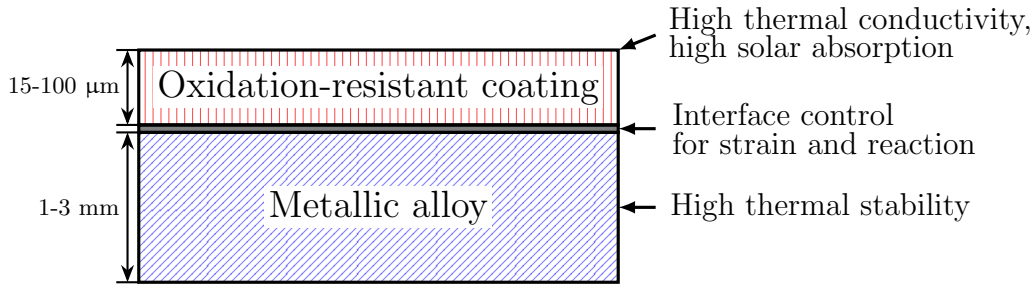

Figure 2.1 Schematic representation of coating-substrate system.

In the present study, the research route is to develop protective ceramic coating(s) deposited onto a high temperature metallic alloy (Figure 2.1). The metallic substrate is selected for its excellent thermal and mechanical properties, while the coating(s) should exhibit good surface properties like high absorptivity and good oxidation resistance to protect the metallic substrate against aggressive oxidizing environments. A careful control of the ceramic/metallic alloy interface

may be required to avoid delamination. Herein, it is expected that this coating(s)/substrate system has combined properties of both ceramics and metals.

2.1 Selection of materials

2.1.1 Coating materials

Ceramic materials usually have very high operating temperatures according to their nature and crystalline lattice. Most of them exhibit good resistance to oxidation. Alumina and zirconia (ZrO_2) could be considered as candidate materials as well due to their ability to be operated at high temperatures. However, the degradation of their thermal conductivity from room temperature to 1000 °C leads to loss of thermal energy during heat transfer and thus lower efficiency. Other potential ceramics could be ultra-high temperature carbides and diborides mentioned in section 1.3.2. However, despite their low thermal emissivity, they are not resistant to oxidation above 1100 °C. MAX phase materials combine both ceramic- and metal-like properties, but the lack of high temperature emissivity data and their difficulty to synthesis in form of coating limit today their application. For this reason, silicon carbide (SiC) and aluminum nitride (AlN) are considered as candidates in this work. These two compounds are composed of abundant elements like Si and Al. They are non-oxides and both of them have the tendency to get oxidized and form a stable, passivating oxide scale in oxidizing environment. In addition, both SiC and AlN retain good thermal conductivity at high temperature. Furthermore, both SiC and AlN do not undergo phase transformation between room temperature and 1100 °C.

Silicon carbide (SiC)

According to prior studies, SiC is one of the potential solar receiver materials due to its high melting point, high thermal stability, good thermal properties, high strength, high absorptivity and oxidation resistance at high temperature. More than 200 SiC polytypes are identified. They are described by different stacking of Si-C double layers along the direction perpendicular to the closed-packed plane, i.e., the cubic (111) or the hexagonal (0001). Among these polytypes, the 3C (cubic)-, 6H (hexagonal)- and 4H (hexagonal)-SiC are reported as the most stable ones. The 3C polytype is the most common polytype in CVD growth below 1300 °C, like in this work. Table 2.1 summarizes the physical, mechanical and optical properties of SiC and Figure 2.2 presents the thermal conductivities of Al_2O_3, AlN and 6H-SiC high purity single crystal as a function of temperature. Their instantaneous thermal expansion coefficients calculated by the first principle theory are plotted in Figure 2.3 [9]. The thermal expansion coefficient of a polycrystalline material with hexagonal crystal structure, $\alpha_{th,L}$ (K^{-1}), is calculated as follows:

$$\alpha_{th,L} = \frac{2\alpha_{th,a} + \alpha_{th,c}}{3} \tag{2.1}$$

where $\alpha_{th,a}$ and $\alpha_{th,c}$ are thermal expansion coefficients of a-axis and c-axis respectively. Data are fitted by a fifth order polynomial as expressed as follow:

$$\alpha_{th,L} = A_0 + A_1 T + A_2 T^2 + A_3 T^3 + A_4 T^4 + A_5 T^5 \tag{2.2}$$

where A_{0-5} are fitting constants listed in Table 2.2 and T is the temperature (K).

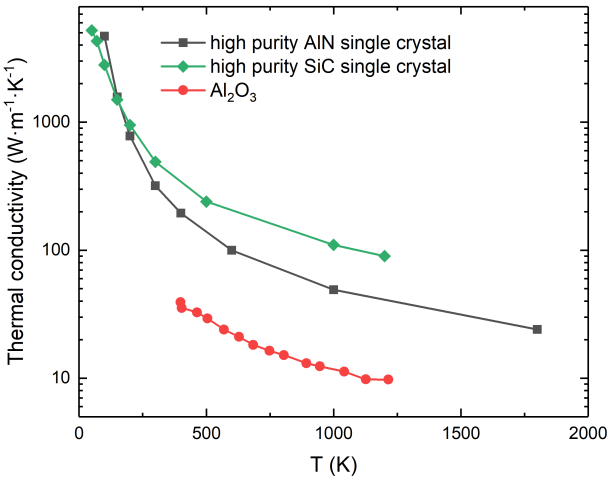

Figure 2.2 Thermal conductivities of Al_2O_3, high purity AlN and SiC single crystals versus temperature [7, 8].

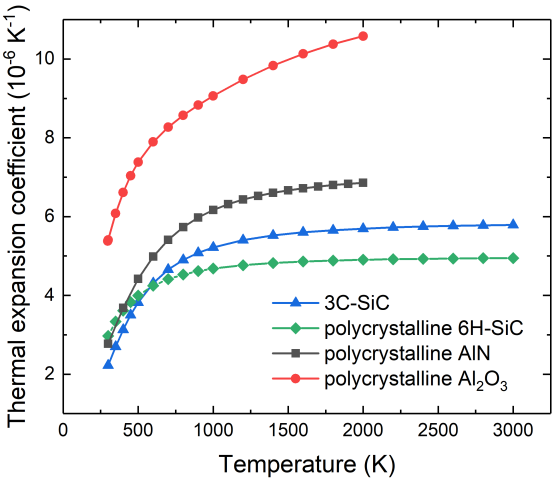

Figure 2.3 Instantaneous thermal expansion coefficient of 3C-SiC, polycrystalline 6H-SiC, AlN and Al_2O_3 calculated by the first principle theory [9].

As seen from Figures 2.2 and 2.3, at high temperature, the thermal conductivity and thermal expansion coefficient of SiC remain high (around 100 W·(m·K)) and low ($<6\times10^{-6}$ K^{-1}) respectively. This is favorable for its use in solar receivers. Moreover, as a good solar absorber material, it has a high solar absorptivity ($\approx$0.85) and a slightly lower emissivity even at high temperature (0.6-0.8 at 1400 K). It corresponds to a α/ε ratio of around 1.06-1.42. However, one of the main issues for using SiC coatings on metallic substrates is the interfacial

reaction between SiC and most of metals at temperatures over 1000 °C. Various products such as metal silicides, metal carbides, ternary metal-silicon-carbides, and unreacted carbon are formed due to metal/SiC reactions [117]. Nevertheless, certain silicides usually have relatively low melting points, leading to interfacial melting, and thus the degradation of the metal/SiC system in aggressive high temperature environments [117]. Therefore, an intermediate layer (or buffer layer, see Figure 2.1) is an essential need for applying SiC coatings on metallic substrates.

Table 2.1 Main physical, mechanical and optical properties of AlN and SiC.

Property	SiC	AlN	Reference
Density ($g \cdot cm^{-3}$)	3.21	3.26	[41]
Young's modulus (GPa)	430	340	[35, 85]
Poison's ratio	0.16	0.21	[35, 85]
Compressive strength (GPa)	0.565-1.379	2.81-3.2	[41, 118, 119]
Tensile strength (MPa)	34.5-150	100-300	[41, 118]
Hardness (GPa)	9.2-9.3	17.7	[41]
Absorptivity	0.85	0.16	[85, 120]
Transmittivity	/	0.5	[85, 120]
Emissivity	0.6-0.8 (1400 K)	0.16	[120, 121]

Table 2.2 Coefficients of fifth-order polynomial fit for the thermal expansion coefficient of polycrystalline AlN, Al_2O_3, 6H-SiC and 3C-SiC [9].

Coefficients	AlN	Al_2O_3	6H-SiC	3C-SiC
A_0 (K^{-1})	-1.763	-2.002	0.243	-2.105
A_1 (K^{-2})	0.021	0.039	0.013	0.020
A_2 (K^{-3})	-2.180×10^{-5}	-6.005×10^{-5}	-1.541×10^{-5}	-2.141×10^{-5}
A_3 (K^{-4})	1.221×10^{-8}	4.828×10^{-8}	8.801×10^{-9}	1.150×10^{-8}
A_4 (K^{-5})	-3.504×10^{-12}	-1.900×10^{-11}	-2.428×10^{-12}	-3.026×10^{-12}
A_5 (K^{-6})	4.057×10^{-16}	2.897×10^{-15}	2.576×10^{-16}	3.098×10^{-16}

Aluminum nitride (AlN)

AlN is a multifunctional material and has been widely investigated for many potential applications in recent years due to its high melting point (>2475 K [41]) and good thermal and chemical stability. Moreover, it is thermodynamically stable with most of metals and ceramics. Since its thermal expansion coefficient (4.03-6.09×10^{-6} K^{-1} [41]) is relatively low, AlN exhibits good thermal shock resistance. In addition, as one of the few high thermal conductivity non-metallic solids, AlN has a theoretical intrinsic thermal conductivity of 319 $W \cdot (m \cdot K)^{-1}$ along c-axis at 300 K. A value as high as 285 $W \cdot (m \cdot K)^{-1}$ for a high purity single crystal AlN has been reported by Slack et al. [7]. Thermal conductivity measured in Slack's work as a function of temperature is shown in Figure 2.2. For polycrystalline AlN, values vary from 10 to 285 $W \cdot (m \cdot K)^{-1}$ depending on the impurities like silicon, sintering

additives, oxygen contamination, microstructure as well as fabrication process [122]. The main mechanical properties of AlN are summarized in Table 2.1. As one of refractory ceramics, AlN is reported to have higher mechanical strength compared to SiC. In spite of the poor absorptivity of bulk AlN in the visible region, its transmittivity is sufficiently high (about 0.5, semi-transparent). It is common to use a transparent AlN coating as an anti-reflection layer for solar selective absorbers. As it is usually thin, solar radiation is transmitted to the substrate material, and therefore, the solar absorption is enhanced.

Table 2.3 Oxidation kinetics of AlN reported in the literature.

Reference	Specimen + additive	Temperature (°C)	Atmosphere	Kinetics
Lavrenko and Alexeev [123]	Bulk	900-1000	Oxygen	Parabolic
Katnani and Papathomas [124]	Powder	700-900	Air	Linear
Sato et al. [125]	Bulk	1150-1250	Wet N_2	Linear
Suryanarayana [126]	Powder	800-1000	Air	Linear
		950-1100		Parabolic
Bellosi et al. [127]	Bulk	1100-1400	Air	Linear
	Bulk+Y_2O_3	1100-1400		Linear
	Bulk+CaC_2	1100-1250		Linear
		1250-1400		Parabolic
Kim and Moorhead [128]	Bulk+Y_2O_3	1100-1200	Wet air	Linear
		1200-1400		Parabolic
Robinson and Dieckmann [129]	Bulk	1000-1300	Air	Linear
Osborne and Norton [130]	Bulk	1150-1350	Air	Linear
		1350-1750		Parabolic
Brown and Norton [131]	Powder	850-950	Air	Linear
		950-1150		Linear
Opila et al. [132]	Bulk+Y_2O_3	1000-1200	Dry oxygen	Parabolic
			Wet oxygen	Linear
Tseng et al. [133]	Bulk	1150-1450	Air	Parabolic
Gu et al. [134]	Bulk	900-1000	Air	Linear
		1100-1150		Linear+Parabolic
Hou et al. [135]	Whiskers	1050-1100	Air	Linear
		1100-1200		Parabolic
Hou et al. [136]	Powder	1000-1150	Dry air	Parabolic
		1000-1100	Wet air	Parabolic
Korbutowicz et al. [137]	Thin film	1012	Dry N_2+O_2	Logarithmic
			Wet N_2	Parabolic
			Wet N_2+O_2	Linear
Cao et al. [138]	Bulk+Y_2O_3	900-1300	Air	Linear
Yeh and Tuan [139]	Bulk+Y_2O_3	1050-1350	Air	Linear

Oxidation of AlN AlN is able to develop thermodynamic stable α-Al_2O_3 in oxidizing environments for temperatures over 1100 °C. The oxidation of AlN is a solid-gas reaction, involving the exchange of oxygen and nitrogen:

$$2AlN(s) + \frac{3}{2}O_2(g) \rightarrow Al_2O_3(s) + N_2(g)$$

The water vapor also plays an important role on the oxidation rate due to the supplementary reaction between AlN and H_2O, as:

$$2AlN(s) + 3H_2O(g) \rightarrow Al_2O_3(s) + N_2 + 3H_2(g)$$

However, the literature on the oxidation of AlN has many contradictory results. Most of them investigated bulk or powder materials. There are few researches concerning the oxidation of AlN coatings or thin films [137, 140–145]. The oxidation rate-limiting process is reported as either the chemical reaction at the oxide/AlN interface or the diffusion of oxygen through the oxide layer. Table 2.3 summarizes the oxidation kinetics of AlN under various conditions reported in previous studies.

Only few researches focus on the oxidation kinetics of AlN coatings or thin films. None of them studied the long-term oxidation (>100 h). Therefore, in the present study, the AlN film is expected as (1) an oxidation resistant layer and (2) a material to improve the absorptivity. We herein select AlN as the prime candidate, not only for its potential in high temperature environments, but for its ability to act as a reaction barrier between SiC and metallic substrates as well.

2.1.2 Metallic substrates

It is worth noting that performance of high temperature components depends on various properties. To optimize the choice, Ashby and Cebon [146] proposed to select the best material using the 'performance index' which is governed by the most important design objectives. The performance index is a combination of the most relevant variables that limit the effectiveness of a material, and it is usually derived from simple models.

In the present study, the substrate materials are expected to have excellent mechanical and thermal properties, which could ensure the effectiveness of heat transfer and a long lifetime. However, the question of which variable(s) is(are) the most relevant constraint(s) for the performance of such substrate material is still not clear. The following discussion will consider the main design objectives for solar receivers, and develop the performance indexes for the selection of substrate materials, based on Ashby's theory [147].

As mentioned before, receiver materials suffer from significant amounts of heat caused by the incident concentrated solar flux. The consequent distortion and the corresponding internal stresses might cause the creep or fracture of substrate materials during the daily operation. The detailed discussion is presented in Chapter 4. To simplify the selection, the effect of coating(s) on the thermal distortion is expected to be neglected, since the thickness of substrates is

commonly much larger than coating materials ($t_{substrate}/t_{coating} > 100$). Only the thermal distortion of substrate materials is taken into account. Moreover, the transient temperature changes due to rapid cooling or heating might lead to the cracking or fracture of coating materials at the coating/substrate interface, and furthermore the lack of protection for the substrate. Therefore, such coating(s)/substrate system should have the capacity to resist to the stresses in the coating(s) induced by thermal transitions. In such case, thermal distortion and thermal shock resistance are the most important design factors for the conception of a coating(s)/metallic substrate system as a solar receiver material. As AlN is selected as the prime coating material, the selection of substrate materials is restricted to materials that (1) resist to creep and fracture caused by thermal distortion and (2) adapted to AlN to resist thermal shock.

Resistance to creep and fracture caused by thermal distortion

Cebon and Ashby [148] showed that the dimensional change for a material undergoing temperature gradient is not only limited by its thermal conductivity (k), but the ratio of thermal conductivity to thermal expansion coefficient (α_{th}), as k/α_{th}. The detailed explanation is shown as follows.

Considering a simple case of heat transfer across a simply supported beam, the thermal strain (ϵ_{th}) of the beam is expressed as:

$$d\epsilon_{th} = \alpha_{th} dT \tag{2.3}$$

while in the steady state, for a given heat flux ($\overrightarrow{q}$), the temperature gradient is proportional to the reciprocal of thermal conductivity:

$$\frac{dT}{dy} = -\frac{q}{k} \tag{2.4}$$

The temperature gradient causes a strain gradient $d\epsilon/dy$ which is related to the ratio of thermal conductivity to thermal expansion coefficient. If there is no constraint, the curvature K is constant such that:

$$K = \frac{d^2\omega}{dx^2} = \frac{d\epsilon_{th}}{dy} = -\alpha_{th}\frac{dT}{dy} = -(\frac{\alpha_{th}}{k})q \tag{2.5}$$

where ω is the deflection of the beam. By integrating along x-axis, the central (maximal) deflection δ is given as:

$$\delta = C \cdot L^2 \cdot q \cdot (\frac{\alpha_{th}}{k}) \tag{2.6}$$

where L is the length of the beam and C is a constant depending on thermal loads and boundary conditions. Other geometries, heat transfer and boundary conditions will change the value of C, but this linear relationship does not change. Therefore, the thermal distortion could be minimized while the material processes a large value of the ratio k/α_{th}.

Morris et al. [112] pointed out a route to extend the analysis of Cebon and Ashby by considering that the stresses caused by thermal distortion could lead to the creep or fracture of substrate materials. Assuming that the material is isotropic, its normal stress is proportional to strain. The stress-gradient and the normal stress at any y-position are expressed as:

$$\frac{d\sigma}{dy} = \frac{d(E \cdot \epsilon_{th})}{dy} = E\frac{d\epsilon_{th}}{dy} = -(\frac{E\alpha_{th}}{k})q \tag{2.7}$$

$$\sigma = -(\frac{E\alpha_{th}}{k})qy \tag{2.8}$$

where E is the Young's modulus of material.

The substrate material is expected to have a long creep life, i.e. under steady-state operation for a long time, the rate of deformation is the limiting factor. Thus, this normal stress might induce creep of material when it approaches to the creep strength (σ_{cr}) defined here as the stress related to a specified creep strain rate (see Section 1.4) [112]. The creep rate is expected to be sufficiently low, as 10^{-9}-10^{-8}/s [112]. Alternatively, stress induced by the thermal loading could also lead to the fracture of material, depending on how near it is to the fracture toughness (K_C) [112]. Therefore, we can develop two performance indexes, Fracture Resistance (FR) and Creep Resistance (CR) which characterize the resistance to fracture and creep respectively as:

$$FR = \frac{K_c \cdot k}{E \cdot \alpha_{th}} \tag{2.9a}$$

$$CR = \frac{\sigma_{cr} \cdot k}{E \cdot \alpha_{th}} \tag{2.9b}$$

To optimize these two performance indexes, high thermal conductivity with reduced thermal expansion coefficient and Young's modulus as well as a sufficiently high creep strength and fracture toughness at expected operating temperature ($\geq$1000 °C) are necessary.

Thermal shock resistance

As discussed before, while the AlN/substrate system is subjected to thermal transitions, i.e. a sudden temperature change ΔT, stresses built up in the AlN layer due to the difference of thermal expansion coefficients between AlN and the substrate material, as:

$$\sigma_{AlN} \approx E_{AlN} \cdot (\alpha_{th,s} - \alpha_{th,AlN}) \cdot \Delta T \tag{2.10}$$

where the subscripts, s and AlN, denotes the substrate material and AlN layer respectively. Accordingly, cracks are expected to form in the AlN layer to release the stress induced by thermal transient while it exceeds the failure strength of AlN. Considering the failure of AlN layer is caused by fracture rather than by plastic yield, the critical stress is expressed as:

$$\sigma_{f,AlN} = \frac{K_{C,AlN}}{\sqrt{t_{AlN}}} \tag{2.11}$$

where t is the layer thickness. Even if the induced stress does not cause the failure, it still weakens the layer.

Then, the thermal shock resistance is therefore defined as the maximum change in temperature ΔT without fracture of AlN, as:

$$\Delta T = \frac{K_{C,AlN}}{E_{AlN} \cdot (\alpha_{th,s} - \alpha_{th,AlN}) \cdot \sqrt{t_{AlN}}} \tag{2.12}$$

It is worth noting that this parameter could be optimized by adopting a substrate material with a similar thermal expansion coefficient to that of AlN.

Results and discussions

A wide range of high temperature metals and alloys were examined regarding their thermal and mechanical data at high temperatures (>1000 °C). Most of materials previously investigated by Morris et al. [112] are also taken into account. However, in many cases precise data are not available, for example the lack of high temperature data (usually of creep strength) for certain materials. Thus, Morris et al. [112] proposed to make the following approximations to build a database for the optimization of the three aforementioned performance indexes:

(1) For parameters like thermal conductivity, thermal expansion coefficient and Young's modulus, if high temperature data are not available, they are approximated by an average over the temperature range from ambient temperature up to several hundreds of degrees Celsius, or approximated by the values at ambient temperature;

(2) When data are unavailable for a given parameter, values are estimated and/or taken from a(some) similar material(s) having this parameter known. For example, the thermal expansion coefficient of certain alloys is estimated as a function of mass fractions of the elements, as:

$$\alpha_{th} = \sum x_i \cdot \alpha_{th,i} \tag{2.13}$$

where x_i is the mass fraction of element i;

(3) If a given parameter is unavailable, the value is taken from the considered corresponding material within the family;

(4) While high temperature steady-state creep data are unavailable, creep strength data at lower temperature (800-900 °C) are taken with a higher creep rate (10^{-9}-10^{-8}/s) or a shorter lifetime (0.1-1 year).

A database composed of 8 families, in total 36 materials, is built by the CES constructor 2017. The relevant data and the corresponding property maps are presented in Annex 1. Figures A.1.1 and A.1.2 show a clear separation of the relative suitability of the families of materials. For example, Fracture Resistance (FR, Eq.(2.9a)), i.e., the resistance of the material to the thermal distortion, depends on high values of fracture toughness (K_C) and thermal conductivity (k) and low values of expansion coefficient (α_{th}) and Young's modulus (E). Refractory-based alloys have high values of FR. For tantalum-based alloys, this is mainly due to their high fracture toughness and low Young's modulus. For molybdenum-

and tungsten-based alloys, the high values of FR results from their high thermal conductivities and low thermal expansion coefficients. Equivalent analyses can be made to understand the values of Creep Resistance (CR, Eq.(2.9b)) and thermal shock resistance (ΔT, Eq.(2.12)). Similar to FR, the value of CR depends on a combination of thermal (k and α_{th}) and mechanical (E and creep strength σ_{cr}) properties of materials. The tantalum-based alloys, Mo-Si-B and TZM alloys have very high CR due to their excellent creep strength.

By contrast, the value of ΔT is only determined by the thermal expansion coefficient of materials. The closer thermal expansion coefficients to that of AlN at high temperature, the higher the value of ΔT is. Tantalum-based alloys have superior values of ΔT due to their similar thermal expansion coefficients to AlN. In conclusion, the material property parameters defined above to describe the general behavior, namely FR, CR and ΔT, are seen to be useful to characterize a given material within the thermal–mechanical–chemical environment of the solar radiation receiver. The maps shown in Figures A.1.1 and A.1.2 are useful to allow a ready vizualisation of the different behaviors of material families. In a first step to select suitable substrates using the property maps, the critical parameters should be firstly determined. Here we assume that the creep resistance is the most important critical parameter for the use in solar receivers. Therefore, tantalum- and molybdenum-based alloys are possible choices.

However, the poor oxidation resistance of tantalum- and molybdenum-based alloys leads to difficulties to characterize the properties of the AlN coatings. Thus, fast-creeping cast FeCrAl alloy and slow-creeping oxide dispersion strengthened (ODS) FeCrAl are selected as alternative substrates despite the low values of CR, FR and ΔT. As recently published by Seiler et al. [149], the choice of these alumina-forming alloys allows a simplification of the complex problem of the system lifetime since this class of alloys has a superior oxidation resistance up to 1250 °C. Thus, it is possible to characterize optical, mechanical and chemical properties of coatings at high temperatures (800-1250 °C). Their outstanding resistance to oxidation is based on their ability to form a very slow growing and protective alumina scale during service [150–155]. However, the relatively low mechanical strength of these ferritic alloys at elevated temperatures strongly limits their application in mechanically stressed components or in cyclic temperature conditions. The ODS Kanthal APMT (Fe-22Cr-5Al-3Mo and oxide inclusions) further improved hot strength and retained alumina protection up to 1300 °C [153]. It combines the excellent oxidation resistance of cast FeCrAl alloys with a higher creep resistance for moderately loaded components at high temperature.

2.2 Processing

Chemical vapor deposition (CVD) is one of major techniques that is widely used for deposition of high quality solid materials. It is able to deposit different materials in various forms: monocrystalline, polycrystalline, amorphous, epitaxial. Moreover, it allows a solid control of the composition and thickness of the film. This technique is also used to deposit coatings with complex shapes and large

dimensions. Compared with other techniques such as Physical vapor transport (PVT), CVD is one of the promising technique for producing freestanding AlN wafers with industrial grade with few or no oxygen contamination which greatly affects the thermal and optical properties. This vapor phase growth method includes various variations, namely, metal-organic CVD (MOCVD), plasma-enhanced CVD (PECVD), hydride vapor deposition, and many other variants. Currently, the most common method is MOCVD, where precursors are usually thermally activated.

For AlN growth, MOCVD is currently available to fabricate commercial AlN templates grown at low temperature by using trimethylaluminum (TMAl) and ammoniac (NH_3) as precursors for Al and N respectively. However, the reaction between these two precursors usually leads to incorporation of impurities (e.g. oxygen and carbon). Nevertheless, the high toxic and pyrophoric nature of reactants (such as TMAl) and expensive reactors lead to difficulties to make the MOCVD growth of AlN a commercially viable process for thick film growth. The hydride vapor phase epitaxy, considered as an alternative industrial growth technique, offers advantages of being able to fabricate AlN without unintentional impurities, with less cost than that of MOCVD. Additionally, it is available to produce thick AlN films with high growth rate via the reaction between aluminum chloride ($AlCl_3$) and NH_3. Since the purity of AlN could greatly influences its thermal conductivity, a careful control of the composition is necessary to achieve a high thermal conductivity for its high temperature application. Hydride based high temperature chemical vapor deposition is therefore selected for the growth of AlN on metallic substrates. The following sections aim to provide an overview of the CVD process and thin film growth mechanisms during vapor deposition.

2.2.1 Overview of CVD

The CVD process involves the reaction of chemical vapor compounds (precursors) over a substrate leading to the deposition of thin films. Figure 2.4 presents the key steps involved in a CVD process:

(1) Transport of precursor gas and carrier gas at a required flow rate into the reactor;

(2) Gas phase reactions of precursors to produce reactive intermediates and gaseous byproducts;

(3) Transport and adsorption of reactants towards the substrate;

(4) Subsequent surface diffusion of adsorbed reactants to preferential sites (ledges, crystalline defects, ...), and formation of a solid film;

(5) Desorption and transport of reaction products away from the surface of the substrate.

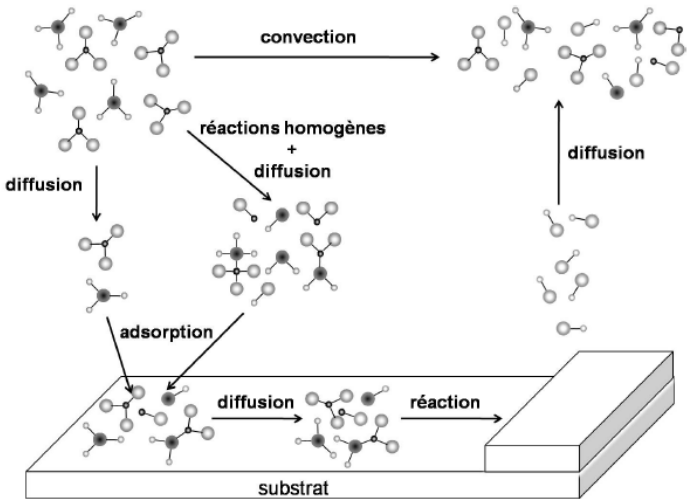

Figure 2.4 Transport and physicochemical mechanisms in a CVD process.

Conventional CVD process

In conventional thermal CVD, the growth mechanism depends on various parameters. Temperature of the substrate (also called deposition temperature), pressure in the reactor and composition and chemistry of gas phase are the primary ones. Figure 2.5 presents the dependence of film growth rate on deposition temperature. Three regimes of growth kinetics have been figured out in this plot:

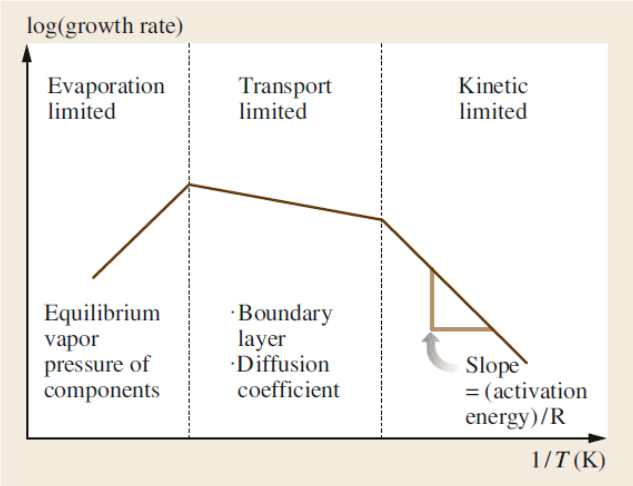

Figure 2.5 Schematic of logarithmic growth rate as a function of deposition temperature in a conventional CVD process.

(1) At low temperature, the growth rate is kinetically controlled by chemical reactions in the gas phase and on the substrate surface. In this region, it follows an Arrhenius law:

$$v = A \cdot exp(\frac{-E_a}{R \cdot T}) \tag{2.14}$$

where v is the film growth rate, A is the pre-exponential factor, E_a is the activation energy, R is the ideal gas constant and T is the deposition

temperature (in K). Figure 2.6 shows a typical kinetic controlled growth of TiN in the temperature range of 650-1400 °C at fixed gas flow rate and pressure. The logarithm of TiN growth rate is plotted as a linear function of reciprocal temperature with an activation energy of 43 kJ·mol^{-1} [10]. Moreover, a uniform film thickness can be achieved by minimizing temperature variation over the substrate surface as the growth rate in this region is only determined by the deposition temperature.

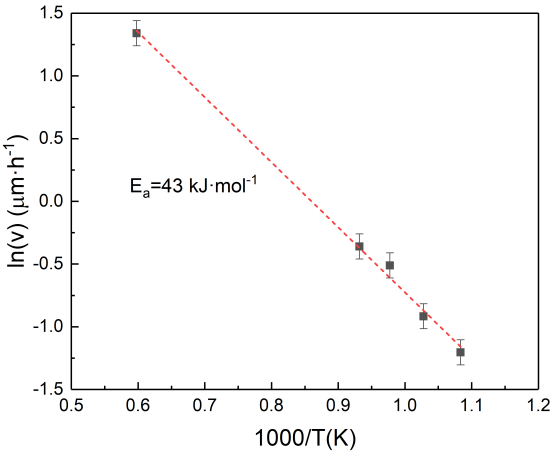

Figure 2.6 Arrhenius plot of growth rate of TiN by CVD as a function of 1/T [10].

(2) As temperature increases, the diffusion of reactants through the boundary layer to the substrate surface is predominant for the film growth. In such case, the effect of temperature on growth rate is not evident. Indeed, when the film growth is limited by the diffusion of reactants, the growth rate is determined by the diffusion coefficients of reactants (D) and the thickness of the boundary layer (δ), such as:

$$v \propto \frac{D}{\delta} \tag{2.15}$$

Therefore, to obtain a constant growth rate when operating in this diffusion controlled regime, a constant thickness of the boundary is required.

(3) By further increasing temperature, there is an etching of the surface and/or depletion of reactants due to homogeneous gas phase nucleation.

2.2.2 Film growth mechanisms

Formation of a continuous film via condensation from a vapor phase go through several distinct stages involving (1) nucleation, (2) growth and (3) coalescence. Once a continuous film is formed through these processes, thickening normally occurs via epitaxial growth on pre-existing grains. Notably, film microstructure and hence its properties (physical, mechanical, ...) evolve during film formation and thickening. Much work so far has intensively studied the film structure evolution during processing involving nucleation, growth, coalescence and thickening. The purpose of this section is to present some general ideas in film growth process, microstructural evolution and film growth stress.

2.2.2.1 Growth process

The events necessary for film nucleation and growth from the vapor phase are schematically illustrated in Figure 2.7(a). Following the adsorption and diffusion of atoms on the surface of the substrate, stable nuclei (or clusters, normally consisting of a few atoms) form at preferred sites on the substrate surface. Besides, the nucleation process is strongly dependent on the crystal structure of the substrate material, lattice defects, surface steps and surface contamination.

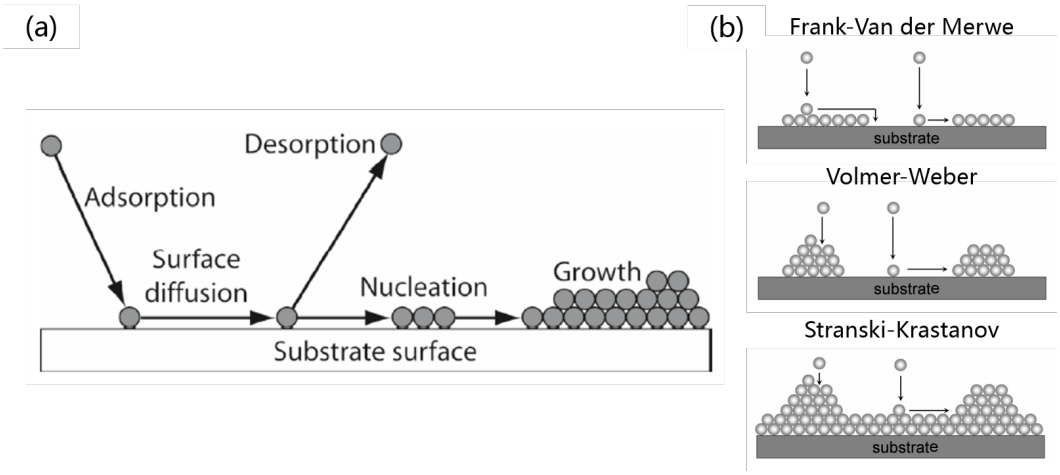

Figure 2.7 Schematic representation showing (a) the events in a typical vapor-phase thin film growth process and (b) three primary growth modes.

As shown in Figure 2.7(b), the diffusion and nucleation of atoms give rise to three primary growth modes: (1) layer-by-layer (also called Frank-van der Merwe or 2D) growth, (2) island (Volmer-Weber or 3D) growth and (3) mixed (Stranski-Krastanov) growth. When adatoms are more strongly attached by the substrate rather than themselves, the layer-by-layer growth mode occurs. New adatoms tend to attach the formed small stable cluster at its periphery to bond with both the substrate and the cluster. Thereby, the planar growth continues. In contrast, when adatoms are more likely to be bound to each other, the small nuclei usually resemble islands in their appearance. The film growth is then proceeded by growth and subsequent coalescence of these 3D islands. The third growth mode, mixed growth, combines the feature of island growth and layer-by-layer growth. At the beginning of this growth mode, adatoms prefer the attachment to the growth surface. However, after formation of one or some monolayer(s), layer-by-layer growth mode becomes unfavorable and subsequent adatoms tend more to gather into islands.

2.2.2.2 Supersaturation and film microstructure

The preceding discussion was primarily concerned with the early stages of film growth on the substrate surface by condensation from a vapor in a qualitative way in terms of the behavior of atoms. In a CVD process, the nucleation and growth processes, which significantly influence the microstructure and properties of deposited film, are greatly affected by the processing parameters. The important

parameters of nucleation and growth are deposition temperature which is related to the mobility of adatoms, and supersaturation which is related to the concentration of adatoms on the surface. For a general chemical reaction,

$$aA_{(g)} + bB_{(g)} \rightarrow cC_{(s)} + dD_{(g)}$$

its supersaturation (β) is defined as the ratio of sum of the gas-phase partial pressure in the real state to the sum of corresponding equilibrium partial pressure. It can be expressed as follow:

$$\beta = \frac{P_A^a + P_B^b + P_D^d}{P_{A,eq}^a + P_{B,eq}^b + P_{D,eq}^d} \tag{2.16}$$

where P_A,P_B, andP_D are the partial pressures of gas A, B, and D in the actual state respectively, $P_{A,eq}$, $P_{B,eq}$, and $P_{D,eq}$ are the corresponding equilibrium partial pressures of gas A, B, and D respectively.

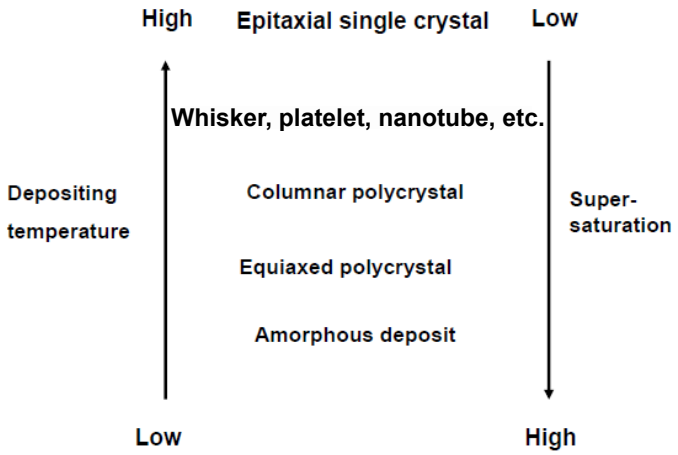

Figure 2.8 Effect of deposition temperature and supersaturation on the deposit morphology.

Blocher [156] has summarized the evolution of film morphology as a function of deposition temperature and supersaturation for PVD materials. The same general trend exists also for materials grown by CVD, as presented in Figure 2.8. Increasing deposition temperature leads to a decrease of supersaturation and thus the evolution of morphology of deposition. In general, at high degree of supersaturation and very low temperature, homogeneous nucleation occurs and powder-like product are formed. If the deposition temperature is increased to a certain value, polycrystalline films are obtained. The epitaxial growth is favored at very high temperature and low degree of supersaturation. Even though the present study deals with the polycrystalline growth of AlN, it is also instructive to provide a global view on epitaxial films since the polycrystalline film growth involves epitaxial growth on initially formed random grains and orientation selection.

Epitaxial films Epitaxial growth has been widely used for the growth of single crystals and thin films for electronic applications (e.g. semiconductor, superconductor, ...). During an epitaxial growth, the single crystalline substrate imposes its crystalline structure to the film material. This crystalline structure is preserved during the growth. When the film material is the same as the substrate material, such epitaxial growth is named *homoepitaxy*. *Heteroepitaxy* corresponds to the epitaxial growth of a film which has different structure and/or nature from the substrate. However, for a successful heteroepitaxy, close crystalline structures and small mismatch in lattice parameters between substrate and film materials are required. If the lattice mismatch is low, e.g. below 0.5% or so, the growth tends to be planar (layer-by-layer growth mode). The material tends to gather into islands if the mismatch is large. When the crystalline structures are too different, the grown films will be polycrystalline or even amorphous.

Polycristalline films Figure 2.9 outlines the fundamental stages of growth of a polycrystalline film on a substrate. During these stages, the microstructure (or grain structure) of the film significantly develops. Generally, the growth of polycrystalline films begins with nucleation of islands on the substrate surface. Once formed, lateral growth of islands leads to island coalescence, which give rise to the formation of grain boundaries. The formed continuous film, usually having a thickness of 10 nm or less, define the initial grain structure of the film material. Subsequently, further film thickening occurs, and the grain structure develops in two fundamentally different ways, as illustrated in Figure 2.9(c) and (d). The evolution of grain structure is strongly affected by the surface diffusivity of the film material, which is a function of the homologous temperature (defined as the ratio of deposition temperature (T_{growth}) to melting point of film material (T_m): T_{growth}/T_m).

When surface diffusion is slow, the formed boundaries are essentially immobile. Therefore, the aforementioned, initially formed grain structure through nucleation, island growth and coalescence remains the base of the film structure. The further film growth occurs predominantly as epitaxial growth on this grain structure, resulting in the formation of columnar grains, as shown in Figure 2.9(c) and (d) [157]. Subsequent competitive growth process lead to an increasing grain size in the lateral direction at the surface of the thickening film. Complete details are provided later. Such type of microstructural evolution usually occurs for the deposition of ceramics and metals having high melting points, even at high deposition temperatures ($0.3<T_{growth}/T_m<0.5$). Moreover, it is reported that, for thermal barrier coatings, the columnar structure could enhance the strain tolerance and thus their lifetime during thermal cycling [158, 159]. By contrast, if the surface diffusivity is sufficiently fast, grain boundaries are mobile. The grain structure evolves during the island coalescence process and continues to evolve during film thickening. In such case, an equiaxed structure is obtained. Its grain size in the lateral direction is typically close to that in the thickness direction. Such microstructure is formed at high homologous temperature ($T_{growth}/T_m>0.5$) and at a higher supersaturation. By post-deposition annealing, it is possible to transform a columnar structure to an equiaxed one.

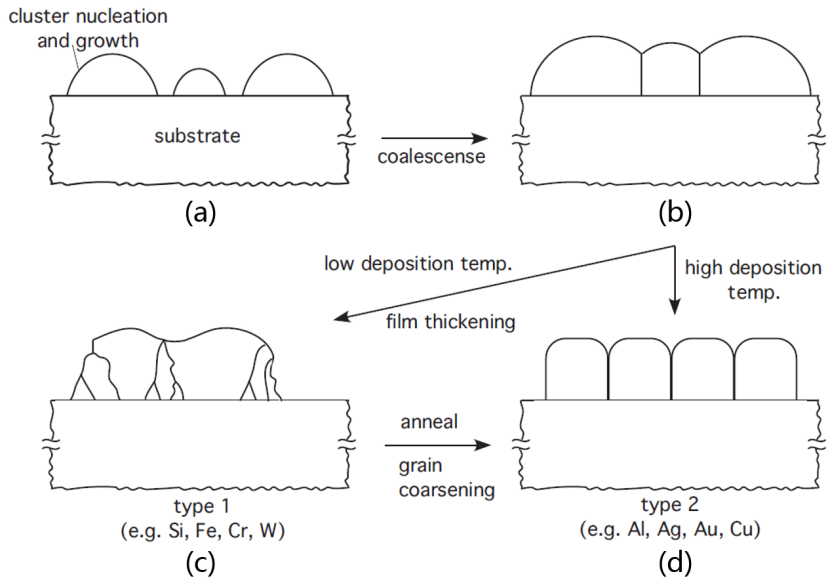

Figure 2.9 Overview of microstructural evolution during growth of a polycrystalline film: (a) nucleation and growth, (b) coalescence of islands leading to the formation of grain boundaries. The subsequent film thickening results in two different microstructures: (c) columnar (at low deposition temperature) and (d) equiaxed (at high deposition temperature). Transformation from columnar microstructure to equiaxed microstructure can be achieved by annealing [11].

As mentioned before, new grains are epitaxially grown on initially formed grain structure during thickening to form a columnar structure. Indeed, during the thickening process, competition between different crystalline planes results in the evolutionary selection of preferred orientations. Van der Drift [12] proposed a mechanism for the orientation selection during film growth in 1967. It is suggested in his study that the vertical growth rate of individual crystals is the key point for crystals to survive. Crystals with a fastest growing crystallographic direction nearly perpendicular to the substrate surface are favored (Figure 2.10). The higher the fastest growth rate, the greater the probability of survival, resulting in the development of texture with a growing direction perpendicular to the substrate. The van der Drift growth mechanism is schematically represented in two-dimensions in Figure 2.11 for the growth of initially (10)-bounded 'cubic' crystals. At the beginning of deposition, random crystals are initially formed on the substrate. These crystals form the base structure of the film. Then, during the epitaxial growth of new grains on these initially formed crystals, the selection of orientation occurs simultaneously. According to the van der Drift's model, when two crystals meet each other, the one having faster vertical growth rate survives and bury the other one. As growth time increases, the evolutionary selection continues and is finally completed by leaving the [11] direction (arrows) nearly perpendicular to the substrate. The film exhibits therefore a columnar structure with a preferred orientation of (11), while the film surface is predominated by (10) planes.

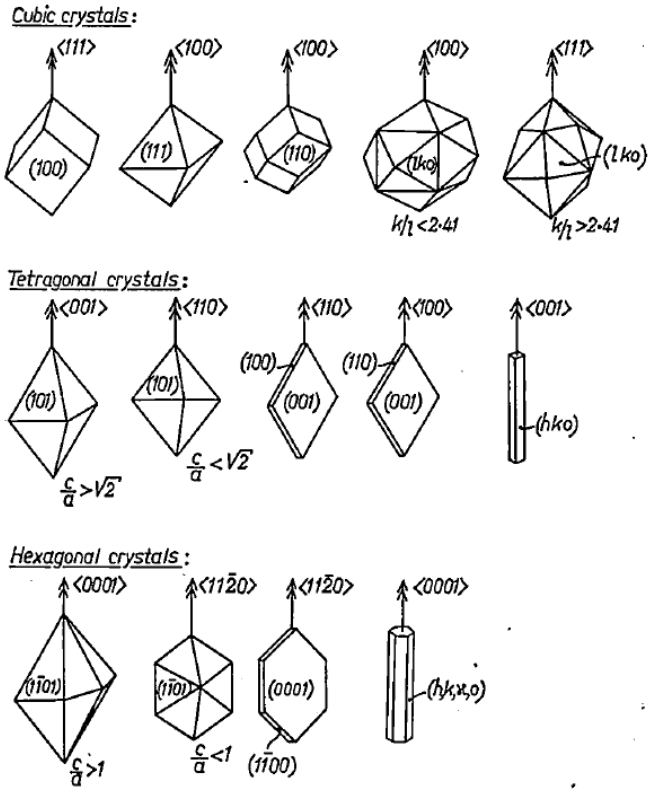

Figure 2.10 Fastest growing directions (double arrows) of a number of free-growing single crystals. Crystals having their fastest direction nearly normal to the substrate envelop the other crystals and gradually determine the preferred orientation of the film [12].

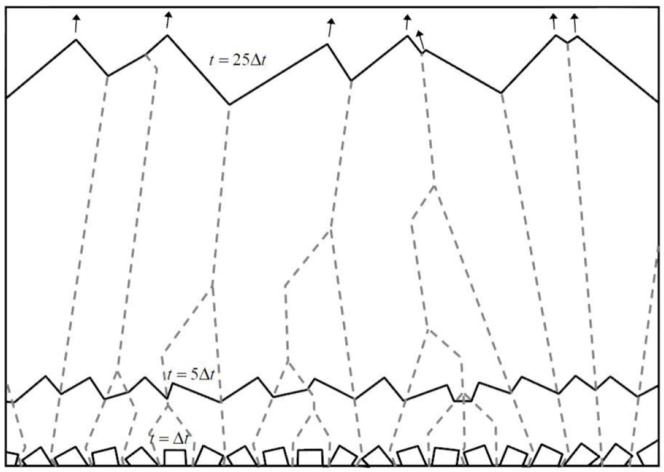

Figure 2.11 Schematic of the two-dimensional growth of randomly distributed (10)-bounded grains on a substrate; Δ t is the shortest time required for two neighbouring grains to meet each other. The selection of orientation proceeds and permits only crystals with their vertical growth rate nearly normal to the substrate surface to grow further [12].

From the view of thermodynamic, the studies on the relationships between supersaturation and crystal orientations were made by Pangarov in 1964 [160], which states that the work of formation of a two-dimensional nuclei of a crystalline plane (hkl) is a function of supersaturation. In a face-centered cubic system, grains are preferentially grown along (111) planes at low degree of supersaturation. The preferred orientation is then changed to (100) and finally to (110) with an increase of supersaturation. For hexagonal close-packed structure, (0001)-oriented grains are favored at low values of supersaturation. While supersaturation increases, the preferred orientation ought to be along $[10\bar{1}1]$ direction. At higher degree of supersaturation, grains can be oriented along $[11\bar{2}0]$ and $[10\bar{1}0]$ directions.

2.2.2.3 Growth stress in polycrystalline films

Intrinsic stress usually arises during the growth of a polycrystalline film. The connection between the stress and Volmer-Weber mode growth stages is not yet fully understood. The stress evolution with increasing film thickness is dependent on the film properties and process conditions such as deposition temperature and growth rate. Generally, the volume-average stress ($\langle\sigma\rangle$, Eq.(2.17)) in a film becomes compressive, then tensile and then again compressive as the film thickness (t_f) increases during the vapor deposition, as shown in Figure 2.12 [11].

$$\langle\sigma\rangle = \frac{1}{t_f}\int_0^{t_f} \sigma(x)dx \tag{2.17}$$

This compress-tensile-compressive stress evolution are intrinsically governed by the following mechanisms:

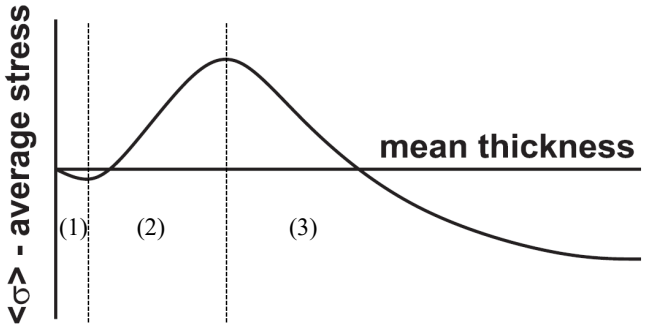

Figure 2.12 General behavior of the volume-average stress in a thin film as a function of mean thickness. The three stages correspond to the surface and/or interface stress, island coalescence and growth of a continuous film respectively [11].

Surface and/or interface stress Generally, during the early stage of nucleation and film growth, compressive stress arises in the film resulting from the different chemical and structural environments of the adatoms at the surface or the interface as compared to the bulk. Upon further growth in volumes of nuclei (or clusters), the internal elastic stress in the crystallites tends to relax as the cluster radius becomes larger. But it still preserve because of the constraint of the substrate (region 1 in Figure 2.12).

Island coalescence During the island coalescence, the formation of grain boundaries and the energy released due to the surface reduction results in tensile stress in the film. This stress increases nonlinearly through the film thickness (region 2 in Figure 2.12). In the case of AlN, this tensile stress can be estimated from the island size just prior to coalescence, such as [13]:

$$\epsilon = \frac{\Delta_{max}}{L} \tag{2.18}$$

$$\Delta_{max} = [2L(2\gamma_{sv} - \gamma_{gb}\frac{1-\nu}{E})]^{\frac{1}{2}} \tag{2.19}$$

where L is the crystallite size just prior to coalescence, Δ_{max} is the maximum gap size between crystallites as illustrated in Figure 2.13, γ_{sv} and γ_{gb} are the surface free energy of the crystallites and grain boundary free energy respectively, E is the Young's modulus and ν is the Poisson's ratio.

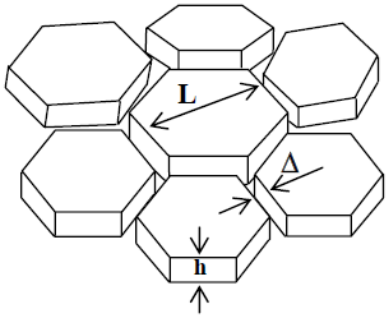

Figure 2.13 Schematic representation of crystallites prior to coalescence [13].

Film thickening Compressive stress develops shortly after the arising of the aforementioned tensile stress (region 3 in Figure 2.12). For a low atomic mobility material, stress is relaxed but remains tensile after such relaxation while stress turns compressive again and reach a steady state for a high atomic mobility material. However, the origins of such compressive stresses in continuous films are less well understood than for the earlier growth stages.

In general, correlations between the intrinsic growth stress in a polycrystalline film and the final microstructure are observed, as presented in Figure 2.14. For the type 1 materials (Figure 2.9(c)), large tensile stresses are generated. By contrast, the higher surface diffusivity of type 2 materials (Figure 2.9(d)) promotes greater stress relaxation. Much smaller stresses are observed.

2.2.3 Experimental set-up

Chloride-hydride based high temperature CVD (HTCVD) process has been developed in SIMaP laboratory 20 years ago. In this process, a supply of gaseous precursors, containing the species to be deposited, is continuously carried out through a carrier gas (argon (Ar), hydrogen (H_2), nitrogen (N_2)) in a water-cooled vertical cold-wall quartz reactor at low pressure. A schematic representation of the HTCVD set-up is illustrated in Figure 2.15. During the experiment, the inner wall of the set-up is continuously cooled by a circulating and recycled water with controlled temperature.

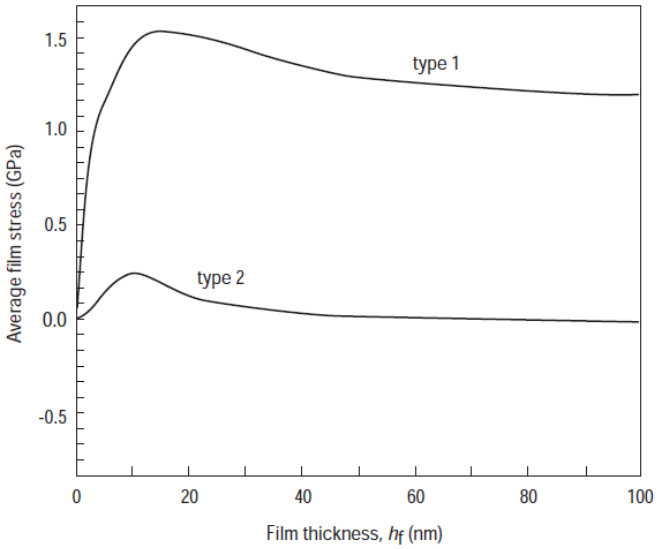

Figure 2.14 The evolution of intrinsic growth stresses during the vapor deposition of type 1 and type 2 materials (Figure 2.9(c) and (d) respectively) as a function of film thickness.

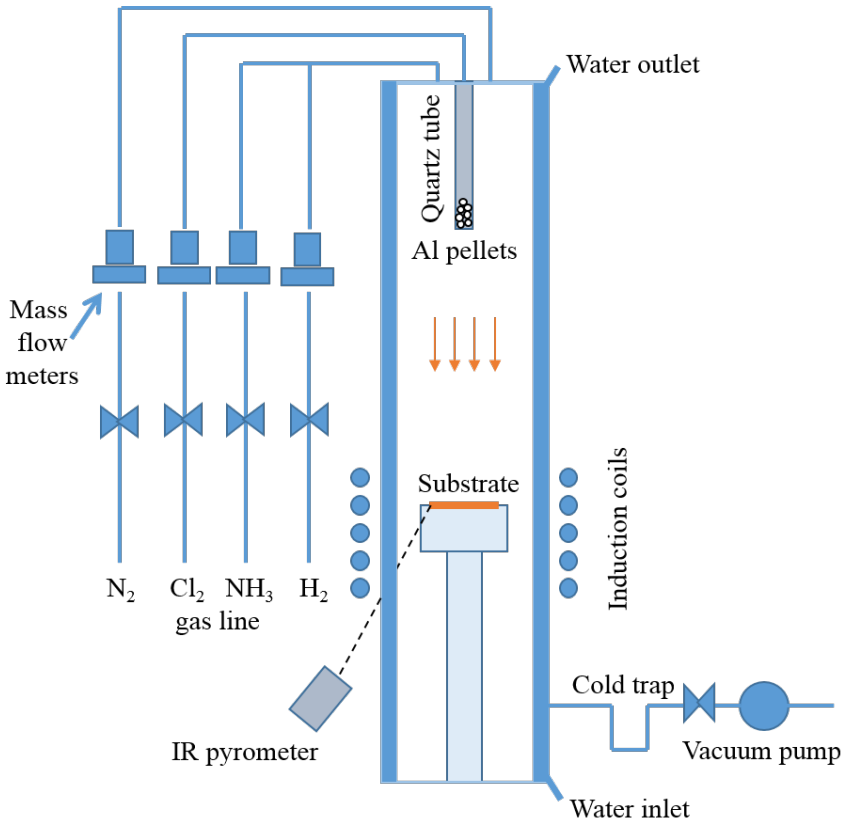

Figure 2.15 Schematic representation of experimental set-up for HTCVD growth of AlN.

The CVD set-up consists of two main compartments. The first part is a small quartz tube containing aluminum pellets used for AlN growth, the so-called chlorination chamber. A gas inlet is located on the top of this quartz tube while its lower part consists of a piece of sintered quartz allowing the evacuation of gas after passing through aluminum (Al) pellets. During the AlN deposition, this chlorination chamber is heated by a resistive system under H_2 for in-situ synthesis of $AlCl_3$ via the reaction between Al and chlorine (Cl_2) at around 540 °C. Cl_2 is chosen rather than hydrogen chloride (HCl) to separate the effect of Cl and H and to avoid too corrosive atmosphere in the chlorination chamber.

The second part is the deposition chamber. Precursors diluted in the carrier gas are transported and thus react on the surface of substrate which is placed on a graphite holder heated by induction. An infrared pyrometer allows the monitoring of the temperature between 600 and 1800 °C. The evacuation of gases is ensured by a pumping system that allows a primary vacuum (between 10^5 and 1 Pa) inside the reactor. The total pressure is regulated by a butterfly valve and measured by a Baratron gauge up to 10^4 Pa. A cold trap cooled with an ice/water mixture is used to capture and condense chlorinated gas which could damage the pump during the operation.

2.3 Characterization methods

Structural characterization techniques

2.3.1 X-ray diffraction

X-ray diffraction (XRD) is a common technique to identify crystalline phases. The method relies on interference between collimated x-rays reflected in the atomic planes of the sample. Constructive interference occurs following the Bragg's law:

$$n\lambda = 2d_{hkl}sin(\theta) \tag{2.20}$$

where λ is the wavelength of X-rays, d_{hkl} is the spacing between the crystalline planes (hkl), θ is the scattering angle and n is the order of the reflection.

2.3.2 Scanning Electron Microscopy

In scanning electron microscopy (SEM) measurements, a focused electron beam is scanned over the surface of the sample. Different interaction can occur when the electrons strike the sample surface: emission of backscattered electrons, Auger electrons, secondary electrons and X-rays. All these signals can be detected, revealing morphology, chemical composition or microstructure of the sample.

A Zeiss Ultra 55 field emission(FE) SEM was employed in this study to analyze the microstructure. This FE-SEM is also equipped with an energy dispersive X-ray spectrometer for elemental analysis. In the present study, the top surface and the cross-sections are analyzed at 3 kV electron beam energy in order to stabilize the mapping and avoid the surface damage.

2.3.3 Electron Back Scatter Diffraction

2.3.3.1 Principles

Electron backscatter diffraction (EBSD) is an electron-beam technique to simultaneously identify the crystallographic orientations and crystal sizes at high spatial resolution. This technique is based on the Kikuchi-like electron diffraction on the crystalline planes of the sample.

2.3.3.2 Speciment preparation

Sample preparation is a very crucial step in EBSD. The deformation, and/or contamination and/or oxidation of the surface region (a few tens of nanometers) may lead to the suppression of EBSD pattern formation. Depending on the nature of the material, there are numerous preparation techniques like mechanical polishing, electrolytic polishing, chemical etching and ion etching. It is essential to develop a suitable protocol for a given material. There are few studies concerning the cross-section preparation of thick AlN (>10 μm)/metallic alloy stacks. Nevertheless, mechanical properties, in particular the hardness, of AlN and metallic alloy are quite different. This can give rise to extreme relief (or undulation) on the cross-sectional surface of the sample. Hence, a sample preparation protocol was established to have an entirely flat cross-sectional surface of AlN coated sample with minimum deformation for EBSD observations:

(1) Metallization of AlN coated sample with a 50 nm Ag thin film on the surface of AlN;

(2) Cut slowly the sample, place it at the egde of a mounting cylinder in a hot mounting press, and hot mount the sample with a conductive resin (PolyFast, Struers);

(3) Grind until planar using 320 grit (46 μm) SiC paper;

(4) 600 grit (26 μm) SiC paper between 8 and 15 N force for about 5-10 min;

(5) 1200 grit (15 μm) SiC paper between 8 and 15 N force for about 5-10 min;

(6) 9 μm diamond solution between 8 and 15 N force for about 10-20 min (this step may be repeated 2-3 times;

(7) 3 μm diamond solution between 8 and 15 N force for about 5-10 min;

(8) 1 μm diamond solution between 8 and 15 N force for about 5-10 min;

(9) 0.04 μm colloidal silica solution (OP-S, Struers; 1:7 diluted with water) for 2 min, then flush the polishing cloth with tepid water for 4 min and finish the flush with ethanol for 2 min to clean the sample surface;

(10) Check the surface state under optical microscopy, make sure that the surface is sufficiently flat and there is no colloidal silica residues on the surface; if not, repeat steps (7)-(9);

(11) Reduce the total height of mounting (to <6 mm) to adjust to the position of EBSD detector components;

(12) Clean the sample for 5 min in acetone and ethanol successively with an ultrasonic bath and dry the sample carefully by compressed air;

(13) Paint the edge of the cross-sectional surface of sample with conductive silver paint to promote electrical conduction.

Throughout the grinding ((3)-(5)) and polishing ((6)-(9)) steps, frequent and careful checks of the sample surface are required to make sure that no relief and no residues (resin, and/or SiC, and/or diamond and/or colloidal silica particles) are introduced on the cross-sectional surface of the sample. It is also suggested to clean the sample in an ultrasonic bath with acetone and ethanol successively to remove the residue after each step. Indeed, after step (10) the surface state is already suitable for SEM observation, but it is recommended to finish the following preparation steps for EBSD.

2.3.3.3 EBSD analysis

Before the insertion of EBSD camera, the sample prepared with aforementioned steps is mounted in the SEM and the stage is tilted to 70°. The sample should be well fixed in a sample holder to avoid sample slippage resulting in inevitable damage to EBSD camera. As AlN is very beam sensitive, high accelerating voltage and small step size may lead to too much energy on the surface and cause damage. We suggest here an accelerating voltage of 15 kV, working distance of 14 mm and step size of 0.1 μm.

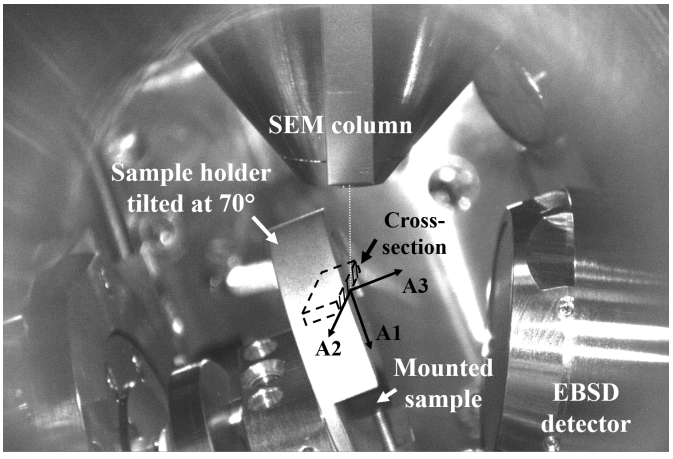

Figure 2.16 Schematic representation of mounted sample and detector for EBSD analysis; A1, A2 and A3 are the rolling direction (ND), transverse direction (TD) and normal direction (ND), respectively, with respect to the cross-sectional surface of mounted sample.

Residual stress measurement Methods

2.3.4 XRD-sin$^2\psi$ method

The XRD-sin$^2\psi$ method is one of the non-destructive methods to determine equi-biaxial in-plane stress in polycrystalline materials. Generally, when in-plane compressive(tensile) stresses are presented in the sample, the lattice parameters for crystal planes parallel to the surface will be expanded(contracted) compared to the lattice parameters in stress-free state. For crystal planes perpendicular to the surface, lattice parameters will be contracted(expanded). For a given (hkl) reflection, the relationship between the average elastic train, ϵ^{ψ}_{hkl}, and the tilt angle, ψ, can be written as [161]:

$$\epsilon^{\psi}_{hkl} = \frac{d^{\psi}_{hkl} - d^{0}_{hkl}}{d^{0}_{hkl}} = 2S_1\sigma + \frac{1}{2}S_2 \sin^2\psi\sigma \tag{2.21}$$

where d^{ψ}_{hkl} and d^{0}_{hkl} are the measured spacing of a (hkl) crystalline plane and stress-free spacing respectively, σ is the in-plane stress, S_1 and S_2 are the X-ray elastic constants.

2.3.5 Raman spectroscopy

Raman spectroscopy is a non-destructive technique based on the inelastic scattering of the incident light by elementary excitations such as phonons. Generally, when a laser beam illuminates a sample, a few of the photons will impinge upon the sample molecules and be rebounded. Most of the collisions are elastic, meaning that no transition of energy occurs between the photon and molecules. On the contrary, when the scattering is inelastic, there is an energy shift between the photon and molecules. Such scattering is also called Raman scattering. The Raman spectra are especially sensitive to the vibrational states of semiconductor materials like AlN which are related to the chemical composition, crystalline quality and residual stress. Hence, this technique is employed in Chapter 3 for non-destructive residual stress analysis.

Information on residual stress in AlN can be extracted from the E_2 phonon frequency. Generally, the biaxial residual stress can be easily deduced by its linear dependence on the shift of the E_2 (high) phonon frequency [162, 163]. The biaxial residual stress is explained as:

$$\sigma_{xx} = (C_{11} + C_{12} - \frac{2C^2_{13}}{C_{33}}) \cdot \epsilon_{xx} \tag{2.22}$$

where C_{ij} is the elastic constant of AlN, σ_{xx} is the biaxial stress (vertical to c-axis) in AlN, and σ_{xx} is the in-plane strain related to the frequency shift of the E_2 phonon of AlN. Yang et al. [163] showed that the E_2 phonon frequency shifts linearly with stress with -4.04±0.3 cm^{-1}·GPa^{-1} with a stress-free phonon frequency of 657.67 cm^{-1}, such as:

$$y = -4.04\sigma_{xx} + 657.67 \tag{2.23}$$

where y is the measured frequency of the E_2 (high) phonon mode.

2.3.6 Photoluminescence piezospectroscopy

Photoluminescence piezospectroscopy (PLPS) is a non-destructive technique for the measurement of residual stresses in thermally grown alumina [164, 165]. The photoluminescence phenomenon occurs in alumina through the excitation of trace chromium ion (Cr^{3+}) impurities. When electrons from Cr^{3+} are excited to unstable, high-energy states with a laser, photons are emitted on decay to their ground state (Figure 2.17(a)). Two distinct ruby fluorescent transitions occur and a characteristic of R-line doublet can be observed in the spectrum of alumina, as shown in Figure 2.17(b).

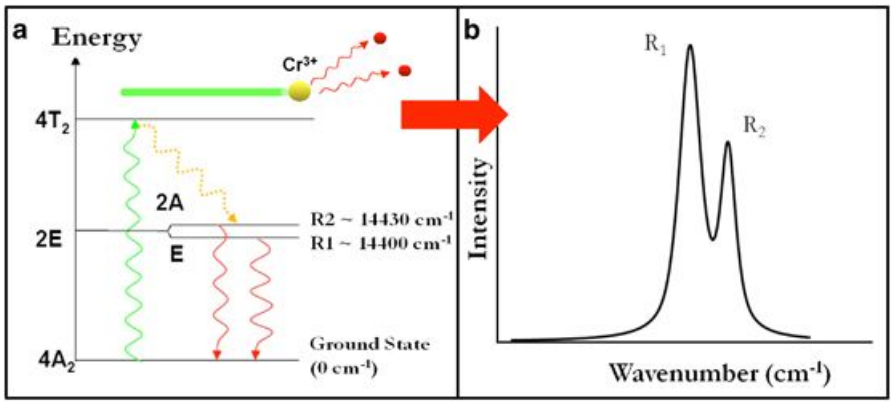

Figure 2.17 (a) Energy emitted from chromium-doped alumina resulting in (b) the R-lines in the spectrum of α-alumina [14].

A shift of frequency of the characteristic R-lines from its stress-free value occurs when the alumina is strained. This is known as the piezospectroscopic effect. The relationship between the biaxial residual stress in polycrystalline Al_2O_3 (σ) and the piezospectroscopic shift of Cr^{3+} ($\Delta\nu$) is given by :

$$\Delta\nu = \frac{2}{3}\Pi_{ii}\sigma \tag{2.24}$$

where Π_{ii} is the piezospectroscopic coefficient. He and Clarke [33] measured the piezospectroscopic coefficients for the two R-lines (Table 2.4). The values of stress-free frequencies for R-lines are 14402 cm^{-1} (1.786 eV) and 14432 cm^{-1} (1.789 eV) [166].

Table 2.4 Piezospectroscopic coefficients for R-lines determined by He and Clarke [33].

	Π_{11} ($cm^{-1}\cdot GPa^{-1}$)	Π_{22} ($cm^{-1}\cdot GPa^{-1}$)	Π_{33} ($cm^{-1}\cdot GPa^{-1}$)	$\Pi_{11}+\Pi_{22}+\Pi_{33}$ ($cm^{-1}\cdot GPa^{-1}$)
R1	2.56	3.50	1.53	7.59
R2	2.65	2.80	2.16	7.61

Experimental set-up for high temperature oxidation under solar radiation

PROMES laboratory has developed several experimental reactors to study high-temperature materials under solar radiation. Among them, the REHPTS (High Temperature and Pressure Solar Reactor) set-up is a reactor implemented at the focus of the 6 kW vertical solar furnace in order to study materials under extreme coupled conditions (corrosive atmosphere and high temperature). The REHPTS set-up is used in open air at atmospheric pressure of 0.87×10^5Pa, the laboratory being located at an altitude of 1500 m. A servo-controlled flat mirror (heliostat) reflects the incoming solar flux towards a facetted hemispherical concentrator. The sample is placed at 25 mm above the focus of the solar furnace. Thus, elevated temperatures on materials may be obtained at very fast rate (up to 100 $K{\cdot}s^{-1}$) on a homogeneous 1 cm diameter area. The temperature is measured using an optical pyrometer (at λ=5 μm) and can be controlled by the opening angle of the shutter, determining the fraction of the concentrated solar flux that is transmitted to the sample.

Optical properties at room temperature (300 K)

The hemispherical reflectivity at 300 K is measured with a Perkin Elmer HDR 950 for the range 0.25 to 2 μm and with a SOC 100 HDR for the range 2 to 25 μm. All samples are considered as opaque. Therefore, the spectral hemispherical emissivity (ε) is assumed as related with the spectral hemispherical reflectivity (ρ) by the following relation (λ is the wavelength):

$$\varepsilon(\lambda) = 1 - \rho(\lambda) \tag{2.25}$$

Solar absorptivity, α_{sol}, is calculated from the measured spectral hemispherical emissivity, $\varepsilon(\lambda)$, and the spectral solar irradiance $I_{sol}(\lambda)$ AM1.5 (ASGM-G173-03) contained in the range of 0.25-2.5 μm (Eq.(2.26)). Total emissivity, ε_{tot}, is obtained from the measured spectral hemispherical emissivity and the calculated spectral blackbody emittance at 300 K, E_{bb} (λ, 300K), according to Planck's law (Eq.(2.27)). The integration for total emissivity is between 0.25 and 25 μm in accordance with the reflectivity measurement. The absorptivity to emissivity ratio (α/ε) is used to evaluate the solar selectivity of materials. In order to enhance the effectiveness of solar receiver, it is necessary to maximize the α/ε ratio of receiver materials.

$$\alpha_{sol} = \frac{\int_{0.25}^{2.5} \varepsilon(\lambda) \cdot I_{sol}(\lambda) \cdot d\lambda}{\int_{0.25}^{2.5} I_{sol}(\lambda) \cdot d\lambda} \tag{2.26}$$

$$\varepsilon_{tot} = \frac{\int_{0.25}^{2.5} \varepsilon(\lambda) \cdot E_{bb}(\lambda, 300K) \cdot d\lambda}{\int_{0.25}^{2.5} E_{bb}(\lambda, 300K) \cdot d\lambda} \tag{2.27}$$

Conclusions

In this chapter, a coating(s)/substrate system is proposed for its use in solar receivers. Aluminum nitride (AlN) and silicon carbide (SiC) are selected as coating

materials due to their good thermal properties. Additionally, SiC has a high absorptivity and the semi-transparency of AlN is expected to improve the solar absorption of the substrate. Three mechanisms of failure under cyclic thermal loading are developed for the selection of substrate materials. The mechanisms correspond to the substrate resistance to fracture, creep and spallation of the AlN coating. Refractory-based alloys have excellent mechanical and thermal properties but poor oxidation resistance at high temperature. The alumina-forming FeCrAl alloys are therefore selected as alternative substrates to simplify the characterizations of coatings at high temperature.

A review of the principles of film growth by CVD is provided, following by a detailed description of the CVD reactor used in the present study. Finally, all the characterization techniques used are presented.

Chapter 3

Deposition and high temperature oxidation of AlN coatings

Introduction

This chapter is dedicated to the experimental study of the HTCVD deposition and oxidation evaluation of AlN coatings on metallic substrates. Two kinds of substrates are selected: (1) refractory metal based alloys like molybdenum-based alloys for their excellent thermal and mechanical properties and (2) FeCrAl alloys which have superior oxidation resistance up to 1250 °C, allowing to reduce the influencing parameters in real-life receivers and to study the potential of AlN coatings for their use in solar receivers.

First, HTCVD deposition conditions are briefly described. Phase equilibria in the ternary system of aluminum and nitrogen with molybdenum, iron and chromium are investigated by the Factsage software package. After deposition, microstructure and residual stress in AlN coatings are analyzed. The effect of the ratio of precursors in the gas phase and the influence of deposition temperature are discussed in detail. Cyclic oxidation of AlN coated samples in the high temperature range (800-1100 °C) are carried out to study the lifetime of AlN coatings and thus their potential for high temperature applications.

3.1 HTCVD deposition conditions

The first substrate is a molybdenum based alloy (Goodfellow Metal) that consists of 99 wt% Mo, 0.5 wt% Ti, 0.1 wt% Zr and C. This alloy is commercially named TZM. Cast and oxide dispersion strengthened (ODS) FeCrAl alloys are also chosen as model substrates. The cast FeCrAl alloy (Goodfellow Metal Fecralloy) consists of 22 wt% Cr, 5 wt% Al, 0.1 wt% Y, 0.1 wt% Zr and Fe (balance). The ODS FeCrAl alloy Kanthal APMT (Sandvik, Kanthal) combines the excellent oxidation resistance of cast FeCrAl alloys with improved creep strength. Its composition is 22 wt% Cr, 5 wt% Al, 3 wt% Mo and Fe (balance). In the analysis below, it is convenient to denote the cast and ODS FeCrAl alloys used in this work by Fecralloy and APMT respectively.

The thickness of TZM, Fecralloy and APMT samples are 1, 2 and 3 mm respectively. Prior to the HTCVD process, all samples were cut into small specimens with dimensions of 15×15 mm. Before loading into the CVD reactor, TZM and Fecralloy were hand-polished with a 320 grit SiC paper. The high creep resistance of APMT together with the large difference of thermal expansion coefficients between APMT (15.4×10^{-6} K^{-1}) and AlN (4.5×10^{-6} K^{-1} [36]) lead to the cracking of AlN films after deposition. To avoid the cracking, an accommodation layer of Al_2O_3 (8.3×10^{-6} K^{-1} [167]) was grown prior to AlN deposition by oxidizing APMT substrates at 1100 °C under ambient air during 25 h. Afterwards, substrates are ultrasonically cleaned for 5 minutes in acetone, ethanol and isopropanol successively.

The schematic representation of the HTCVD set-up has been presented in section 2.2.3. The chlorination tube is filled with aluminum pellets and installed at the top of the reactor. The substrate is placed on a graphite susceptor coated with AlN. The reactor is subsequently evacuated at ambient temperature and then purged by argon (Ar) at least three times. This step aims to evacuate the impurities from external environment (e.g. absorbed water) in the reactor. Afterwards, the chlorination chamber is heated up to about 540 °C and cleaned by H_2 at a flow rate of 400 sccm ($cm^3{\cdot}min^{-1}$) for 30 min to purify the aluminum pellets and limit the contamination by oxygen. Subsequently, substrates are heated up to desired deposition temperature under H_2 with a fixed ramp rate of 2%/min (about 30 °C·min^{-1}). The H_2 flow rate is increased to 2250 sccm at this step. Prior to deposition, a thermal cleaning under H_2 atmosphere is carried out for 10 min.

The AlN coating is grown under conditions of high N content with the interrupted growth method. In this method, the supply of Al and N precursors are closed for 10 min after 1 h of deposition at the same growth temperature. This growth process is expected to enhance the nucleation step, to improve the surface flatness and to limit grain growth in the columnar structure. Figure 3.1 shows the interrupted growth process. Depositions are carried out in the temperature range 1100-1200 °C (1200 °C for TZM and 1100 °C for Fecralloy and APMT). The total pressure inside the reactor is set to 2000 Pa. Growth of AlN is initiated by adjusting flow rates of NH_3 and Cl_2 to desired values. $AlCl_3$ is in situ formed via reaction of Al pellets with chlorine gas in the chlorination tube. The chlorination temperature is fixed at about 540 °C, which aims to preferentially form $AlCl_3$ with full conversion of Cl_2. NH_3 is used as the source gas of N, while H_2 is used as the carried gas. The ratio of precursors, abbreviated as N/Al ratio, is defined as the $NH_3/AlCl_3$ ratio in the gas phase. The N/Al ratio is varied from 3 to 45 by keeping Cl_2 flow rate at 20 sccm and varying the NH_3 flow rate from 40 to 600 sccm (see section 3.5.1). We assume that the chlorination reaction yield is 1 and that the $AlCl_3$ is the dominant gaseous species in these conditions. Therefore, the relationship between N/Al ratio and flow rate of NH_3 and Cl_2 at the inlet can be expressed as:

$$\frac{N}{Al} = \frac{v(NH_3)}{v(AlCl_3)} = \frac{v(NH_3)}{\frac{2}{3}\cdot v(Cl_2)} = \frac{3}{2}\cdot\frac{v(NH_3)}{v(Cl_2)} \tag{3.1}$$

where v denotes the gas flow rate. After growth, the samples were cooled down to room temperature at a rate of about 30 °C·min^{-1} in nitrogen (N_2) with a flow

rate of 2250 sccm. At the final step (room temperature), N_2 is replaced by Ar to purge the reactor and the exhaust line.

The surface morphology of polycrystalline AlN layers is characterized by field emission scanning electron microscopy (FE-SEM). The crystal structure and the orientation of the films aree identified by electron backscattered diffraction (EBSD) and X-ray diffraction (XRD) analysis using a X'PERT PRO MPD PANalytical 2-circles diffractometer (Cu Kα radiation (λ=1.54 Å), θ-θ).

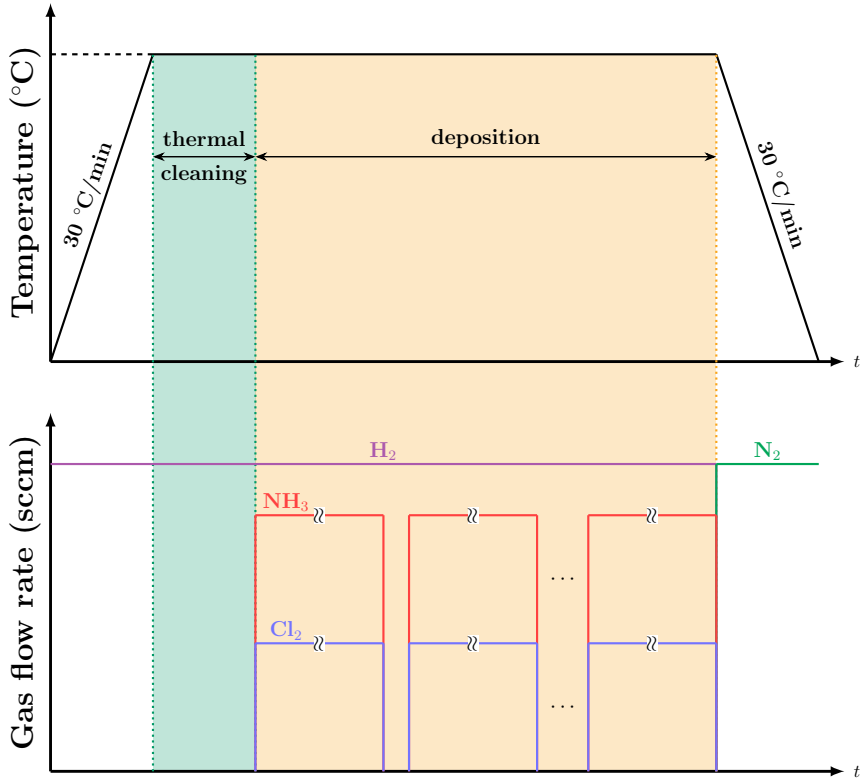

Figure 3.1 Interrupted growth mode used for AlN deposition in this study

3.2 Chemical stability between substrates and AlN

In the present study, the ternary phase diagrams are investigated to study the stability and compatibility of AlN with different types of substrates. Ensuring the stability of the AlN/metal structure allows to prevent chemical reactions at the AlN/metal interface through the entire deposition process. In the present study, a bibliographic investigation on the phase diagrams and thermodynamic properties in Al-N-M (M=Mo, Cr and Fe) ternary systems is conducted and completed with thermodynamic calculations using the Gibbs Energy Minimizing Software, Factsage. The databases used are SGTE and TDnucl. The Factsage software allows to determine chemical reactions and calculate the compositions in the system at equilibrium by choosing temperature and pressure.

Schuster and Nowotny [168] have investigated the phase equilibria in the Al-N-Mo and Al-N-Cr ternary systems at temperatures between 1000 °C and 1500 °C. No ternary phase was observed in this temperature range in these two systems. In the present study, the isothermal phase equilibria of Al-N-Cr/Fe and Al-N-Mo ternary systems were calculated by Factsage at 1100 °C and 1200 °C respectively. The phase diagrams (Figure 3.2) show AlN in thermodynamic equilibrium with Fe and Cr at 1100 °C, and with Mo at 1200 °C. No Fe-N and Mo-N phases were observed due to the low solubility of nitrogen in Fe and Mo. This suggests that no interfacial reaction between the selected substrates and AlN will take place during the deposition.

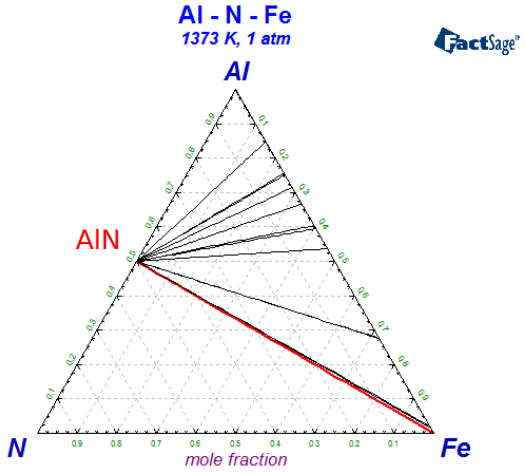

(a) Al-N-Fe phase diagram at 1100 °C

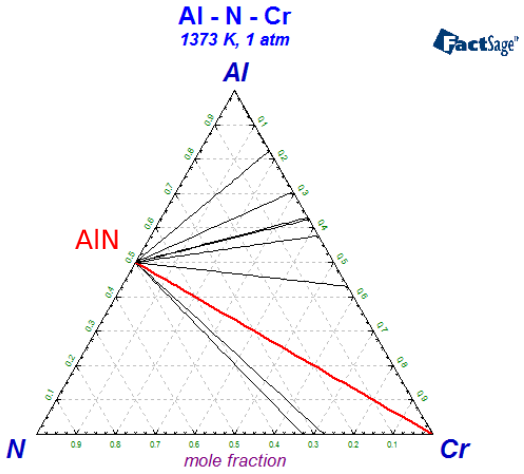

(b) Al-N-Cr phase diagram at 1100 °C

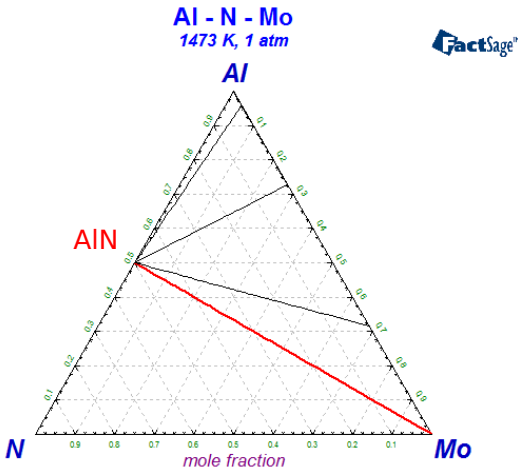

(c) Al-N-Mo phase diagram at 1200 °C

Figure 3.2 Calculated ternary phase diagrams at (a, b) 1100 °C and (c) at 1200 °C of the systems: (a) Al-N-Fe, (b) Al-N-Cr, and (c) Al-N-Mo.

3.3 AlN deposition on TZM

3.3.1 Microstructure of AlN coatings

Our previous studies of AlN deposition by high temperature CVD have been made in a large range of temperature, pressure and flow rate of precursors [169–173]. It was shown that the surface morphologies of AlN are sphere-like at lower temperatures (800 °C), and become plate-like when the temperature increases (above 1000 °C) [15, 171, 173]. At high temperature, the surface diffusion of chemical species is enhanced, resulting in the formation of 1-3 μm size faceted grains [15, 174]. Claudel et al. [15, 174] studied the growth of polycrystalline AlN on (0001) α-Al_2O_3 sapphire, (0001) off axis 4H SiC, and graphite at temperatures between 1100 and 1800 °C. Their work shows that the growth of AlN can be divided into two regimes: (1) at low temperature (below 1300 °C in the case of AlN grown on graphite), the AlN growth rate decreases linearly with the inverse of temperature, which corresponds to a kinetic regime; and (2) at high temperature, the growth of AlN layers is limited by the diffusion of the reactive species towards the substrate [15, 174]. The evolution of growth rate as a function of the inverse of temperature follows the theoretical calculations of transport phenomena [174].

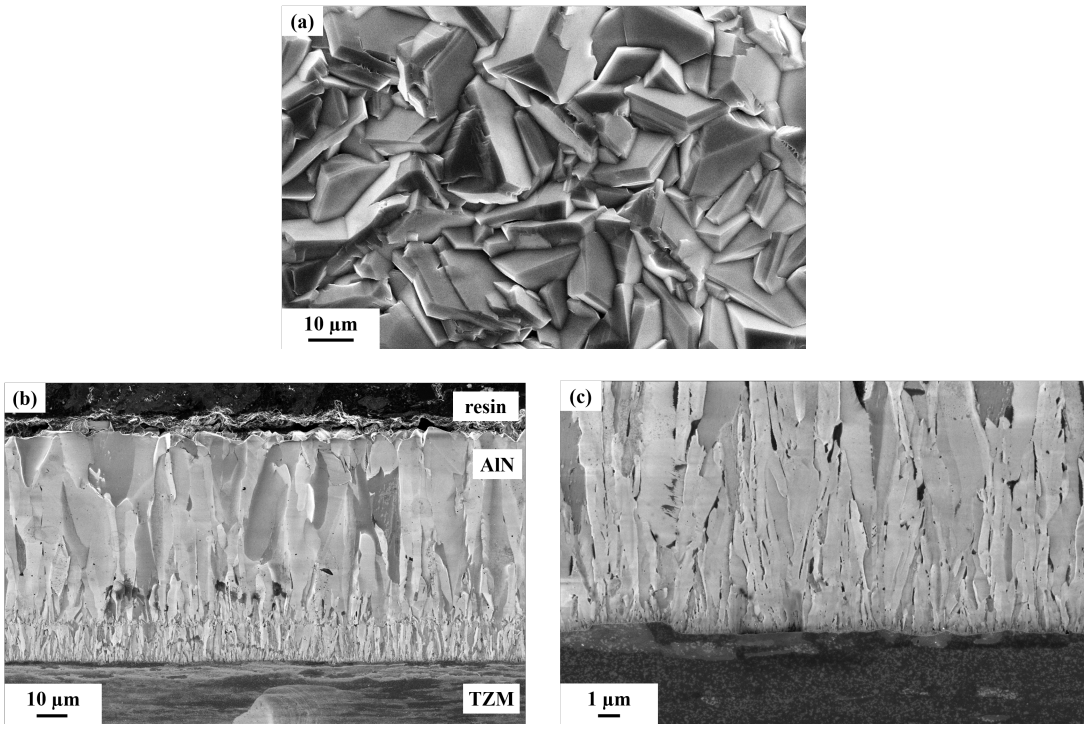

Figure 3.3 Surface morphology and microstructure of AlN coating deposited on TZM substrate at 1200 °C: (a) surface morphology, (b) cross-sectional microstructure and (c) a high magnification of (b) at the AlN/TZM interface

In the present study, AlN coatings are grown on TZM substrates at 1200 °C with a N/Al ratio of 3. Flow rate of NH_3 and Cl_2 are 40 sccm and 20 sccm respectively.

The deposition time is 3 h for AlN growth and 10 min of interruption per hour at the same temperature (described in section 3.1). As shown in Figure 3.3, the AlN layer, deposited at a growth rate of about 20 μm·h^{-1} with ±5% uncertainties, presents a faceted surface morphology and a columnar microstructure with large grains. The grain width is around 15 μm at the surface. The grain size increases from the AlN/TZM interface to the surface. Moreover, it is worth noting that the as-deposited structure is stable. As expected in section 3.2, neither interfacial reaction nor delamination of AlN layer occurs at the AlN/TZM interface. However, there exists a porosity in the AlN coating, notably close to the AlN/TZM interface (Figure 3.3(c)).

Figure 3.4 shows the θ-2θ X-ray diffraction patterns of the as-grown AlN coating. The fine peaks correspond to a good crystallization of the AlN coating. It should be pointed out that the semi-polar plane $(11\bar{2}2)$ is preferred at 1200 °C. The $(11\bar{2}2)$ preferred orientation is in agreement with our previous study but the temperature is lower (1300 °C in [15]). It is of major importance to note that the preferred orientation strongly depends on process parameters, N/Al ratio in the gas phase, deposition temperature, partial pressure of each precursor, etc. The selection mechanism is more pronounced when the growth rate and the temperature increase [173]. Claudel et al. [15] presented the evolution of preferred orientations for polycrystalline AlN layer on graphite from $(11\bar{2}2)$ to $(21\bar{3}1)$, and finally to $(11\bar{2}0)$ with increasing deposition temperature from 1200 to 1600 °C, as shown in Figure 3.5. This observation corresponds to the van der Drift growth model [12] in which the preferred orientation selected during the growth process is determined by the fastest growth direction nearly perpendicular to the substrate. The $(11\bar{2}2)$ plane corresponds to the crystalline plane parallel to the TZM substrate and seems to be the most stable orientation at 1200 °C.

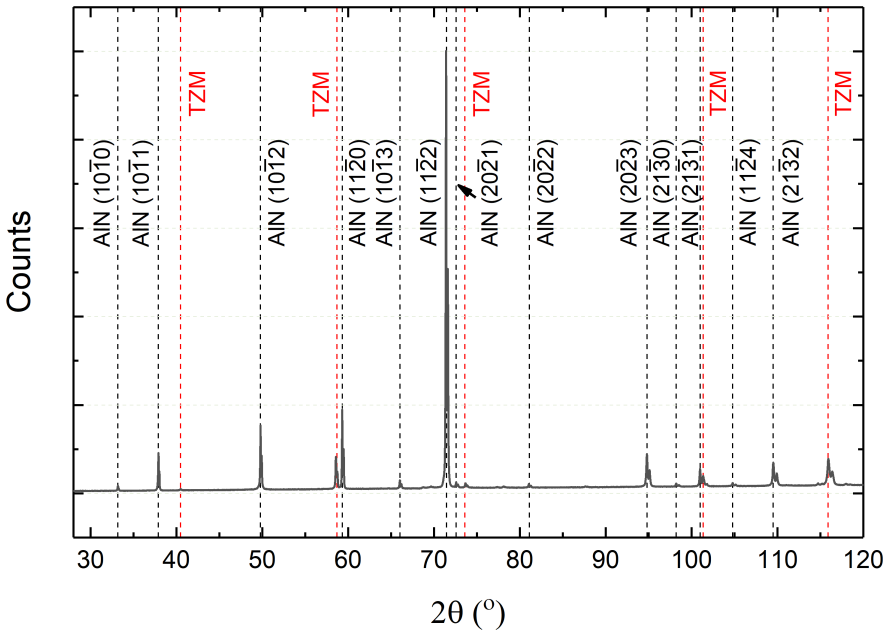

Figure 3.4 θ-2θ X-ray diffraction spectrum of AlN coating grown on TZM at 1200 °C.

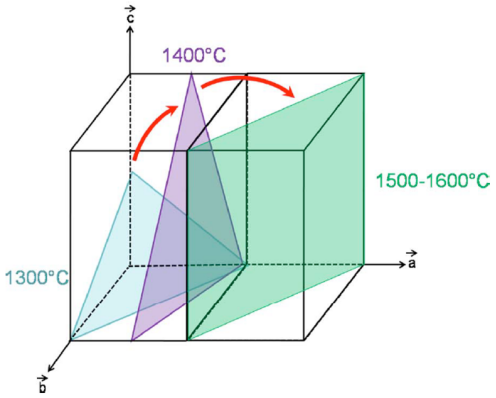

Figure 3.5 Preferred orientations changed from $(11\bar{2}2)$ to $(21\bar{3}1)$, and finally to $(11\bar{2}0)$ with increasing deposition temperature in the work of Claudel et al. [15].

3.3.2 Residual stress

During the growth of polycrystalline AlN, intrinsic growth stresses are created from the coalescence of islands and the subsequent thickening. Its magnitude depends on the growth conditions. Moreover, thermal stresses are generated by temperature variations and thermal expansion mismatch between the layer and substrate. The system is curved to maintain the boundary continuity.

The biaxial residual stress in AlN coating, noted as σ_{res} in the following for the sake of clarity is, to a first approximation, assumed to be constant throughout its thickness, and can be expressed as the sum of intrinsic and thermal stresses:

$$\sigma_{res} = \sigma_g + \sigma_{th} \tag{3.2}$$

where σ_g is the intrinsic growth stress due to deposition, and σ_{th} is the thermal stress which is roughly estimated by the following equation:

$$\sigma_{th} = \frac{E_{AlN}}{1 - \nu_{AlN}} \cdot \int_{T_{growth}}^{T_{final}} (\alpha_{th,s}(T) - \alpha_{th,AlN}(T))dT \tag{3.3}$$

where E_{AlN} and ν_{AlN} are the Young's modulus and Poisson's ratio of AlN respectively, T_{growth} is the deposition temperature, T_{final} is usually room temperature, $\alpha_{th,s}$ is the thermal expansion coefficient of substrate and $\alpha_{th,AlN}$ is that of AlN.

Various methods could be used to estimate or determine residual stress in a layer. The Stoney formula is usually used to estimate it, such as:

$$\sigma_{res} = \frac{E_s}{1 - \nu_s} \cdot \frac{t_s^2}{t_{AlN}} \cdot (\frac{1}{R} - \frac{1}{R_0}) \tag{3.4}$$

where E_s is the Young's modulus of substrate, ν_s is its Poisson's ratio, t_s is its thickness, t_{AlN} is the thickness of deposited AlN, R and R_0 are the radii of curvature after and before deposition respectively.

The Stoney formula requires the consideration of the following assumptions [175, 176]:

- uniform thickness in both film and substrate;
- film thickness much more small than that of substrate (typically $\frac{t_s}{t_{AlN}} > 1000$);
- both film and substrate are homogeneous, isotropic and linearly elastic;
- thickness of film/substrate system should be much smaller than its in-plane dimensions (x-y plane), the film stress is isotropic or equibiaxial whereas out-of-plane stress and all shear stress vanish;
- curvature of the system (1/R) is uniform.

The curvature is usually measured with a mechanical profilometer. The main disadvantage of this method is that it requires a direct contact with the sample, and involves a risk of physical damage. Measurement of curvature is also very sensitive to the surface quality of the sample [177]. Nevertheless, it is difficult to fulfill all the assumptions for the use of Stoney formula. In many case, to ensure sufficient precision in the curvature measurement, coatings are deposited on specially prepared substrates [178].

In the present study, the non-destructive technique XRD-sin$^2\psi$ was used to determine in-plane stress in AlN coatings. Different from Stoney formula presented above which is related to the specimen curvature, this technique is based on the relative displacement of atomic planes. Details have already been presented in Chapter 2.

Compressive stresses are measured in the AlN coating at room temperature (25 °C). The thickness of AlN coating on TZM is around 60 μm. The measured residual stress in the coating is -232±14 MPa while the estimated thermal stress is -353.98 MPa with $\alpha_{th,s}$=5.2×10^{-6} K^{-1} and $\alpha_{th,AlN}$=4.5×10^{-6} K^{-1}. Young's modulus and Poisson's ratio of AlN are 340 GPa and 0.21 respectively. Thus, the intrinsic growth stress can be deduced from Eq.(3.2). The growth stress is thus tensile and its value is 122±14 MPa.

Raghavan and Redwing [179] have investigated the in-situ curvature evolution during MOCVD growth of AlN layer on (111) silicon and (0001) sapphire substrates from 600 to 1100 °C. They have calculated the corresponding stresses using the Stoney formula. Their work demonstrates the tensile growth stress, and reveals its time-independence. The value of growth stress drops from >1 GPa to <400 MPa when the deposition temperature decreases from 900 to 800 °C on (111) Si substrates. On (0001) sapphire substrates, the same trend is observed but the stress values are higher [179]. Boichot et al. [180] assessed the influence of process parameters on the stress in the AlN film using a design of experiment (DOE) approach, and stated that deposition temperature is of secondary importance. This contradiction can be explained by the transformation from epitaxial growth at temperatures over 900 °C (growth stress>1 GPa) to the low temperature polycrystalline growth of defective AlN film (growth stress<400 MPa) in the work

of Raghavan and Redwing [179]. Complete details are provided below. It has also been shown in the work of Boichot et al. [180] that the tensile growth stress remained relatively constant with the change of growth rate. Gan et al. [181] found that the value of intrinsic growth stress is related to the preferred orientations of AlN. The films were deposited using a filtered cathodic arc technique. Their work indicates that low growth stress (250 MPa) is obtained when the grown AlN film is (0001) oriented. At high stress level (3.5-4 GPa), the c-axis is constrained to remain parallel to the substrate [181].

The growth stress value obtained in the present work (122 MPa) is lower than that reported in the literature [179, 181]. This difference might result from various parameters like substrates, microstructure, thickness and preferred orientations of AlN, etc. As mentioned in section 2.2.2, the polycrystalline growth process consists of (1) nucleation, (2) island growth, (3) coalescence of islands and (4) thickening. In the reference [180], the primary island nucleation is claimed to be the main contributor to the growth stress during the deposition. The tensile growth stress is more pronounced when the primary island size is smaller. Moreover, it is reported that the primary island size is found to be higher with an increase of temperature (about 35 nm at temperatures over 1200 °C) [180]. In such case, the higher the deposition temperature of AlN, the larger are the primary islands, and thus the lower is the growth stress value.

Raghavan and Redwing [182] believed that the island coalescence has also a strong effect on growth stress. In their work, the maximum growth stress is a function of grain size and grain boundary energy. The transformation of high temperature epitaxial growth to low temperature polycrystalline growth of AlN leads to an increase of grain boundary energies, and thus a decrease in growth stress. This might be a reasonable explanation for the lower growth stress in our polycrystalline AlN coatings. Moreover, Raghavan and Redwing [182] reported that the decrease of grain size in the epitaxial growth leads to an increase of growth stress in AlN. We assume here that similar to the high temperature epitaxial growth in [179, 182], the growth stress also depends on the grain size of AlN in our high temperature polycrystalline growth. Thus, large grain size might result in small growth stress in AlN coating. Furthermore, the thermal expansion coefficient is temperature dependent. The rough estimation of thermal stress using a constant thermal expansion coefficient can lead to the underestimation of the growth stress. More precise calculations (see Chapter 4) are required. In summary, the low growth stress obtained in the present work could be explained by the high deposition temperature (or large primary island size of AlN), large grain size of AlN, polycrystalline microstructure and the uncertainties in thermal stress estimation.

3.4 Oxidation of AlN coatings on TZM

3.4.1 Oxidation conditions

Oxidation of TZM coated with AlN on both faces is carried out in the REHPTS set-up of PROMES laboratory (Chapter 2) in open air at atmospheric pressure of

0.87 10^5 Pa as the set-up is located at 1500 m of altitude. The thickness of AlN coating is 15 μm. The sample was ultrasonically cleaned before loading into the reactor, and subsequently heated up to 1327 °C. The oxidation was interrupted after 8 min due to formation of smoke in the reactor. It corresponds to the formation of a volatile species, molybdenum trioxide (MoO_3).

3.4.2 Microstructure

Figure 3.6 presents macroscopic images of AlN coated TZM before and after oxidation. The formation of volatile MoO_3, which is confirmed by XRD and Raman analysis, lead to the formation of macroscopic holes on both front-side and backside surface. SEM images observed at the edge and center of the backside surface after oxidation are shown in Figure 3.7. The sample exhibits two different surface morphologies. At the edge, the failure of AlN coating leads to the formation and subsequent condensation of MoO_3 on the surface (Figure 3.7(a)). At the center, however, a mixture of Al_2O_3 and AlN is observed as shown in Figure 3.7(b). Small pores formed on the surface are due to the exchange of N_2 and O_2 during the oxidation of AlN. Moreover, grain boundaries and micro-cracks are formed on the surfaces.

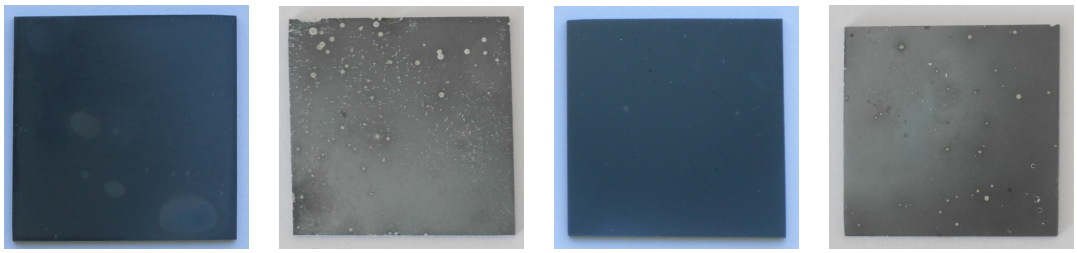

(a) (b) (c) (d)

Figure 3.6 Macroscopic images of AlN coated TZM sample (a,c) before and (b,d) after oxidation: (a,b) front-side and (c,d) backside.

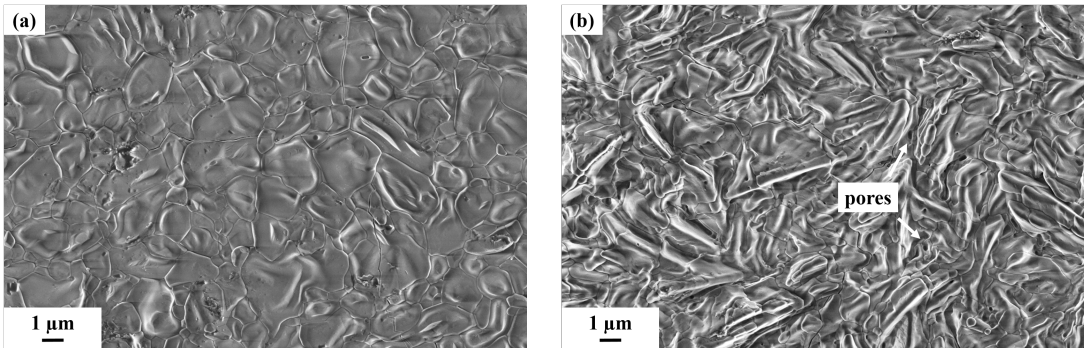

Figure 3.7 Two different surface morphologies of AlN coated TZM sample after 8 min of oxidation at 1327 °C: (a) at the edge and (b) at the center.

Different cross-sections are performed to characterize AlN coatings after oxidation (Figure 3.8). The AlN coatings remain dense, homogeneous and adherent on TZM substrate at both center (Figure 3.8(a)) and edge (Figure 3.8(b)). We can therefore note that the oxidation of molybdenum is probably not due to an edge effect. Al_2O_3 was formed on the top of AlN coating, which is also confirmed by EDX mapping. Neither diffusion between the substrate and AlN (Figure 3.8(d)), nor micro-cracks in the AlN coating and/or alumina layer was observed. This suggests that Al_2O_3 plays its protective role when AlN coating is adherent. However, as depicted in (Figure 3.8(c)), gaps between AlN crystallites are fast diffusion paths for oxygen. Oxidation occurred within the AlN coating. These paths mainly come from the formation of grain boundaries with large surface to volume ratios during the 3D (Volmer-Weber) growth.

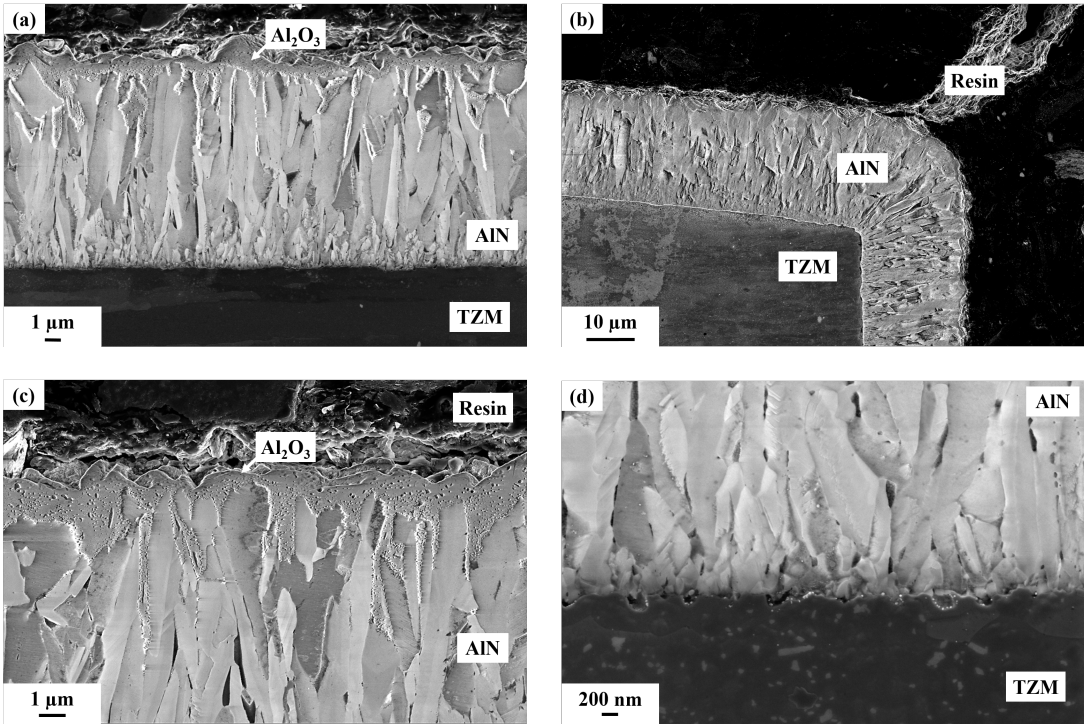

Figure 3.8 Microstructure of AlN coated TZM sample after 8 min of oxidation at 1327 °C: (a) at the center, (b) at the edge, (c) at the Al_2O_3/AlN interface and (d) at the AlN/TZM interface.

Figure 3.9 presents (a) the total loss of adhesion of AlN coating resulting in the formation of MoO_3 on the surface and (b) the partial loss of AlN leading to the oxidation of AlN and Mo. As shown in Figure 3.9(a), the failure of AlN coating at high temperature leads to a loss of protection of the substrate, resulting in the formation and the condensation of MoO_3 on TZM substrate. This is in agreement with the observed smoke during oxidation and the surface morphology presented in Figure 3.7(a). However, in Figure 3.9(b), the formed alumina-based layer has been removed from the substrate, suggesting that AlN coating remained adherent and protect TZM substrate, but failed afterwards. This partial loss of adhesion can be attributed to initial cracks amplified by the growth of the alumina layer and/or

thermal stresses. Mo oxidized during the delamination of AlN coatings. The oxidation of AlN and Mo occur simultaneously, resulting in a complex temporal evolution. The minor elements of TZM, Ti and Zr, diffused into the Al_2O_3 layer as presented in Figure 3.9(b).

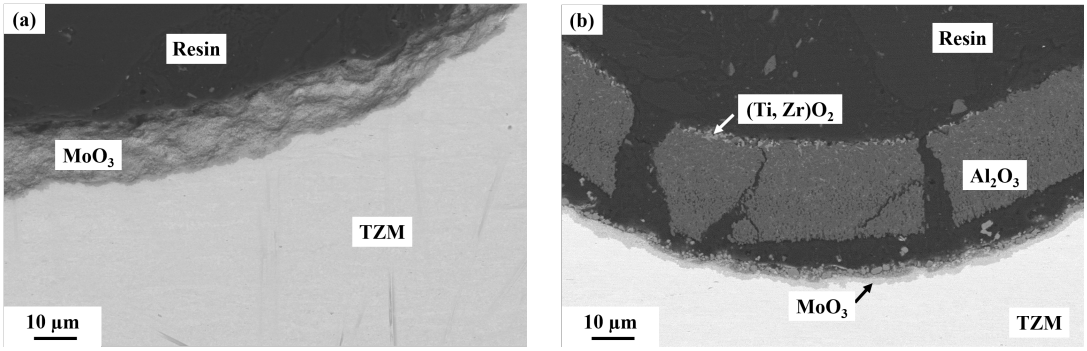

Figure 3.9 Loss of adhesion of AlN coating during oxidation resulting in: (a) formation of MoO_3 and (b) competitive oxidation of AlN and Mo.

Moreover, it is interesting to note that TZM is usually consolidated by powder metallurgy (PM) process. This technology usually produces a component with inevitable porosity even after sintering. Figure 3.10(a) shows a 'laminated' defect located on the lateral sides of the substrate. Such defects have been observed on bare samples and could result from the processing technique or from cutting prior to deposition. The coating is adherent to the edge of this defect after deposition. However, there was almost no deposition inside the defect (Figure 3.10(b)). The presence of this type of defect will lead to a loss of protection during oxidation.

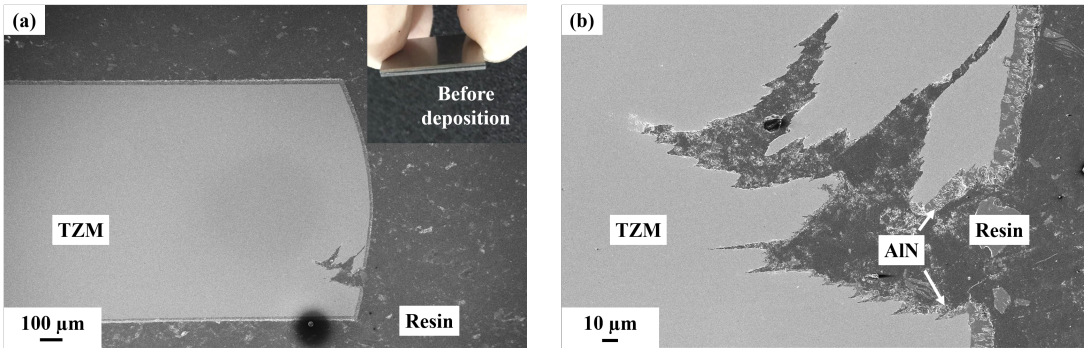

Figure 3.10 'Laminated' defect located on the lateral side of the substrate: (a) SEM cross-section image after deposition of AlN with a macroscopic image of TZM substrate before deposition and (b) a high magnification of the 'laminated' defect shown in (a).

Previous discussions show the difficulty to infiltrate AlN coating into the 'laminated' defects, originated from the processing technique or from cutting. Nevertheless, cracks amplified by the growth of alumina and/or thermal stresses at high temperature lead to inadequate protection of AlN coatings for TZM.

Therefore, it is necessary to develop an adequate surface coating on the TZM substrate prior to deposition of AlN to provide a first protection for TZM. Indeed, aluminization and silicidation of TZM via halide activated pack cementation to protect TZM from high temperature oxidation have been studied in the past few years [183–186]. Molybdenum aluminide, or molybdenum silicide thin layers, developed through diffusion of Al or Si into TZM substrate, are protective for high temperature applications. Therefore, the development of silicide coatings and/or aluminide coatings by CVD is a key point to address in a further study.

3.5 AlN deposition on FeCrAl alloys

As discussed in Chapter 2, fast-creeping cast FeCrAl alloy (Fecralloy) and slow-creeping ODS FeCrAl (APMT) are selected as model substrates due to their excellent oxidation resistance at high temperature. In previous sections, the high temperature oxidation of AlN revealed the appearance of cracks and delamination of AlN coatings, and thus a loss of protection for the TZM substrate.

In such a case, the choice of oxidation resistant Fecralloy and APMT allows the simplification of the complex problem of system lifetime. Thus, it is possible to characterize optical, mechanical and chemical properties of AlN coatings at high temperature. Furthermore, these model systems, AlN/Fecralloy and AlN/APMT, allows the study of the effects of creep properties of substrates. In the following, stresses in AlN and Al_2O_3 layers during cyclic oxidation are measured by Raman spectroscopy and photoluminescence respectively.

3.5.1 Microstructure of AlN coatings on Fecralloy

This section aims to evaluate the influence of N/Al ratio in the gas phase on the microstructure and grain size of AlN coatings deposited on Fecralloy substrates. N/Al ratios are varied over a range of 3 to 45. One hour of deposition at 1100 °C is performed for all ratios. The operating conditions are listed in Table 3.1.

Table 3.1 Conditions for the deposition of AlN on Fecralloy to study the influence of N/Al ratio

Sample	Temperature (°C)	Pressure (Pa)	N/Al ratio	H_2 (sccm)	N_2 (sccm)	Cl_2 (sccm)
AlN-20	1100	2000	3	2250	40	20
AlN-23	1100	2000	11.25	2250	150	20
AlN-24	1100	2000	18	2250	240	20
AlN-22	1100	2000	22.5	2250	300	20
AlN-21	1100	2000	45	2250	600	20

Effect of N/Al ratio

As discussed in the section 3.3.1, the enhancement of surface diffusion at high temperature leads to the formation of large size faceted grains. It was also

shown that low N/Al ratios are preferable to have dense layers at temperatures over 1000 °C. Previous results were obtained on silicon, sapphire and graphite materials. Surface morphologies and cross-sections are shown in Figure 3.11, to characterize the evolution of microstructure, grain size and texture as a function of N/Al ratio. Similarly to AlN coatings grown on TZM substrate presented in the section 3.3.1, all deposited AlN coatings are composed of pyramid-shape crystals. No cracks or delamination are observed. The grain size increases from the AlN/Fecralloy interface to the surface at all N/Al ratios. The small grains at the AlN/Fecralloy interface are the result of random nucleation at the beginning of the growth. The competition between these randomly oriented small grains lead to a columnar microstructure. SEM cross-section images (Figure 3.11 (f)-(j)) reveal that the average grain size decreases from 1.15 μm to 200 nm with increasing N/Al ratio in the gas phase. This is in agreement with a decrease of supersaturation. Additionally, AlN layers grown at a low N/Al ratio equal to 3 are denser than the others. This is in good agreement with our previous studies [169–173].

The growth rate of AlN decreases from 15 to 2 μm·h^{-1} (with an uncertainty of $\pm$5%) with increasing the N/Al ratio, in contradiction with the results reported by Claudel et al. [187, 188]. It was found in their work that the experimental growth rate remains relatively constant at the same deposition temperature, which is in good agreement with thermodynamic predictions based on the minimization of Gibbs energy. Their model consists of a complete thermodynamic modeling and simulation of heat transfer, mass transport, gas flow dynamics and chemical reactions based on available literature data and experimental data of AlN growth on AlN templates. Details of this model can be found in [169, 173]. The conflicting results in the present study are due to the recirculating gaseous species when increasing the NH_3 flow rate (N/Al$\geq$18). The same phenomenon is observed by fluid dynamic modelling but at higher pressure ($\geq$4000 Pa). Moreover, due to the independence of AlN growth rate on N/Al ratio investigated by Claudel et al. [187, 188], the variation of N/Al ratio in the gas phase is assumed to be the only reason for the evolution of surface morphology and microstructure in this work.

The recirculation of gases (N/Al$\geq$18) in the reactor leads to a inhomogeneity of AlN coating, as shown in Figures 3.11(a), (c) and (e). The N/Al ratio is also one of major process parameters that affect the preferred orientation of AlN layers. At high degree of supersaturation, i.e., N/Al>5, immobile grain boundaries are formed through coalescence of initial small islands with large surface to volume ratios. Subsequent grain coarsening occurs through epitaxial growth on these grains. The competitive growth processes lead to an incomplete orientation selection, and thus weakly textured grains. Figure 2.10 explains the mechanisms for the evolution of preferred orientations during growth processing.

XRD patterns of deposited AlN coatings with respect to N/Al ratio are shown in Figure 3.12. The degree of preferred orientation of different crystalline planes are calculated using the following formula (Eq.(3.5)) from Harris's work [189] and summarized in Table 3.2.

$$T_{c(hkl)} = \frac{I_{(hkl)}/I_{0(hkl)}}{(1/M)\cdot[\sum_M I_{(hkl)}/I_{0(hkl)}]} \tag{3.5}$$

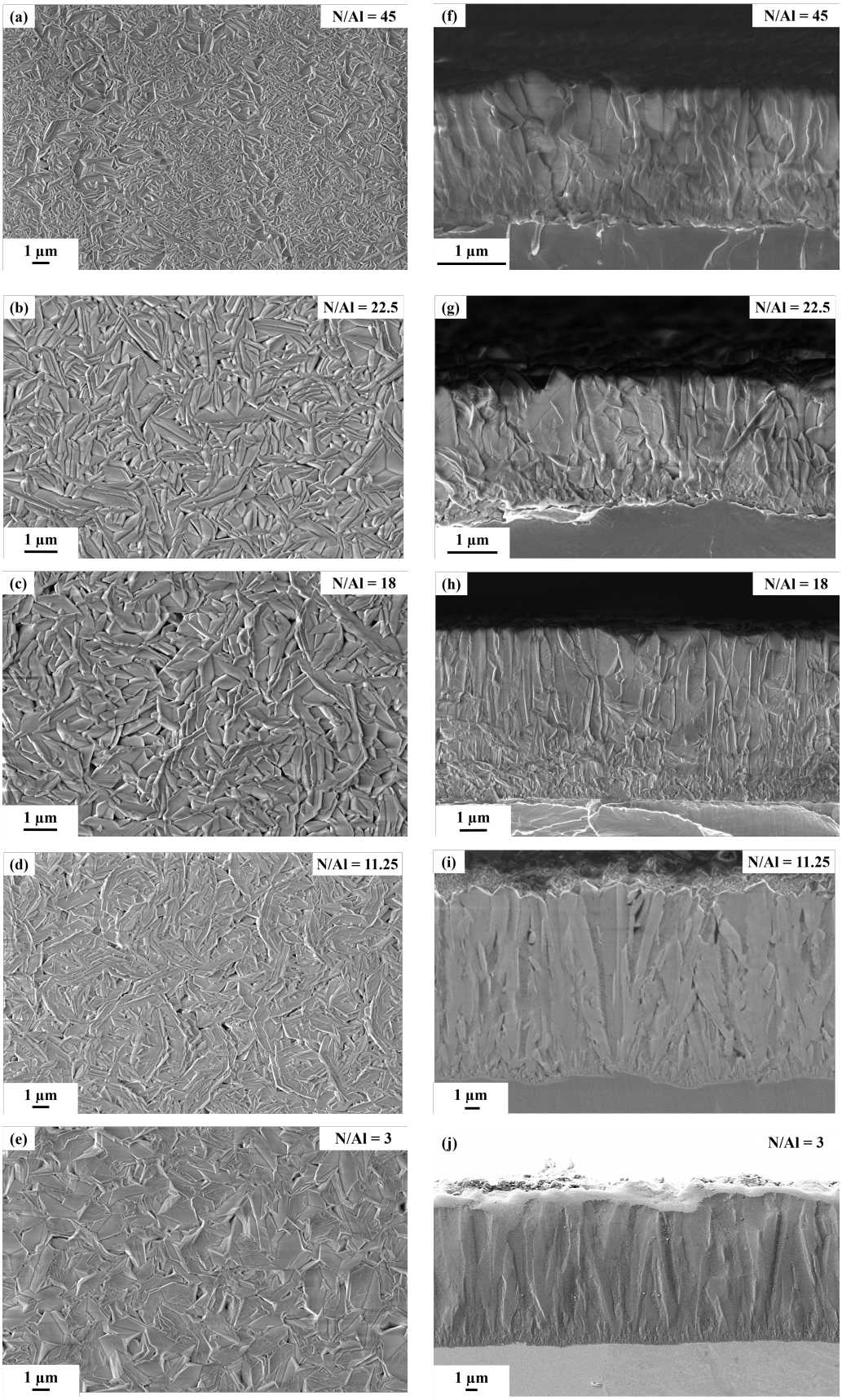

Figure 3.11 (a)-(e) Surface morphologies and (f)-(j) cross-sections of AlN coatings processed on Fecralloy at T=1100 °C, P=2000 Pa, Cl_2 flow rate of 20 sccm, NH_3 flow rate varying from 40 to 600 sccm, N/Al ratio estimated by $NH_3/AlCl_3$ inlet flow rate ratio assuming that $AlCl_3$ is the predominant $AlCl_x$ specie.

where $T_{c(hkl)}$ is the texture coefficient of the crystalline plane (hkl), $I_{(hkl)}$ is the measured integrated intensity, $I_{0(hkl)}$ is the relative integrated intensity of the corresponding plane in ICDD diffraction PDF-2 data (file 00-066-0534 used here for AlN), and M the number of reflections. For a perfectly random polycrystalline structure, the texture coefficient of each orientation should be equal to 1. An increase (decrease) in the texture coefficient from unity indicates a higher (lower) degree of preferred orientation of AlN with respect to the substrate. The deviation of the texture coefficient also corresponds to the change in planar density along a particular plane compared to ideal values [190]. Crystalline planes taken into account in this work are $(10\bar{1}0)$, (0002), $(10\bar{1}1)$, $(10\bar{1}2)$, $(11\bar{2}0)$, $(10\bar{1}3)$, $(11\bar{2}2)$, $(20\bar{2}1)$ and $(20\bar{2}3)$. For example, the $(10\bar{1}2)$ orientation is favored for the AlN coatings proceeded at a N/Al ratio of 3 ($T_{c(10\bar{1}2)}$=3.882), while the $(10\bar{1}0)$ orientation is disfavored ($T_{c(10\bar{1}0)}$=0.003).

Table 3.2 Texture coefficients for AlN deposited with different N/Al ratio

Crystalline planes (hkil)	2θ (°)	Texture coefficient				
		N/Al=3	N/Al=11.25	N/Al=18	N/Al=22.5	N/Al=45
$(10\bar{1}0)$	33.222	0.003	0.131	0.056	0.247	0.096
(0002)	36.053	0.474	0.666	0.383	1.400	1.182
$(10\bar{1}1)$	37.939	0.381	0.855	0.845	1.313	0.692
$(10\bar{1}2)$	49.832	3.482	1.547	1.880	1.647	2.092
$(11\bar{2}0)$	59.359	0.004	0.098	0.064	0.168	0.228
$(10\bar{1}3)$	66.070	0.931	1.363	1.027	1.284	1.801
$(11\bar{2}2)$	71.450	0.328	2.746	2.956	1.026	0.961
$(20\bar{2}1)$	72.643	0.037	0.155	0.165	0.324	0.279
$(20\bar{2}3)$	94.861	3.361	1.439	1.624	1.590	1.669

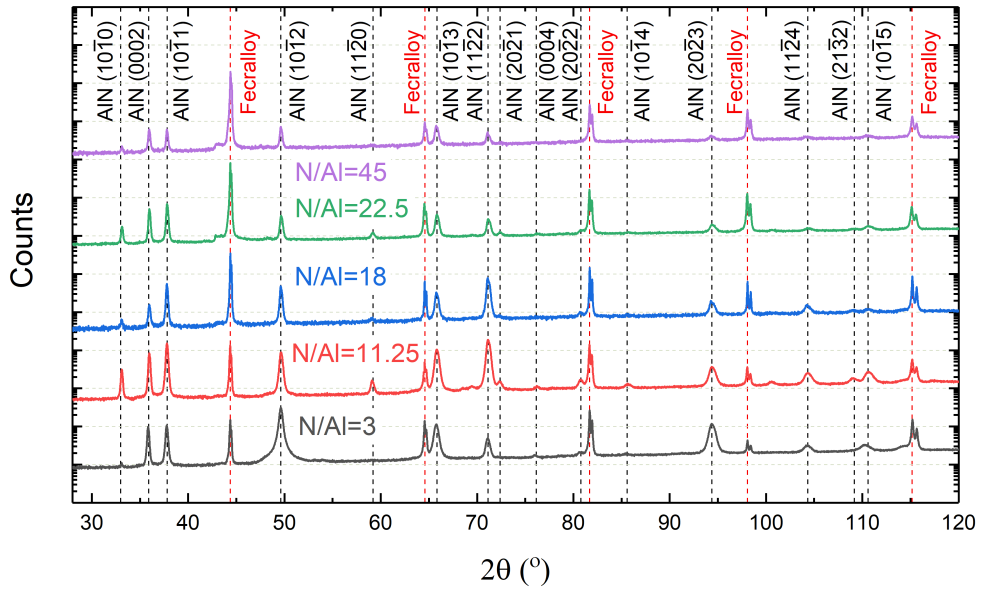

Figure 3.12 Effect of N/Al ratio on preferred orientation(s) of AlN deposited at 1100 °C on Fecralloy.

The texture coefficient analysis indicates that the (hki0) plane is disfavored regardless of N/Al ratio. However, orientations along semi-polar planes $(10\bar{1}2)$ and $(20\bar{2}3)$ are preferred. The $(10\bar{1}3)$ and $(11\bar{2}2)$ orientations are also favored at higher N/Al ratio (higher NH_3 flow rate and higher supersaturation), which corresponds to the study of Dollet et al. [17]. However, the texture of $(11\bar{2}2)$ plane is less pronounced when the degree of supersaturation is extremely high, i.e. N/Al$\geq$22.5, whereas the (0002) tends to be one of preferred orientations. Nevertheless, this orientation is disfavored at a N/Al ratio of 45. Dollet et al. [17] suggest that the $(11\bar{2}2)$ orientation will become predominant if the film is thicker, whereas in their work the (0002) preferred orientation is only observed when the thickness is less than 4 μm. In the present study, the thickness of AlN deposited at extremely high supersaturation (N/Al$\geq$22.5) is less than 3 μm. The existence of (0002) preferred orientation is thus in good agreement with the work of Dollet et al. [17]. It is concluded that the (0002) orientation is obtained at the early stage of deposition at a high degree of supersaturation, but the geometrical selection favors the $(11\bar{2}2)$ orientation during the growth.

Moreover, according to the van der Drift growth mechanism [12], the selection of orientations is proceeded during the growth process, resulting from the competition between initially formed random crystals. The orientation is more pronounced when its growth rate normal to the substrate is faster. Dollet et al. [17] pointed out that the growth rate of $(11\bar{2}2)$ is a little bit higher than that of $(10\bar{1}1)$ planes. Thus, the $(11\bar{2}2)$ orientation should be more favored than $(10\bar{1}1)$ due to its higher vertical growth rate. Our experimental observations confirm this trend except at N/Al=22.5. The texture coefficient of $(11\bar{2}2)$ plane is lower than that of $(10\bar{1}1)$ plane. It is, probably, because the thickness of deposited AlN in this condition is low. The competition between crystal growth along these two planes is still not completed. The angle between $(11\bar{2}2)$ plane and the normal vector to the substrate is 32°. It is close to the angle between $(10\bar{1}1)$ plane and the normal vector (28°25'). This means that the angle between the vertical growth rate of these two crystalline planes is only 3°35'. Thus, for a sample exhibiting $(10\bar{1}1)$ and $(11\bar{2}2)$ textures with a certain thickness, the selection of orientations must be very low, and a large thickness is required to for the determination of the final preferred orientation [17]. Hence, the (0002) and $(10\bar{1}1)$ orientations will be finally replaced by $(11\bar{2}2)$ up to a certain thickness.

The inverse pole figure (IPF) coloring of hexagonal AlN and crystal orientation mappings (derived by EBSD) of AlN coatings processed with N/Al ratios of 3 and 11.25 are shown in Figure 3.13. The A1 axis is perpendicular to the substrate surface (parallel to the thickness direction). Black pixels and regions denote unindexed points and areas where orientation measurements were unsatisfactory. The significant discontinuity at the AlN/substrate interface could be correlated to the height gradient due to the grinding and polishing processes during the metallographic preparation. Moreover, AlN is a semiconductor with a wide band gap (6.2 eV). Its intrinsic insulation properties lead to low resolution of patterns at grain boundaries. As expected, AlN deposited at a low degree of supersaturation (N/Al=3) is denser, and the immobile grain boundaries seem to be less pronounced.

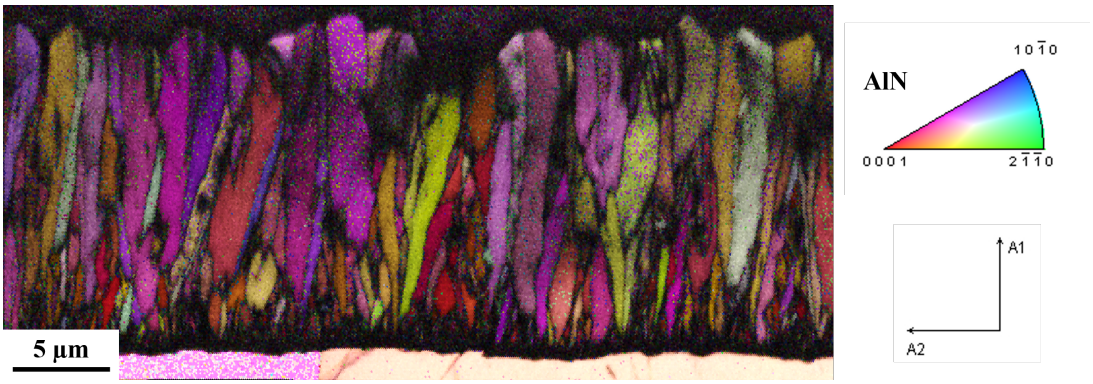

(a) N/Al=3

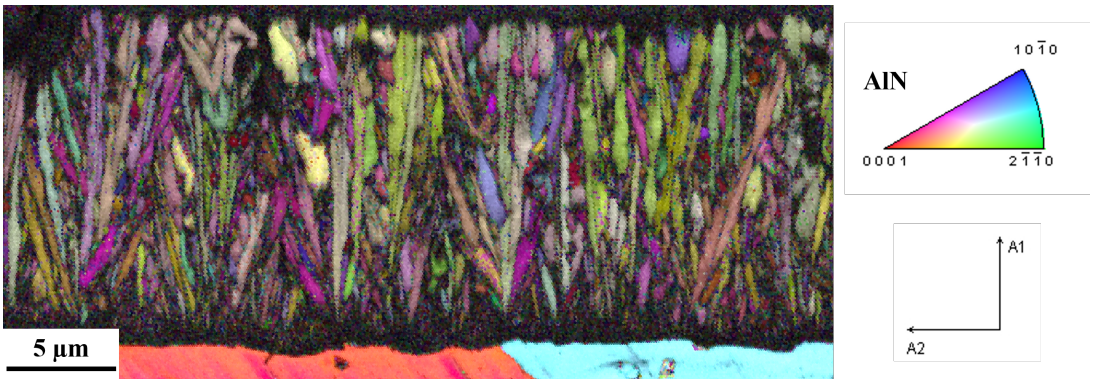

(b) N/Al=11.25

Figure 3.13 EBSD orientation mappings of coated systems shown in Figure 3.11: (a) N/Al=3 and (b) N/Al=11.25; the A1 axis is perpendicular to the substrate surface.

Grains grown along the directions of [60$\bar{6}$7], [80$\bar{8}$7] and [40$\bar{4}$7] with a maximum tolerance of 20° are denoted in Figure 3.14(a) by red, green and blue colors respectively. These crystal directions correspond to the normal direction of semi-polar plans (10$\bar{1}$2), (20$\bar{2}$3) and (10$\bar{1}$3). In fact, the 4 indices of crystal direction perpendicular to plane (hkil) (l≠0) is [HKI$\frac{L}{\Lambda^2}$], with $\Lambda=\frac{2}{3}(\frac{c}{a})^2$, a and c are the lattice parameters of AlN. Most of grains in Figure 3.14(a) are revealed, indicating that (10$\bar{1}$2), (20$\bar{2}$3) and (10$\bar{1}$3) are preferred during the growth. Whereas the texture coefficient calculed from XRD patterns shows a disfavor of (10$\bar{1}$3) orientation ($T_{c(10\bar{1}0)}$ <1). This can be explained by the local nature of EBSD analysis. Results may have less statistical relevance. Detailed analysis of pole figure are presented in Annex 2.

Similarly, for an AlN coating deposited at a higher degree of supersaturation (N/Al=11.25), grains grown along [60$\bar{6}$7], [80$\bar{8}$7], [40$\bar{4}$7] and [66$\bar{12}$7] (normal to (11$\bar{2}$2) plane) directions with a maximum tolerance of 20° are denoted in Figure 3.14(b) by red, green, blue and yellow colors respectively. It should be pointed out that the fraction of (11$\bar{2}$2) oriented grains denoted by the orientation map is larger than other orientations, which is consistent with the observation from the texture coefficient presented above. To conclude, the increase of NH_3 flow rate strongly modifies the relative growth rate of {10$\bar{1}$1} and {0001} crystals, which alters the geometrical selection of orientations [17].

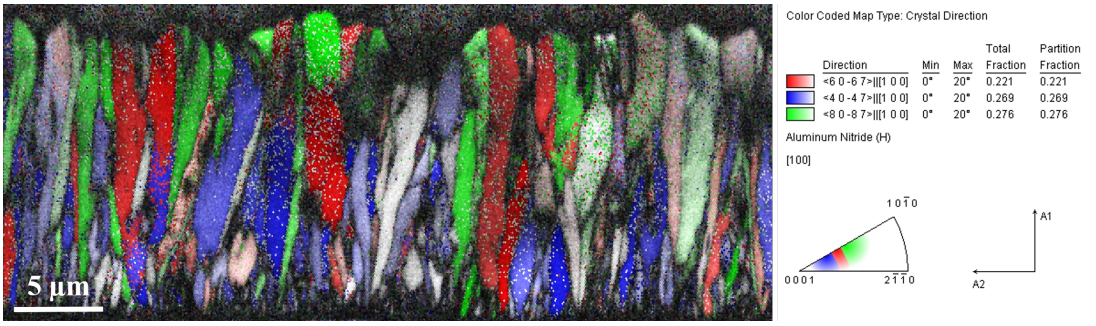

(a) N/Al=3

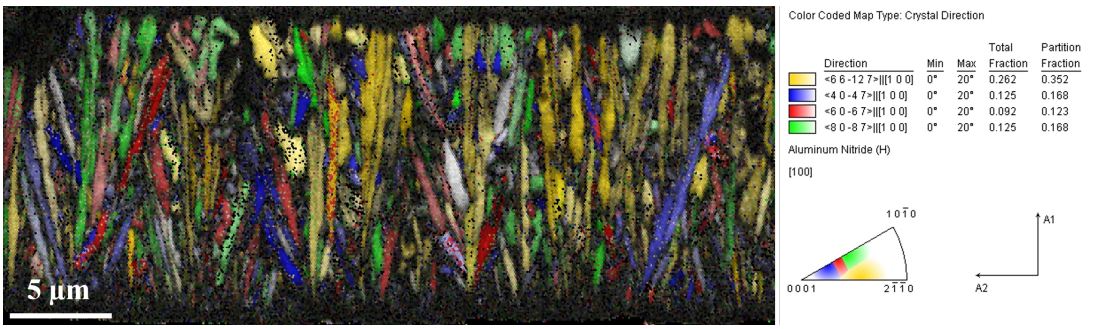

(b) N/Al=11.25

Figure 3.14 EBSD orientation mappings of coated systems shown in Figure 3.11 along selected directions: (a) N/Al=3 and (b) N/Al=11.25. For each map, reference directions are selected and the color assignment is presented at the right side; the A1 axis is perpendicular to the substrate surface.

Moreover, Van der Drift [12] stated that the higher the vertical growth rate of a crystal is, the greater its probability of survival is. The preferred orientation(s) is(are) more pronounced with an increase of film thickness. Our observations for AlN coatings having $(10\bar{1}2)$ and $(20\bar{2}3)$ preferred orientations are in agreement with the evolutionary selection mechanism of van der Drift. Indeed, from previous discussions (texture coefficient analysis and EBSD orientation mapping), the $(10\bar{1}2)$, $(10\bar{1}3)$ and $(20\bar{2}3)$ preferred orientations were observed for AlN coatings deposited with a N/Al ratio of 3 for 1 h (thickness of about 15 μm). But, contributions of other orientations were also visible and could not be neglected (see Figure 3.15(a)). However, when the thickness of AlN is increased to 45 μm, the AlN coating is clearly highly $(10\bar{1}2)$-textured. The sharpness of this orientation is also increased with the increasing thickness. The $(20\bar{2}3)$ is also preferred, and the ratio of intensity of $(20\bar{2}3)$ orientation over $(10\bar{1}2)$ remains around 0.33. By contrast, the $(10\bar{1}3)$ orientation was no longer preferred and intensities of other orientations are negligible. This means that the orientation selection is completed at this thickness.

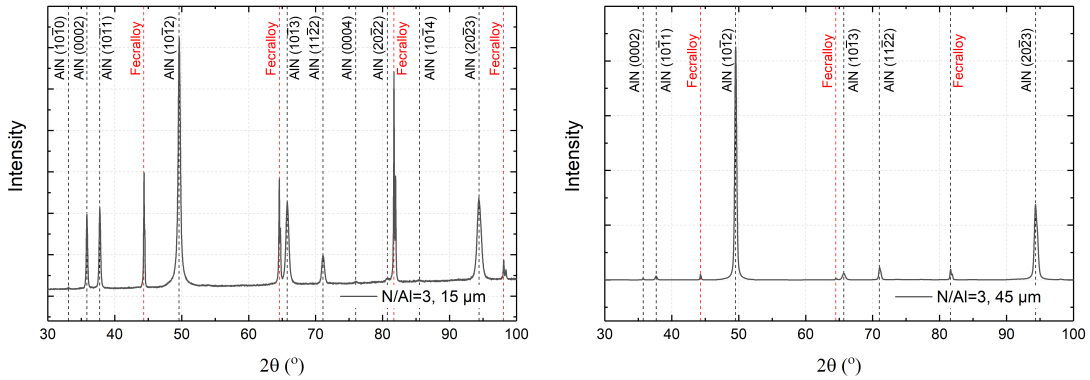

(a) thickness of AlN: 15 μm (b) thickness of AlN: 45 μm

Figure 3.15 XRD θ-2θ patterns of AlN coatings deposited at 1100 °C with thickness of (a) 12 μm and (b) 45 μm.

Effect of deposition temperature

Generally, increasing deposition temperature leads to an increase of grain size due to a decrease of supersaturation [15, 174, 187]. Moreover, as mentioned above, at high temperature, large-size faceted grains are formed due to an enhancement of surface diffusion of chemical species. Crystals of around 20 μm size are typically observed at 1200 °C (Figure 3.16(a)). From X-ray diffraction (Figure 3.16(b)), it is interesting to mention that at 1200 °C, $(10\bar{1}2)$ orientation is still predominant. The preference of $(20\bar{2}3)$ orientation is also observed. However, compared to AlN coatings deposited at 1100 °C with the same thickness (Figure 3.15(b)), relative intensities of $(10\bar{1}3)$ and $(11\bar{2}2)$ increase. Thus, the selection of orientation in this case are uncompleted. Indeed, the AlN coating deposited on TZM substrate under the same conditions is $(11\bar{2}2)$-textured, but it thickness is larger (60 μm). In such case, it is difficult to attribute this change of preferred orientation to the substrate

or the incomplete orientation selection. More experiments are required to study this mechanism.

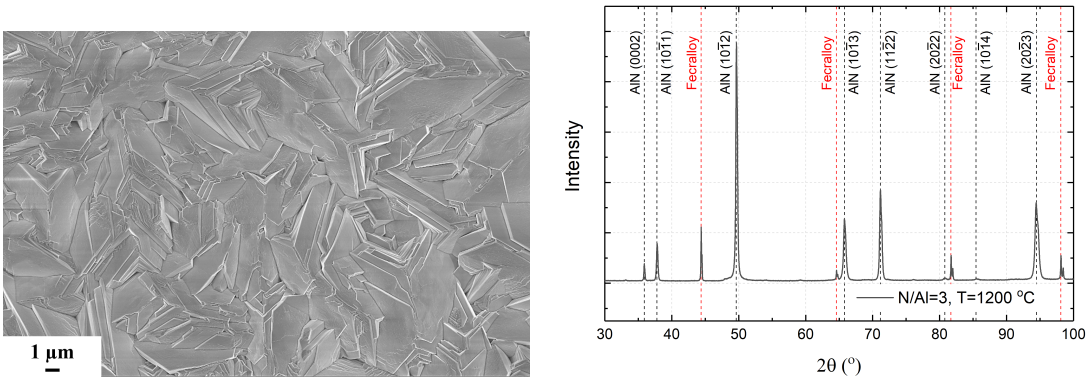

(a) (b)

Figure 3.16 (a) Surface morphology and (b) XRD θ-2θ patterns of AlN coating deposited at 1200 °C with a N/Al ratio of 3. Its thickness is around 45 μm.

The processing conditions called 'standard' for the characterization of high temperature properties of AlN coated substrates are those leading to dense and textured layers with a growth rate close to 15 μm·h^{-1} (N/Al=3, P=2000 Pa, T=1100 °C, and H_2 flow rate of 2250 sccm).

3.5.2 Microstructure of AlN coatings on pre-oxidized APMT

From the results of the previous section, a N/Al ratio of 3 is selected to develop a dense AlN coating on APMT. An accommodation layer of Al_2O_3 was grown prior to AlN deposition through thermal oxidation at 1100 °C for 25 h (thickness of about 1.5 μm). The AlN deposition was conducted at 1100 °C under interrupted growth mode, including 3 h of deposition and 10 min of interruption per hour (see section 3.1). The growth rate of AlN is around 15 μm·h^{-1} ('standard' processing conditions).

Surface morphology and cross-sectional microstructure of the AlN coatings are shown in Figure 3.17. They are identical to those grown on Fecralloy under the same conditions (see Figure 3.11(e) and (j)). Notably, the AlN coating is adherent to the oxide scale on APMT (Figure 3.17(c)). XRD θ-2θ patterns (Figure 3.18) show the dominance of (11$\bar{2}$2) orientation. (10$\bar{1}$2) and (20$\bar{2}$3) orientations still exist, but their relative intensities decrease when compared to the case of AlN coating deposited on Fecralloy under the same conditions. Moreover, (0002) orientation is less pronounced whereas (10$\bar{1}$1) is preferred. The selection of orientation seems to be uncompleted in such case. Nevertheless, it should also be pointed out that the change of preferred orientations results in porosities within the AlN layer grown on pre-oxidized APMT. As discussed in section 3.4.2, such microstructure can lead to a large number of preferred paths for oxygen diffusion and thus poor oxidation resistance of the AlN layer.

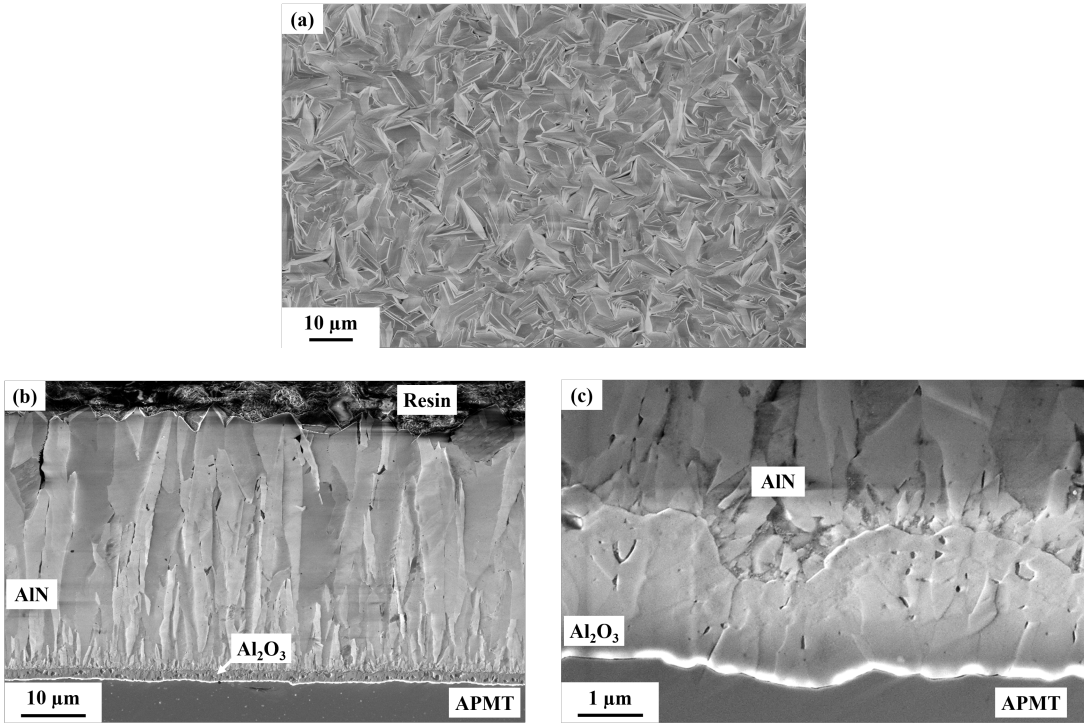

Figure 3.17 Surface morphology and microstructure of AlN coating deposited on pre-oxidized APMT at 1100 °C: (a) surface morphology, (b) cross-sectional microstructure and (c) a high magnification of (b) at the AlN/Al_2O_3 interface. The thermally grown Al_2O_3 on APMT is used to accommodate large difference of CTE between AlN and APMT.

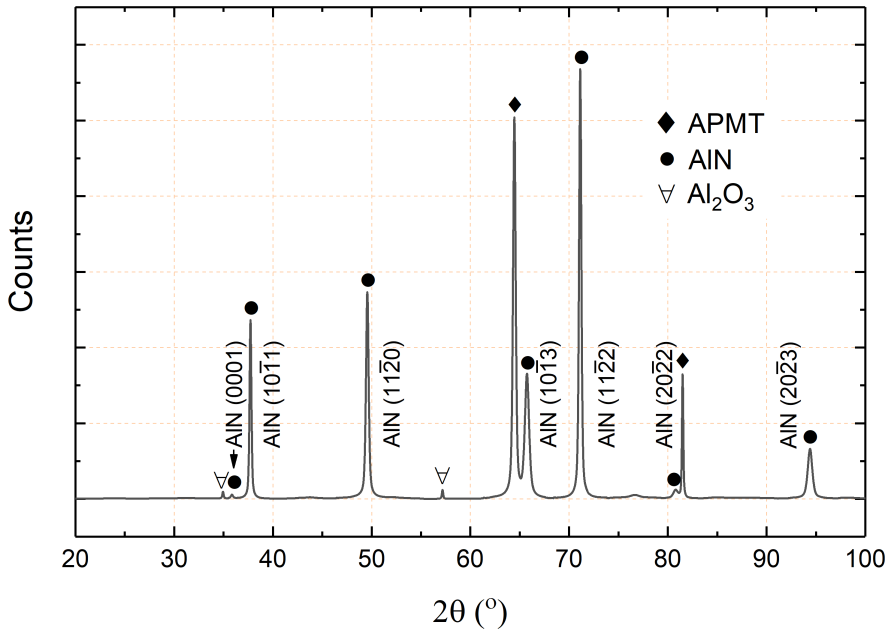

Figure 3.18 θ-2θ X-ray diffraction spectrum of AlN coating grown on pre-oxidized APMT at 1100 °C with a N/Al ratio of 3.

3.6 Oxidation of AlN coatings on Fecralloy and APMT

3.6.1 Oxidation conditions

Cyclic oxidations are performed to evaluate the oxidation resistance of AlN coatings. Prior to oxidation, all samples are ultrasonically cleaned. Cyclic oxidation of as-grown AlN coated and uncoated samples polished to a 1200 grit surface finish is carried out in the 800-1100 °C temperature range in air at ambient pressure in a Nabertherm P310 tube furnace equipped with a 99.7% purity alumina tube (Sceram ceramics). The temperature is calibrated before each experiment and the furnace power is controlled by feedback from a S-type thermocouple placed near the sample. To evaluate the oxidation performance of AlN coatings, uncoated samples are also oxidized at 1100 °C in the same conditions. After each oxidation cycle, the samples are taken out from the furnace and cooled down to room temperature in air. The weight changes of oxidized samples are measured by a laboratory digital balance with a readability of 0.1/1 mg.

3.6.2 Oxidation of uncoated Fecralloy and APMT

Fecralloy and APMT are some of the most oxidation resistant materials for high temperature applications (up to 1250 °C in air) among the corrosion resistant alloys [150–155, 191, 192]. Their excellent oxidation resistance relies on the formation of slow-growing, dense and adherent alumina scale. The oxidation kinetics and oxide growth mechanisms of Fecralloy and APMT have been extensively investigated in past years [16, 150–155, 191–194].

3.6.2.1 Oxidation kinetics

The oxidation of Fecralloy and APMT is written as:

$$Al(s) + \frac{3}{2}O_2(g) \longrightarrow Al_2O_3(s)$$

The corresponding thickness of the oxide scale, $t_{Al_2O_3}$, can be estimated using:

$$t_{Al_2O_3} = \frac{2M_{Al_2O_3}}{3M_{O_2}\rho_{Al_2O_3}} \cdot \frac{\Delta m}{S} \tag{3.6}$$

where $M_{Al_2O_3}$ and M_{O_2} are the molecular weight of Al_2O_3 and O_2 respectively. $\rho_{Al_2O_3}$ is the density of Al_2O_3 (3.97×10^3 kg·m^{-3}), and Δm/S is the mass gain divided by the surface area of the oxidized Fecralloy and APMT.

The oxide scale growth of an alumina-former usually follows a power-law which can be expressed as:

$$t_{Al_2O_3} = k_p \cdot t^n \tag{3.7}$$

where k_p is the kinetic parameter, t is oxidation period and n is the oxidation rate exponent. Using Eq.(3.6) and Eq.(3.7), the mass gain, Δm/S, also has a power-law time dependence, such as:

$$\frac{\Delta m}{S} = k_p' \cdot t^n \tag{3.8}$$

where

$$k_p^{'} = \frac{3M_{O_2}\rho_{Al_2O_3}}{2M_{Al_2O_3}} \cdot k_p \tag{3.9}$$

Experiments made by O^{18} tracer distribution in the alumina scale have indicated short-circuit diffusion of oxygen as the driving force of oxidation [195]. The scale thickness theoretically increases as a function of the square root of time exposure, i.e., n=0.5. This oxidation kinetics is also called parabolic kinetics. In reality, the growth rate of Fe-Cr-Al alloys exhibits a large deviation from parabolic kinetics. Figure 3.19 shows the mass gain ($mg{\cdot}cm^{-2}$) of Fecralloy and APMT versus time (h) during cyclic oxidation at 1100 °C. Their oxidation parameters $k_p^{'}$ and n are summarized in Table 3.3. As expected, we observed a decrease of mass gain rate for both Fecralloy and APMT while exposure time increases, meaning that protective alumina scale has been developed on these two alloys. It is also important to point out that the exponent n approaches 0.33 for both Fecralloy and APMT, showing a sub-parabolic, almost cubic, scale growth kinetics. Our results on uncoated Fecralloy and APMT are in agreement with the literature [153, 195].

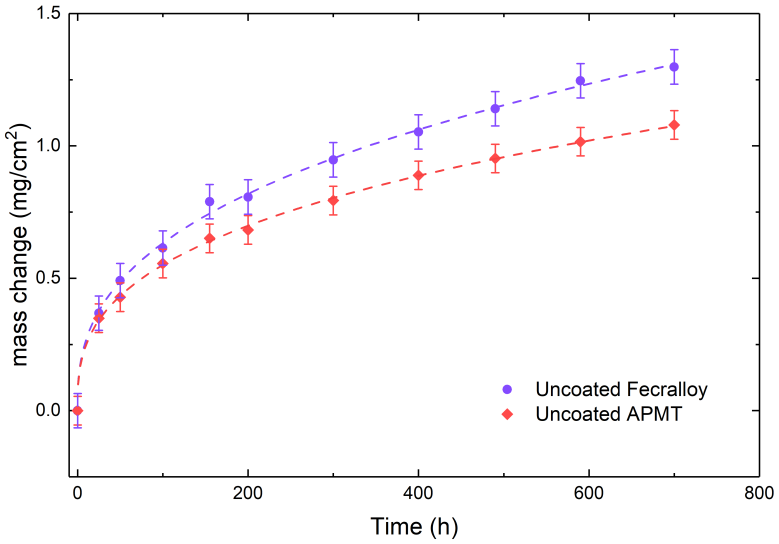

Figure 3.19 Oxidation kinetics of uncoated Fecralloy and APMT at 1100 °C in this study.

Table 3.3 Kinetic parameters for the oxidation of Fecralloy and APMT at 1100 °C

Sample	$k_p^{'}$ ($mg{\cdot}cm^{-2}{\cdot}h^{-n}$)	n
Uncoated Fecralloy	0.1117	0.376
Uncoated APMT	0.1135	0.343

Naumenko et al. [195] suggest that the deviation from the ideal parabolic to sub-parabolic kinetic can be attributed to lateral grain size change within the oxide scale with time. They found that the growth mechanism is driven by grain boundary oxygen diffusion in combination with competitive growth of alumina grains [151, 195]. A result of this competition is a time-dependent exponent n,

which starts with a value of 0.5, and decreases rapidly and finally approaches 0.33 after a long exposure. It was also proposed that the sub-parabolic regime can be related to compressive stress in the oxide scale [194]. This compressive oxide growth stress is claimed to affect the chemical potential gradient of mobile species which is also an influencing factor on the lateral growth of alumina grains [194].

Moreover, as can be seen on Figure 3.19, the oxidation rate of Fecralloy is a little faster than that of APMT. This observation is in fair agreement with results reported in literature [153, 191, 196]. Thermogravimetric analysis in the work of Jonsson et al. [153] demonstrated that the oxygen diffusion through an alumina layer on APMT is in fact lower than in Fecralloy up to 1250 °C. Indeed, the decrease of oxygen diffusion rate is connected to the introduction of reactive elements (REs, e.g., Y, Zr, Hf, La) as oxide dispersion in APMT. The added RE elements, segregated to the grain boundaries of alumina scales during oxidation, block and reduce transport of cations and anions [193, 196]. Moreover, the RE oxide dispersions in APMT not only improve its oxidation resistance but also the high temperature mechanical properties such as creep resistance [193].

3.6.2.2 Surface morphology

The surface morphology of Fecralloy and APMT after 25 h of oxidation at 1100 °C are presented in Figure 3.20. XRD and SEM/EDX analysis show that the alumina grown on both Fecralloy and AMPT is α-alumina. The grain size of Al_2O_3 is larger on Fecralloy than on APMT. Moreover, facetted crystallites are found on alumina grown on Fecralloy. SEM/EDX analysis point analysis, showing 32 at% Al, 61 at% O and 7 at% Mg, implies that these crystallites contain MgAl spinel oxide ($MgAl_2O_4$). This is confirmed by the additional small peaks presented in the XRD θ-2θ patterns. The formation of $MgAl_2O_4$ spinel occurs by the diffusion of Mg (impurity) from the bulk Fecralloy into the oxide scale, and the reaction between Mg and Al_2O_3 [197]. It should also be mentioned that the Mg-enrichment and spinel formation at the gas/scale interface lead to the development of porosity, which is also observed in the literature [196, 197]. For alumina scales on APMT, no spinel grains were observed by SEM nor detected by XRD.

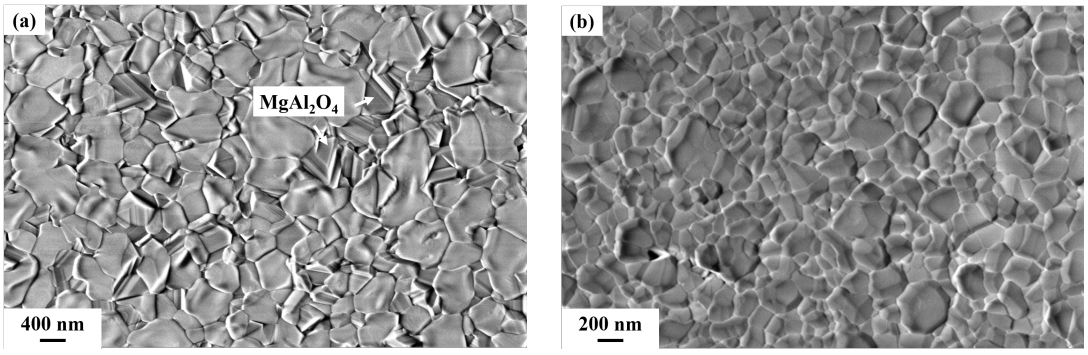

Figure 3.20 Surface morphology of (a) Fecralloy and (b) APMT after 25 h of oxidation.

3.6.2.3 Lifetime prediction

The lifetime of uncoated alloys is a function of aluminum available in the alloy because Al is progressively depleted by the growing scale. The critical Al level, initially 5 wt%, before oxidation failure occurs, strongly depends on cycling, creep and material dimensions [152, 153]. Figure 3.21 [16] shows the typical mass change of Fecralloy during oxidation until breakaway. In the initial stage, the oxidation follows a sub-parabolic law previously presented until reaching a certain scale thickness. After that, the oxide scale starts to spall, resulting in a decrease of mass with time. The scale is re-healed since there is still enough Al in the bulk alloy. In this stage, scale spallation and formation of new oxide scale occur simultaneously, which significantly contributes to the consumption of Al in the bulk alloy. When the Al concentration reaches a critical level, breakaway oxidation occurs and leads to a loss of protection for the alloy. Typically, at least 2 wt% of Al in the alloy is necessary to maintain the growth of a pure alumina layer. For lower concentrations, iron and chromium oxides are formed at a high rate. It was shown that the studied Fecralloy and APMT can withstand more than 10 000 h before scale spallation and catastrophic oxidation at 1200 °C [152, 153].

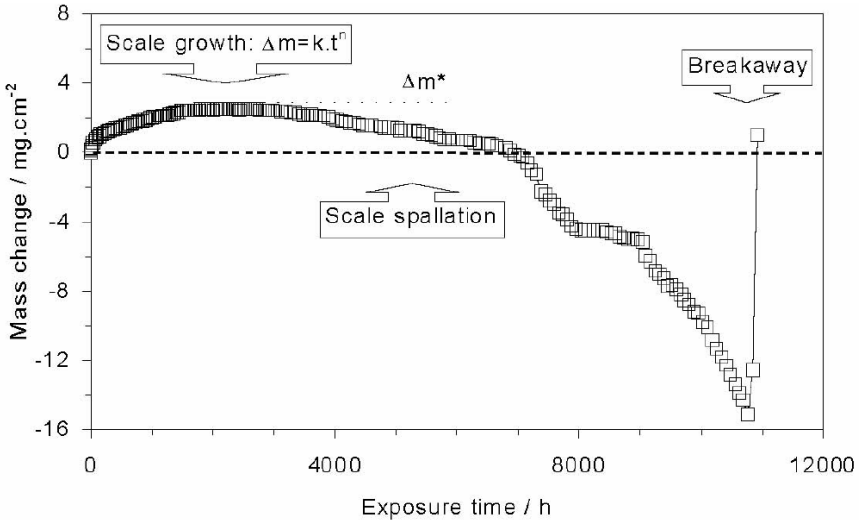

Figure 3.21 Oxidation curve of a typical commercial Fecralloy (2 mm thick) at 1200 °C [16].

3.6.3 Oxidation of AlN coatings

There are few data concerning the oxidation of AlN coatings or thin films [137, 140–145]. We expect that AlN plays two roles, firstly as an oxygen sink that reacts to alumina and secondly as a better absorbing layer than metallic alloys. As a function of the adherence of the coating and of the oxide scale, the lifetime of different class of alloys could be extended owing to the aluminum reservoir. In this section, cyclic oxidation of AlN coated samples were conducted in the 800-1100 °C temperature range to study the oxidation kinetics of AlN coatings. Microstructure of AlN and grown Al_2O_3 after oxidation and evolution of residual stress are examined.

3.6.3.1 Oxidation kinetics

For AlN coated samples, the oxidation of AlN is a solid-gas reaction involving the exchange of oxygen and nitrogen:

$$2AlN(s) + \frac{3}{2}O_2(g) \longrightarrow Al_2O_3(s) + N_2(g)$$

The thickness of the scale was evaluated taking into account nitrogen liberation:

$$\frac{\Delta m}{S}(AlN) = \frac{m_{O_2}}{S} - \frac{m_{N_2}}{S} \tag{3.10}$$

$$t_{Al_2O_3} = \frac{M_{Al_2O_3}}{\rho_{Al_2O_3} \cdot (\frac{3}{2}M_{O_2} - M_{N_2})} \cdot \frac{\Delta m}{S}(AlN) \tag{3.11}$$

where M_{N_2} is the molecular mass of nitrogen, and the alumina scale is assumed to be 100% dense. Similar to Eq.(3.8), the mass gain from oxidation of AlN coatings could be written as:

$$\frac{\Delta m}{S}(AlN) = k_p(AlN) \cdot t^n \tag{3.12}$$

where k_p(AlN) follows an Arrhenius equation:

$$k_p(AlN) = k_0 \cdot exp(-\frac{E_a}{R \cdot T}) \tag{3.13}$$

where k_0 is the pre-exponential factor, E_a is the activation energy, R is the gas constant and T is the oxidation temperature (in K).

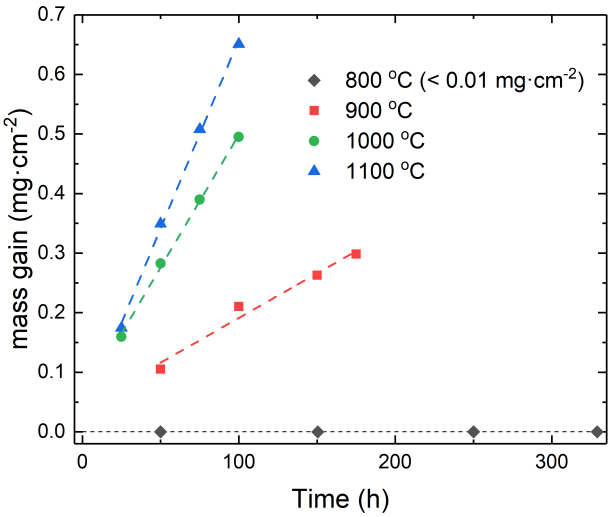

Figure 3.22 Oxidation kinetics of AlN coatings in the temperature range of 800-1100 °C.

Figure 3.22 shows the mass gain of AlN coated APMT during the cyclic oxidation at different temperatures. The total oxidation duration is 300 h at 800 °C, 175 h at 900 °C, as well as 100 h at 1000 and 1100 °C. For AlN coated samples, the mass gain is small at 900 °C. The mass gain for oxidation at 800 °C after 300 h is not detected due to the limited precision of the balance. It can be

therefore concluded that the oxidation of AlN in the temperature range of 800-900 °C is very small, which is in good agreement with literature [198]. However, in this temperature range, the surface is not fully covered by the oxide layer. The oxidation process proceeds linearly and is governed by the surface area of the unreacted AlN. From XRD, only θ- and γ-alumina are detected. The mass gain abruptly increases at 1000 °C, which is in agreement with previous results [131, 198]. Long-term (1470 h) oxidation of AlN coatings grown on Fecralloy and pre-oxidized APMT were carried out at 1100 °C. As shown in Figure 3.23, the mass gains remain small, about 1.5 to 2 mg·cm^{-2}. These mass gains correspond to an average scale thickness of 30-40 μm considering a 100% dense α-alumina scale (the only oxide detected by XRD).

Generally, the two limiting steps of the oxidation mechanism are (1) oxygen diffusion through the oxide layer to the surface of the nitride film and (2) nucleus formation and chemical reaction to form the oxide layer. The same observations can be found in the oxidation of other nitride materials [199]. At temperatures between 800 and 1100 °C, at the beginning of oxidation, kinetics is linear indicating that the limiting phenomena are surface reactions. As a result, the oxidation exponent equals to 1. For each temperature, the kinetic parameters were obtained by a linear regression of mass gain as a function of oxidation time. They are listed in Table 3.4. After that, according to Eq.(3.13), the pre-exponential factor (k_0) and activation energy (E_a) were obtained through a linear regression of the logarithm of $k_p(AlN)$ as a function of reciprocal temperature (1/T). Values are 33.27 mg·cm^{-2}·h^{-1} and 97 kJ·mol^{-1} respectively. The duration of the linear regime is proportional to the thickness of the AlN layer, 150 h for a 15 μm layer and 500 h for a 45 μm layer at 1100 °C (Figure 3.23). For longer times, AlN is fully oxidized and the oxidation of the substrate takes place (Figure 3.23). The order of the reaction increased, suggesting that the oxidation is driven by diffusion, which is consistent with our previous discussions.

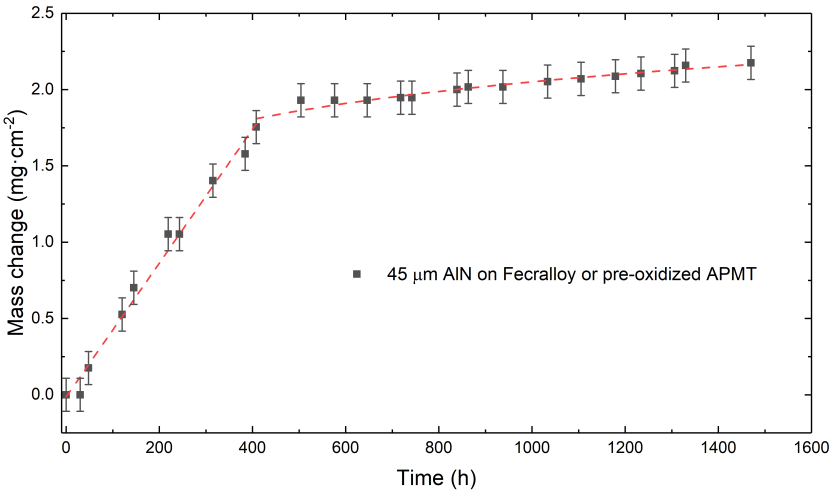

Figure 3.23 Oxidation kinetics of Fecralloy and pre-oxidized APMT coated with AlN (45 μm) at 1100 °C.

Table 3.4 Oxidation kinetic parameter, k_p, for AlN in the temperature range of 800-1100 °C.

Temperature (°C)	$k_p(AlN)$ (mg·cm^{-2}·h^{-n})
900	0.0015
1000	0.0041
1100	0.0063

3.6.3.2 Microstructure

The surface morphology of Fecralloy and APMT coated with AlN (N/Al=3) after 120 h of oxidation at 1100 °C are shown in Figure 3.24. Many small pores formed by the release of N_2 are found on the surface, and become connected to form a porous alumina layer (Figure 3.25(a)). These pores are observed for all the N/Al ratios investigated (not presented here) and cannot be related to the density of the layer. Moreover, gross cracks were formed at the edge of AlN coated Fecralloy. These cracks, related to residual stress in the oxide scale, could be re-healed by newly formed alumina. After 1470 h of oxidation, there is no delamination of oxide scales or cracks on APMT coated with AlN. Alumina grains form a network on the surface. The size of pores are larger than that formed in the first hours (120 h) of oxidation.

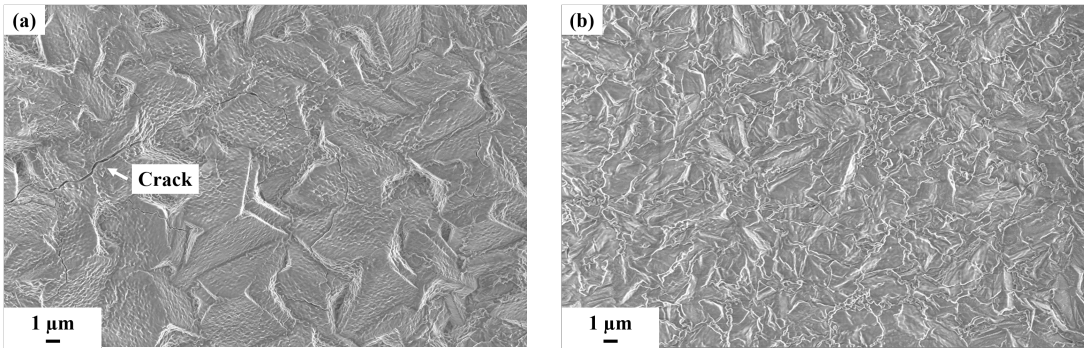

Figure 3.24 Surface morphology of AlN coated samples after 120 h of oxidation: (a) Fecralloy coated with 45 μm of AlN and (b) Pre-oxidized APMT coated with 15 μm of AlN)

Figure 3.25(a) presents a typical microstructure of the porous layer. Different from a columnar alumina scale developed on uncoated Fecralloy (Figure 3.25(b)), the alumina scale on AlN coating is porous. The size of the pores varies from 20 to 500 nm. Indeed, the reaction of AlN with air involves the release of nitrogen. In the first hours, the driving force for the oxidation of AlN is the formation of small pores, which generate large fresh surface area leading to further reaction to take place. This is confirmed by the linear kinetics previously observed. The pores remain interconnected throughout the oxidation. Such microstructure enables the penetration of oxygen, leading to fast oxygen diffusion in the AlN layer and rate-limiting reaction at the alumina/AlN interface.

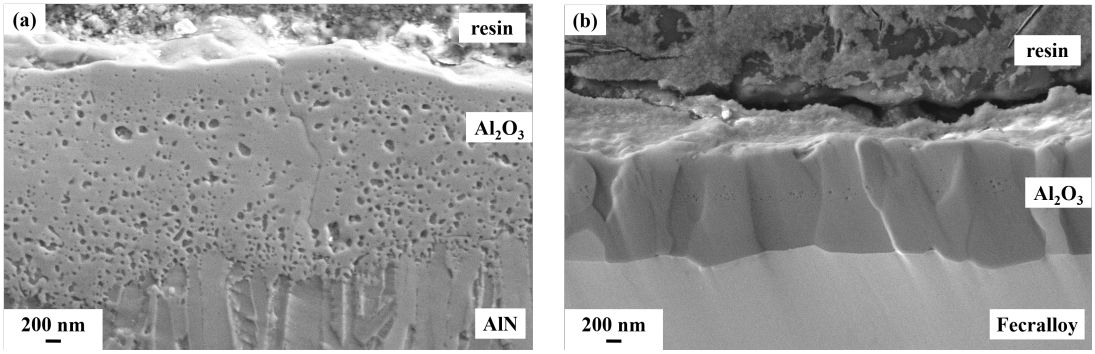

Figure 3.25 SEM cross-section images after 94 h of oxidation at 1100 °C of Fecralloy: (a) coated with 10 μm AlN (N/Al=11.25) and (b) uncoated.

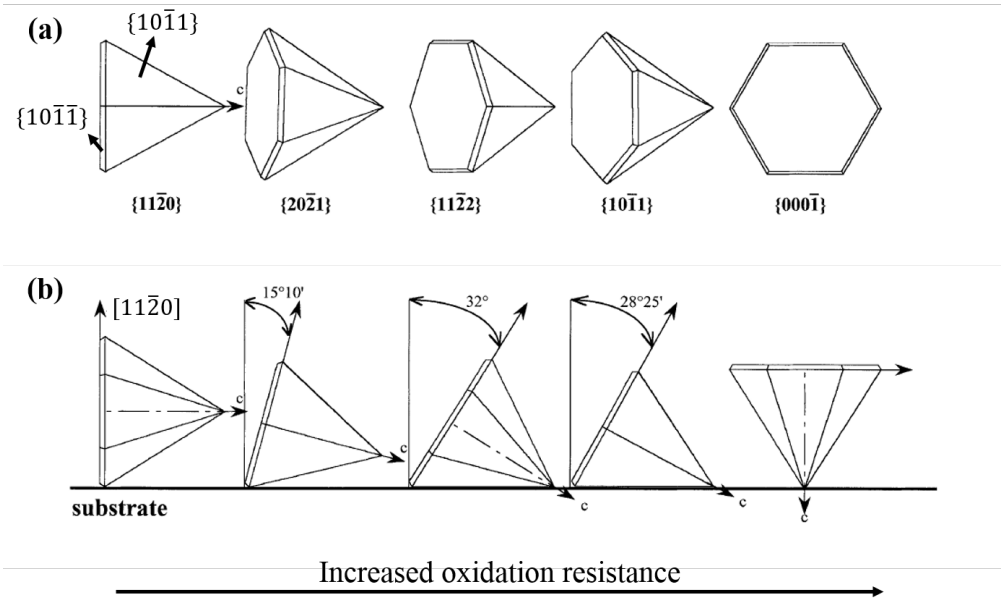

Figure 3.26 Simulated crystals for various orientations: (a) surface morphology and (b) view at 90°. [17]

However, the oxidation resistance of AlN is claimed to be dependent on its preferred orientation(s) [200, 201]. Itoh et al. [200] has found that highly (0001)-textured thick AlN film (thickness >15 μm) followed a parabolic oxidation law at high temperatures (1050-1200 °C). Casaux et al. [201] suggested that oxidation resistance of AlN is related to the position of c-axis with respect to the substrate. When AlN is (0001)-oriented, c-axis is normal to the surface of the substrate, which leads to the greater compactness of the AlN crystalline network and thus better oxidation resistance. However, when c-axis is parallel to the substrate, i.e., grains preferentially oriented along $[11\bar{2}0]$ direction, the oxidation rate of such an AlN film increased abruptly [201]. They explained that the total area formed by orthogonal projection of (0001) planes is the key point for the oxidation resistance of AlN [201]. The change of texture leads to a variation of surface morphology and thus apparent (0001) planes with respect to the incident oxygen flow (normal to the surface of substrate). The larger the area is achieved, the better the oxidation resistance is. For example, the surface morphology of $(11\bar{2}0)$-oriented AlN is dominated by pyramidal $(10\bar{1}1)$ crystalline planes (Figure 3.26), which would lead to the formation of an alumina layer less passivating than that obtained from (0001) planes. If the grains are grown along $(11\bar{2}2)$ orientation, the total area formed by orthogonal projection of (0001) planes increases whereas that of $(10\bar{1}1)$ planes decreases. The oxidation resistance is therefore improved. We have also found that oxygen diffusion is enabled within $(11\bar{2}2)$-oriented AlN layer (grown on TZM) during high temperature oxidation due to its porosity and the resulting large quantities of preferred paths for oxygen diffusion (see section 3.4.2). The same phenomenon has also been observed for AlN grown with a N/Al ratio of 5, for which $(11\bar{2}2)$ orientation is preferred. Such porosity can be another reasonable explanation for the poorer oxidation resistance for $(11\bar{2}2)$-oriented AlN coating.

For longer times (when AlN is totally converted to Al_2O_3), the substrate is oxidized by oxygen diffusion through the porous layer and the oxidation proceeds as in the substrate. Figure 3.27 shows the microstructure after 1470 h of oxidation. Two alumina layers with different microstructure are developed on the APMT substrate. The top alumina layer is porous and comes from the oxidation of the AlN coating. The grain size of alumina is 40±10 nm (calculated by the Debye-Scherrer formula). The bottom layer is dense and results the oxidation of the substrate. Neither cracks or delamination in alumina layers are observed. This phenomenon is of great importance to show the potential of AlN/FeCrAl bilayer for the use in high temperature applications. Generally, in multilayer coating systems, the weak interface is the oxide/metal interface. Severe cyclic conditions lead to the formation of micro-cracks close to oxide/metal interface, and thus crack growth and delamination of the whole coating system. The failure of protective oxide scales results in fast degradation of substrates. However, in our study, oxide scales remain adherent even after consumption of the entire AlN coating. This suggests that there is an opportunity for the use of AlN/FeCrAl bilayer under cyclic conditions without spallation. In such a case, FeCrAl could be used as a bond-coat to support an AlN coating which is oxidation resistant for hundreds of hours at a temperature of 1000 °C or few years in the temperature range of 800-900 °C. To finalize the evaluation of AlN coating for the use at high temperature,

it is now necessary to study the evolution of residual stress in AlN and Al_2O_3 layers during cyclic oxidation.

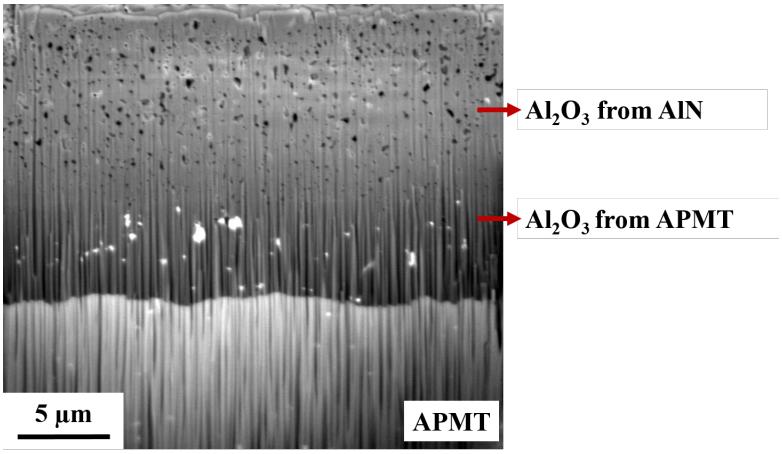

Figure 3.27 Cross-section after 1470 h of oxidation at 1100 °C of pre-oxidized APMT coated with 15 μm AlN ('standard' processing conditions).

3.6.4 Residual stress evolution during cyclic oxidation

As discussed in Chapter 1, materials used in solar receivers undergo daily extreme thermal cycling which inevitably introduces stresses into the different materials. Generally, the induced stress can significantly affect the durability of materials. Therefore, apart from its oxidation resistance, it is also necessary to study the time evolution of residual stress in the AlN and grown Al_2O_3 layers during thermal cycling, to characterize the potential of AlN coatings for their use in solar receivers.

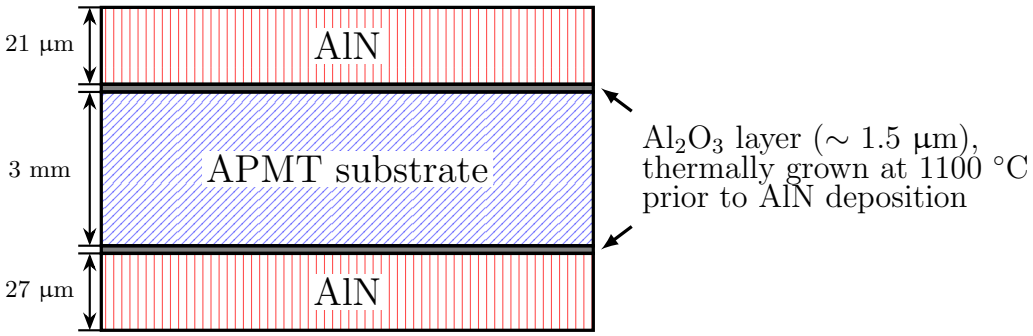

Figure 3.28 Schematic representation of the pre-oxidized APMT coated with AlN coatings for cyclic oxidation.

In the present study, cyclic oxidation (15 thermal cycles in 30 h) of a pre-oxidized APMT coated with AlN coating on both faces is performed from 1100 to 25 °C in a tube furnace (see section 3.4.1). For the sake of clarity, the alumina layer thermally grown on APMT prior to the deposition of AlN coating is denoted as alumina-buffer layer in the following section. The oxidation duration is 1 h per

cycle in the first 10 cycles, and then changes to 5 h per cycle. The thickness of AlN coatings are 21 and 27 μm on the front-side and backside of the substrate respectively (Figure 3.28). In the analysis below, it is convenient to use 'top layer' and 'bottom layer' to denote the layers on the front-side and backside of the substrate respectively. Residual stress measurements in AlN and grown Al_2O_3 top layers at ambient temperature are carried out by Raman spectroscopy and photoluminescence after each cycle with a T64000 spectrometer (Horiba Jobin-Yvon). The excitation source is an Ar^+-laser with 514 nm wavelength. Its power is adjusted to prevent shift of frequency resulting from heating of samples. Details of these technologies has been already presented in Chapter 2.

It is shown in Figure 3.29 that compressive stresses are developed in both AlN and growing Al_2O_3 top layers. The stress in AlN at t=0 (Figure 3.29(a)) correspond to the elastic response of the stack of AlN/alumina-buffer layer/APMT just after deposition. Due to a large difference of thermal expansion coefficients between AlN and APMT, large compressive stress (-1.7 GPa) is developed in the AlN top layer. With increasing oxidation time, the stress in AlN top layer increased rapidly to about -2.65 GPa after 5 h of oxidation, and then gradually increased to -2.75 GPa after 30 h (Figure 3.29(a)). These high values comes from a complex dependence on the high thermal stresses developed during cooling and the strains accumulated from creep deformation of materials at high temperature.

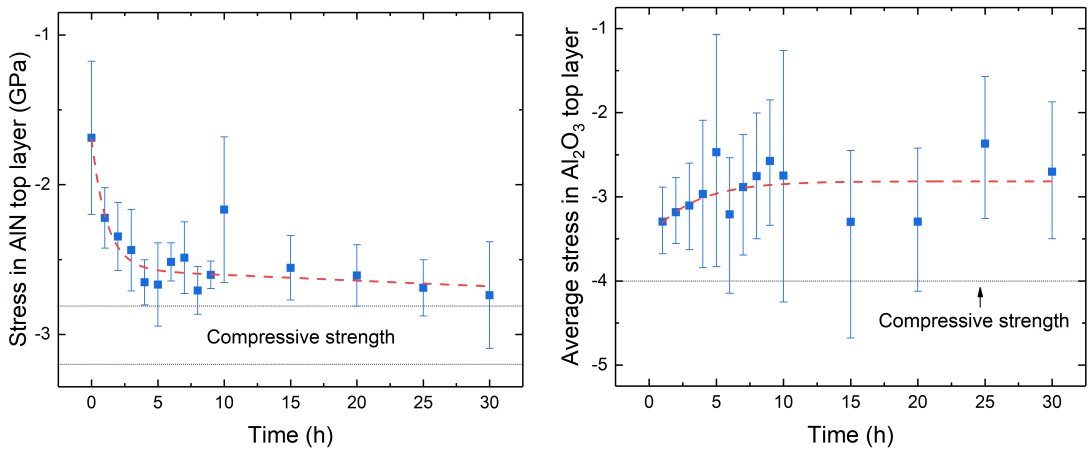

Figure 3.29 Residual stress in (a) AlN and (b) Al_2O_3 top layers, dashed lines are used for eye guidance and dotted lines represent the compressive strength of AlN and Al_2O_3.

As previously mentioned, an Al_2O_3 layer was thermally grown on APMT prior to deposition to accommodate the large thermal mismatches between AlN and APMT. The measured stress in this accommodation layer after deposition is about -3.83 GPa. During the early stage of oxidation, the presence of characteristic luminescence lines from both θ-Al_2O_3 and α-Al_2O_3 (not presented here) indicates that they are both co-existing phases in the growing Al_2O_3 layer (on AlN). The stress is compressive and decrease gradually during this transient period. After

5 h of oxidation, luminescence spectra of θ-Al_2O_3 disappears, confirming the transformation of alumina from metastable phase to the thermodynamically stable α-Al_2O_3 phase. The stress in the growing Al_2O_3 top layer tends to yield a mean value of -2.75 GPa. More detailed discussions on how residual stresses in AlN and growing Al_2O_3 layers affect the lifetime of AlN coating during the thermal cycling are presented in Chapter 4.

3.6.5 Lifetime evaluation for AlN coatings

For a given temperature, there are three major factors that may govern the lifetime of AlN coatings: (1) the oxidation rate (or alumina growth rate), (2) the bonding strength of thermally grown alumina and (3) the residual stress in AlN coating. As shown in Figure 3.27, the measured thickness of the oxide scale after oxidation at 1100 °C for 1470 h is about 20 μm, which corresponds to the theoretical value (see section 3.6.3). This suggests that the scale does not reach the critical thickness for spallation. The oxide layers remain adherent even after consumption of the entire coating. While stress in alumina scale plays an important role, its value should be close to the failure strength of alumina, whether at high temperature or ambient temperature. We have shown that the compressive stress in alumina scale at ambient temperature was relaxed as the oxidation time increases, and eventually approached to a constant value (about -2.75 GPa) which is much smaller than its compressive strength (-4.0 GPa [118]). There is no spallation and/or failure of alumina scale during the cooling stage.

We have shown that the alumina growth rate follows an Arrhenius law (E_a= 97 kJ·mol^{-1}). In the low temperature range (800-900 °C), the alumina growth rate remains low. When temperature is higher than 1000 °C, the alumina growth rate increases abruptly. Moreover, we previously showed that the oxidation of AlN coating follows linear kinetics in the 800-1100 °C temperature range. If we exclude the presence of microcracks (not detected) that could lead to a higher growth rate of the oxide layer and the spallation of the AlN coating due to cyclic thermal stresses, the lifetime of a 15 μm coating can be estimated at 800 °C for a few years and 1100 °C for a few hundred hours. However, there is a lower mismatch of thermal expansion of alumina (8.3×10^{-1} K^{-1}) and AlN (4.2×10^{-6} K^{-1}) in comparison with Fecralloy and APMT (15.4×10^{-6} K^{-1}). The weak interface is the alloy/AlN interface and compressive stress develops during the cooling stage. We have shown that compressive residual stress in AlN coating at ambient temperature increased with time, and finally tended toward a value of about -2.75 GPa, which approaches to the compressive strength of AlN (-2.81 to -3.2 GPa [118, 119]). This indicates that the residual stress in AlN coating is also an important factor for the lifetime of AlN coated systems exposed to solar radiation. The detailed stress evolution is presented in Chapter 4.

It is also worth noting that discrete microcracking of the coating is observed from the first hours of oxidation but without delamination of the initial layer (except sometimes on the edges of the sample). Besides, the presence of water vapor can modify oxidation reactions, increase oxide growth rate and contribute to the formation of hydroxyl compounds (see section 2.1.1) [137]. It is difficult

to conclude that this coating is effective under severe cyclic conditions close to 1100 °C. However, for working temperatures between 800 and 900 °C, the service life of this coating can reach several years if there is no delamination or spallation of the AlN coating.

Conclusions

In this chapter, AlN coatings on molybdenum-based alloys (TZM) and iron-based alloys (Fecralloy and APMT) have been synthesized by HTCVD and extensively characterized in terms of microstructure, oxidation and durability. On TZM substrates, AlN coatings grown at 1200 °C exhibit a faceted surface morphology and a columnar microstructure. Grains are preferentially grown along $(11\bar{2}2)$ crystalline planes. The compressive residual stresses in AlN coatings yield a value of about 122 MPa. This value, lower than those reported in literature, can be accounted for by various parameters such as high deposition temperature, large grain size, approximations in thermal stress estimation, etc. However, such $(11\bar{2}2)$-textured microstructures enable fast diffusion of oxygen through short-circuits between AlN crystallites, and therefore a loss of protection of the substrate. This is consistent with the observation of alumina formed at grain boundaries of AlN coatings. Besides, it is difficult to infiltrate 'laminated' defects resulting from the processing technique or from cutting. Aluminization and silicidation of the TZM substrate conducted prior to deposition are considered as potential techniques to provide a first protection for the substrate.

To further study the potential of AlN coatings for their use under solar radiation, they were grown on oxidation-resistant Fecralloy and APMT substrates at 1100 °C. The surface morphology and microstructure of AlN coatings are identical on these two substrates. We have investigated the evolution of microstructure and preferred orientation(s) as a function of N/Al ratios. These studies show that the increase in the N/Al ratio leads to an increase of supersaturation, and thus to a decrease of grain size. At a low degree of supersaturation (N/Al<5), the semi-polar crystalline plan $(10\bar{1}2)$ is preferentially grown. The orientation selection is not complete. At a high degree of supersaturation, i.e., N/Al higher than 5, the $(11\bar{2}2)$ orientation is favored and grains are more randomly grown. Moreover, only the coating grown at low N/Al ratio is dense.

In this study, the oxidation of Fecralloy and APMT at 1100 °C follows a sub-parabolic kinetic law. These results are in good agreement with data from literature. The grown oxide scale has a columnar structure. The cyclic oxidation of AlN coated Fecralloy or APMT between 800-1100 °C follows a linear kinetics in this temperature range. The oxidation of AlN follows an Arrhenius law with an activation energy of 97 $kJ{\cdot}mol^{-1}$. The alumina layer is porous. Such microstructure enables the fast diffusion of oxygen through the alumina layer and the rate-limiting reaction occurs at the Al_2O_3/AlN interface. This confirms the linear kinetics. Afterwards, AlN coating is completely converted to Al_2O_3 and the oxidation proceeds in the substrate. Two adherent alumina layers with different microstructures (porous and columnar) are developed on the substrate.

It should be reminded that no cracks or delamination are observed during the oxidation. This suggests a promising use of FeCrAl as a bond-coat to support AlN coatings for high temperature applications. However, during thermal cycling, residual stresses in AlN coatings at ambient temperature are rapidly increased, and finally approaches to their compressive strength, whereas stresses in the grown Al_2O_3 layers are gradually increased and are far from this value.

It is difficult to conclude that AlN coatings are effective under severe cyclic conditions and temperatures close to 1100 °C. However, for working temperatures between 800 and 900 °C, the service life of this coating can reach several years. To finalize the evaluation of this coating for solar receivers, it is now necessary to study its absorptivity in the wavelength range of solar radiation.

Chapter 4

Thermomechanical model of multilayer coating systems

Introduction

As emphasized in previous chapters, similar to thermal barrier coatings (TBCs), receiver materials are subjected to extreme cyclic thermal loading in air for extended periods. In the present study, AlN and/or SiC coatings are deposited to protect metallic substrates against oxidation degradation. The periodic temperature changes and/or non-uniform temperature fields within the layers during operation lead to the generation of thermal stresses in the system. Moreover, as the operation period extends, high temperature phenomena like creep deformation, oxidation as well as phase transformation take place, leading to the redistribution of stress field in the system. Therefore, delamination and/or failure of coatings occur when the stress is coatings approaches their critical strength, resulting in a loss of protection for the metallic substrate in high temperature environment. For this reason, ongoing researches focus on stress evolution in multilayer coating systems subjected to external (thermal and/or mechanical) loading(s) to fulfill the following objectives:

(1) to understand the role of external loads and the influence of the aforementioned high temperature phenomena;

(2) to estimate and further improve the reliability and durability of the coating(s)/substrate systems.

Hsueh et al. [202–205] have proposed an analytical model, based on classical beam theory, to evaluate the thermal-elastic stress of a multilayer system, in which a closed-form solution independent of the number of layers is obtained. In this model, only the linear elastic behavior of materials is taken into consideration. However, it provides a theoretical frame for developing models to account for the roles of external loading, oxide growth and creep. Based on Hsueh's model, Limarga and Wilkinson [206, 207] established a model to simulate the oxide growth on metallic alloys under a bending load in isothermal conditions, in which the creep deformations of both oxide and substrate at high temperature were considered. But, the thermal gradient inside the system due to different thermal

conductivities were not taken into account. They also studied the interaction between creep deformation and parabolic oxide growth using the model of Evans et al. [208]. Their analyses show that the growth of a creep-resistant oxide favors the reduction of overall creep deformation in the oxide/alloy system [206]. Zhang et al. [209] proposed a model to analyze the stress evolution in the film/substrate bilayer system with creeping time. In their analysis, the effects of either the film or the substrate subjected to high temperature creep deformation were investigated. However, the creep strain evolution along the thickness direction was not taken into account. Chen et al. [210] developed Zhang's model by considering the stresses in the system as a function of coordinate in the thickness direction and creeping time. Comparisons between results of these two models and finite element results have been conducted, showing the good validity of Chen's model. Dong et al. [211] modeled the stress evolution during single face oxidation of FeCrAlY alloy at high temperature. The prediction was compared with experimental data in literature. Their results showed that models based on elastic deformation behavior overestimate the stress evolution in the system. The creep deformation effects of both oxide and alloy play an important role on stress relaxation at high temperature. Very recently, Li et al. [212] studied the multilayer coatings/substrate system subjected to thermal cycling, and derived a semi-analytical model to predict the stress evolution of the system, including thermal gradient, oxide scale growth and creep relaxation. However, the multilayer coating system in this model is considered to be in a stress-free state before cycling. The model does not take into account the intrinsic growth stress in the coatings after deposition.

The present study aims to develop a semi-analytical model to predict the thermomechanical stress evolution under cycling conditions of coatings/substrate systems, which can account for intrinsic deposition stress, thermal mismatch, oxidation and creep deformation. This model is derived from the model of Hsueh and Li. It could be used for arbitrary stack of layers with arbitrary thicknesses.

The details of our analytical model are presented in section 4.1. In section 4.2, verification and comparison with benchmarking are made to validate the accuracy of the model. General comments and explanations on the evolution of stress and creep strain fields and curvature in the system are presented in section 4.3. Finally, the section 4.4 is dedicated to the parametric study. Based on this numerical analysis, the relevant parameters are given together with the limitation of the multilayer coating systems for high temperature solar receivers.

4.1 Synopsis of the model

4.1.1 Concepts of stress evolution

Residual stress induced by CVD In the present study, AlN and/or SiC coatings are grown on metallic substrates by HTCVD. As described in sections 2.2.2 and 3.3.2, growth strain and thermal strain mismatches in coatings and substrate lead to changes of in-plane dimensions within the system to maintain the mechanical equilibrium. The system is subjected to residual stresses, and

thus becomes curved. A bending moment is therefore developed at ambient temperature.

Thermal gradient When the multilayer system is subjected to a thermal gradient through its thickness, the top and bottom surfaces of the system are heated to different temperatures. Usually, in a gas turbine, the temperature difference in the TBCs could be up to 300 °C [213]. This non-uniform temperature field and thermal expansion coefficient mismatches of different layers and substrate, result in a non-uniform distribution of thermal stress in the system. The bending moment is thus redeveloped. In such a case, the stress difference at the interface of two adjacent layers is enhanced, which might lead to a loss of adherence for coatings.

Creep deformation When the thermal gradient is held for a period of time at an elevated temperature, each individual layer undergoes creep deformation at different creep rates. The creep deformation mismatches induce the redistribution of stress field in the system.

High temperature oxidation Oxidation of coatings takes place at high temperature. The oxide scale growth is associated with lateral expansion, which affects the stress evolution in the system. Moreover, the exchange of thickness between the oxide scale and coating leads to an evolution of the system structure (thickness) during the thermal cycling.

Stress evolution Typically, oxide phases are more creep resistant than most of the metals and alloys. The creep induced stress is dependent on the differential creep rate. However, the creep rate of each constituent depends on the magnitude and direction of the stress in the constituent [18]. The evolution of the system structure and distinct creep deformation within the system strongly affect the coating adherence and thus the integrity of the multilayer coating system. Nevertheless, the relaxation or accumulation of stress in the system during the holding period further affects the residual stress field when the system is cooled down.

To summarize, the present model accounts for the following factors:

- Cyclic thermal loading including a fast heating from ambient temperature (T_{amb}) to operating temperature, a holding period at operating temperature, and a fast cooling from operating temperature to T_{amb} in each cycle;
- Thermal gradient in the multilayer coating system during the holding period;
- Creep deformation in the coatings, substrate and the oxide scales at high temperature;
- Evolution of system structure due to the growth of oxide scales at high temperature and consideration of related stresses.

The following section describes how the present model is implemented, and how it is used to evaluate the stress evolution in the multilayer coating system during thermal cycling.

4.1.2 Model construction

Schematic representation

A typical, stress-free multilayer system with a substrate coated in both faces is schematically illustrated in Figure 4.1(a). The n individual layers are stacked to the upper part of a substrate, while m layers are stacked to the lower part. Each interface is considered to be flat and the bonding between two adjacent layers is considered to be perfect. The z-axis coordinate is defined such as the mid-plane of the substrate is located at z=0. The subscript t and b denote the layers above (z>0) or below (z<0) the substrate respectively, as well as i the layer number ranging from 1 to n (or m). The t1 layer is in direct contact with the upper surface of substrate. The thickness of substrate, oxide, and individual coating layers are denoted as t_s, $t_{o,t}$ or $t_{o,b}$, and $t_{c,ti}$ or $t_{c,bi}$ depending on its z position, respectively. $t_{o,t}$ represents the thickness of the oxide grown on the top surface of the system whereas $t_{o,b}$ is that of the oxide on the bottom surface. The z coordinate of interface between coating layer i+1 and i is defined as $z_{c,ki}$ with the following relationship:

$$\begin{aligned} z_{c,ki} &= sign(k) \cdot (\frac{t_s}{2} + \sum_{j=1}^{i} t_{c,kj}) \\ sign(k) &= \begin{cases} 1 & k = t \\ -1 & k = b \end{cases} \end{aligned} \tag{4.1}$$

Moreover, the z coordinates at the outer-surface of the oxides are:

$$z_{o,t} = \frac{t_s}{2} + \sum_{i=1}^{n} t_{c,ti} + t_{o,t} \tag{4.2a}$$

$$z_{o,b} = -(\frac{t_s}{2} + \sum_{i=1}^{m} t_{c,bi} + t_{o,b}) \tag{4.2b}$$

Usually, the total thickness of a multilayer coating system is much smaller than its in-plane dimensions (x-y plane). The system could be considered to be an infinite thin plate (typically $t_s / \sum t_{c,kj} > 100$). In such case, its bending results in an equal biaxial in-plane stress, i.e. $\sigma_x = \sigma_y$. Moreover, all materials are considered to be isotropic.

Residual stress induced by CVD

We assume an initial stress-free state for the substrate at the deposition temperature and a uniform temperature field within the system during deposition. In polycrystalline growth, films grow in the Volmer-Weber mode. As described in section 2.2.2, polycrystalline films usually grow through the nucleation of discrete crystal clusters or islands on the surface of substrate. Successive stages including the growth of islands, impingement of islands and their coalescence take place to form a continuous surface, and thus grain boundaries. The film thickness just after coalescence of islands is usually of the order of 10 nm or less. Subsequently, the film evolves by grain coarsening and grain growth, which leads to further

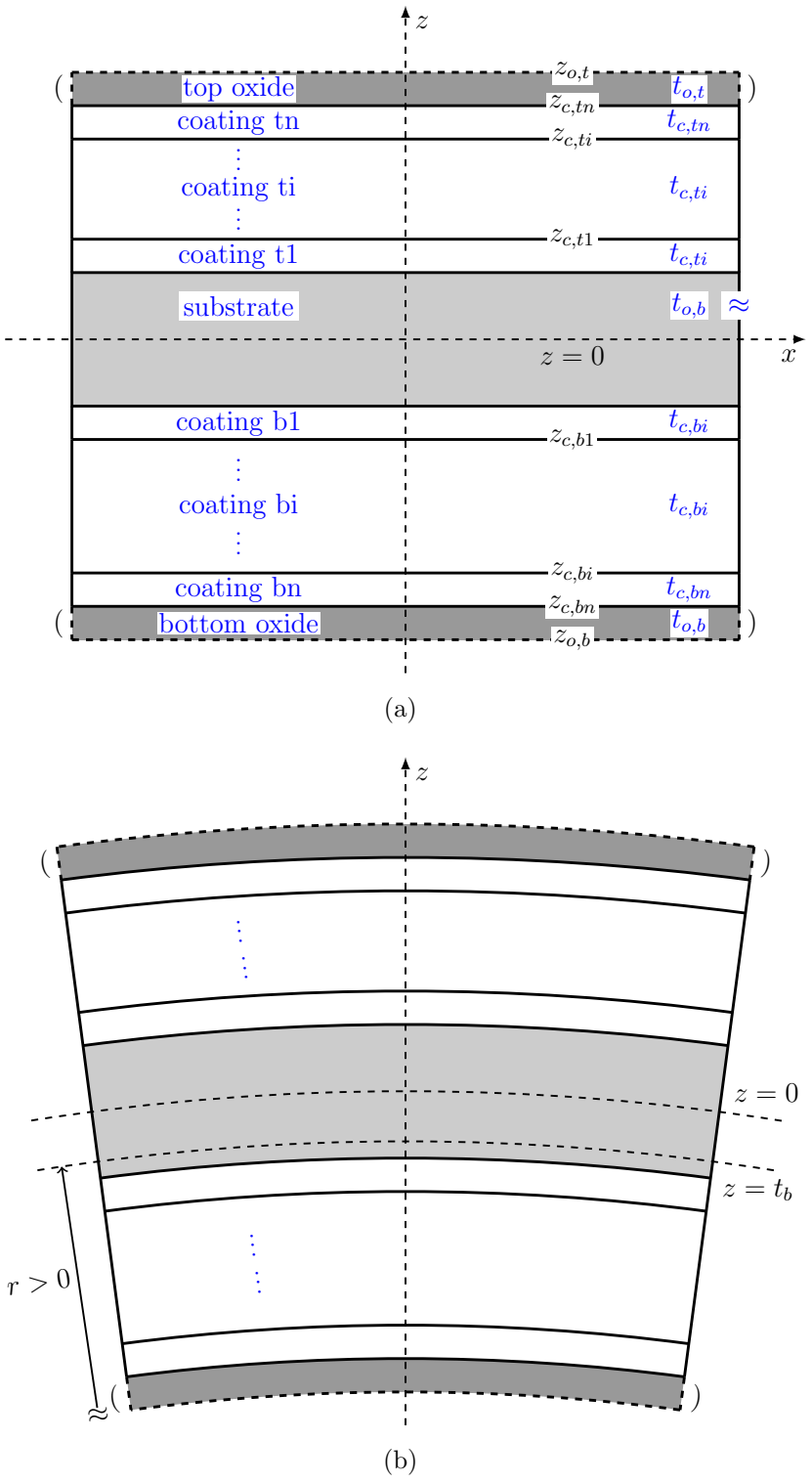

Figure 4.1 Schematic representation of the multilayer coating system: (a) a typical stress-free multilayer coating system; and (b) bending of the system induced by asymmetric stresses, leading to a convex curvature.

thickening [157]. The evolution of growth stresses through these complex stages is not yet fully understood. However, for a given process, the growth stresses are usually reproducible and the final values remain constant at ambient temperature for a long time [11]. Therefore, it is assumed that the value of growth stress is constant for each coating (or film), and uniform throughout the thickness of the corresponding layer.

In the present study, we suppose an elastic relationship between the growth stress and strain, as:

$$\sigma_{c,g,i} = -\frac{E_{c,i}}{1-\nu_{c,i}} \cdot \epsilon_{c,g,i} \tag{4.3}$$

where $E_{c,i}$ and $\nu_{c,i}$ are the Young's modulus and Poisson's ratio of coating i respectively. $\sigma_{c,g,i}$ is the final growth stress for coating i, $\epsilon_{c,g,i}$ is the corresponding strain. The opposite sign between stress and strain is due to the substrate constraint. For the following analysis, $\sigma > 0$ denotes tensile stress while $\sigma < 0$ denotes compressive stress.

Stresses arising from the changes in physical environment also contribute to residual stress distribution within the system. Different from the growth stresses, such externally induced stresses are commonly referred to as extrinsic stresses. In many cases, only the thermal stress is taken into account. The thermal stress is a consequence of thermal strain mismatches due to different thermal expansion coefficients of layers and the temperature fluctuation from the deposition temperature (T_{growth}) to ambient temperature (T_{amb}). For each layer, the thermal strain is written as:

$$\epsilon_{th,i} = \int_{T_{growth}}^{T_{final}} \alpha_{th,i}(T)dT \tag{4.4}$$

where α_{th} is the thermal expansion coefficient, T_{growth} and T_{final} denote the deposition and final temperature (generally equal to ambient temperature) of CVD growth respectively.

Based on classical beam theory, Hsueh [202] assumed that the total strain of the system could be decomposed into a uniform strain to maintain displacement compatibility and a bending moment induced by asymmetric stresses. The total strain is thus described as:

$$\epsilon = c + \frac{z - t_B}{r} \tag{4.5}$$

where c is the uniform strain, $z=t_B$ the position of the bending axis and r the radius of curvature. In Hsueh's definition [202], r is positive when the curvature of system (1/r) is convex, and vice versa (Figure 4.1(b)). The biaxial residual stresses in each coating (or film) and in the substrate are expressed as:

$$\sigma_{c,i} = \frac{E_{c,i}}{1-\nu_{c,i}}(c + \frac{z - t_B}{r} - \epsilon_{c,g,i} - \epsilon_{c,th,i}) \tag{4.6a}$$

$$\sigma_s = \frac{E_s}{1-\nu_s}(c + \frac{z - t_B}{r} - \epsilon_{s,th}) \tag{4.6b}$$

where E is the Young's modulus, and ν the Poisson's ratio of materials. The stress distribution within the system is depending on the three unknown parameters c, t_b, and r, which can be determined upon three boundary conditions [202]. The detail are given in section 'Stress evolution' (on Page 96).

Thermal gradient

The previous section describes the stress inherent to the deposition of the coatings by CVD. In the following, we consider stress arising from the use of the system (CVD grown layers and substrate) under solar radiation. Here, we consider a general case in which the multilayer coating system is subjected to an imposed heat flux, $\overrightarrow{q}$, at the top surface only (Figure 4.2). The top and bottom surfaces of the system are rapidly heated up to different temperatures T_t and T_b, as shown in Figure 4.2.

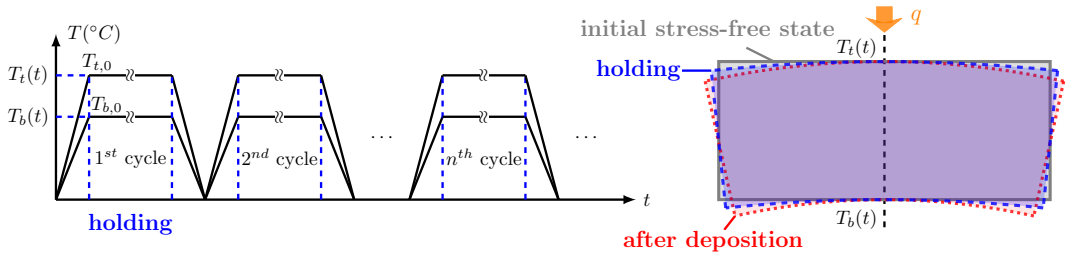

Figure 4.2 Schematic representation of thermal cycling conditions and the corresponding bending behavior of the multilayer coating system; q is the absolute value of imposed heat flux, T_t(t) and T_b(t) are the time-dependent temperatures at the top and bottom surfaces respectively.

To simplify the problem, we assume that (1) the heat transfer within the system during the thermal cycling is only steady-state conduction; (2) no interfacial, convection and thermal radiation resistance exist; (3) the heat flux is maintained constant during the thermal cycle and (4) the temperature of heat transfer fluid is the same as the temperature at the bottom surface (i.e., T_{HTF}=T_b). According to the Fourier's law, for the multilayer coating system illustrated in Figure 4.1, the relationship between the heat flux $\overrightarrow{q}$ and the surface temperatures can be expressed as:

$$q = -\frac{T_t(t) - T_b(t)}{R_{total}(t)}$$
$$R_{total}(t) = \frac{t_s(t)}{k_s} + \frac{t_{o,t}(t)}{k_{o,t}} + \frac{t_{o,b}(t)}{k_{o,b}} + \sum_{i=1}^{n} \frac{t_{c,ti}(t)}{k_{c,ti}} + \sum_{i=1}^{m} \frac{t_{c,bi}(t)}{k_{c,bi}} \tag{4.7}$$

where T_t(t) and T_b(t) are time-dependent temperatures at the top and bottom surfaces respectively. R_{total} is the total thermal resistance of the system and k the thermal conductivity. It is assumed that thermal conductivities are constant

during thermal cycling. Using Eqs. (4.1), (4.2) and (4.7), we can derive the temperature at the position z for a given time t:

$$T(z,t) = \begin{cases} T_b(t) + q\frac{z_{o,b}(t)-z}{k_{o,b}} & z_{o,b}(t) < z \leq z_{c,bm}(t) \\ T_b(t) + q(\frac{-\frac{t_s(t)}{2}-z_{c,bi}(t)-z}{k_{c,bi}} - \sum_{j=i+1}^{m}\frac{t_{c,bj}(t)}{k_{c,bj}} - \frac{t_{o,b}(t)}{k_{o,b}}) & z_{c,bi}(t) < z \leq z_{c,b(i-1)}(t) \\ T_b(t) + q(\frac{-\frac{t_s(t)}{2}-z}{k_s} - \sum_{i=1}^{m}\frac{t_{c,bi}(t)}{k_{c,bi}} - \frac{t_{o,b}(t)}{k_{o,b}}) & \frac{-t_s(t)}{2} < z \leq \frac{t_s(t)}{2} \\ T_b(t) + q(\frac{\frac{t_s(t)}{2}+z_{c,t(i-1)}(t)-z}{k_{c,ti}} - \frac{t_s(t)}{k_s} - \sum_{i=1}^{m}\frac{t_{c,bi}(t)}{k_{c,bi}} - \frac{t_{o,b}(t)}{k_{o,b}}) & z_{c,t(i-1)}(t) < z \leq z_{c,ti}(t) \\ T_b(t) + q(\frac{z_{o,t}(t)-z}{k_{o,t}} - R_{total}(t) + \frac{t_{o,t}(t)}{k_{o,t}}) & z_{c,tn}(t) < z \leq z_{o,t}(t) \end{cases} \tag{4.8}$$

The thickness of the system will vary during the thermal cycling due to the oxidation of coatings at high temperature. Therefore, the temperature field, T(z,t) is redistributed at each time step.

Creep deformation

High temperature materials usually undergo mechanical degradation like creep at elevated temperature. Creep is a time-dependent plastic deformation, resulting from rate-controlling mechanism, dislocation climb and stress-induced vacancy flow at elevated temperature [18]. It is the main cause of high temperature failure of materials [18, 214].

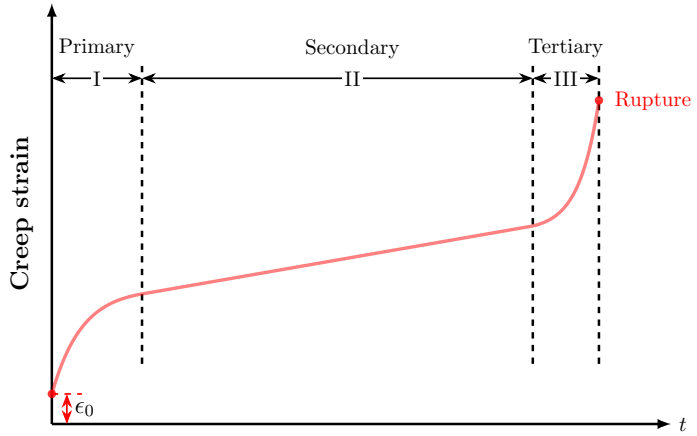

Figure 4.3 Basic creep strain curve including primary, secondary, and tertiary creep stages.

Generally, the creep behavior of a material can be divided into three stages: (1) primary or transient; (2) secondary or steady-state; and (3) tertiary or acceleration, as shown in Figure 4.3 [18]. The strain ϵ_0 corresponds to the strain at the instant of loading. In the primary stage, strain increases from ϵ_0 to ϵ_1. However, the creep strain rate (also referred to as creep rate) decreases with time. This may be due to strain hardening and changes in dislocation substructure [214, 215]. In the secondary stage, creep is a balance

between hardening (due to plastic strain) and dynamic recovery (e.g., dislocation annihilation) [215]. The creep rate remains constant under constant true von Mises stress (tension, compression or torsion), and corresponds to the inflection point of creep deformation [18, 215]. It is also known as minimum creep rate. In the tertiary stage, the creep rate accelerates, and the strain accumulates much faster than in the previous stage, leading to the fast rupture of the material.

It is worth noting that during the thermal cycling, the creep rate of a material can vary substantially with time depending on the time-dependent stress distribution of the system. Figure 4.4 shows the dependence of creep strain on stress and temperature. With increasing stress and/or temperature, the extend of secondary creep stage and rupture time t_r decrease whereas the minimum creep rate rises.

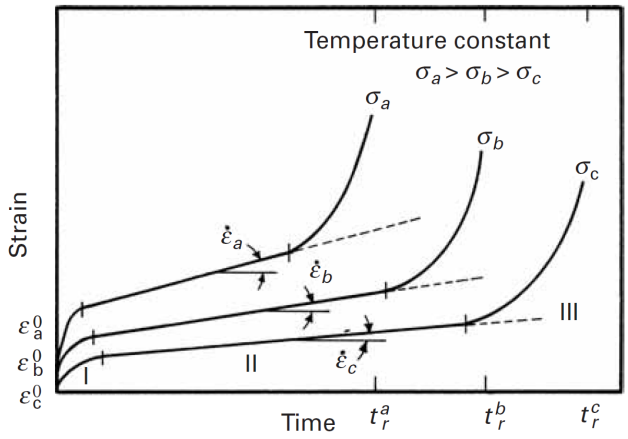

(a)

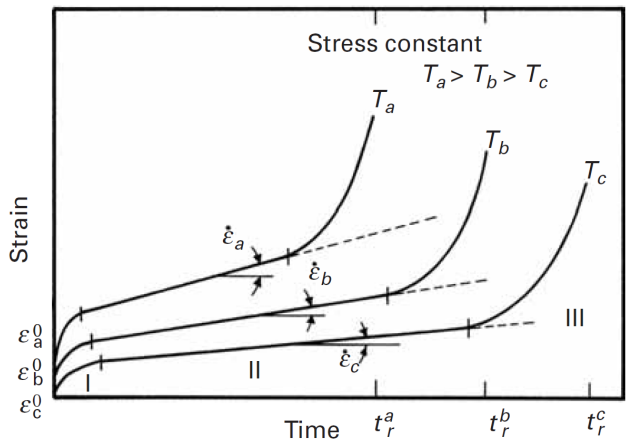

(b)

Figure 4.4 Dependence of creep strain on stress and temperature: (a) creep strain versus time at a constant temperature with different stress levels; and (b) creep strain versus time at a constant engineering stress and different temperatures [18].

In the present study, to simplify the model, the secondary creep stage is assumed during thermal cycling since a large fraction of the creep life is within this stage

[215]. The temperature and stress dependence of creep is difficult to represent in a general manner. Based on Norton's power law [216], a largely phenomenological, macroscopic relationship between steady-state creep rate, $\dot{\epsilon}_{cr}$, and corresponding stress, σ_{cr}, is expressed as follows:

$$\dot{\epsilon}_{cr} = sign(\sigma_{cr}) \cdot A \cdot exp(-\frac{Q_{cr}}{kT}) \cdot \sigma_{cr}^{n} \tag{4.9}$$

where A is the creep prefactor, k is the Boltzmann's constant, Q_{cr} is the activation energy for creep, and n is the creep exponent. Q_{cr} is often found to be the activation energy of lattice self-diffusion [215]. The sign function $sign(\sigma_{cr})$ is defined as $\sigma_{cr}/|\sigma_{cr}|$.

We assumed that heating and cooling periods are relatively short compared to the holding period, i.e., 10 h of holding time and less than 1 min of heating and cooling. Therefore, creep behavior is neglected during the heating and cooling periods, and the creep strains accumulate only during the high temperature holding period. Moreover, creep is considered in all the elements of the structure: the coatings, growing oxide scales and substrate. The instantaneous creep strain at z coordinate, $\epsilon_{cr}(z,t)$, is written as:

$$\epsilon_{cr}(z, t + dt) = \epsilon_{cr}(z, t) + \dot{\epsilon}_{cr}(z, t) \cdot dt \tag{4.10}$$

Here also, the creep strain is recalculated for each time step due to the evolution of the system structure and the stress field during thermal cycling.

High temperature oxidation

During the high temperature exposure, oxidation takes place. Oxide scales are formed at the outer surfaces of the system. The growth of scales is accompanied by the generation of a large residual stress due to the intrinsic oxide growth strain in the lateral direction, resulting in the redistribution of the stress field in the system. In the present study, it is assumed that this oxide growth strain (also called lateral growth strain in the analysis below) is affected by oxidation kinetics:

(1) In the case of diffusion-controlled oxidation, the oxide growth follows a parabolic law such as:

$$t_o = k_p \cdot t^{\frac{1}{2}} \tag{4.11}$$

where k_p is the kinetic constant, and t is the oxidation time. t_o is defined in the previous sections as the oxide scale thickness.

During isothermal oxidation, the oxide scale freely grows in the lateral direction as well as thickening if the adjacent layer does not impose any constraint. Since the oxide is not free to expand laterally, the oxide scale is constrained and in-plane stresses are induced [217]. The lateral growth strain corresponds to the expansion of the oxide scale in the lateral direction under hypothetical stress-free conditions. In the case of diffusion controlled oxidation of metals, Rhines and Wolf [218] pointed out that the counter-current diffusion of cations and anions leads to the formation of new oxide

along grain boundaries lying perpendicular to the interface (location A in Figure 4.5). This results in the generation of lateral strain. The addition of very thin extra scale can generate large stresses [218]. If the oxide is formed at the oxide/alloy interface (location B) or outer-surface (location C), no lateral strain will be created. Based on the work of Rhines and Wolf [218], Clarke [19] developed a model using edge dislocation climb process to model the lateral growth strain. The model predicts the linear relationship between lateral strain rate, $\dot{\epsilon}_{o,l}$, and oxide thickening rate, $\dot{t}_o$, in the absence of any stress relaxation [19]:

$$\dot{\epsilon}_{o,l} = \eta_l \cdot \dot{t}_o \tag{4.12}$$

where η_l is a coefficient as a function of kinetic parameters.

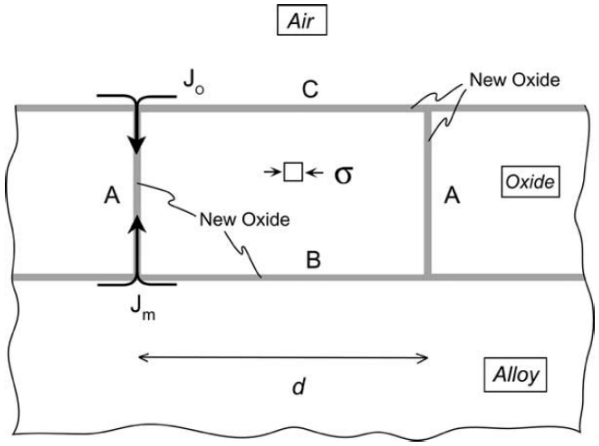

Figure 4.5 Possible locations to form new oxide scales, where J_o and J_m are diffusion fluxes of oxygen and metal ions respectively [19].

In the case of the oxidation of nitride ceramics, few studies have focused on the stress evolution during high temperature oxidation. Therefore, Eq.(4.12) is extended to the oxidation of ceramic coatings in the present study. Moreover, as for creep deformation mentioned above, the oxidation is assumed to take place only during the holding period. The lateral strain is considered to be independent of the position z and uniform throughout the thickness since the thickness of the oxide scale is assumed to be very small for each time step [212]. Thus, the time-dependent lateral strain of oxide, $\epsilon_{o,l}(t)$, can be written as:

$$\epsilon_{o,l}(t + dt) = \epsilon_{o,l}(t) + \dot{\epsilon}_{o,l}(t) \cdot dt \tag{4.13}$$

(2) When the oxidation is controlled by a surface reaction, the oxide scale grows linearly. We assumed that in this analysis the lateral growth strain, $\epsilon_{o,l}$, is constant when oxidation follows linear kinetics.

Furthermore, when the oxide scale grows, the coating thickness decreases. Assuming an isotropic behavior for both coating and substrate, the decreasing thickness of the oxidized coating can be expressed as:

$$-dt_{coating} = (\frac{\Omega_{coating}}{\Omega_{oxide}})^{\frac{1}{3}} \cdot dt_{oxide} \tag{4.14}$$

where $\Omega_{coating}$ and Ω_{oxide} are the volume of coating and oxide per metal ion respectively.

Summary of assumptions

The aforementioned assumptions are:

- Initial stress-free state for substrate at deposition temperature, and a uniform temperature field in the coatings/substrate system during deposition;
- Temperature field in the system is assumed to be uniform at ambient temperature;
- Steady-state thermal conduction within the system when it is subjected to thermal loading;
- Secondary creep and oxidation take place only at high temperature, and are neglected during the heating and cooling periods;
- Creep strain accumulates following Norton's power law;
- Linear relationship between lateral growth strain rate and oxide thickening rate when parabolic oxidation kinetics occurs;
- Constant intrinsic growth strain for coatings and constant thermal conductivities during thermal cycling;
- The lateral growth strain remains constant when the oxide growth is linear;
- Perfect bonding between two adjacent layers.

According to the assumptions shown above, creep strain and lateral strain could be update as:

$$\begin{cases} \epsilon_{cr}(z, t + \Delta t) = \epsilon_{cr}(z, t) + \dot{\epsilon}_{cr}(z, t) \cdot \Delta\tau \\ \epsilon_{o,l}(t + \Delta t) = \epsilon_{o,l}(t) + \dot{\epsilon}_{o,l}(t) \cdot \Delta\tau \end{cases} \tag{4.15}$$

with

$$\Delta\tau = \begin{cases} \Delta t & \text{during the holding period} \\ 0 & \text{during the heating and cooling process} \end{cases} \tag{4.16}$$

where Δt is the time increment and $\Delta\tau$ the increment of holding time.

Stress evolution

Based on Hsueh's model [202], the total strain is decomposed into a uniform constraint and a bending moment as described in the section 4.1.2. Following Eq.(4.5), the instantaneous total strain, $\epsilon(z, t)$, at the position z is expressed as:

$$\epsilon(z, t) = c(t) + \frac{z - t_B(t)}{r(t)} \tag{4.17}$$

where c(t), t_B(t) and r(t) are the time-dependent uniform curvature, bending axis position and radius of curvature, respectively (see Eq.(4.5)).

Thus, the corresponding biaxial stress at the position z ($\sigma(z,t)$) is written as:

$$\begin{cases} \sigma_{o,b}(z,t) = \frac{E_{o,b}}{1-\nu_{o,b}}[\epsilon(z,t) - \epsilon_{o,th,b}(z,t) - \epsilon_{o,cr,b}(z,t) - \epsilon_{o,l,b}(z,t) - \epsilon_{0,b}] & z_{o,b}(t) \leq z \leq z_{c,bm}(t) \\ \sigma_{c,bi}(z,t) = \frac{E_{c,bi}}{1-\nu_{c,bi}}[\epsilon(z,t) - \epsilon_{c,th,bi}(z,t) - \epsilon_{c,cr,bi}(z,t) - \epsilon_{c,g,bi}] & z_{c,bi}(t) \leq z \leq z_{c,b(i-1)}(t) \\ \sigma_{s}(z,t) = \frac{E_{s}}{1-\nu_{s}}[\epsilon(z,t) - \epsilon_{s,th}(z,t) - \epsilon_{s,cr}(z,t)] & \frac{-t_s(t)}{2} \leq z \leq \frac{t_s(t)}{2} \\ \sigma_{c,ti}(z,t) = \frac{E_{c,ti}}{1-\nu_{c,ti}}[\epsilon(z,t) - \epsilon_{c,th,ti}(z,t) - \epsilon_{c,cr,ti}(z,t) - \epsilon_{c,g,ti}] & z_{c,t(i-1)}(t) \leq z \leq z_{c,ti}(t) \\ \sigma_{o,t}(z,t) = \frac{E_{o,t}}{1-\nu_{o,t}}[\epsilon(z,t) - \epsilon_{o,th,t}(z,t) - \epsilon_{o,cr,t}(z,t) - \epsilon_{o,l,t}(z,t) - \epsilon_{0,t}] & z_{c,tn}(t) \leq z \leq z_{o,t}(t) \end{cases} \tag{4.18}$$

where ϵ_{cr}, $\epsilon_{o,l}$, ϵ_g, and ϵ_{th} are respectively the creep strain (Eqs. (4.9), (4.15) and (4.16)), the lateral growth strain (Eqs. (4.12), (4.15) and (4.16)) in the oxides, the intrinsic CVD growth strain (Eq.(4.3)) in the coatings and the thermal strain. $\epsilon_{0,t}$ and $\epsilon_{0,b}$ represent the total strain at the top and bottom surface of system just before the formation of first layer of oxide, respectively. The instantaneous thermal strains, ϵ_{th}, are defined as the expansion due to temperature change from the temperature at which the stress-free state could be assumed to the instantaneous temperature at the position z, such as:

$$\begin{cases} \epsilon_{o,th,b}(z,t) = \int_{T_{oxide}(z)}^{T(z,t)} \alpha_{th,o,b}(T)dT & z_{o,b}(t) \leq z \leq z_{c,bm}(t) \\ \epsilon_{c,th,bi}(z,t) = \int_{T_{growth,bi}}^{T(z,t)} \alpha_{th,c,bi}(T)dT & z_{c,bi}(t) \leq z \leq z_{c,b(i-1)}(t) \\ \epsilon_{s,th}(z,t) = \int_{T_{growth,s}}^{T(z,t)} \alpha_{th,s}(T)dT & \frac{-t_s(t)}{2} \leq z \leq \frac{t_s(t)}{2} \\ \epsilon_{c,th,ti}(z,t) = \int_{T_{growth,ti}}^{T(z,t)} \alpha_{th,c,ti}(T)dT & z_{c,t(i-1)}(t) \leq z \leq z_{c,ti}(t) \\ \epsilon_{o,th,t}(z,t) = \int_{T_{oxide}(z)}^{T(z,t)} \alpha_{th,o,t}(T)dT & z_{c,tn}(t) \leq z \leq z_{o,t}(t) \end{cases} \tag{4.19}$$

T(z,t) is the instantaneous temperature at the position z (Eq.(4.8)), T_{growth} is the CVD growth temperature (section 'Residual stress induced by CVD') and $T_{oxide}(z)$ is oxidation temperature of the oxide scale at the position z.

As described in section 'Residual stress induced by CVD', three boundary conditions are used to determine the three unknown parameters c, t_B, and r [202]:

(1) **The resultant force due to the uniform strain component is zero**, therefore:

$$\begin{aligned} &\int_{z_{o,b}(t)}^{z_{c,bm}(t)} \frac{E_{o,b}}{1-\nu_{o,b}}[c(z,t) - \epsilon_{o,th,b}(z,t) - \epsilon_{o,cr,b}(z,t) - \epsilon_{o,l,b}(z,t)]dz \\ &+ \sum_{i=1}^{m} \int_{z_{c,bi}(t)}^{z_{c,b(i-1)}(t)} \frac{E_{c,bi}}{1-\nu_{c,bi}}[c(z,t) - \epsilon_{c,th,bi}(z,t) - \epsilon_{c,cr,bi}(z,t) - \epsilon_{c,g,bi}(z,t)]dz \\ &+ \int_{-\frac{t_s(t)}{2}}^{\frac{t_s(t)}{2}} \frac{E_s}{1-\nu_s}[c(z,t) - \epsilon_{s,th}(z,t) - \epsilon_{s,cr}(z,t)]dz \\ &+ \sum_{i=1}^{n} \int_{z_{c,t(i-1)}(t)}^{z_{c,ti}(t)} \frac{E_{c,ti}}{1-\nu_{c,ti}}[c(z,t) - \epsilon_{c,th,ti}(z,t) - \epsilon_{c,cr,ti}(z,t) - \epsilon_{c,g,ti}(z,t)]dz \\ &+ \int_{z_{c,tn}(t)}^{z_{o,t}(t)} \frac{E_{o,t}}{1-\nu_{o,t}}[c(z,t) - \epsilon_{o,th,t}(z,t) - \epsilon_{o,cr,t}(z,t) - \epsilon_{o,l,t}(z,t)]dz = 0 \end{aligned} \tag{4.20}$$

(2) **The resultant force due to the bending component is zero**, therefore:

$$\int_{z_{o,b}(t)}^{z_{c,bm}(t)} \frac{E_{o,b}}{1-\nu_{o,b}} \cdot \frac{z-t_B(t)}{r(t)} dz + \sum_{i=1}^{m} \int_{z_{c,bi}(t)}^{z_{c,b(i-1)}(t)} \frac{E_{c,bi}}{1-\nu_{c,bi}} \cdot \frac{z-t_B(t)}{r(t)} dz$$
$$+ \int_{-\frac{t_s(t)}{2}}^{\frac{t_s(t)}{2}} \frac{E_s}{1-\nu_s} \cdot \frac{z-t_B(t)}{r(t)} dz + \sum_{i=1}^{n} \int_{z_{c,t(i-1)}(t)}^{z_{c,ti}(t)} \frac{E_{c,ti}}{1-\nu_{c,ti}} \cdot \frac{z-t_B(t)}{r(t)} dz$$
$$+ \int_{z_{c,tn}(t)}^{z_{o,t}(t)} \frac{E_{o,t}}{1-\nu_{o,t}} \cdot \frac{z-t_B(t)}{r(t)} dz = 0 \tag{4.21}$$

(3) **The sum of bending component with respect to the bending axis is zero**, therefore:

$$\int_{z_{o,b}(t)}^{z_{c,bm}(t)} \sigma_{o,b}(z,t) \cdot [z-t_B(t)] dz + \sum_{i=1}^{m} \int_{z_{c,bi}(t)}^{z_{c,b(i-1)}(t)} \sigma_{c,bi}(z,t) \cdot [z-t_B(t)] dz$$
$$+ \int_{-\frac{t_s(t)}{2}}^{\frac{t_s(t)}{2}} \sigma_s(z,t) \cdot [z-t_B(t)] dz + \sum_{i=1}^{n} \int_{z_{c,t(i-1)}(t)}^{z_{c,ti}(t)} \sigma_{c,ti}(z,t) \cdot [z-t_B(t)] dz$$
$$+ \int_{z_{c,tn}(t)}^{z_{o,t}(t)} \sigma_{o,t}(z,t) \cdot [z-t_B(t)] dz = 0 \tag{4.22}$$

The resolution of this set of equations is done by a genetic algorithm.

Implementation of the model

Eqs. (4.20) to (4.22) are iteratively solved with a MATLAB (MATLAB 2019a) code. To simplify the model, it is assumed that the oxide scale is very thin. Thus, the oxidation temperature of the top and bottom of oxide scales are assumed to be constant, as $T_{t,0}$ and $T_{b,0}$ respectively, throughout the holding period. The initial and final temperatures of each thermal cycle are defined as T_{amb}=25 °C. The procedure is shown in Figure 4.6 and the main steps are summarized as follows:

Step 1: Initiate the multilayer coating system. The creep strain and oxide lateral growth strain are initiated to be 0, i.e. $\epsilon_{cr}(z,0)=0$, and $\epsilon_{o,l}(0)=0$. Impose the CVD growth strain in coating i, $\epsilon_{c,g,i}$, the deposition temperature T_{growth} and the final ambient temperature T_{amb}.

Step 2: Calculate the residual stresses within the system using Eqs. (4.4) to (4.6), and the three boundary conditions described in the section 4.1.2; then, impose the heat flux $\overrightarrow{q}$ and start the thermal cycling;

Step 3: Impose a time increment Δt;

Step 4: Determine the instantaneous z coordinate, z(t), using Eqs. (4.1), (4.2), (4.11) and (4.14);

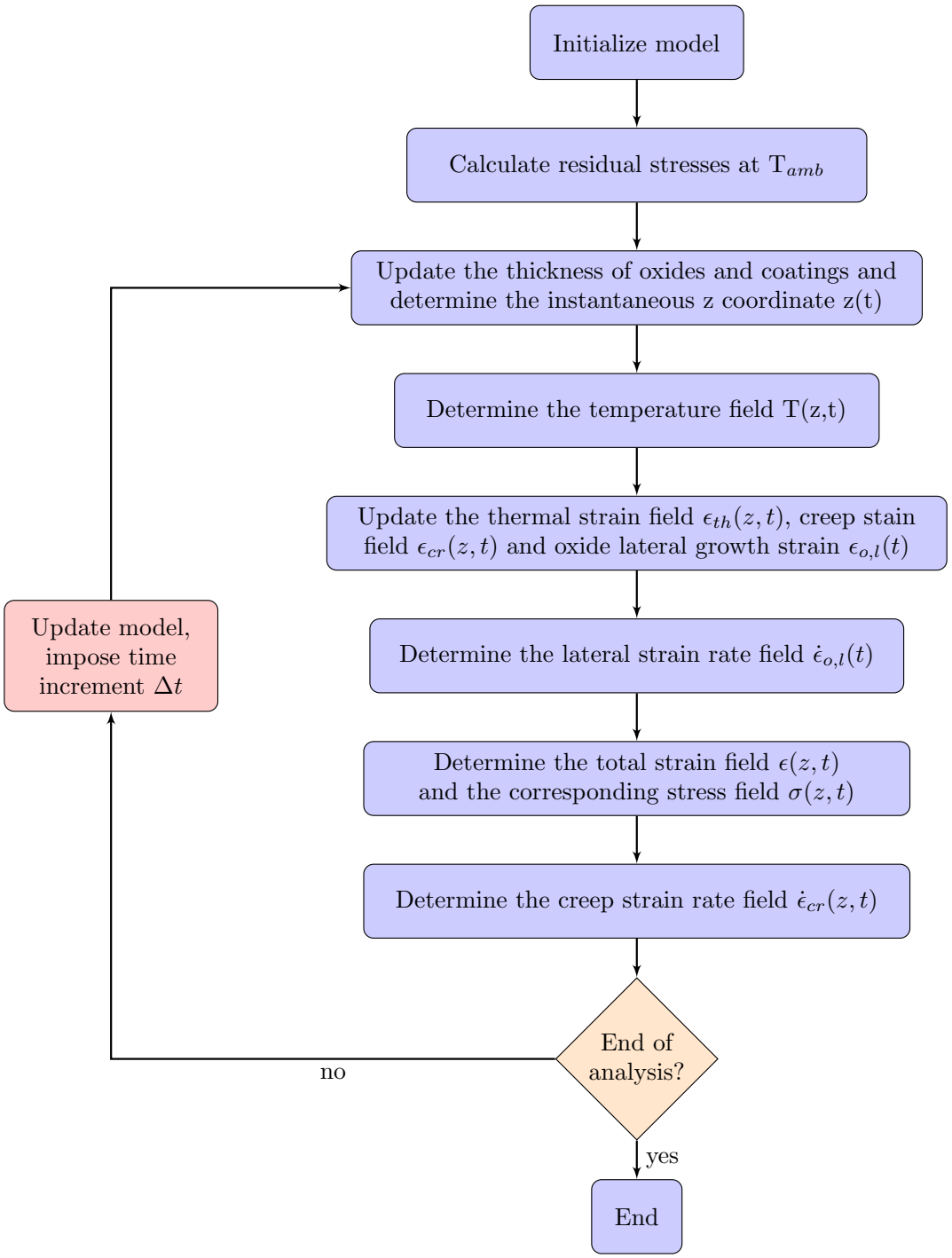

Figure 4.6 Flow chart of the model.

Step 5: Determine the temperature field T(z,t) within the system using Eq.(4.8);

Step 6: Determine the thermal strain field $\epsilon_{th}(z,t)$ using Eq.(4.19), update the creep strain field $\epsilon_{cr}(z,t)$ and the lateral strain $\epsilon_{o,l}(t)$ by Eqs. (4.15) and (4.16); then calculate the lateral strain rate $\dot{\epsilon}_{o,l}(t)$ field for next iteration with Eqs. (4.11) and (4.12);

Step 7: Solve Eqs. (4.20) to (4.22) by a genetic algorithm to obtain c(t), t_b(t) and r(t);

Step 8: Determine the total strain field ϵ(z,t) and the corresponding stress field σ(z,t) using Eqs. (4.17) and (4.18); then update the creep strain rate field $\dot{\epsilon}_{cr}(z,t)$ for the next iteration with Eq. (4.9);

Step 9: If it is the end of thermal cycling, finish the analysis; otherwise, back to Step 3 for next iteration.

4.2 Verification of the model: comparison with finite element analysis

Finite element analysis (FEA) is widely used for the analysis of a fully coupled thermomechanical problem. In this section, FEA is employed to verify the accuracy of the proposed analytical model using a commercial software package ANSYS 19.1 (ANSYS, Inc., USA). Results (stress and inelastic strain evolution) from FEA and the present model are compared and discussed.

4.2.1 Finite element model

The system studied here represents a TZM substrate coated with AlN coatings on both faces. The system is symmetric about its mid-surface. The material properties and the input parameters for the benchmarking are listed in Tables A.3.1 and A.3.2, respectively. The intrinsic CVD growth stress of AlN coating and the oxide growth are not taken into account in this benchmarking. It is convenient to use 'top coating' and 'bottom coating' to denote the coating layers above and below the substrate respectively.

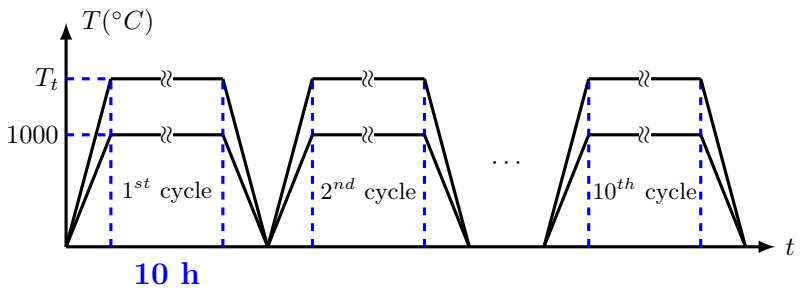

Figure 4.7 Schematic representation of thermal loading history for FEA.

4.2.2 Comparison between FEA and analytical model calculations

Values of stresses after deposition calculated by FEA with MPC boundary condition are in good agreement with those of the analytical model (Table 4.1). The AlN coatings exhibit compressive stresses, whereas the stress in the substrate is tensile due to the higher thermal expansion coefficient of TZM. The stress in the coating is one order of magnitude higher than that in the substrate.

Table 4.1 Stresses in AlN coatings and TZM substrate after deposition calculated by FEA with MPC boundary condition and the analytical model.

Material	**Stress (MPa)**	
	FEA	Analytic model
AlN	-319	-319
TZM	38	38

The temperature distribution after heating, along the z direction, is shown in Figure 4.8. There is a good agreement between the results of the analytical model and FEA. The top surface is heated to 1137 °C, showing a total of 137 °C temperature difference within the system: 20 °C in each AlN coating and 97 °C in the substrate. The temperature gradient in the substrate (10^5 °C·m^{-1}) is lower than that in the AlN coating (3×10^5 °C·m^{-1}) due to its higher thermal conductivity.

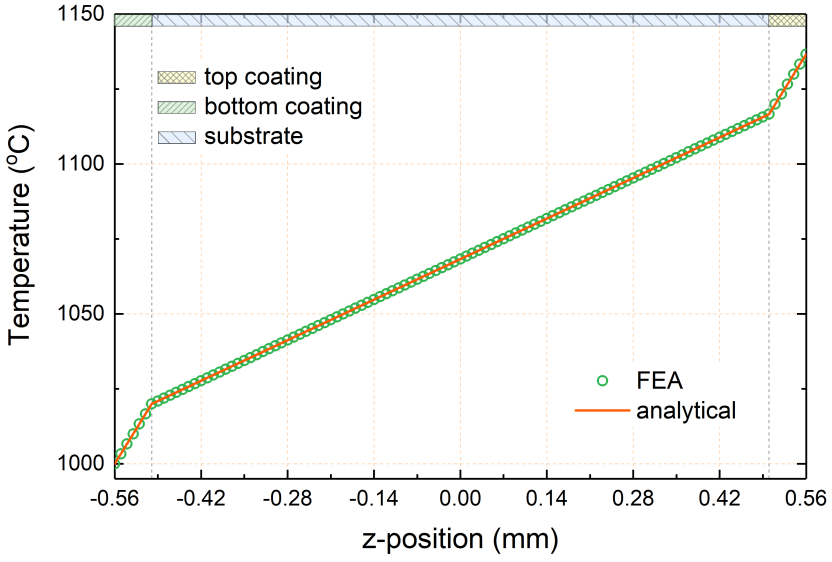

Figure 4.8 Comparison between FEA and the present model for the temperature distribution along the thickness direction.

Comparison of normal stress and creep strain between the proposed model and the FEA are displayed in Figures 4.9 and 4.10. The analytical results are consistent with the finite element simulation. This confirms the validity of the

proposed model. Moreover, compared with the FEA, the analytical model can easily integrate the different high temperature phenomena such as oxidation. It is therefore confident to use the present analytical model for calculating stress evolution in multilayer coating systems. Detailed discussions on the evolution of stress and creep strain during thermal cycling are presented in the next section.

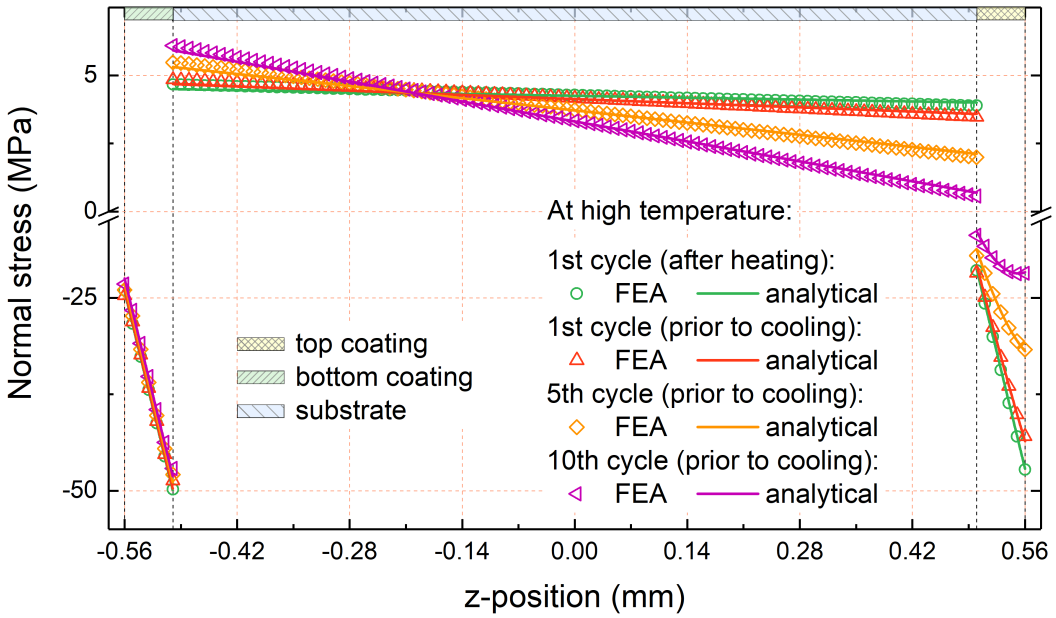

(a) Stress distribution at high temperature during the thermal cycling

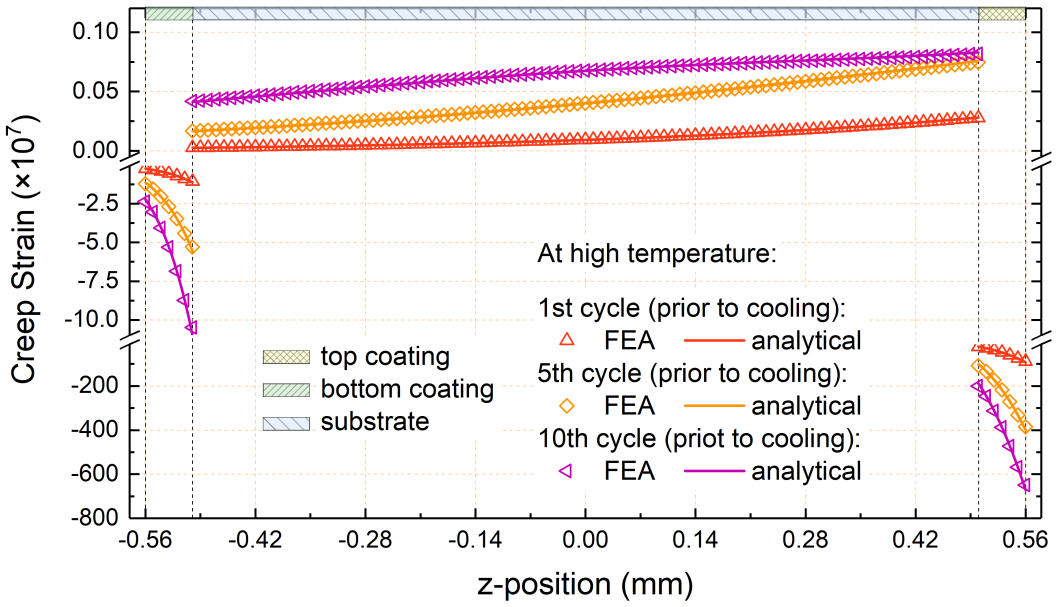

(b) Creep strain distribution at high temperature during the thermal cycling

Figure 4.9 Comparison between FEA and the present model: (a) normal stress and (b) creep strain distribution at high temperature.

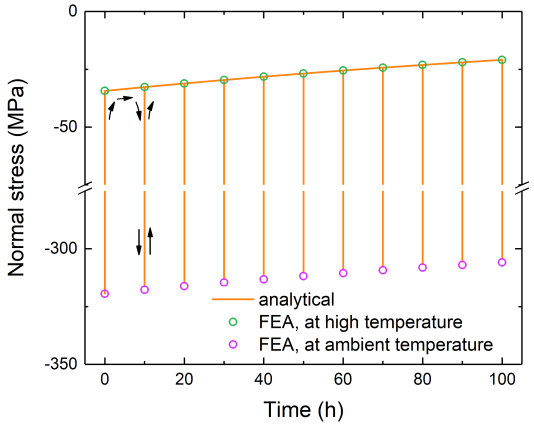

(a) Stress at the center of AlN top coating

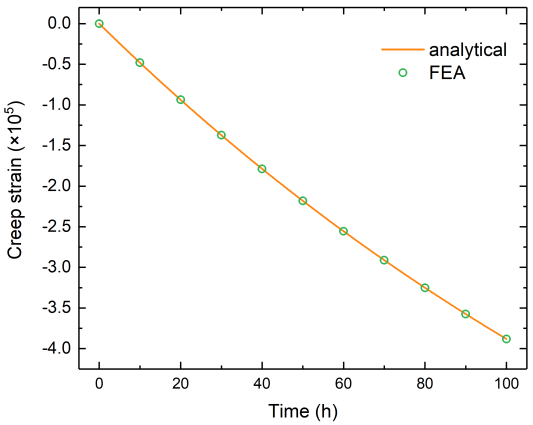

(b) Creep strain at the center of AlN top coating

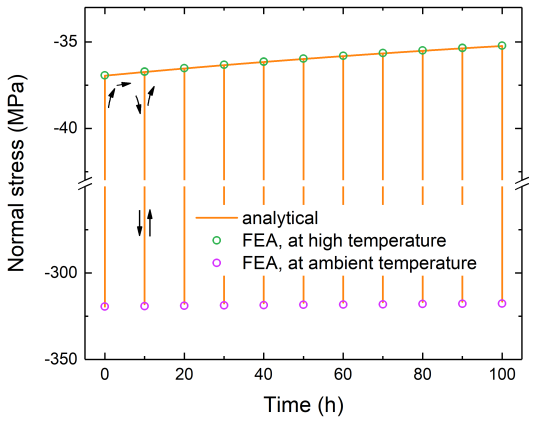

(c) Stress at the center of AlN bottom coating

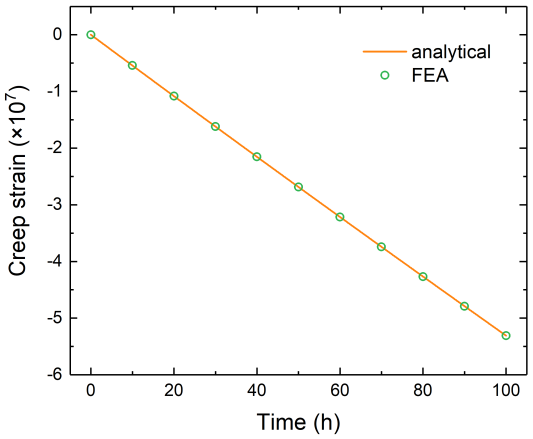

(d) Creep strain at the center of AlN bottom coating

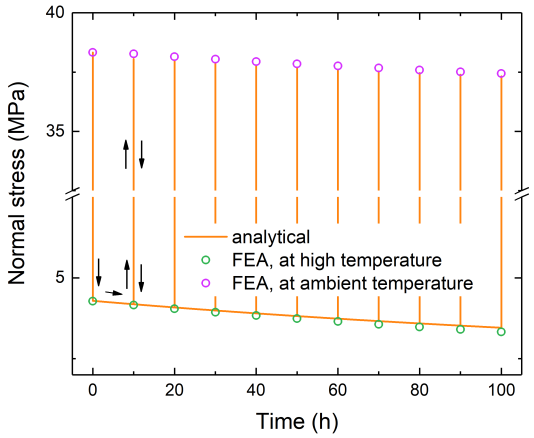

(e) Stress at the center of the substrate

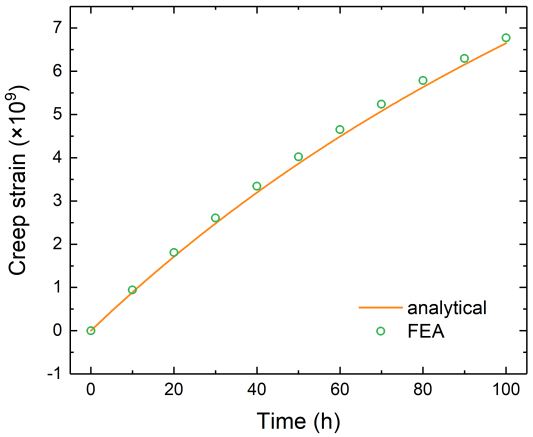

(f) Creep strain at the center of the substrate

Figure 4.10 Evolution of (a, c, e) normal stress and (b, d, f) creep strain at the center position of (a, b) top coating, (c, d) bottom coating and (e, f) substrate.

4.3 Time evolution of stress and creep strain in the multilayer system

4.3.1 Simplified model: without oxidation

To have a clear understanding of the evolution of the stress field during thermal cycling, it is firstly assumed that no oxidation takes place at high temperature. Therefore, the temperature difference shown in Figure 4.8 is unchanged within the system when it is subjected to a thermal gradient. This simplified model allows to study how thermomechanical properties (thermal expansion coefficients and creep properties) of materials alter the stress field distribution during thermal cycling.

Case I: Non-constrained AlN coatings during deposition

We first of all consider a static AlN/TZM/AlN system where the growth stress is not developed in AlN coatings during deposition, i.e., ϵ_g=0 (Eq.(4.3)). Thermal loading parameters and comparisons with FEA are presented in section 4.2.2. We here discuss in detail how the curvature, stress and creep strain evolve during thermal cycling.

Figure 4.11 shows the quantitative evolution of the bending curvature (1/r) of the system during the cyclic thermal loading (Figure 4.7). The system is symmetric about its mid-plane after deposition, i.e. $\frac{1}{r}$=0. When the system is initially subjected to a thermal loading, the curvature of the system increases to 0.501 m^{-1}. This indicates that the system is curved to form a convex shape, and the stress distribution along the z-direction is asymmetric about the mid-plane of the system. The positive curvature here is due to the large temperature difference and the related thermal expansion mismatches within the system. Subsequently, the bending curvature slightly decreases with increasing time (from 0.501 to 0.490 m^{-1} for 10 thermal cycles). As the oxidation of AlN coatings is not taken into account in the current analysis, if the system does not undergo creep deformation, the curvature remains constant until the system is cooled down. The realistic decrease of the bending curvature with time results from the accumulation of creep strains and related stress relaxation in the system.

At the end of each thermal cycle, the cooling of the system, from high temperature to ambient temperature, gives rise to a negative increment of curvature ($\Delta\frac{1}{r}|_{HT\rightarrow T_{amb}}$). For example, the curvature changes from 0.499 to -0.001 m^{-1} ($\Delta\frac{1}{r}|_{HT\rightarrow T_{amb}}$=0.500 m^{-1}) during the cooling stage of the first thermal cycle. Indeed, the large temperature change leads to a significant enhancement of thermal strain mismatches between the AlN coatings and substrate. To compensate such mismatches, the bending strain is strongly reduced to maintain the system equilibrium. The phenomenon of such a negative increment of bending curvature during the cooling stage is helpful in understanding the variation of curvature during thermal cycling, in particular in the case when the value of this increment is significantly reduced (as it will be seen in sections 4.3.2 and 4.4). In the present analysis, the negative increment of curvature during the cooling stage,

$\Delta\frac{1}{r}|_{HT\rightarrow T_{amb}}$, results in a reversal of the curvature at ambient temperature from convex to slightly concave during the whole thermal cycling.

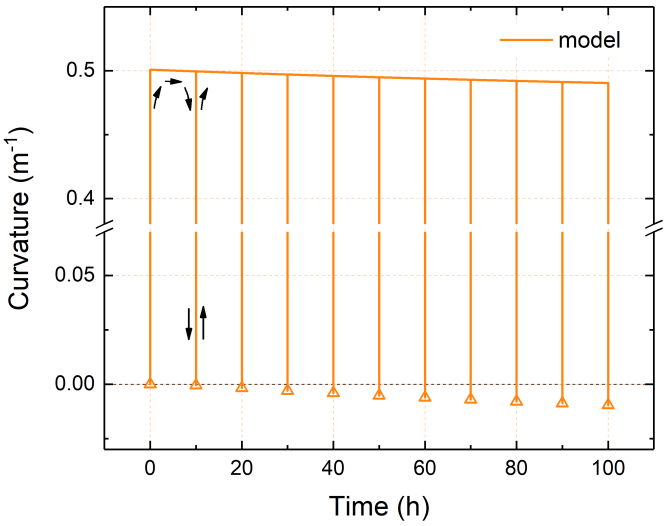

Figure 4.11 Time-dependent curvature of the system predicted by the analytical model; triangles represent the curvature at ambient temperature.

Figure 4.9 shows the distribution of normal stress and creep strain at high temperature (1000-1137 °C temperature difference presented in Figure 4.8) in the AlN coatings and substrate along the thickness direction. As seen from Figure 4.9(a) (green curves and points), after the first heating in the first cycle, the coating layers are under compression due to the lower thermal expansion coefficient of AlN, whereas the substrate is under tension. These stresses, denoted as high temperature thermoelastic stress $\sigma_{0,HT}(z)$ in the analysis below, are related to the thermoelastic response of the system to the thermal load. Moreover, stresses are linearly distributed in an individual layer, and asymmetric about the mid-plane of the system. This confirms the formation of the bending curvature after heating shown in Figure 4.11. As time extends, stresses in the AlN top coating (0.50 mm≤z≤0.56 mm, see Figure 4.9) are relaxed, while in the bottom coating (-0.56 mm≤z≤0.50 mm, see Figure 4.9) stresses remain linearly distributed. In the substrate, the stress gradient is slightly enhanced due to the decrease of curvature.

Figure 4.9(b) depicts the evolution of creep strain field during thermal cycling. It is shown that the development and accumulation of creep strain mainly take place in the AlN top coating. This can be explained by the Norton's creep power law. The creep deformation rate is dependent on the material temperature. Since the AlN bottom coating is cooler than the top coating as shown in Figure 4.8, the creep behavior of the top and bottom coatings are different. The creep strains in the bottom coating are two order of magnitude less than those in the top coating (10^{-7} vs. 10^{-5}). As a result, the stress relaxation in the AlN bottom coating is less significant (see purple curves and points in Figure 4.9(a)). The creep strain in the substrate is much smaller than those in the AlN coatings, resulting from lower stresses (Norton's creep power law) and better creep resistance of TZM.

Figure 4.10 depicts the time evolution of normal stress and creep strain at the center of AlN coatings and substrate. Stresses and creep strains in both AlN coatings and substrate evolve nearly linearly until the end of exposure to high temperature. Indeed, the low high temperature thermoelastic stress (less than -50 MPa in AlN coatings and 6 MPa in the substrate) result in low creep strain rate according to the Norton's creep power law. The accumulated creep strains after thermal cycling in the system are at least one order of magnitude less than the thermal strains (Table 4.2). The thermal strain mismatches are more important than the creep strain mismatches within the system. In such a case, the temperature fluctuation in the layer (Eq.(4.19)) became the predominant effect on the stress evolution within the system.

Table 4.2 Calculated thermal strains at high temperature and accumulated creep strains after ten thermal cycles at the center of the AlN top coating, substrate and AlN bottom coating.

	AlN top coating	**Substrate**	**AlN bottom coating**
Thermal strain, ϵ_{th}	-3.3×10^{-4}	-8.5×10^{-4}	-6.8×10^{-4}
Accumulated creep strain, ϵ_{cr}	-3.9×10^{-5}	6.6×10^{-9}	-5.3×10^{-7}

In summary, this analysis shows that, despite the lack of intrinsic growth stress and oxidation, the different creep behavior between coatings and substrate can lead to stress relaxation during thermal cycling. However, the global relaxation of the system is not significant even after 10 thermal cycles. Indeed, the good thermal conductivities and low difference of thermal expansion coefficients between AlN and TZM result in low thermoelastic stresses in both AlN coatings and TZM at high temperature. Therefore, the coatings and substrate slowly creep and cannot fully relax their initial high temperature stresses. In such a case, in spite of the existence of creep mismatches within the substrate, it is the thermal properties of materials that strongly affect the stress evolution during thermal cycling.

Additionally, the use of constant thermal expansion coefficients in this analysis can lead to an underestimation of thermal strains. Nevertheless, the high temperature thermoelastic response determines the evolution of creep strain in coatings and substrate, which in turn, alter the subsequent stress evolution. Therefore, to provide accurate analysis, instantaneous thermal expansion coefficients (as a function of temperature) are employed in the following analysis.

Case II: Constrained AlN coatings during deposition

To avoid underestimation of thermal strains, instantaneous thermal expansion coefficients (as a function of temperature) are used in the calculations. They are fitted by a fifth-order polynomial (section 2.1.1). It is also suggested to use the instantaneous thermal expansion coefficients of pure molybdenum due to the lack of those of TZM. Fitting data for AlN and TZM are provided in Table 4.3.

Table 4.3 Coefficients of fifth-order polynomial fit for the thermal expansion coefficients of AlN and pure molybdenum (used for the calculation of thermal strain of TZM in the following analysis) [9, 34].

Coefficients	**AlN**	**TZM**
A_0 (10^{-6}·°C^{-1})	2.474	5.171
A_1 (10^{-6}·°C^{-2})	1.117×10^{-2}	-5.918×10^{-3}
A_2 (10^{-6}·°C^{-3})	-1.328×10^{-5}	3.522×10^{-5}
A_3 (10^{-6}·°C^{-4})	8.680×10^{-9}	-5.012×10^{-8}
A_4 (10^{-6}·°C^{-5})	-2.950×10^{-12}	3.164×10^{-11}
A_5 (10^{-6}·°C^{-6})	4.057×10^{-16}	-7.078×10^{-15}

Moreover, in order to better understand how creep behavior affect the stress evolution during thermal cycling, we consider the intrinsic growth stress in AlN coatings. Indeed, we have shown in Chapter 3 the existence of tensile growth stress in AlN coatings deposited on TZM. It is stated that this growth stress remains constant even after a long time post deposition. Such growth stress will contribute to the initial elastic response of the system, and therefore alter the creep behavior of materials. However, the value of growth stress varied from several hundreds of MPa to few GPa in literature. In an attempt to better illustrate the effect of creep deformation on the evolution of stress field during thermal cycling, a high stress value of 1291 MPa (i.e. growth strain of -0.3%, Eq.(4.3)) was chosen for the following analysis.

Table 4.4 Thermoelastic stresses and creep strains after 10 thermal cycles at the center of the AlN coatings and substrate calculated using constant and instantaneous thermal expansion coefficients.

	Results	**Constant CTE**	**Instantaneous CTE**
AlN top coating	stress after deposition (MPa)	-319	-702
	stress after heating (MPa)	-34	-129
	accumulated creep strain, ϵ_{cr}	-3.9×10^{-5}	-1.5×10^{-4}
substrate	stress after deposition (MPa)	38	84
	stress after heating (MPa)	4	20
	accumulated creep strain, ϵ_{cr}	6.6×10^{-9}	7.8×10^{-7}
AlN bottom coating	stress after deposition (MPa)	-319	-702
	stress after heating (MPa)	-37	-188
	accumulated creep strain, ϵ_{cr}	-5.3×10^{-7}	-2.7×10^{-6}

Time evolution of normal stress and creep strain at the center of AlN coatings and substrate are plotted in Figure 4.12. $\sigma_g = 0$ is used to illustrate the calculation using instantaneous thermal expansion coefficients for which the growth stress in AlN coatings was not taken into account (orange curves). Compared to Figure 4.10, the use of instantaneous thermal expansion coefficients results in

higher calculated thermal strains in both AlN coatings and substrate, and thus higher thermoelastic stress levels (orange circles at t=0 in Figures 4.12(a), 4.12(c) and 4.12(e)). Larger creep strains are therefore developed in the system. Values are summarized in Table 4.4 for clarity. This reveals that the accurate data for thermal expansion coefficients is necessary. A small variation of the thermal expansion coefficient can induce a large change in the stress calculation.

However, the increase of creep strains does not significantly influence the stress evolutions. Stresses in the system after 10 thermal cycles remain almost elastic (orange curves in Figures 4.12(a), 4.12(c) and 4.12(e)). As discussed in the previous section, this calculation confirms that the stress evolution is predominately dependent on thermal properties of materials if (1) they are creep-resistant materials; (2) they have good thermal conductivities at high temperature; (3) the differences of their thermal expansion are not large and (4) no other parameter contribute to the elastic response of the system to the thermal load.

When the growth stress in AlN is considered (σ_g=1291 MPa, green curves in Figure 4.12), AlN coatings are under compression (458 MPa) after deposition whereas the stress in the substrate is tensile (-55 MPa). The applied thermal load does not change the stress sign, but results in larger stresses in the system (1031, 972 and -119 MPa in the top coating, bottom coating and substrate respectively). As shown in Figure 4.12, stress relaxation and accumulation of creep strains within the system are more significant (green curves) compared with the case of σ_g=0 (orange curves). Creep strains are one order of magnitude higher in AlN coatings and two orders of magnitude higher in the substrate (Figures 4.12(b), 4.12(d) and 4.12(f)). This large difference results from the larger high temperature thermoelastic stress within the system. According to the Norton's creep power law, for a given temperature, the larger the stress is, the higher the creep strain rate can be obtained. As a result, larger stress relaxations are observed.

Evolution of curvature with thermal cycling is displayed in Figure 4.13. With a high value of growth stress (σ_g=1291 MPa), the curvature decreases with exposure time at the beginning of thermal cycling (i.e., in the first two cycles), as shown in Figure 4.13(a). This indicates that the system at that time is relaxed. However, the curvature increases with increasing time, which means that the asymmetry of the system is strengthened. This suggests that there exists a large stress gradient within the system. Moreover, this increase of curvature at high temperature leads to a reverse of curvature from concave to convex at ambient temperature.

To better understand the variation of curvature, the stress gradient evolution within the system during thermal cycling is studied. Figure 4.14 presents the distribution of normal stress and creep strain at high temperature along the z direction. As previously observed in Figure 4.9(b), the accumulation of creep strains is more pronounced in the AlN top coating than the bottom coating (two order of magnitude after 10 thermal cycles, see Figures 4.14(b) and 4.14(d)) due to the temperature difference. Therefore, the stress relaxation is more evident in the top coating. The stress relaxation rate, defined as $\frac{\sigma(z,t)-\sigma_{0,HT}(z)}{\sigma_{0,HT}(z)}$, reaches 46% at the center of the AlN top coating, while only 8% of stress relaxation is occurred after 10 thermal cycles.

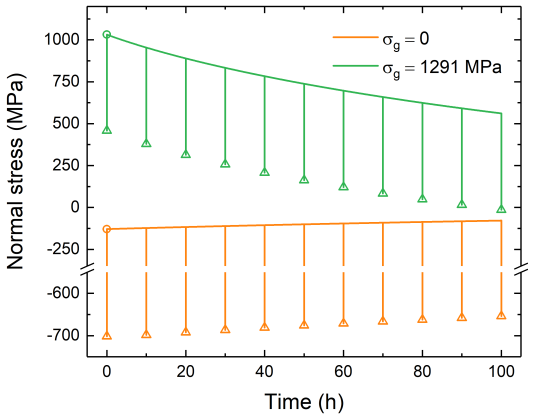

(a) Stress at the center of AlN top coating

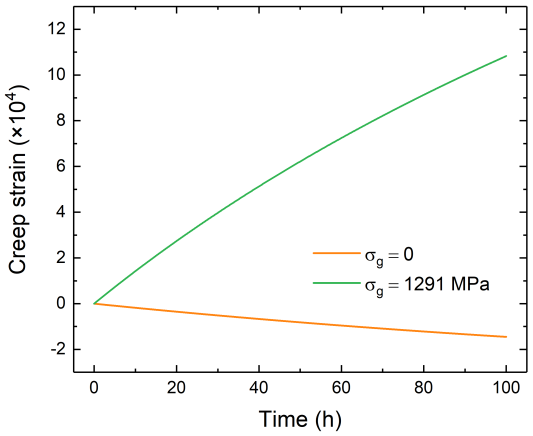

(b) Creep strain at the center of AlN top coating

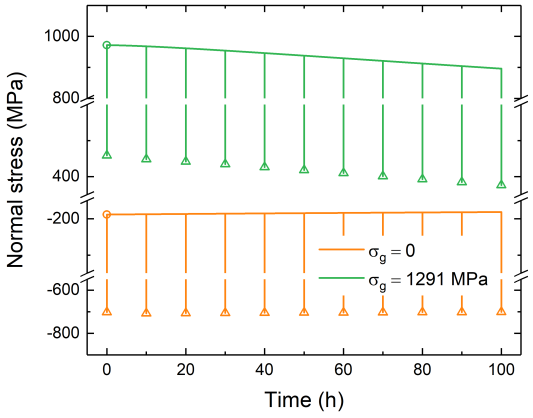

(c) Stress at the center of AlN bottom coating

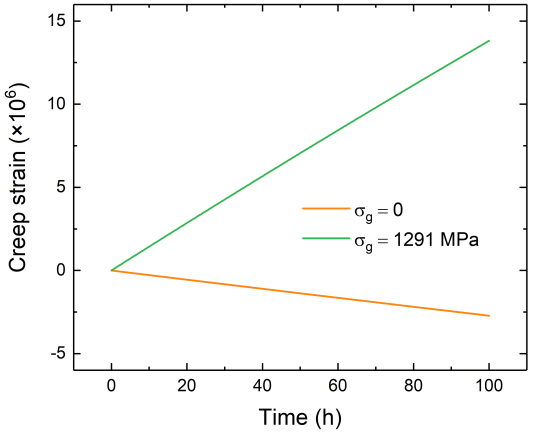

(d) Creep strain at the center of AlN bottom coating

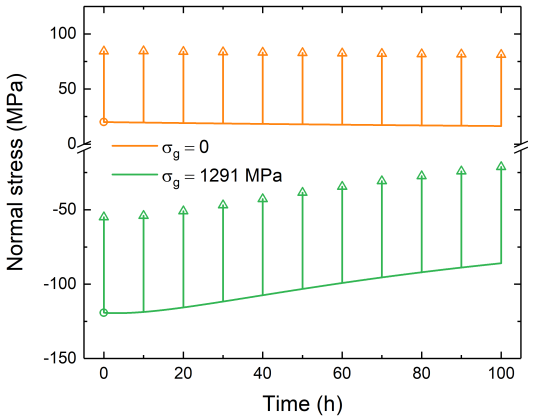

(e) Stress at the center of the substrate

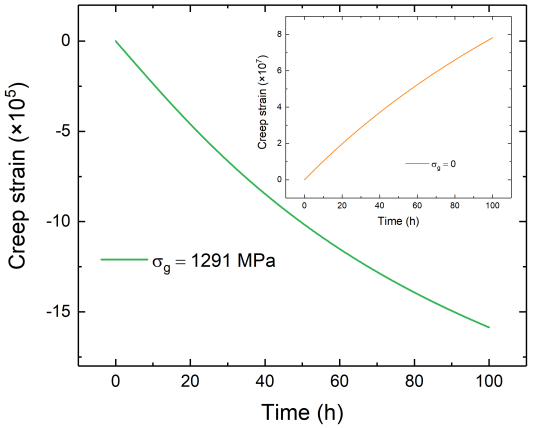

(f) Creep strain at the center of the substrate

Figure 4.12 Effect of growth stress in AlN coatings: evolution of (a, c, e) normal stress and (b, d, f) creep strain at the center position of (a, b) top coating, (c, d) bottom coating and (e, f) substrate; circles and triangles represent the thermoelastic stresses ($\sigma_{0,HT}$) and stresses at ambient temperature respectively.

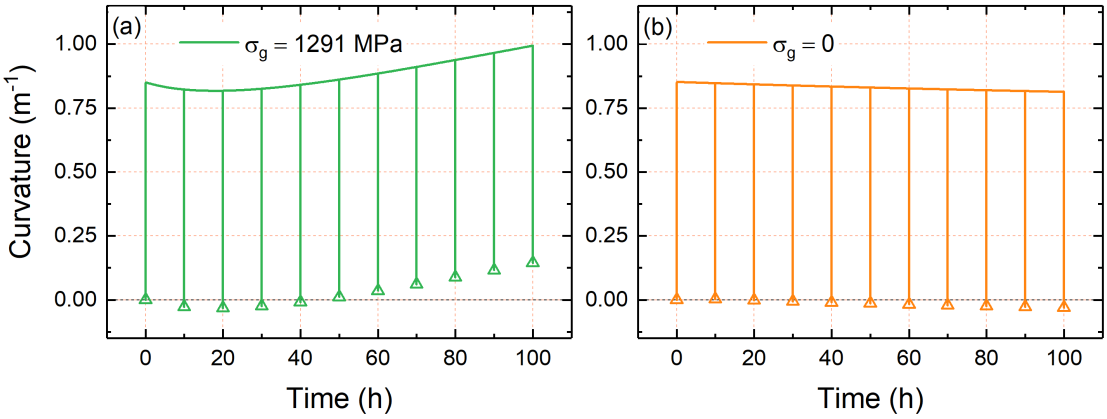

Figure 4.13 Evolution of the curvature of the system calculated (a) with and (b) without consideration of intrinsic CVD growth stress in the AlN coating; triangles represent the curvature at ambient temperature.

In the thick substrate, due to the temperature distribution along the z direction (temperature difference of 97 °C, see Figure 4.8) and the Norton's creep power law, the creep strain is more pronounced in the upper part of the substrate (z>0). After the first thermal cycle, the creep stain in the lower part of the substrate (z<0) is almost negligible, whereas it has a value of around 10^{-4} in the upper part (red curve in Figure 4.14(f)). This non-uniform distribution of creep strain induces a stress relaxation in the upper part of the substrate but a slight increase of stress in the lower part (green and red curves in Figure 4.14(e)). The stress tends to be uniformly distributed in the substrate (red curve in Figure 4.14(e)). Such a decrease of the stress gradient in the substrate leads to the relaxation of the system. This is supported by the larger decrease of bending curvature (Figure 4.13(a)) at the early stage of thermal cycling compared with the case of σ_g=0 (Figure 4.13(b)).

As time extends, the stress relaxation continues in the upper part of the substrate, while the stress increase also continues to take place in the lower part. The stress distribution slope reverses from negative to positive, whereas it remains negative in the case of σ_g=0 (not presented here). The reversal of stress distribution slope, however, strengthens the asymmetry of the system. Therefore, the bending curvature increases to maintain the system equilibrium, which explains the curvature evolution shown in Figure 4.13(a).

The above discussions reveal the different behavior between the upper and lower part of the substrate. Therefore, the evolution of stress and creep strain at the center of the substrate shown in Figures 4.12(e) and 4.12(f) cannot represent the global stress evolution within the substrate. The evolution of stress and creep strain in the substrate at interfaces (z=±0.5 mm) are investigated (Figure 4.15). As previously discussed, at AlN top coating/substrate interface (z=0.5 mm), creep strain is rapidly increased due to the higher temperature (orange curve in Figure 4.15(b)), leading to a large stress relaxation (orange curve in Figure 4.15(a)). The stress relaxation decreases the creep strain rate, which in turn, also reduces the stress relaxation. Such a negative feedback leads to a

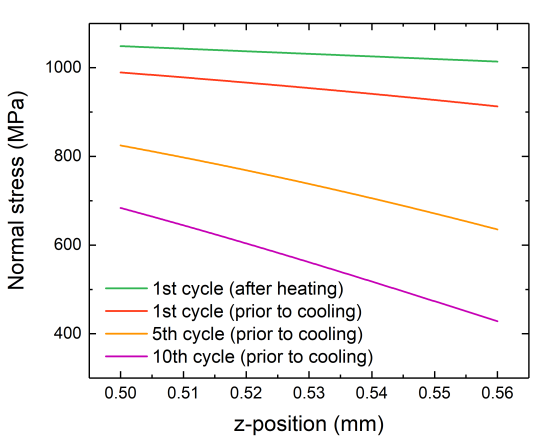

(a) Stress distribution in AlN top coating

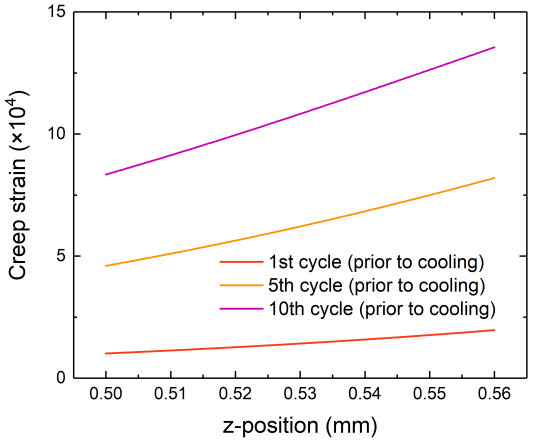

(b) Creep strain distribution in AlN top coating

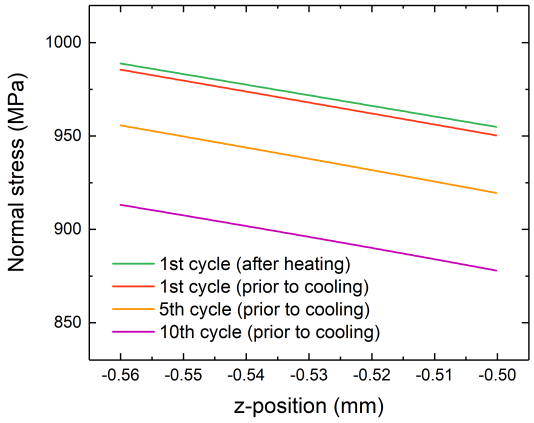

(c) Stess distribution in AlN bottom coating

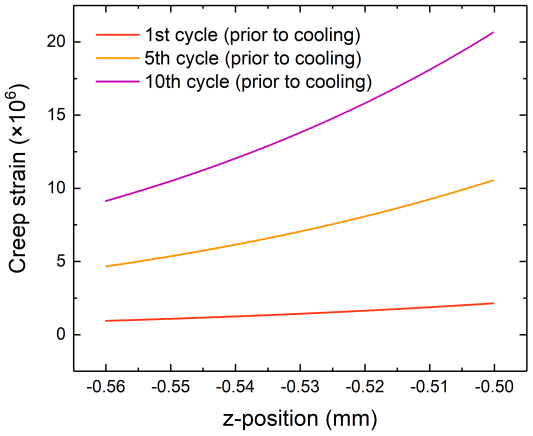

(d) Creep strain distribution in AlN bottom coating

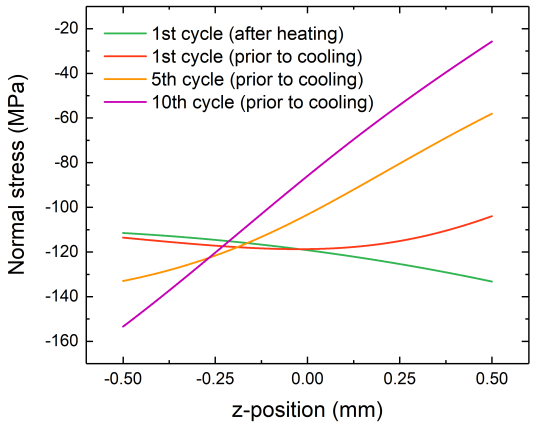

(e) Stress distribution in the substrate

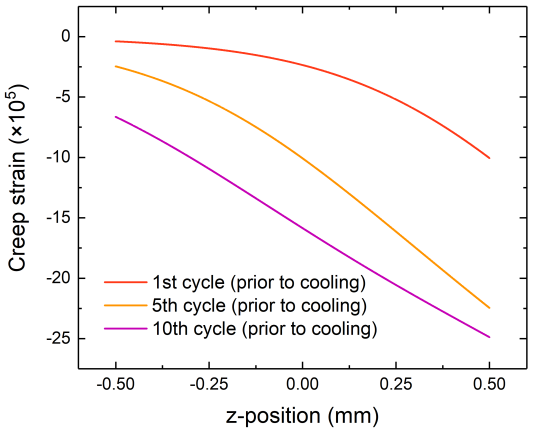

(f) Creep strain distribution in the substrate

Figure 4.14 Evolution of distribution of (a, c, e) normal stress and (b, d, f) creep strain fields at the center of (a, b) top coating, (c, d) bottom coating and (e, f) substrate.

saturation of creep strain.

On the contrary, at the AlN bottom coating/substrate interface (z=-0.5 mm), the stress accumulation results in an increase of creep strain rate (Norton's creep power law). As time extends, the development of creep strain accelerates, resulting in an accumulation of stress (green curves in Figure 4.15). As a result, the asymmetry of the system is enhanced, as observed in Figure 4.24(a), the curvature increases with thermal cycles.

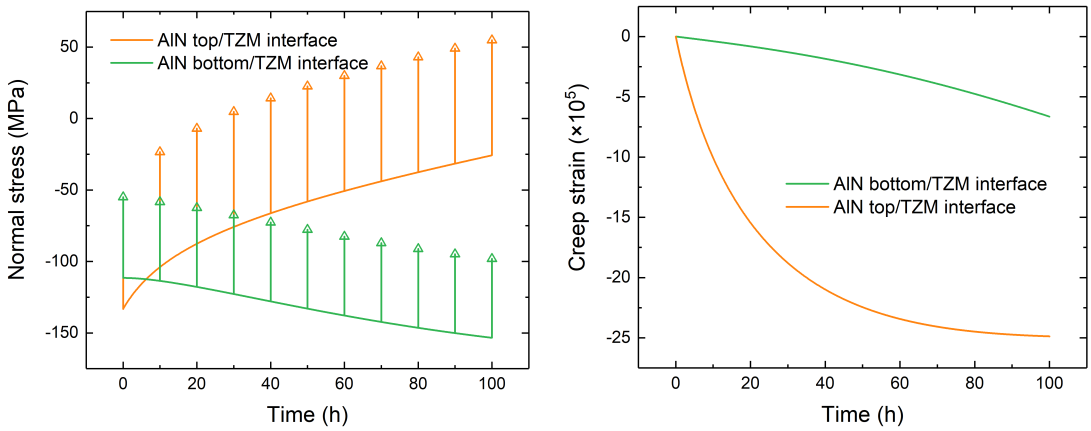

(a) Stress in the substrate at interfaces (z=±0.5 mm)

(b) Creep strain in the substrate at interfaces (z=±0.5 mm)

Figure 4.15 Evolution of (a) normal stress and (b) creep strain at the coating/substrate interfaces; triangles represent stresses at ambient temperature.

To conclude, the stress evolution within the system during thermal cycling is a complex function of various parameters involving the thermomechanical properties of materials, temperature difference due to the imposed heat flux and intrinsic growth stress in AlN coatings. Generally, the high temperature thermoelastic stress in the system and the temperature difference determine the early stage of creep deformation. In AlN coatings, the creep deformation cannot fully relax the intrinsic growth stress. The stress distribution is almost linear regardless of high temperature exposure time (Figures 4.14(a) and 4.14(c)). In the thick substrate, the larger temperature difference leads to different stress and creep strain evolutions in its upper and lower part. The system asymmetry is thus strengthened, resulting in an increase of curvature with the number of cycles.

4.3.2 Complete model: growing oxide scales

To further study the stress evolution during thermal cycling, oxidation is taken into account in the following analysis. The intrinsic CVD growth stress of 1291 MPa in AlN coatings are also considered. Thermomechanical properties of Al_2O_3 are summarized in Table A.3.3. In Chapter 3, we found a linear oxidation kinetics (parameters listed in Table A.3.3) for AlN in the temperature range of 800-1100 °C. Herein, the lateral strain of oxide scale is fixed as 0.1% (see section 'High temperature oxidation' on Page 94). An external thickening of oxide scales

is also assumed in the current analysis, i.e., the new oxide is formed on the external surface of the already grown oxide scale. This section helps to understand how the exchange of thickness between oxidizing coating and the growing oxide scale alter the evolution of stress within the system.

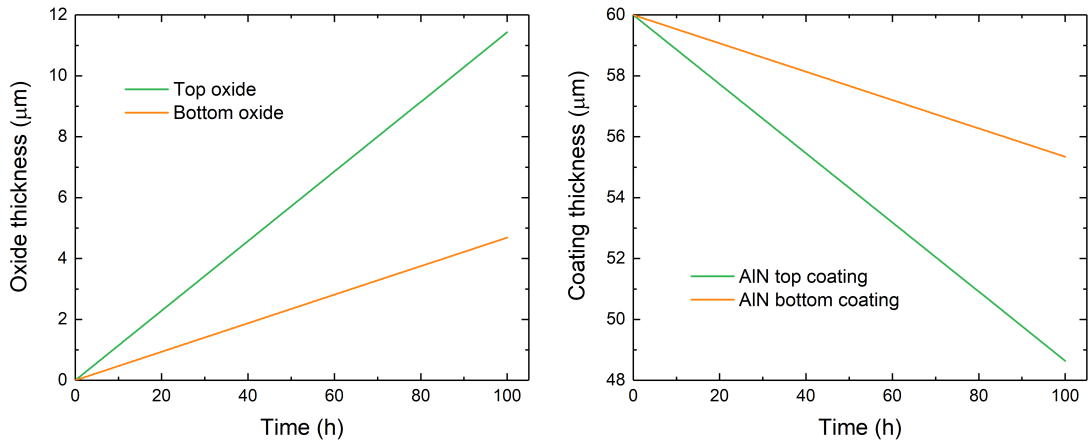

(a) Thickness of the oxide scales versus time. (b) Thickness of the AlN coatings versus time

Figure 4.16 Thickness of the oxide scales and AlN coatings during thermal cycling on the top and bottom surfaces of the system.

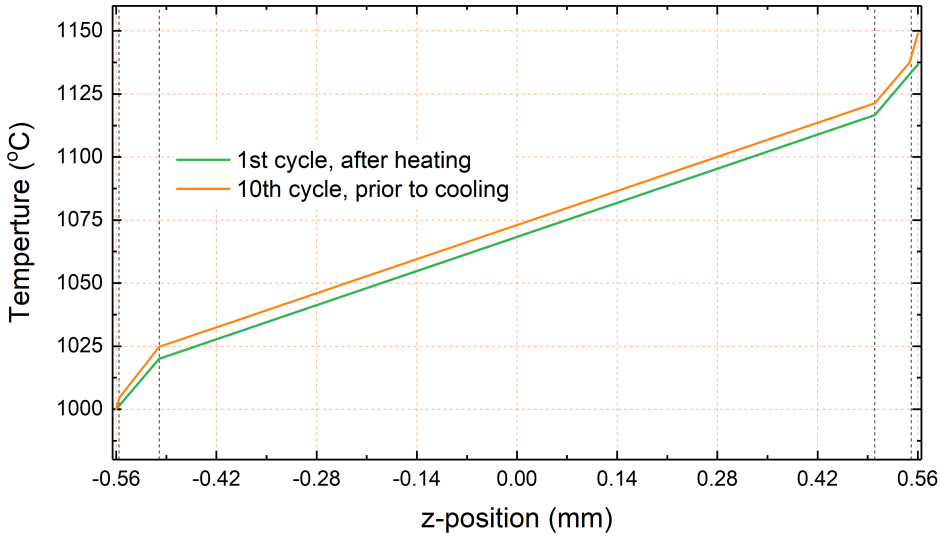

Figure 4.17 Temperature redistribution due to the oxidation of AlN coatings.

The thickness of the oxide scales and coatings versus time are presented in Figure 4.16. Due to the temperature difference, the oxide growth rate at the top surface of the system is 2.5 times higher than that at the bottom surface. The thickness exchange factor (from AlN to Al_2O_3, Eq.(4.14)) is around 1.01. Therefore, the increase of the total thickness of the system is not significant. However, the transformation from thermal conductive AlN to Al_2O_3 leads to a redistribution of the temperature field and related thermal strain field during thermal cycling. As illustrated in Figure 4.17, the temperature in both coatings

and substrate increases with the time. The temperature at the top surface of the system is 12 °C higher after 8 thermal cycles. According to the Norton's creep power law, the creep strain field is also redistributed due to this structure evolution.

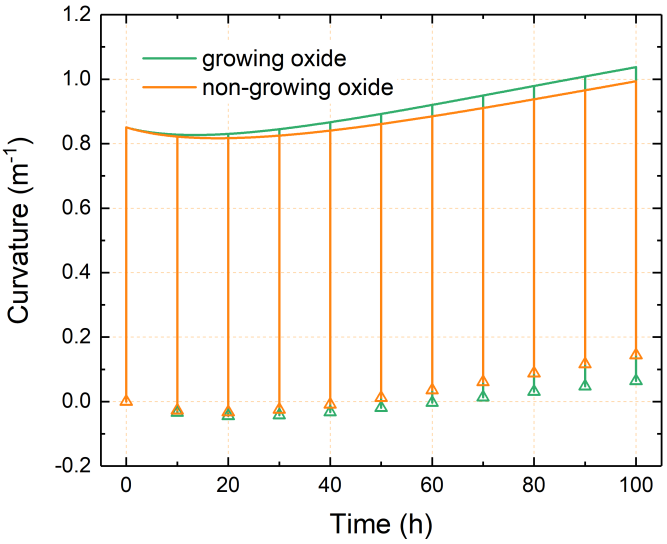

Figure 4.18 Curvature evolution of the system taking into account the high temperature oxidation of AlN coatings; the curvature evolution without consideration of oxidation (orange curve) has been already presented in Figure 4.13(a). Triangles represent the curvature at ambient temperature.

Figure 4.18 presents the evolution of bending curvature with and without consideration of the high temperature oxidation of AlN coating. Both two curvature decreases and increases subsequently with increasing time. This indicates that the stress gradient in the thick substrate is strengthened according to previous discussions (see Case II in section 4.3.1). In particular, while oxidation is taken into account in the simulation (green curve in Figure 4.18, the increase of curvature is accelerated and the negative increment of curvature from high temperature to ambient temperature, $\Delta\frac{1}{r}|_{HT\rightarrow T_{amb}}$, raises with increasing thermal cycles.

In order to understand the curvature evolution, we herein investigate the evolution of stress and creep strain within the system. Stresses in the substrate at both center and interfaces are all presented because the high temperature difference in the substrate induces a different behavior between its upper and lower part (see Case II in section 4.3.1). In the oxide scales and AlN coatings, we only illustrate the stress and creep strain evolutions at the oxide/coating and coating/substrate interfaces respectively. The t_{oxide}=0 in Figure 4.19 is used to illustrate the evolution without taking into consideration the oxidation of coatings (Case II in section 4.3.1).

As previously presented (section 4.3.1), the applied thermal load leads to a deformation of the coating system. Both AlN coatings and substrate undergo creep deformation. Simultaneously, very thin oxide scales develop asymmetrically

on the front-side and backside of the system resulting from the temperature difference (Figure 4.16(a)). Compressive stresses (-515 MPa) are introduced in the oxide scales due to their lateral expansion and the constraint by the system. The decrease rate of curvature is reduced so that the system continuity could be maintained. Subsequently, the already grown oxide scales are subjected to creep. As time extends, creep strains develop in the top (z>0) and bottom (z<0) oxides and leads to a stress relaxation in both oxide scales as shown in Figure 4.19(b). The development and accumulation of creep strain in the top oxide scale is more significant ($\sim 10^{-3}$). Stress in the top oxide is rapidly relaxed to near 0 and reverses afterwards from compressive to tensile. The corresponding creep strain is thus slightly decreased as illustrated (green curve in Figure 4.19(b)). In the bottom oxide, the creep strain is smaller at the beginning and the stress relaxation is slower. Moreover, the development of oxide scales results in a redistribution of the temperature field (Figure 4.17). Therefore, the thermal strain field is also redistributed along the z direction. Then, the competition between the growth of new oxides, redistribution of thermal strain field and creep deformation of materials decrease the relaxation rate of curvature.

Globally, the stresses and creep strains in both AlN coatings and substrate are almost unaffected by the presence of growing oxide scales (Figure 4.19(c)-(h)). Stress in both the top and bottom coatings are relaxed throughout the thermal cycling. Creep strain in the top coating is nearly two order of magnitude larger than that in the bottom coating due to the higher temperature, resulting in a faster stress relaxation in the top coating. In the thick substrate, as already seen in section 4.3.1 (Case II), fast stress relaxation and creep saturation takes place at the AlN top coating/substrate interface, while stress accumulation and acceleration of creep strain development are observed at the AlN bottom coating/substrate interface. The slope of stress distribution is also reversed from negative to positive (not presented here), and the stress gradient in the system is further strengthened (Figure 4.19(g)). This phenomenon, in together with the asymmetric oxide growth discussed above, accelerate the curvature increase and further enhance the system asymmetry. The higher curvature, however, gives rise to a slightly slower stress relaxation in AlN coatings but faster in substrate (∼10 MPa).

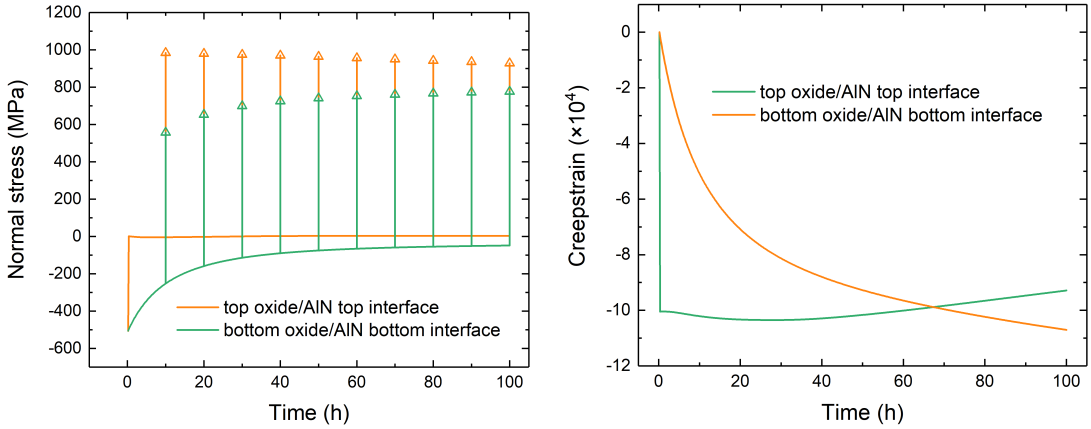

(a) Stress in the oxide scales at oxide/coating interface

(b) Creep strain in the oxide scales at oxide/coating interface

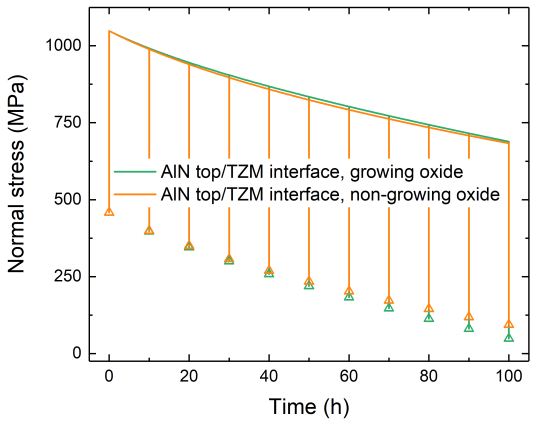

(c) Stress in the coating at AlN top coating/substrate interface

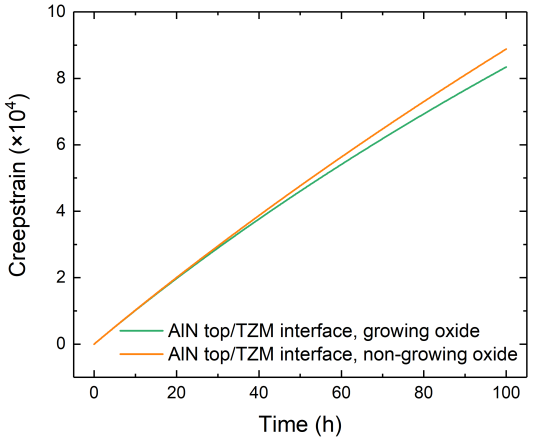

(d) Creep strain in the coating at AlN top coating/substrate interface

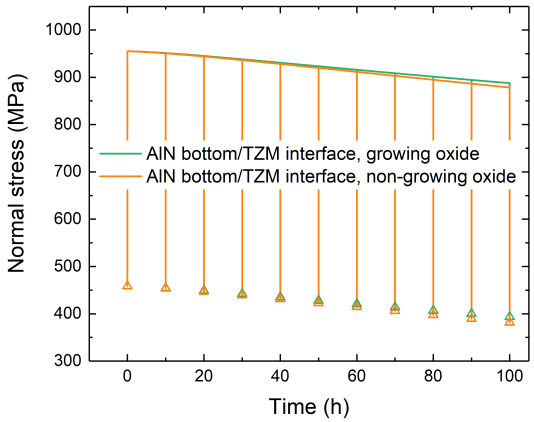

(e) Stress in the coating at AlN bottom coating/substrate interface

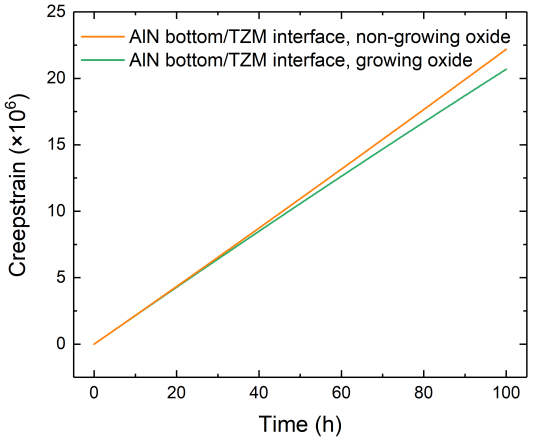

(f) Creep strain in the coating at AlN bottom coating/substrate interface

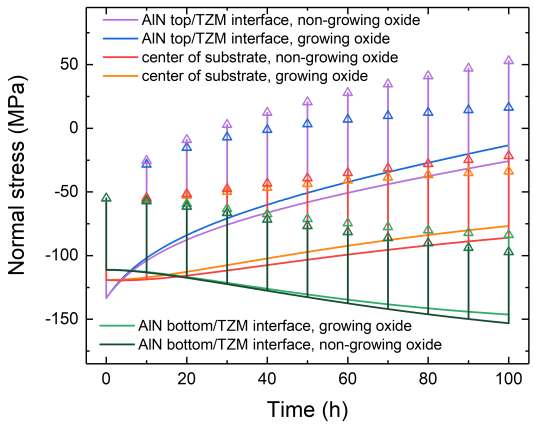

(g) Stress in the substrate

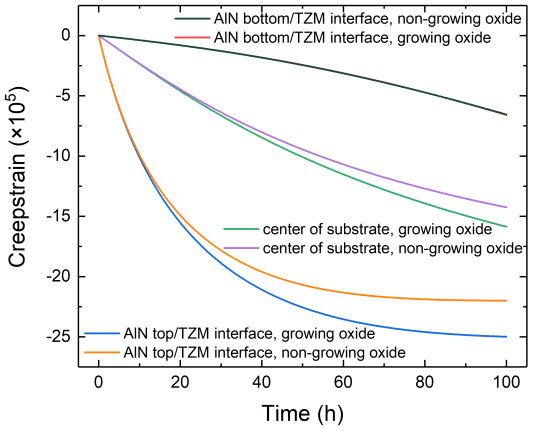

(h) Creep strain in the substrate

Figure 4.19 Effect of high temperature oxidation: evolution of (a, c, e, g) normal stress and (b, d, f, h) creep strain in (a, b) oxide scales at oxide/AlN coating interface, (c, d, e, f) AlN coatings at (c, d) AlN top coating/substrate and (e, f) AlN bottom coating/substrate interfaces; and (g, h) the substrate; triangles represent stresses at ambient temperature.

Notably, stresses at ambient temperature are mainly determined by the difference of thermal expansion coefficients between the oxide scales, coatings and substrate. As the thermal expansion coefficient of Al_2O_3 is larger than that of AlN and TZM, large tensile stress is generated in the oxide scales at high temperature. Although perfect bonding between two adjacent layers during the thermal cycling is assumed in our analytic model, the magnitude of stress in the oxide scales indicates that the oxide layers undergo tensile cracking and/or delamination at ambient temperature.

The current analysis reveals the dominance of the formation of oxide scales on the evolution of stress and curvature during the early stage of thermal cycling. The following competitions between oxidation, temperature redistribution and creep relaxation lead to a decrease of the relaxation rate of curvature. Creep deformation of materials dominates the stress evolutions. The curvature is subsequently increased due to the continuous asymmetric oxide growth and the change from negative stress distribution to positive in the substrate. This analysis also highlights the huge tensile stresses in the oxide scales at ambient temperature (1198 MPa in the top oxide scale). Such large stresses may induce cracks, interfacial delamination and/or spallation of oxides at ambient temperature. This phenomenon suggests that the design of a multilayer system should take into account materials with close thermal expansion coefficients. In conclusion, analyses made in this section and section 4.3.1 examined the stress evolution during thermal cycling with respect to a TZM substrate coated with AlN coatings on both surfaces, and reveal that:

1. the use of instantaneous thermal expansion coefficients can improve the accuracy of the model;

2. creep deformation of materials relaxes the system despite the lack of consideration of intrinsic growth stress in the coatings and the high temperature oxidation. Moreover, the temperature difference induces different creep strain evolution in the coatings;

3. intrinsic growth stress in the coatings enhances the asymmetrical evolution of stresses in the system. The coatings and substrate creep faster. However, the different stress evolution in the upper and lower part of the substrate strengthens the asymmetry of the system;

4. high temperature oxidation results in an exchange of thickness between the coatings and oxide scales. The asymmetric oxidation on the front-side and the backside of the system further enhances the system asymmetry. Nevertheless, the large tensile stress in the oxide scales at ambient temperature limits the application of AlN as a high temperature coating (T>1000 °C).

4.4 Effects of individual factors

In order to estimate the thermomechanical behavior of AlN coatings under solar radiation, and to further investigate their lifetime (or durability) for the

use of solar receivers, the effect of extrinsic (heat flux, temperature) and intrinsic (initial coating stress and properties) factors in the daily operation should be individually studied. Herein, the effect of the thermal conditions (temperature gradient, temperature of heat transfer fluid), intrinsic growth stress from CVD in AlN coatings, creep properties of materials, oxide scale growth kinetics (linear and parabolic) on the stress evolution are respectively investigated. For the sake of clarity, the modeling conditions listed in Table 4.5 are called 'standard' in the following analysis. Material properties in Tables 4.3, A.3.1 and A.3.3 are also adopted as 'standard' properties. The evolution of curvature, stress and creep strain of the 'standard' modeling conditions are represented by orange curves in sections 4.4.1 to 4.4.5. Moreover, the stress evolution are studied only at three positions: (1) in the top oxide scale at oxide/AlN interface, (2) in AlN top coating at coating/substrate interface and (3) at the center of the substrate.

Table 4.5 'Standard' modeling conditions used.

Conditions	**Values**
Heat flux ($MW{\cdot}m^{-2}$)	1
Temperature at the bottom surface of the system (°C)	1000
Intrinsic CVD growth stress in AlN coatings (MPa)	1291
Oxidation kinetics	linear
Lateral strain in oxide scales	0.1%

4.4.1 Effect of heat flux

The value of heat flux, q, is varied from 0.5 to 10 $MW{\cdot}m^{-2}$ to illustrate the effect of temperature gradients on the stress evolution. The q=0.5, 1 and 10 $MW{\cdot}m^{-2}$ are adopted to represent the low, medium (realistic) and extremely high thermal load during thermal cycling.

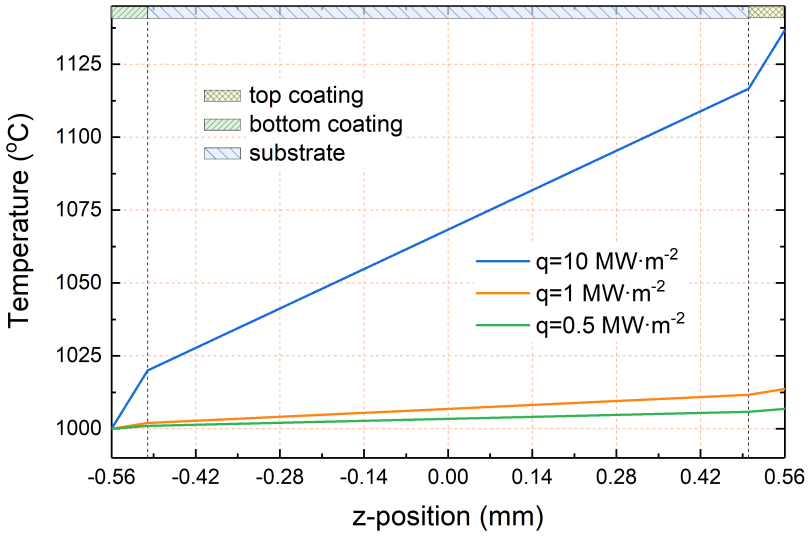

Figure 4.20 Temperature distribution along the z direction when the system is initially subjected to a thermal load.

As shown in Figure 4.20, the initial temperature difference (just after heating in the first cycle) in the system is 137, 14 and 7 °C for a heat flux of 10, 1 and 0.5 MW·m^{-2} respectively. It should be reminded here that the temperature difference within the system has a strong effect on the evolution of stress, creep strain and oxide growth, as depicted in Figures 4.16 and 4.19. The large temperature difference (q=10 MW·m^{-2}) gives rises to the asymmetrical evolution of stress and creep strain in the substrate as previously discussed. By contrast, the overall temperature difference is negligible (less than 15 °C after 10 thermal cycles) when the imposed heat flux is low (≤1 MW·m^{-2}). The corresponding difference of creep strain rate is also reduced in each individual layer, and the stress evolutions on both side of the system are almost symmetric. Therefore, stresses at the aforementioned three positions (Figure 4.21) can represent the stresses in oxide scales, coatings and substrate respectively.

Table 4.6 Thickness of the top oxide scales after 100 h of thermal cycling.

Heat flux, q (MW·m^{-2})	**Top oxide thickness (μm)**
10	11.4
1	5.2
0.5	4.9

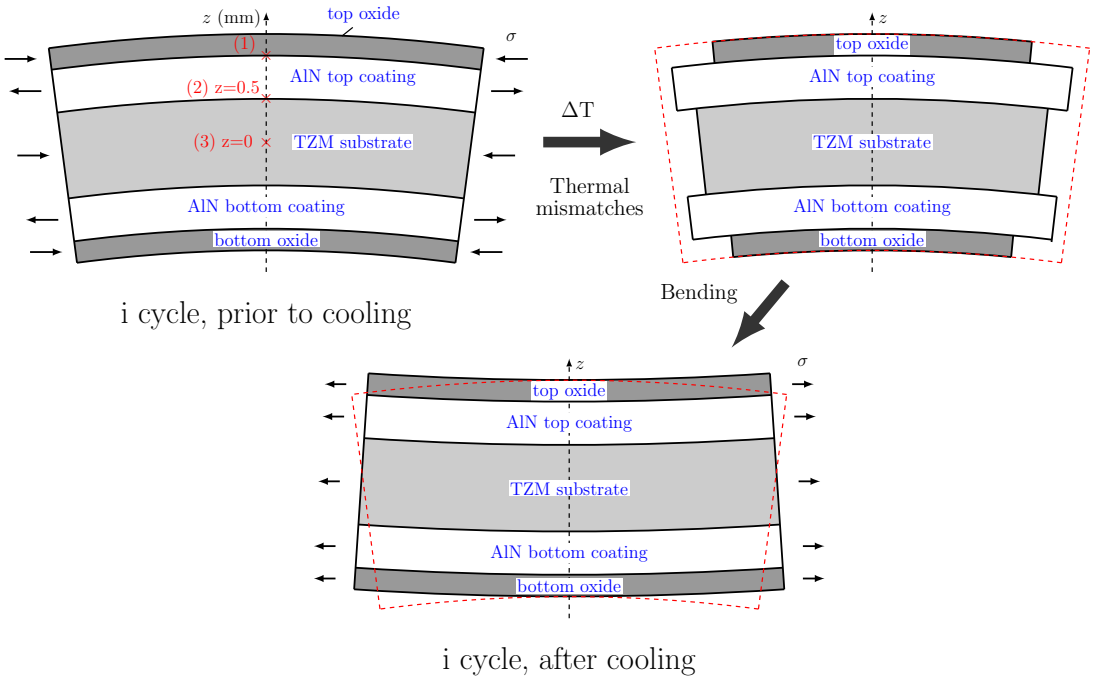

Figure 4.21 Schematic representation showing the curvature variation due to temperature change from high temperature to ambient temperature; red dashed line represents the structure of the system prior to cooling in i cycle; (1), (2) and (3) indicate the three representative positions mentioned above.

Figure 4.22(a) shows the evolution of the bending curvature. Regardless of the imposed heat flux, the curvature decreases at the beginning of thermal cycling and then increases with time. The lower the imposed heat flux is, the later the curvature increase takes place. However, the curvature variation is not obvious for the medium and low heat fluxes (orange and green curves). The curvatures remain nearly constant throughout the thermal cycling with a low value (of less than 0.1 m^{-1}). Indeed, as shown in previous sections (Case II in section 4.3.1 and section 4.3.2), the stress relaxation in the upper part of the substrate is faster than that in the lower part due to a higher temperature and a corresponding larger creep strain even with a very small initial temperature difference. Stress gradient are firstly reduced and is then enhanced for the three heat fluxes investigated (not presented here), which is consistent with the decrease and the subsequent increase of curvature.

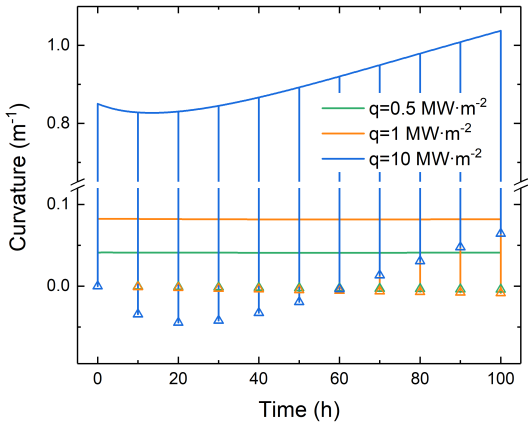

(a) Curvature

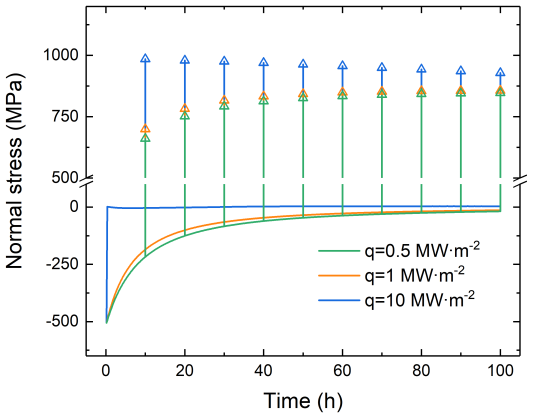

(b) Stress in oxide at oxide/AlN top coating interface

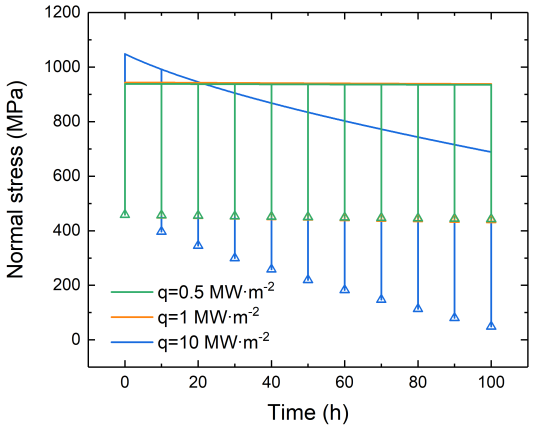

(c) Stress in coating at AlN top coating/substrate interface

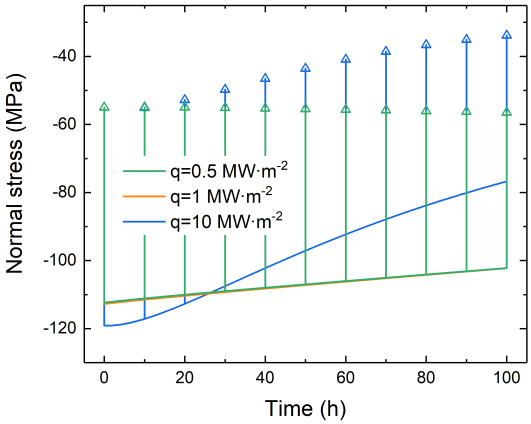

(d) Stress at the center of the substrate

Figure 4.22 Effect of heat fluxes on (a) evolutions of the curvature, and stress evolutions at (b) oxide/AlN top coating interface (on oxide side), (c) AlN top coating/substrate interface (on coating side) and (d) the center of substrate; triangles represent the curvature and/or stresses at ambient temperature.

Moreover, it is observed that the curvature increment during the cooling stage,$\Delta\frac{1}{r}|_{HT\rightarrow T_{amb}}$, increases with increasing time regardless of heat fluxes investigated. This can be explained by thicker oxide scales (compared to the last thermal cycle). The change of curvature during the cooling stage is due to the large temperature change and the enhancement of inevitable thermal strain mismatches (see Case I in section 4.3.1). As shown in Figure 4.21, the high thermal expansion coefficient of Al_2O_3 gives rise to larger compressive thermal strain during the cooling stage of the i thermal cycle. To maintain the system equilibrium, the curvature decreases or reverses from positive to negative to introduce additional compressive stress in the upper part (z>0) of the system and tensile stress in the lower part (z<0). Theses stresses are proportional to the curvature increment $\Delta\frac{1}{r}|_{HT\rightarrow T_{amb}}$. As the oxidation of Al_2O_3 is linear, the thickness of the oxide scales is much larger prior to cooling in i+1 cycle (Figure 4.16(a)). The thermal strain mismatches within the system are therefore enhanced. The introduction of the same quantity of stress as in the i cycle will induce a disequilibrium in the system. As a result, $\Delta\frac{1}{r}|_{HT\rightarrow T_{amb}}$ increases to compensate the introduced bending stresses so that the mechanical equilibrium of the system can be achieved.

Figure 4.22(b) shows the similar stress evolutions in the top oxide scales for heat fluxes of 1 and 0.5 MW·m^{-2}, while stress is strongly relaxed with a heat flux of 10 MW·m^{-2}. This can be explained by the higher oxidation temperature, which induced higher creep relaxation in the oxide scales according to the Norton's creep power law (see sections 4.3.1 and 4.3.2). In the AlN top coating, stresses evolve nearly elastically (around 930 MPa) with a low heat flux ($\leq$1 MW·m^{-2}) as shown in Figure 4.22(c). When the imposed heat flux is high, the higher temperature in the top coating gives rise to higher creep strain and a more significant stress relaxation. Same trends have been observed for stress at the center of substrate (Figure 4.22(d)). Moreover, for heat fluxes of 1 and 0.5 MW·m^{-2}, the stress gradient within the thick substrate is negligible, while a high heat flux of 10 MW·m^{-2} results in a complex evolution of stress field in the substrate (Figure 4.19(g) in section 4.3.2).

In conclusion, the value of imposed heat flux has a strong effect on the evolution of curvature and stress during thermal cycling. A high value of heat flux results in a high temperature difference, which leads to different stress evolutions in the upper and lower part of the system (section 4.3.2). For low heat fluxes, the temperature difference within the system can be neglected, as shown in Figure 4.20. The oxidation and the stress evolution are nearly identical on both sides of the system. The curvature evolution is less significant. Therefore, the evolution of stress within the system is mainly controlled by the creep relaxation of materials. Stresses in the coatings and substrate evolve nearly elastically during the thermal cycling, whereas stresses in the oxide scales are relaxed towards zero.

4.4.2 Effect of temperature at the bottom surface of the system

As previously discussed, the temperature plays an important role on the oxidation of AlN coatings, thermal expansion mismatches, as well as the creep

behavior of materials. Therefore, to further understand the effect of thermal conditions in solar receivers, it is instructive to study how the targeted temperature of heat transfer fluid, i.e., the temperature at the bottom surface of the system, alters the stress evolution during thermal cycling. The heat flux is considered to be constant with a value of 1 $MW{\cdot}m^{-2}$ in the following analysis. In such a case, the initial temperature difference within the system is only 14 °C. The features of stress are almost similar about the mi-plane of the system (see section 4.4.1).

Three different temperatures, 900, 1000 and 1100 °C, are selected in the current analysis to illustrate the influence of temperature at the bottom surface of the system (T_b). The curvature evolution is strongly affected by the heat transfer fluid temperature as shown in Figure 4.23(a). For T_b of 900 °C, the curvature slightly increases throughout the cycling and tends to be stable at the end. However, the curvature relaxes and subsequently raises as presented before for T_b of 1000 and 1100 °C. For T_b=1100 °C (green curve in Figure 4.23(a)), the increase of curvature is earlier and faster. Indeed, while increasing T_b, despite the insignificant temperature difference in the system, the reduce of stress gradient in the thick substrate is accelerated due to the larger creep strain. Stresses are rapidly redistributed, leading to the sign change of the stress distribution slope. Stress gradient is subsequently enhanced as discussed previously. However, for low T_b (900 °C), the stress gradient in the substrate reduction is insignificant (the magnitude of creep strain is two order smaller). Therefore, the increase of curvature is mainly due to the asymmetric transformation of AlN to Al_2O_3.

Table 4.7 Temperature at the top surface of the system and the thickness of the top and bottom oxide scales after 10 thermal cycles.

T_b (°C)	T_t (°C)	Thickness (μm)	
		Top oxide	Bottom oxide
900	914	2.4	2.1
1000	1014	5.2	4.7
1100	1115	10.0	9.2

Figures 4.23(b) to 4.23(d) show the stress evolutions at the three representative positions. As expected, the high T_b leads to the fast stress relaxations in each individual layer because of temperature dependence of creep strain rate. These findings are consistent with the discussions given before. It is interesting to note that stress in the oxide scale relaxes for T_b of 1000 °C while the evolutions of that in both AlN top coating and substrate remains nearly elastic. This can be explained by the better creep resistance of AlN and TZM. Nevertheless, the faster relaxation of stress, however, results in larger tensile stress at ambient temperature.

This section reveals that for a given thermal gradient (q constant), the higher the targeted temperature of heat transfer fluid (T_b) in a solar receiver is, the more rapid the linear growth of oxide scales becomes. As a result, the curvature increase is more significant. As the creep deformation is strongly related to the temperature (Norton's power law), low T_b can reduce the stress relaxation in the

oxide scales, which in turn, decreases their tensile stresses at ambient temperature (green points in Figure 4.23(b)).

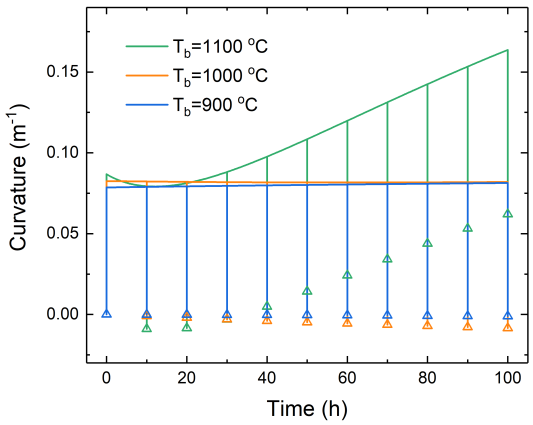

(a) Curvature

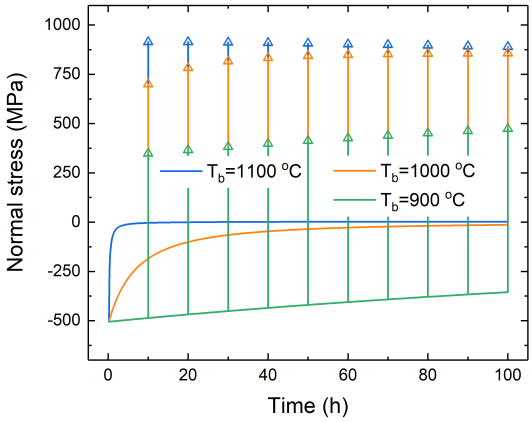

(b) Stress in oxide at oxide/AlN top coating interface

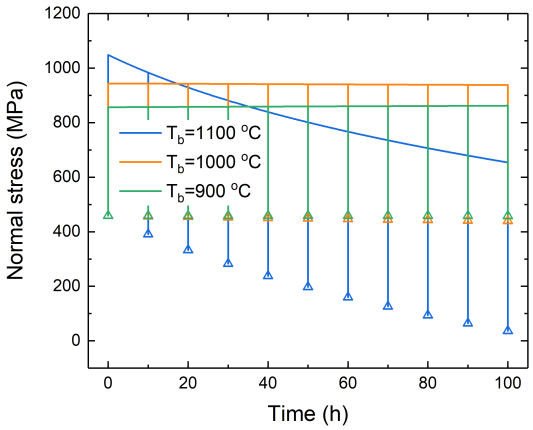

(c) Stress in coating at AlN top coating/substrate interface

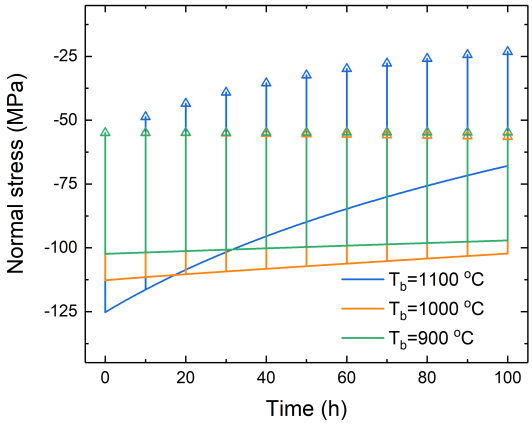

(d) Stress at the center of the substrate

Figure 4.23 Effect of temperature at the bottom surface on (a) evolutions of the curvature of the system, and stress evolutions at (b) oxide/AlN top coating interface (on oxide side), (c) AlN top coating/substrate interface (on coating side) and (d) the center of substrate; triangles represent the curvature and/or stresses at ambient temperature.

The analyses in this section and section 4.4.1 discussed the effect of thermal conditions in daily operation. In conclusion, the variations of curvature are not only determined by the temperature difference (related to imposed heat flux), but the temperature in the material (which determines the creep strain and oxidation rate) as well. In general, employment of a low to medium heat flux and/or a low to medium heat transfer fluid temperature helps in maintaining the curvature in an acceptable interval (<0.1 m^{-1}) in the duration investigated (100 h). The calculations also reveal that stress in oxide scale is one of factors that determined the lifetime of the system. In spite of small thermal mismatches between AlN, TZM and Al_2O_3, cooling at the end of each thermal cycle gives rise

to a reversal of stress in oxide from compressive to tensile. The stress relaxation at high temperature, however, leads to an increase of tensile stress in the oxide at ambient temperature with increasing thermal cycles. In case of the 'standard' thermal conditions (q=1 $MW \cdot m^{-2}$ and T_b=1000 °C), the curvature remains nearly constant and stresses in individual layers are mainly controlled by their creep behaviors.

4.4.3 Effect of intrinsic growth stress in the AlN coating

In an attempt to further investigate the durability of AlN coating and characterize its lifetime under solar radiation, we now focus on the effect of intrinsic growth stress arising from the deposition, which is related to the microstructure of the AlN coating, and therefore can be controlled by the deposition conditions. In this section, the intrinsic CVD growth stress, σ_g, is ranged from 430 to 1291 MPa. The 'standard' thermal conditions are also adopted. Figure 4.24 summarizes the evolution of curvature and stresses at the three representative positions under the influence of intrinsic CVD growth stress. Figures 4.24(a) and 4.24(b) show that the evolution of curvature and stress in the oxide scale are almost unaffected. The general feature of the variation of curvature is determined by the evolution of stress gradient in the thick substrate as explained in previous sections (sections 4.4.1 and 4.4.2). The small difference observed after 10 thermal cycles is related to the creep mismatches between the fast-creeping Al_2O_3 and the slow-creeping {coatings+substrate}. Figure 4.25 illustrates how such creep mismatches affects the curvature evolution:

(1) compressive stresses in the oxide scales generates large creep strains as Al_2O_3 creeps much faster;

(2) creep strains in the {coatings+substrate} are much smaller;

(3) creep strains in the AlN coatings and substrate have the same magnitude but the opposite sign.

The bending curvature slightly varies around 0.083 m^{-1} to maintain the system equilibrium. With a higher intrinsic CVD growth stress in coatings, stresses in both AlN coatings and substrate are higher, which results in larger creep strains. The creep mismatches between the oxide scales and {coatings+substrate} is enhanced but this enhancement is not significant. As a result, the curvature relaxation is only slightly enhanced at the beginning of thermal cycling.

Figures 4.24(c) and 4.24(d) show that the intrinsic stress only influence the thermoelastic response of the system. This is because, as discussed above, the creep strain in the {coatings+substrate} are very small ($\sim 10^{-5}$). The shifts of high temperature thermoelastic stresses in coatings and substrate remain almost constant till the end of thermal cycling for the three values of intrinsic CVD growth stress investigated.

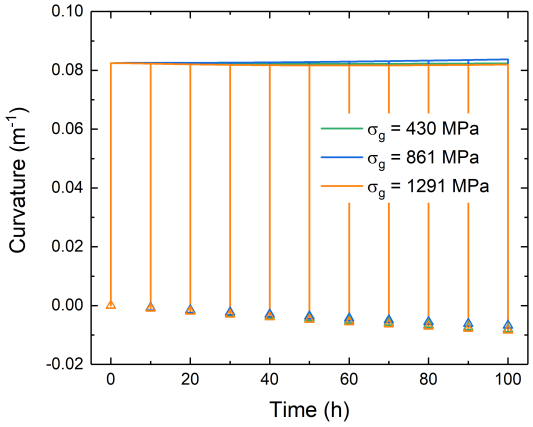

(a) Curvature

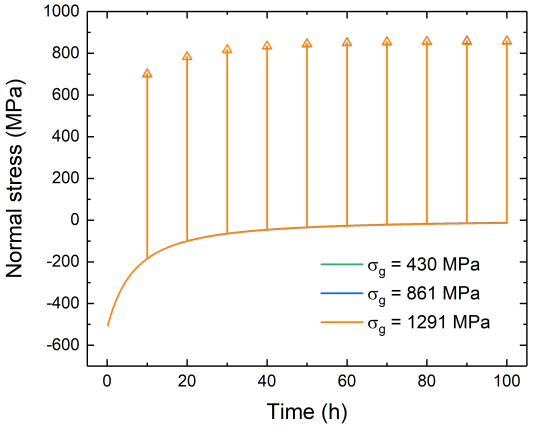

(b) Stress in oxide at oxide/AlN top coating interface

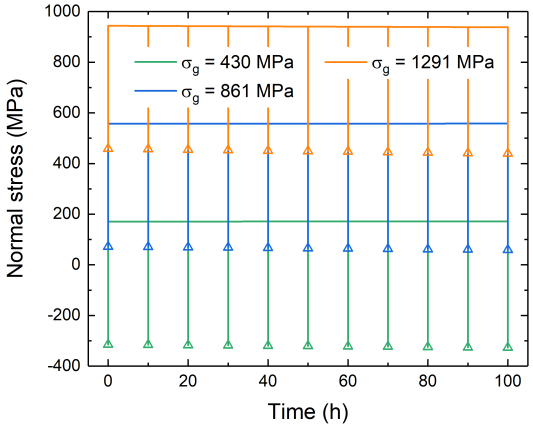

(c) Stress in coating at AlN top coating/substrate interface

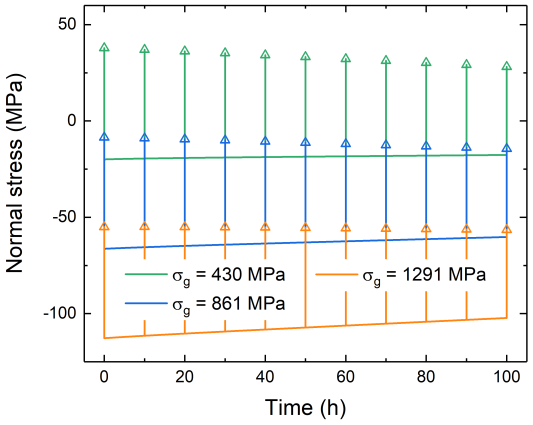

(d) Stress at the center of the substrate

Figure 4.24 Effect of intrinsic CVD growth stress in AlN coatings on (a) evolutions of the curvature of the system, and stress evolutions at (b) oxide/AlN top coating interface (on oxide side), (c) AlN top coating/substrate interface (on coating side) and (d) the center of substrate; triangles represent the curvature and/or stresses at ambient temperature.

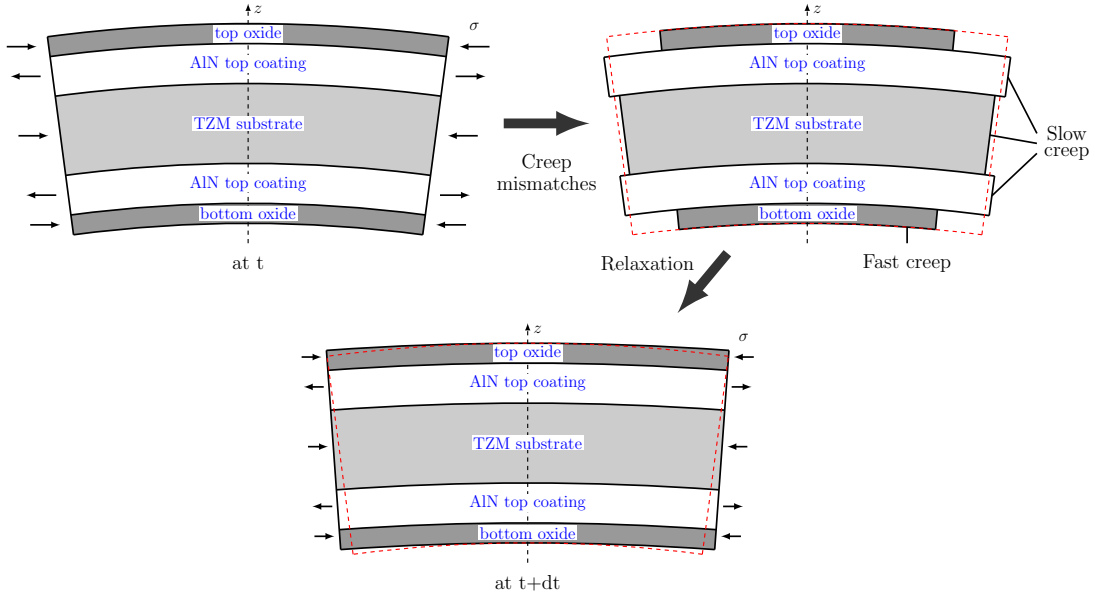

Figure 4.25 Schematic representation showing the curvature variation due to creep mismatches between the oxide scales and the {coatings+substrate}; red dashed line represent the structure of the system at time t.

4.4.4 Effect of creep deformation

As shown in the previous section, the stress evolution in individual layers is predominately affected by the creep relaxation of materials. In order to better understand the effect of creep deformation, the creep behavior in the oxide scales, the substrate, and the coatings are respectively studied in the following sections.

Effect of creep in oxide scale

The oxide is assumed to be elastic (without creep deformation, A_o=0) in this analysis. The curvature and stress evolutions are compared with the realistic case (A_o=6.472×10^6 $MPa^{-n}{\cdot}s^{-1}$). As shown in Figure 4.26(a), the evolution of curvature is almost unaffected by the creep properties of the oxide. This is in agreement with previous discussions:

(1) the asymmetric oxide growth on the front-side and backside of the system leads to an enhancement of system asymmetry, which corresponds to the curvature increase (section 4.3.2);

(2) the enhancement of creep mismatches between the {coatings+substrate} and the oxide scales slightly retards the curvature increase.

Stresses in the coatings (Figure 4.26(c)) and substrate (Figure 4.26(d)) are slightly changed due to the small change of the curvature. The compressive stress in the elastic oxide cannot be relaxed due to the lack of creep deformation.

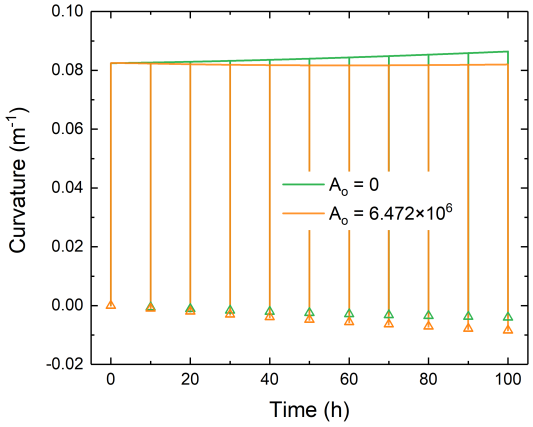

(a) Curvature

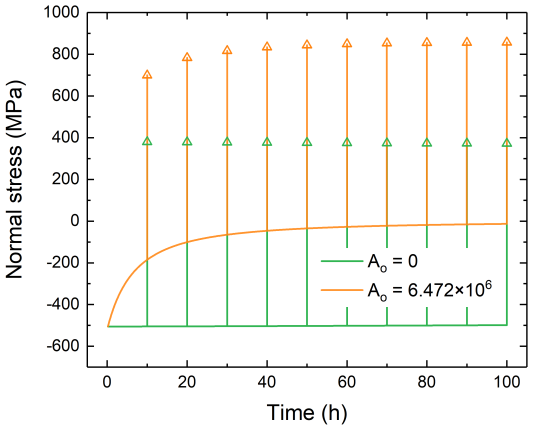

(b) Stress in oxide at oxide/AlN top coating interface

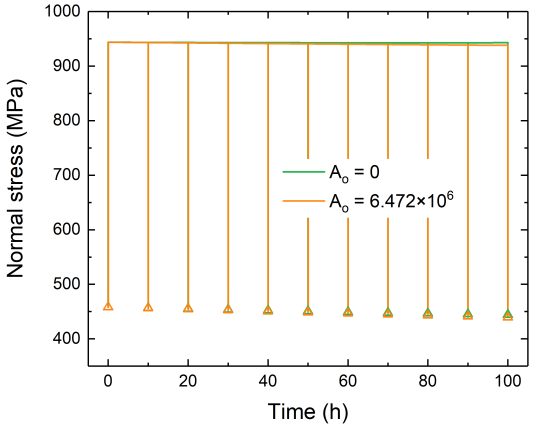

(c) Stress in coating at AlN top coating/substrate interface

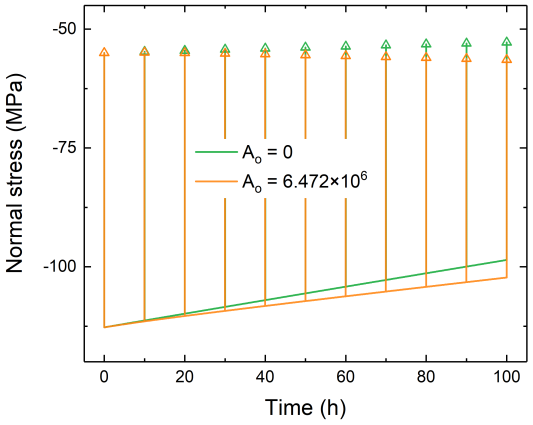

(d) Stress at the center of the substrate

Figure 4.26 Effect of creep properties of the oxide scale on (a) evolutions of the curvature of the system, and stress evolutions at (b) oxide/AlN top coating interface (on oxide side), (c) AlN top coating/substrate interface (on coating side) and (d) the center of substrate; triangles represent the curvature and/or stresses at ambient temperature.

Effect of creep in substrate

The creep prefactor of the substrate, A_s, is assumed to range from zero to 1.796×10^6 $MPa^{-n}\cdot s^{-1}$. The A_s=0 is used to illustrate the effect of the use of an elastic substrate (i.e. no creep deformation at high temperature), and the A_s=1.796×10^3, 1.796×10^5, 1.796×10^6 $MPa^{-n}\cdot s^{-1}$ are used to model the slow-creeping TZM (realistic), medium-creeping and fast-creeping substrates, respectively. The evolution of curvature and stresses in the oxide scales, coatings and substrate for the substrate with an elastic behavior are in agreement with those for the realistic TZM substrate. This confirms that the creep mismatches between the oxide scales and the {coatings+substrate} do not have a significant effect on both curvature and stress evolutions.

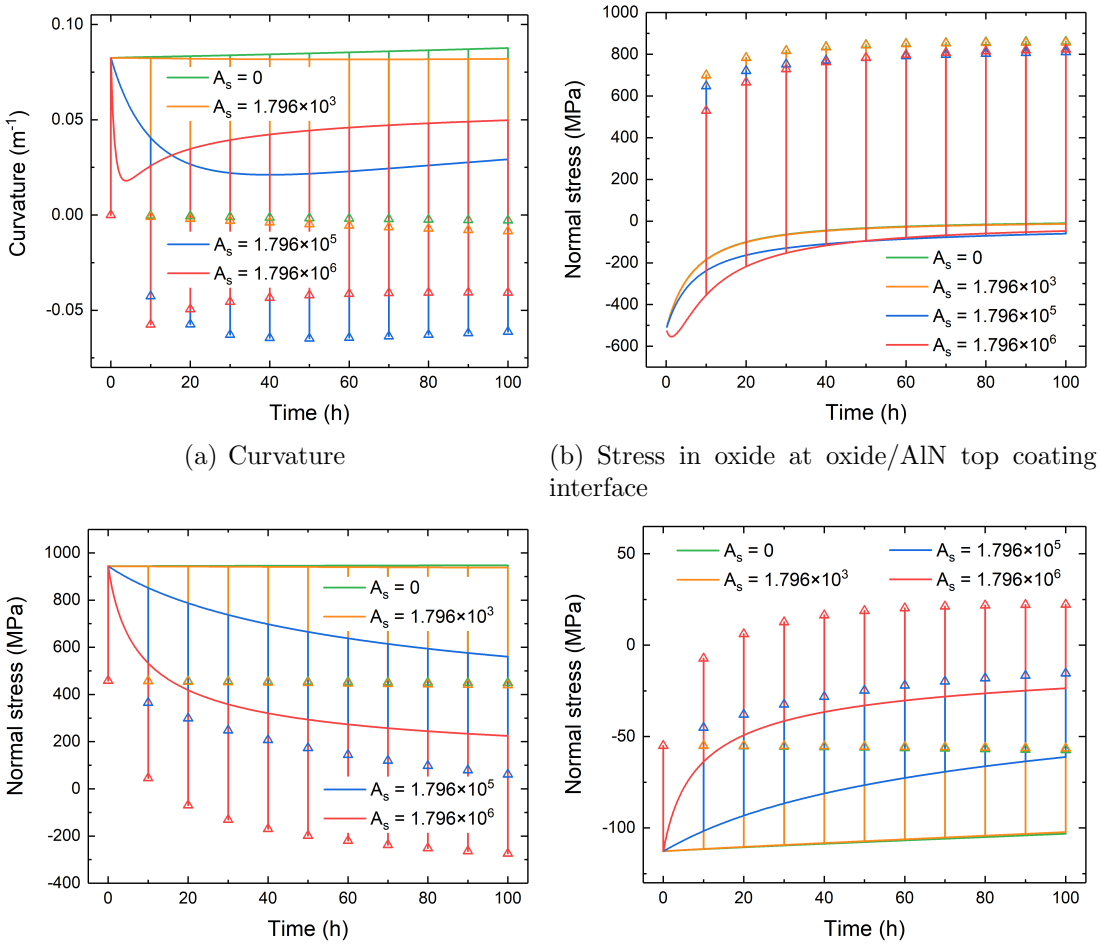

(a) Curvature

(b) Stress in oxide at oxide/AlN top coating interface

(c) Stress in coating at AlN top coating/substrate interface

(d) Stress at the center of the substrate

Figure 4.27 Effect of creep properties of the substrate on (a) evolutions of the curvature of the system, and stress evolutions at (b) oxide/AlN top coating interface (on oxide side), (c) AlN top coating/substrate interface (on coating side) and (d) the center of substrate; triangles represent the curvature and/or stresses at ambient temperature.

However, when the creep resistance of the substrate is reduced, i.e., A_s increases, the creep behavior of such a medium-creeping substrate is comparable to that of the oxide scales. The creep mismatches within the {coatings+substrate} are no longer negligible. Large compressive creep strains are generated in the substrate. As a result, the bending curvature is largely relaxed to achieve the equilibrium of the force and moment in the system. The strong reduction of bending strain enhances stress relaxation in AlN coatings (blue in Figure 4.27(c)). However, it delays that in oxide scales (blue curve in Figure 4.27(b)). The large A_s leads to a faster stress relaxation in the substrate as well as in the coatings (red curves in Figures 4.27(c) and 4.27(d)). The curvature is quickly relaxed, which give rise to an enhancement of stress in the oxide scales. The competition between acceleration of creep strain development in the oxide scales and saturation of compressive creep strain in the substrate results in a subsequent increase of curvature. Stress relaxation takes places in the oxide scales resulting from the corresponding increase of bending strain. With increasing time, the stress relaxation within the system results in a gradual decrease of curvature.

Effect of creep in AlN coating

To study the effect of creep behavior in AlN coatings, the creep prefactor of AlN coating, A_c, is ranged from zero to 2.928×10^{13} $MPa^{-n}\cdot s^{-1}$. As illustrated in Figure 4.28, there is almost no difference of the general features of curvature evolution and stress evolutions in the oxide scales, AlN coatings and substrate between the elastic coating (A_c=0) and realistic AlN coating (A_c=2.928×10^{10} $MPa^{-n}\cdot s^{-1}$). This observation is in agreement with the discussion of creep properties of the substrate in the previous section. Large tensile creep strains are accumulated in the coatings when A_c increases. As shown in Figure 4.28(a), the bending strain is enhanced to maintain the system equilibrium (blue and red curves). Such enhancement speeds up when A_c is larger (A_c=2.928×10^{13}, red curve). The stress relaxations in the coatings and the substrate are also accelerated (red curves in Figures 4.28(c) and 4.28(d). Creep strains in individual layers saturate. Therefore, the creep mismatches tend to be stable. The asymmetry of the system is reduced. This is supported by the subsequent decrease of the curvature.

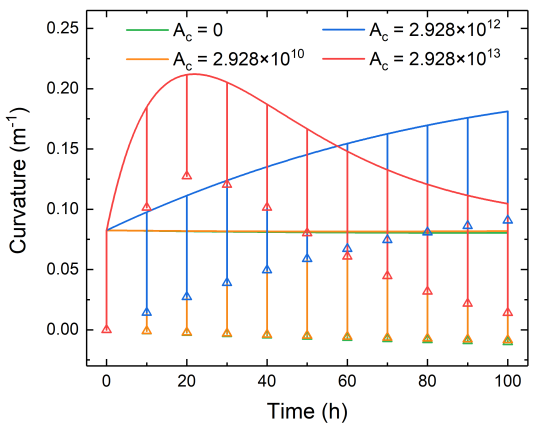

(a) Curvature

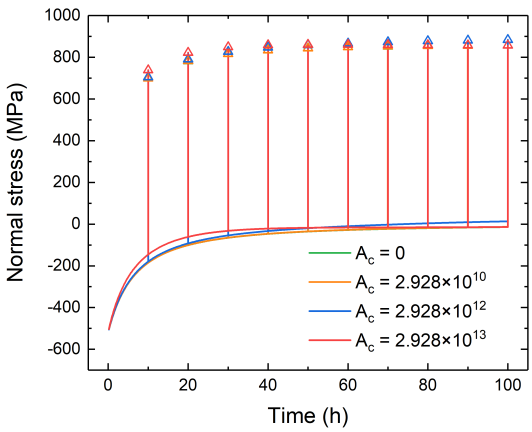

(b) Stress in oxide at oxide/AlN top coating interface

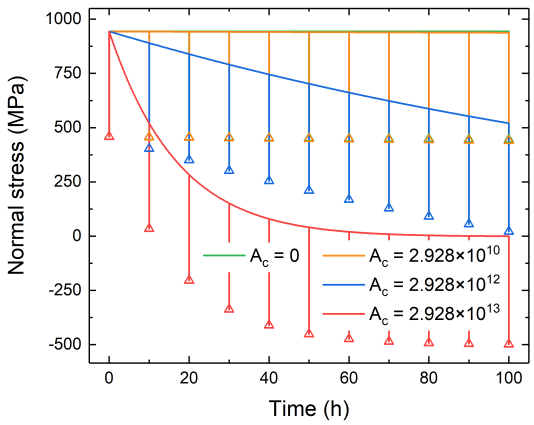

(c) Stress in coating at AlN top coating/substrate interface

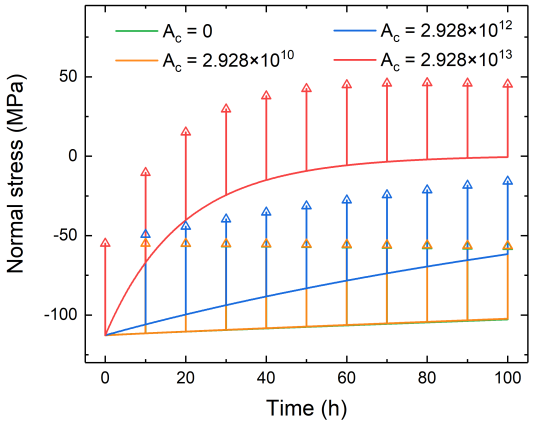

(d) Stress at the center of the substrate

Figure 4.28 Effect of creep properties of the AlN coatings on (a) evolutions of the curvature of the system, and stress evolutions at (b) oxide/AlN top coating interface (on oxide side), (c) AlN top coating/substrate interface (on coating side) and (d) the center of substrate; triangles represent the curvature and/or stresses at ambient temperature.

In summary, the curvature and stresses evolutions in AlN coatings and substrate are nearly unaffected by the creep properties of the oxide. Stresses in the oxide scales are relaxed to nearly stress-free state upon creep deformation. By contrast, large creep rates in the substrate or AlN coatings facilitate the stress relaxations in both coatings and substrate, whereas the overall stress evolutions in the oxide scales are almost unaffected. For the curvature, large creep rates in the substrate leads to a rapid curvature relaxation at the beginning and a subsequent increase. The increase of creep rate in the AlN coating, however, also increases the curvature. When the creep strains in the coatings and the substrate saturate, the curvature starts to decrease and tends to be stable.

4.4.5 Effect of oxide scale growth kinetics

Previous discussions showed that the linear oxide growth can introduce large thermal mismatches within the system, which affects the curvature evolution at ambient temperature. We assume herein that the parabolic oxidation kinetics can be extended in the temperature range of 1000-1100 °C, to study the effect of oxidation kinetics. As assumed in section 4.1.2, when the diffusion is the rate-limiting step of oxidation, the lateral strain rate of the oxide scale is proportional to its growth rate (Eq.(4.12)).

Chou and Hou [219, 220] have proposed a model to explicitly express the reacted fraction of oxidation, ξ as a function of oxidation duration t, such as:

$$\xi = (\frac{1}{\Theta_T} \cdot exp(-\frac{\Delta E_d}{R \cdot T}) \cdot t)^{\frac{1}{2}} \tag{4.23}$$

where ΔE_d is the activation energy of diffusion and Θ_T is a constant related to oxygen partial pressure. For the oxidation of AlN, the relationship between mass

gain and the reacted fraction can be written as follow:

$$\xi = \frac{\Delta m}{m_0} \cdot \frac{M_{AlN}}{\frac{1}{2} M_{Al_2O_3 - M_{AlN}}} \tag{4.24}$$

where M_{AlN} and $M_{Al_2O_3}$ are the molecular masses of AlN and Al_2O_3 respectively, and m_0 the initial mass of AlN. From oxidation experiments in the temperature range of 1327-1527 °C, values of Θ_T and ΔE_d are obtained as 5.7 s^{-1} and 2.309×10^5 $J \cdot mol^{-1}$, respectively. The lateral growth strain rate constant η_g, for the parabolic growth of oxide, is assumed to be 10×10^4 to clarify the stress evolution.

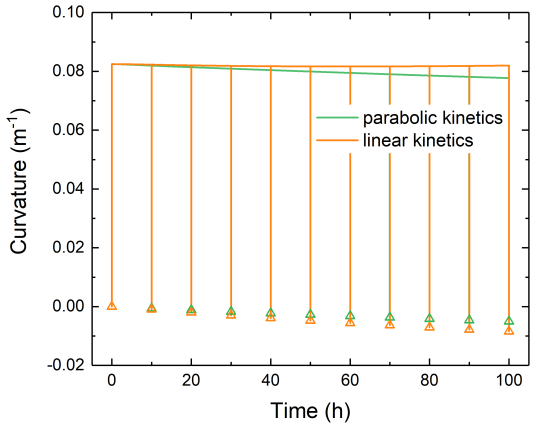

(a) Curvature

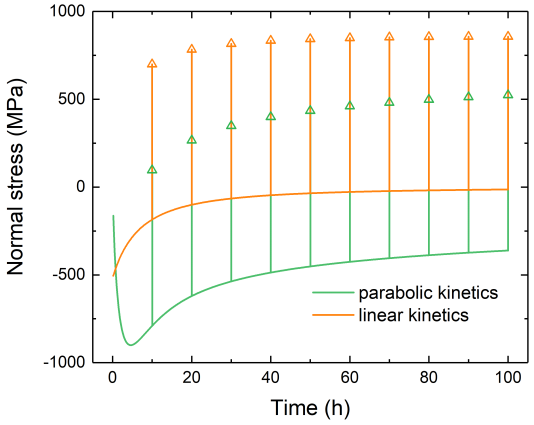

(b) Stress in oxide at oxide/AlN top coating interface

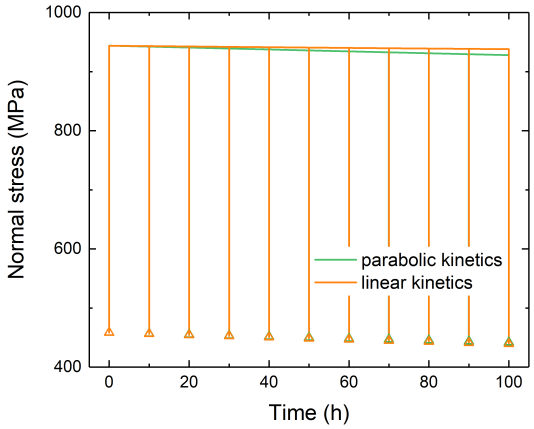

(c) Stress in coating at AlN top coating/substrate interface

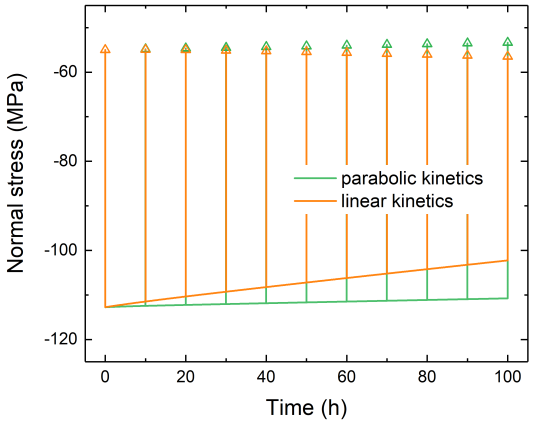

(d) Stress at the center of the substrate

Figure 4.29 Effect of oxidation kinetics of AlN on (a) evolutions of the curvature of the system, and stress evolutions at (b) oxide/AlN top coating interface (on oxide side), (c) AlN top coating/substrate interface (on coating side) and (d) the center of substrate; triangles represent the curvature and/or stresses at ambient temperature.

The evolution of curvature and stresses at the three representative positions are depicted in Figure 4.29. Stresses in the coatings and substrate are nearly

unaffected by the oxidation kinetics, whereas the curvature and stress in the oxide scales have different features of evolution. Indeed, as the oxide growth is limited by diffusion, the thickness of the oxide scales is much lower than in the case of linear growth. The thermal mismatches are thus limited. The curvature continues to decrease till the end of the thermal cycling. The variation of $\Delta\frac{1}{r}|_{HT\rightarrow T_{amb}}$ is also reduced. In the oxide scales, we observe an increase and a subsequent decrease of stress. This results from the competition between the accumulation of compressive creep strain and development of lateral strain in the oxide scales. At the end of thermal cycling, stresses in the oxide scales are relaxed to reach a constant (∼-0.5 GPa), which means that a steady competition exists between stress build-up (constraint of the lateral expansion) and stress relaxation (upon creep deformation).

4.5 Assessment of the creep properties used in the simulation

We have extensively investigated various factors in the previous sections to study how the daily operation in solar receivers and the design of materials alter the stress evolution within a multilayer coating system. Based on the model and the above discussions, it is therefore possible to estimate the lifetime of AlN coatings for their use in solar receivers. Moreover, the above discussions show that the use of a refractory-based alloy as substrate can induce huge tensile stress in the oxide scales during the cooling stage. This is due to its lower thermal expansion coefficient than that of Al_2O_3. In this section, we consider the relatively slow-creeping FeCrAl alloy, APMT, as the substrate. As it has a larger thermal expansion coefficient, compressive stress are introduced in the oxide scales during the cooling stage.

In Chapter 3, we have found that after 30 h of cyclic oxidation (in a laboratory furnace) at 1100 °C for a pre-oxidized APMT coated with AlN on both surfaces (see section 3.6.4), stresses at ambient temperature in both the oxide scales and coatings tend to be stable (-2.75 GPa). The schematic representation of the sample is shown in Figure 3.28. To further verify the accuracy of the model, we here compared the experimental measurements and stress predicted by the proposed analytical model. The thermomechanical properties of APMT are summarized in Table A.3.4. Due to the lack of creep properties for APMT, we herein use the creep parameters of another ODS FeCrAl alloy (MA956) for the calculations. For AlN and alumina, their properties previously used are adopted. The temperature field is assumed to be uniform in this case.

Figure 4.30 depicts the evolution of stresses at ambient temperature in the top oxide and AlN top coating by experimental measurements (blue points and curves) and model calculations (orange and green curves). The orange curves represent the calculation using creep properties of AlN listed in Table A.3.1, while the green curve represents the calculations assuming a fast-creeping AlN (A_c=5.856×10^{12} $MPa^{-n}{\cdot}s^{-1}$). For the oxide scale, results obtained by the current model are in good agreement with experimental data with a shift of around -0.5

GPa. The stress decreases gradually with the increase of oxidation time regardless of the creep prefactor of AlN. On the contrary, the slow-creeping AlN leads to a gradual increase of compressive stress (orange curve in Figure 4.30(b)), which is in contradiction with experimental measurements. However, when AlN creeps faster (green points and curve), the feature of stress evolution is similar to that of experimental results, but there still exists an offset of around 0.5 GPa. This indicates that the creep parameters used in the model is not sufficiently accurate. In reality, AlN creeps faster. It is also suggested that the creep properties of AlN are related to its grain size [221]. This is one of the key points to be addressed in the next step study.

Moreover, it should be pointed out here that, unlike the previous analyses using TZM as the substrate, large compressive stresses are introduced into the oxide scales and AlN coatings during the cooling stage because the thermal expansion coefficient of AMPT is much larger. The steady stress evolutions in the oxide scale and the coating ($\geq$10 h) indicate that stresses at high temperature are fully relaxed and tend to be stable. Therefore, the stresses at ambient temperature is solely determined by the thermal mismatches within the system. The offset between experimental results and model calculations, however, is mainly due to the use of inaccurate thermal expansion coefficients.

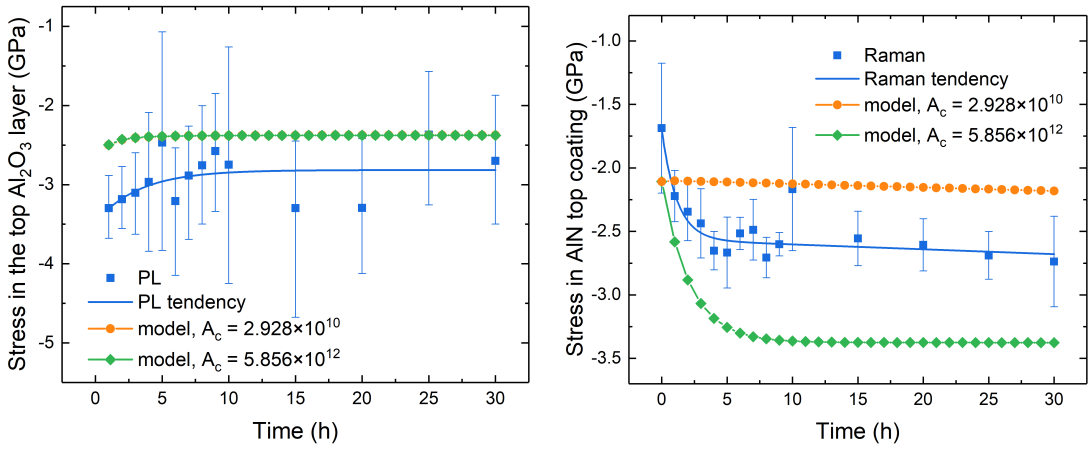

(a) (b)

Figure 4.30 Measured (blue points and curves) and calculated (orange and green curves) stresses at ambient temperature in (a) the top oxide and (b) AlN top coating; the residual stresses in top oxide and AlN top coating are measured by photoluminescence and Raman spectroscopy respectively (section 3.6.4).

4.6 Limitation of the model

Despite the fact that modeling results have the same feature as in experimental results, the following issues need to be addressed in the future work:

(1) large tensile stresses at ambient temperature in the oxide scales calculated in the model are likely to cause failure of the oxide scales during the cooling

stage. Delamination and/or spallation of the oxide scale can take place at the oxide/AlN coating interface. Nevertheless, cracking perpendicular to this interface will lead to an exposure of the fresh coating to the oxygen, which may introduce an acceleration of oxidation. Fracture toughness of alumina can be introduced into the model. A threshold of stress is set and beyond which the oxide growth rate is accelerated.

(2) It is assumed in section 4.1.2 that the oxide scales are thin enough so that the oxidation temperature can be assumed to be constant. This is valid for the linear growth of alumina at low temperature ($\leq$1000 °C) and the parabolic growth at medium temperature ($\leq$1250 °C). However, as temperature increases, the oxidation rate increases following an exponential function. This assumption is no longer accurate, and deviates the calculation of thermal expansion mismatches from a realistic case. It is already shown that the thermal mismatches, in particular resulting from surface-reaction limiting oxidation (linear), have important effects on the curvature evolution.

(3) Limarga and Wilkinson [206, 207] have shown that for diffusion-controlled reaction, the stress has a strong effect on the diffusion flux and thus the scale growth kinetics, which subsequently influences the evolution of thermal strain mismatches, and in turn, alters the stress evolution. In spite of linear oxidation of AlN employed herein, the introduction of interaction between stress and oxidation into the model allows to extend it.

Conclusions

An analytic model is developed in this chapter to study the stress evolution in a multilayer coating system under solar radiation. The temperature difference within the system, oxidation growth, intrinsic growth stress in the coatings via vapor deposition and creep deformation of materials are taken into account in the model. Special analyses were made for a molybdenum-based substrate (TZM) coated with 60 μm AlN on both surfaces. The proposed model is validated by the comparison of stress and creep strain evolutions with finite element analysis.

To further investigate the durability of the multilayer system for its use in solar receivers, various factors involving the thermal conditions in the solar receivers (thermal gradient and targeted temperature of heat transfer fluid), intrinsic CVD growth stress in the coatings (related to the microstructure of coatings), oxide scale growth kinetics (linear or parabolic) and creep deformation of materials are examined. In summary,

(1) the oxidation rate of the top and bottom coatings are controlled by the thermal conditions. The transformation of AlN to Al_2O_3 results in a significant curvature relaxation, and thus alters the stress evolutions.

(2) the intrinsic growth stress in the coatings does not have significant effect on the overall evolution of curvature and stresses.

(3) creep properties of the oxide only affects the stress evolution in the oxide scales. Creep properties of the coatings and substrate strongly affect the evolution of curvature and stresses in the coatings and substrate, whereas the overall stress evolution in the oxide scales is unaffected.

(4) the cooling stage introduce large thermal stresses in the individual layers. If the thermal expansion coefficient of the oxide is the largest, the oxide scales are under tension at ambient temperature (e.g. TZM used as the substrate) whereas compressive stresses are introduced in the oxide scales when the thermal expansion coefficient of the substrate is larger than that of the oxide (e.g. APMT used as the substrate).

(5) parabolic oxidation kinetics reduces the thickness of grown oxide scales (compared to the linear growth). Therefore, the evolution of curvature is thus nearly unaffected by the parabolic oxide growth. The competition between compressive creep strain accumulation and lateral expansion in the oxide scales determines the feature of their stress evolutions. A balance is formed between the creep relaxation and lateral growth of the oxide at the end of thermal cycling.

Therefore, it is proposed that, to enhance the durability of the aforementioned multilayer coating system (TZM substrate coated with AlN coatings) for the use in solar receiver, a low to medium heat flux can reduce large stress gradient within the system (at the beginning of thermal cycling). A low targeted temperature of heat transfer fluid (<1000 °C) helps to avoid the cracking and/or delamination of oxide scales during the cooling stage. The selection of slow-creeping AlN and TZM as the coating and substrate leads to a nearly elastic evolution of stresses in coatings and substrate. A low intrinsic growth stress is suggested to reduce the elastic response of the system so that a better durability of the system could be obtained.

To further complete the criteria for the selection of material summarized in Chapter 2, it should be highlight that the thermal mismatches between the oxide, coating, and substrate should be reduced as much as possible. The choice of material having smaller thermal expansion (than the oxide) as the substrate will lead to a tensile residual stress in the oxide at ambient temperature, which is considered to cause cracking and spallation of the oxide scale.

In Chapter 3, we have concluded that, according to its oxidation behavior, for working temperatures between 800 and 900 °C, the service life of AlN can reach several years without consideration of delamination and/or spallation. In this chapter, it is shown that it is possible to find out optimal operating conditions and substrate to obtain better durability for AlN coating for its use in solar receivers. Moreover, the proposed model can be extended and used in other high temperature applications where high temperature, aggressive environment is coupled with mechanical loading to predict the stress evolution within the coating system, such as thermal-barrier coatings, and to estimate their lifetime.

Chapter 5

Potential of AlN and SiC coatings for their use in solar receivers

Introduction

The previous two chapters have experimentally and numerically investigated the potential of AlN coatings for high temperature applications (T≥1000 °C). In the first part of this chapter, optical properties of AlN coatings are studied to finalize the coating evaluation for solar receivers.

The second part concerns the potential of SiC as a coating material for solar receivers. First, the HTCVD deposition conditions of SiC coatings are briefly introduced. After deposition, microstructure and oxidation resistance of the as-grown SiC coatings on different substrates are investigated. Finally, optical properties of SiC coatings are characterized to evaluate their potential in solar receivers.

5.1 Optical properties of AlN coatings

Optical properties measurements are carried out in collaboration with PROMES (CNRS, France) laboratory. The coatings are all processed in 'standard' conditions (Chapter 3) on Fecralloy and APMT. Figure 5.1 presents the hemispherical spectral emissivity of uncoated Fecralloy, AlN coated Fecralloy before and after four fast cycles of oxidation (20 min/cycle) in REPHTS (see section 2.3) from 25 to 1225 °C. Table 5.1 reports the values of the solar absorptivity (α_{sol}), total emissivity (ε_{tot}) and α/ε ratio calculated for these samples from the integrated values of spectral emissivity, using Eqs. (2.26) and (2.27). It is observed in Figure 5.1 and Table 5.1 that the AlN coating improves the solar absorptivity of the Fecralloy substrate. In the same way, the coating also increases the total emissivity but it stays lower than the solar absorptivity as the α/ε ratio is higher than one. Nevertheless, the oxidation of the AlN coating tends to decrease the solar absorptivity.

Figure 5.2 presents the hemispherical spectral emissivity of uncoated APMT, AlN coated pre-oxidized APMT before and after cyclic oxidation from 25 to

1225 °C in the REHPTS set-up, and also after 100 h of oxidation at 1100 °C in a conventional furnace (see Figure 3.25(a) in section 3.6.3) for the microstructure of the studied sample). Table 5.2 summarizes the values of the solar absorptivity, total emissivity and α/ε ratio for these samples from the integrated values of spectral emissivity calculated by Eqs. (2.26) and (2.27).

Table 5.1 Calculated values (Eqs. (2.26) and (2.27)) of the solar absorptivity, total emissivity and α/ε ratio for uncoated Fecralloy and Fecralloy coated with AlN (40-50 μm) before and after cyclic oxidation.

Sample	α_{sol}	ε_{tot}	α/ε
Uncoated Fecralloy	0.39	0.05	7.0
AlN coated	0.87	0.62	1.4
AlN coated, after 4 oxidation cycles	0.68	0.57	1.2

Table 5.2 Calculated values (Eqs. (2.26) and (2.27)) of the solar absorptivity, total emissivity and α/ε ratio for the uncoated APMT, AlN (40-50 μm) coated APMT before and after cyclic oxidation in the REHTPS set-up, and after 100 h of oxidation in a furnace.

Sample	α_{sol}	ε_{tot}	α/ε
Uncoated APMT	0.51	0.15	3.4
AlN coated	0.89	0.71	1.2
AlN coated, after 4 oxidation cycles	0.88	0.73	1.2
AlN coated, after 100 h of oxidation in a furnace at 1100 °C	0.49	0.67	0.7

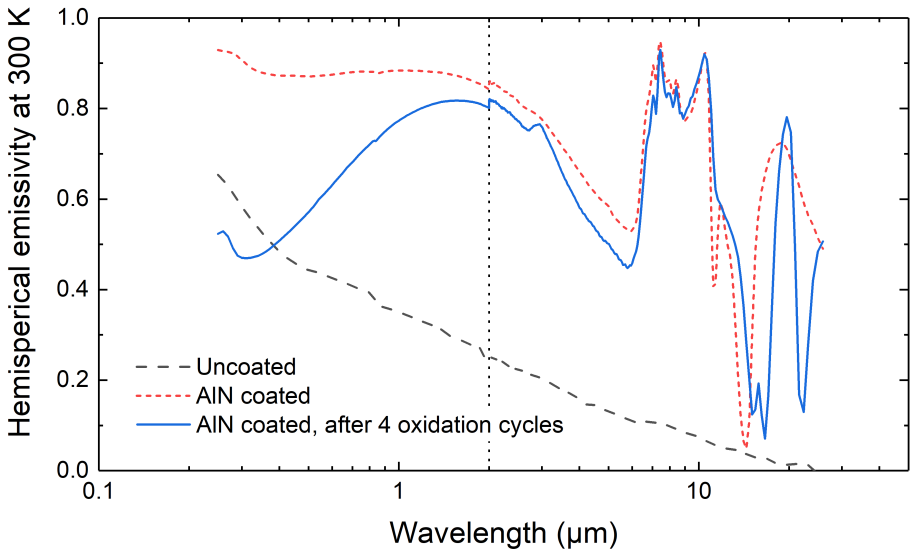

Figure 5.1 Hemispherical spectral emissivity of uncoated Fecralloy, AlN coated Fecralloy before and after 4 fast oxidation cycles (25-1225 °C in the REHTPS set-up; the thickness of the 'standard' AlN layer is around 45 μm.

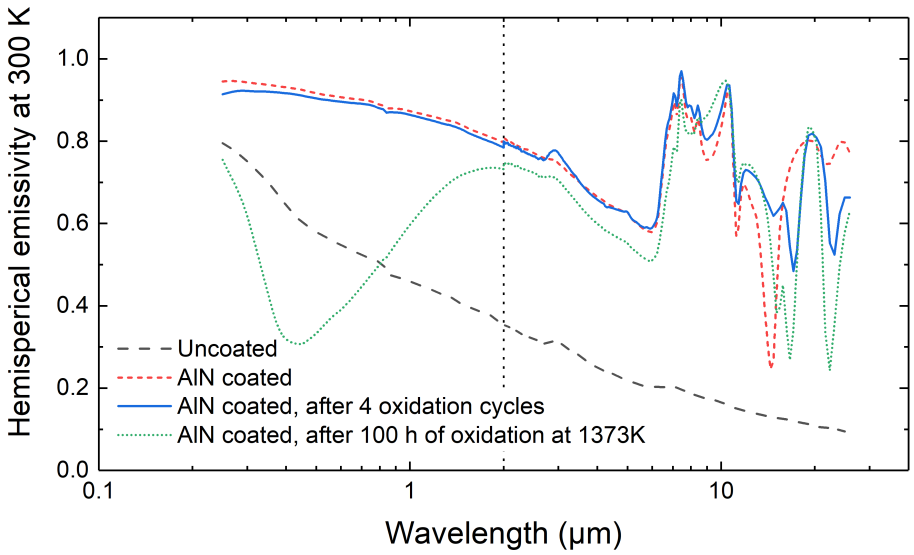

Figure 5.2 Hemispherical spectral emissivity of uncoated APMT, AlN coated APMT before and after 4 fast oxidation cycles (25-1225 °C in the REHTPS set-up, and after 100 h of oxidation in a conventional furnace at 1100 ∘C; the thickness of the 'standard' AlN layer is around 45 μm.

The optical properties of uncoated APMT are slightly higher than the ones of the uncoated Fecralloy. Consequently, the total emissivity of AlN deposited on APMT is higher than the one of AlN deposited on Fecralloy (0.71 vs. 0.62, respectively). The optical properties of AlN deposited on APMT or Fecralloy follow the same trends and the same α/ε ratio are found after cyclic oxidation. After 100 h of exposure in air at 1100 °C, the solar absorptivity of AlN/APMT (or Fecralloy) is reduced to 0.49, due to the transformation of AlN into a non-optically selective layer of alumina. The thicker the alumina layer is, the more the solar absorptivity is reduced: α/ε ratio varies from 1.2 after one hour of oxidation to 0.7 after one hundred hours.

The measurement of the optical properties of the stack AlN/FeCrAl alloys showed a significant solar absorptivity in the solar spectrum (from 0.4-0.5 to around 0.9) and an α/ε ratio close to 1. However, the development of the alumina scale leads to a decrease of the absorptivity. Indeed, the reflectivity of Al_2O_3 is very high in the solar spectrum, and thus its solar absorptivity in this region is low. As a result, it is not recommended to use alumina-forming coatings for solar receivers at temperature higher than 1000 °C. However, for lower temperatures (800-900 °C), the influence of alumina is not so significant as its growth rate is reduced. It is possible to use AlN coatings in solar receivers in this temperature range. New measurement of optical and thermal properties, as well as durability are needed to complete the evaluation of this coating.

In summary, AlN coating is not the ideal material for solar receivers working in air at temperature higher than 1000 °C. However, it is an efficient barrier on metals for the deposition of other ceramic coatings like SiC on high temperature alloys.

5.2 SiC coatings for solar receivers

To further increase the optical properties and oxidation resistance of the proposed coatings/substrate system (Figure 2.1) for solar applications, SiC coating is investigated in the following sections. As previously discussed in section 2.1.1, herein, AlN coatings is used as diffusion and chemical barriers to avoid high temperature reaction between SiC and metallic substrates. Material properties of SiC are presented in Table 2.1, Figure 2.2 and Figure 2.3.

5.2.1 HTCVD deposition conditions

Substrates coated with AlN coatings (thickness of around 15 μm) are used for the deposition of SiC coatings. The details of the CVD apparatus and details of process prior to deposition can be found in sections 2.2.3 and 3.1 respectively. The SiC coating is deposited via halide CVD using silane (SiH_4, 3% in H_2) and propane (C_3H_8) as source gases. The flow rate of these two gases are 500 and 15 sccm respectively. H_2 with a flow rate of 1500 sccm is used as the carrier gas. The deposition temperature is maintained at 1100 °C and the total pressure inside the reactor is kept at 2000 Pa. The deposition duration is 3 h and the growth rate of SiC is around 30 μm h^{-1} with $\pm$5% uncertainties.

5.2.2 Stack SiC/AlN/TZM

5.2.2.1 Microstructure

The surface morphology and cross-section of as-graown SiC coating are presented in Figure 5.3. Pyramid-like grains with a small grain size ($\sim$1 μm) are observed. As shown in Figure 5.3, the as-deposited structure is stable. Neither interfacial reaction nor delamination of SiC and AlN coatings occurs at the interfaces. Moreover, the SiC coating is dense. No voids are observed. The XRD θ-2θ analysis illustrates that the as-grown SiC coating is composed of 3C-SiC and 2H-SiC polytypes.

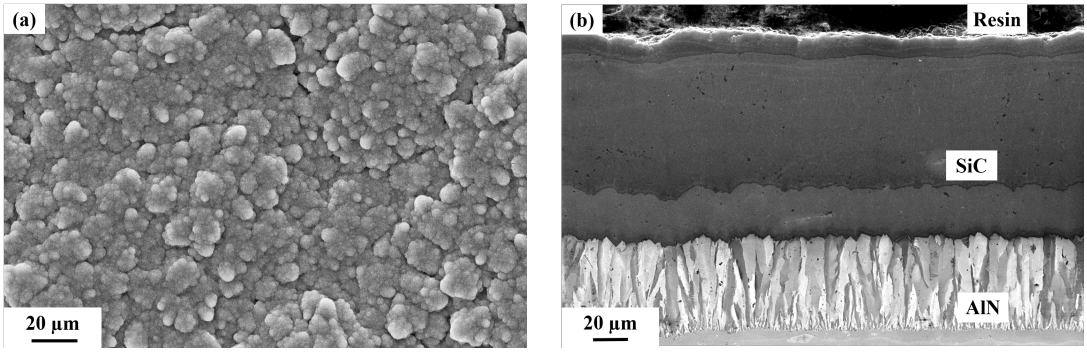

Figure 5.3 (a) surface morphology and (b) cross-section of SiC coating grown on TZM substrate coated with an AlN layer (15μm).

5.2.2.2 High temperature oxidation

The TZM substrate coated with SiC/AlN bilayers on both faces is cyclically oxidized in a conventional furnace for 5.5 h at 1100 °C. Detailed conditions can be founded in section 3.6.1. As shown in Figure 5.4, contrary to expectations, a quasi-linear mass loss is observed due to the formation of volatile oxide MoO_3. A small crack at the edge of the sample is observed after 3 h of oxidation, and the failure of the sample occurs due to the crack propagation (Figure 5.4(b)). The substrate material evaporates from this spalled piece, corresponding to the linear mass loss in Figure 5.4(a). The formation of cracks and the subsequent failure of the sample can be attributed to the large stresses in the coatings and/or substrate during cyclic oxidation. New measurements and numerical predictions of the evolution of stresses in SiC and AlN coatings are necessary for the future study.

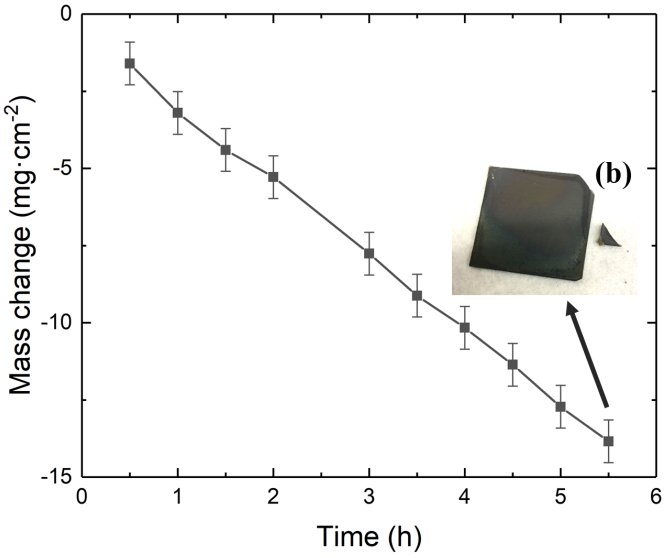

Figure 5.4 (a) Mass change of SiC/AlN coated TZM sample during cyclic oxidation at 1100 °C and (b) macroscopic image showing the failure of the sample after 5.5 h of oxidation.

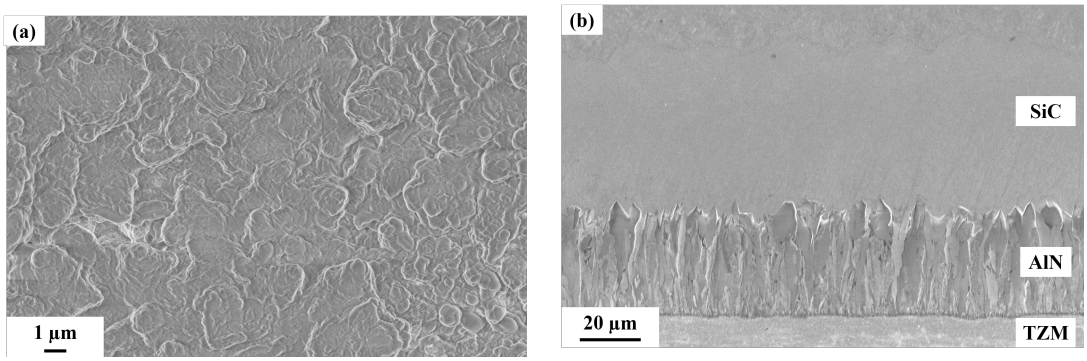

Figure 5.5 (a) Surface morphology and (b) cross-section of SiC coating grown on TZM substrate coated with an AlN layer (15μm).

Figure 5.5 shows the surface morphology and cross-section of the sample after oxidation. The SiC/AlN bilayer remains dense, homogeneous and adherent on TZM substrate at the center of the sample. This suggests that the SiC coating plays its protective role when it is adherent and without cracking. Signal of Si, C and O elements are detected by SEM/EDX system on the sample surface, indicating the formation of a thin SiO_2 layer on the surface. This is confirmed by XRD θ-2θ analysis (Figure 5.6).

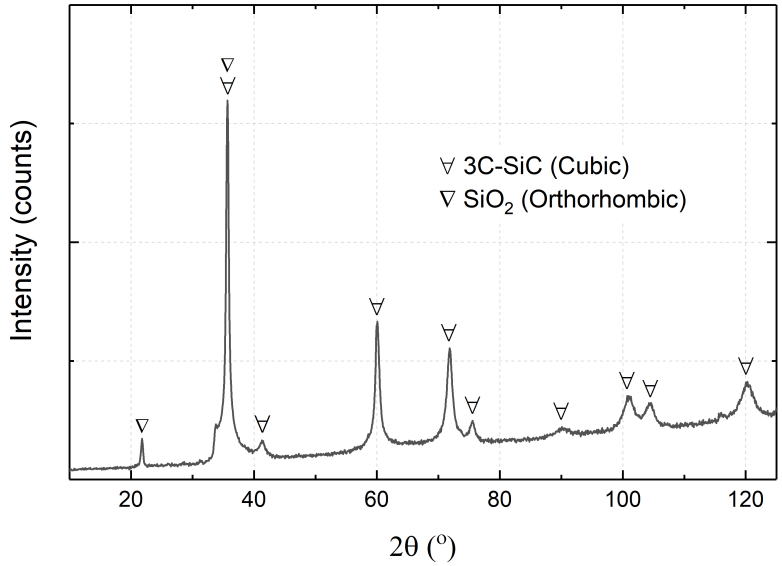

Figure 5.6 XRD θ-2θ patterns of the SiC/AlN coated TZM sample after cyclic oxidation.

5.2.3 Stack SiC/AlN/FeCrAl alloys

The previous discussions shown that the poor oxidation resistance of refractory metal based alloys leads to difficulties to characterize the high temperature properties of the coatings. In the following sections, the FeCrAl alloys, Fecralloy and APMT, are used as alternative substrates to characterize the oxidation resistance and optical properties of the SiC coating. AlN buffer coatings are deposited under 'standard' conditions for 1 h (thickness of around 15 μm).

5.2.3.1 Microstructure and oxidation resistance

The surface morphology of SiC coatings on AlN coated Fecralloy and pre-oxidized APMT are shown in Figure 5.7. Pyramid-like grains of SiC coating are obtained on AlN coated Fecralloy while grains are smaller (<200 nm) on pre-oxidized APMT coated with a 15 μm AlN layer. Spallation of the SiC coating and cracks are also observed (Figure 5.7(b)). This is mainly due to the higher thermal expansion coefficient of APMT and its higher creep resistance. Therefore, it is suggested to only use Al_2O_3 (thickness of around 1.5 μm, see section 3.5.2) as a barrier layer to accommodate the large difference of thermal expansion coefficients between SiC and APMT. The surface morphology of the SiC coating on pre-oxidized APMT is similar to that grown on AlN coated Fecralloy (Figure 5.7(a)).

Cross-sections (Figure 5.8) show that SiC coatings on both AlN coated Fecralloy and pre-oxidized APMT are dense and adherent. Neither interfacial reaction nor delamination of SiC coatings are observed.

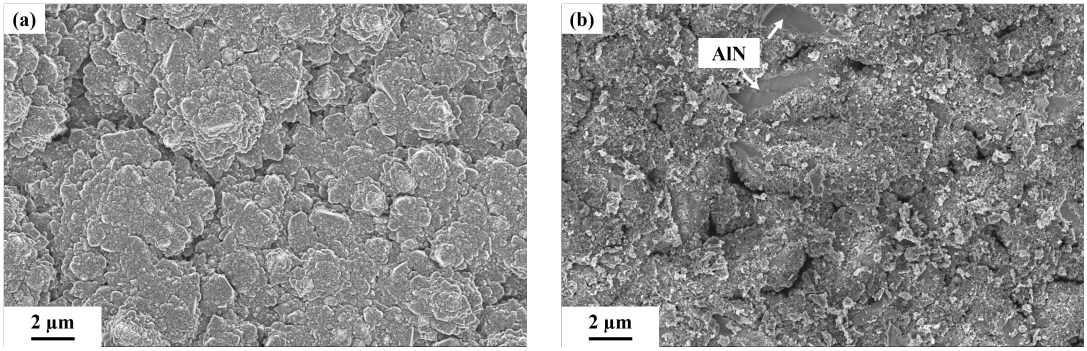

Figure 5.7 Surface morphology of SiC coatings grown on (a) AlN coated Fecralloy and (b) pre-oxidized APMT coated with an AlN layer.

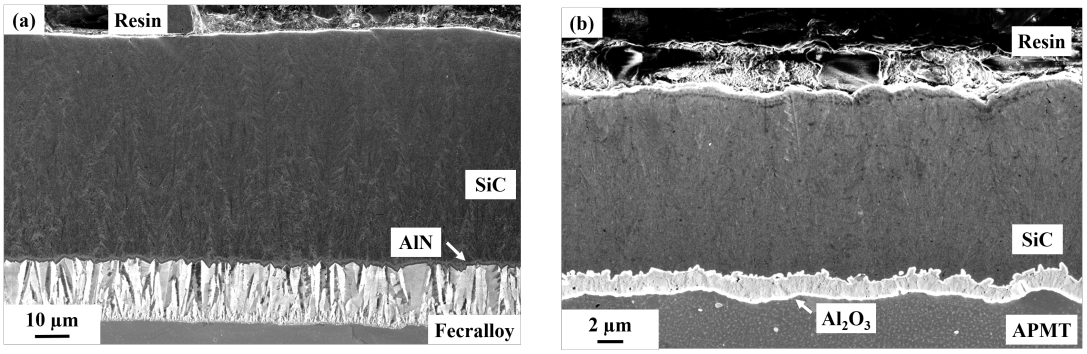

Figure 5.8 Cross-sections of the SiC coatings grown on (a) AlN coated Fecralloy and (b) pre-oxidized APMT.

However, the large difference of thermal expansion coefficients between Fecralloy and SiC/AlN bilayer gives rise to the delamination of the SiC/AlN bilayer during the cyclic oxidation at 1100 °C. The Al_2O_3 accommodation layer does not result in delamination of the SiC coating after 375 h of oxidation, but macro-cracks are observed. In such cases, it is difficult to characterize the oxidation resistance of the grown SiC coatings.

To simplify the characterizations, cyclic oxidation of SiC coatings deposited on bulk polycrystalline AlN are carried out at 1100 °C. The thickness of the SiO_2 layer is approximately 2 μm (measured by ellipsometry, not presented here) after 800 h of oxidation, while the thickness of alumina grown on the same wafer under same conditions is around 200 μm. This result indicates that the oxidation of SiC coatings at 1100 °C is very low, and it can play its protective role if it remains adherent.

5.2.3.2 Optical properties

To finalize the evaluation of the SiC coating for solar receivers, it is now necessary to study the absorptivity in the wavelength range of solar radiation. Figure 5.9 presents the hemispherical spectral emissivity of uncoated Fecralloy and Fecralloy coated with SiC/AlN bilayer before and after three fast oxidation cycles in REPHTS from 25 to 1225 °C. The values of the solar absorptivity (α_{sol}), total emissivity (ε_{tot}) and α/ε ratio are summarized in Table 5.3. The solar absorptivity of uncoated Fecralloy is largely increased with a top coating of SiC. The total emissivity is also increased. Compared with AlN coatings (Table 5.1), the use of an additional SiC coating slightly improve the solar absorption, and decreases the thermal radiation. Therefore, the α/ε ratio slightly increases. Moreover, the oxidation of SiC coatings does not degrade its optical properties. On pre-oxidized APMT, similar results are obtained (Table 5.4 and Figure 5.10). This indicates a great interest for using SiC coatings in solar receivers due to their high solar absorptivity and good spectrum selectivity (α/ε >1). Further studies are required to determine their radiative properties at high temperatures and for longer oxidation durations.

Table 5.3 Calculated values (Eqs. (2.26) and (2.27)) of the solar absorptivity, total emissivity and α/ε ratio for uncoated Fecralloy and Fecralloy coated with SiC/AlN bilayer before and after cyclic oxidation.

Sample	α_{sol}	ε_{tot}	α/ε
Uncoated Fecralloy	0.39	0.05	7.0
SiC/AlN coated	0.92	0.56	1.6
SiC/AlN coated, after 3 oxidation cycles	0.96	0.57	1.7

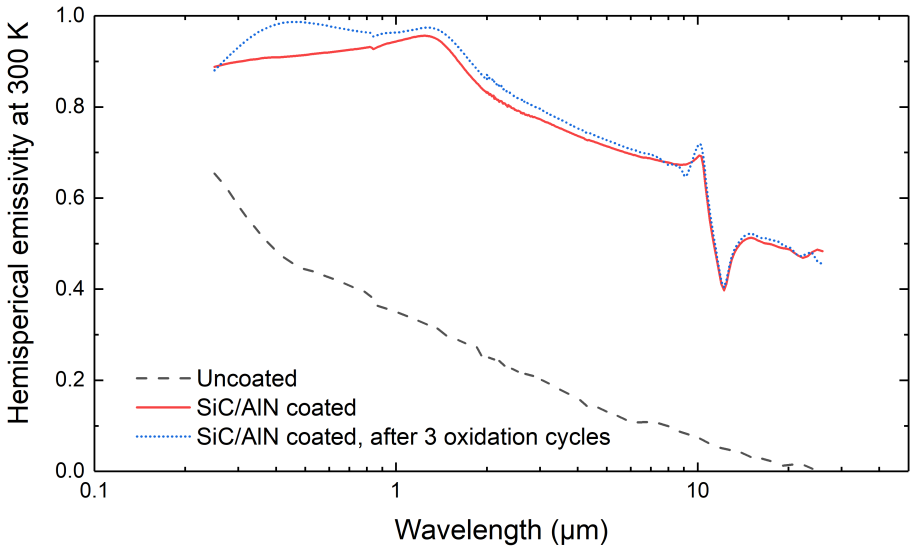

Figure 5.9 Hemispherical spectral emissivity of uncoated Fecralloy and SiC/AlN coated Fecralloy before and after 3 fast oxidation cycles (25-1225 °C in the REHTPS set-up; the thickness of the 'standard' AlN layer is around 15 μm.

Table 5.4 Calculated values (Eqs. (2.26) and (2.27)) of the solar absorptivity, total emissivity and α/ε ratio for uncoated and SiC/AlN coated pre-oxidized APMT.

Sample	α_{sol}	ε_{tot}	α/ε
Uncoated Fecralloy	0.39	0.05	7.0
SiC/AlN coated	0.91	0.60	1.5

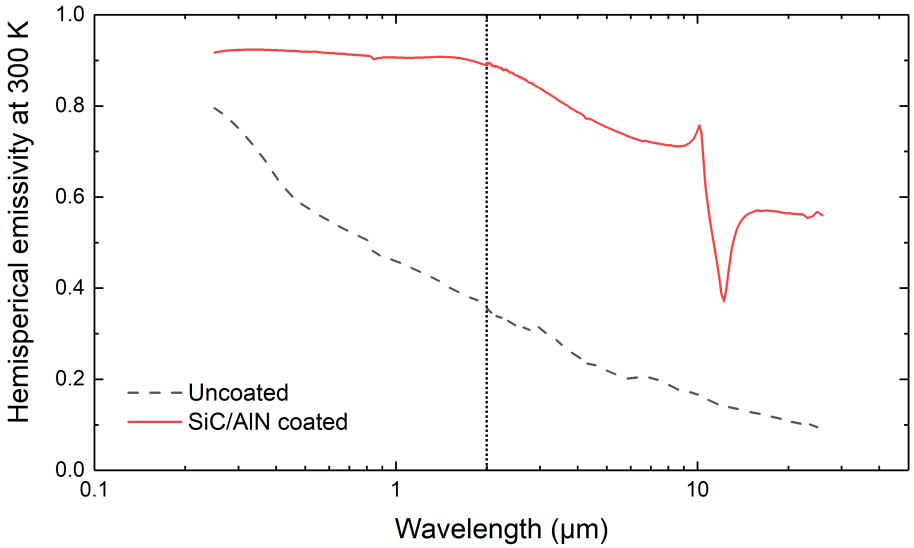

Figure 5.10 Hemispherical spectral emissivity of uncoated and SiC/AlN coated APMT; the thickness of the 'standard' AlN layer is around 15 μm.

Conclusion

This chapter firstly studied the optical properties of AlN coatings. The AlN coating improves the solar absorptivity of the substrate, but also increases the emissivity. However, the development of alumina layer leads to a degradation of solar absorptivity. This coating is not the ideal material for CSP receivers working in air at temperature higher than 1100 °C. However, it is an efficient barrier to avoid the reaction between metallic substrates and the SiC coating which has a high absorptivity.

The SiC coatings are grown on different substrates coated with an AlN layer by HTCVD. It is found that this coating has a much better oxidation resistance than AlN (2 μm of SiO_2 layer after 800 h of oxidation at 1100 °C). The room-temperature optical measurements have shown that the SiC/AlN coatings improve the solar absorptivity of the substrate while maintaining an interesting spectral selectivity. However, the stresses generated in the coatings during severe cyclic oxidation lead to the formation of cracks and/or spallation of the SiC/AlN layer. Our further studies will therefore mainly aim to study the stress evolution by the analytical model proposed in Chapter 4, and/or to develop another accommodation layer.

General conclusion

In this thesis, a coating(s)/substrate system is proposed for high temperature applications ($\geq$ 1000 °C) in order to improve the performance of concentrating solar power (CSP) plants. In particular, two ceramic coatings, aluminum nitride (AlN) and silicon carbide (SiC) coatings, deposited by high temperature chemical vapor deposition (HTCVD) are selected as potential coating materials for solar receivers. For the substrates, two families of alloys are selected. First, refractory-based alloys are selected for their excellent thermal and mechanical properties. Second, alumina-forming iron-based alloys (Fecralloy and APMT) are also investigated because they develop stable alumina scales and help to simplify the characterization of the optical, mechanical and chemical properties of coatings at high temperatures (800-1200 °C).

The potential of AlN coatings used in solar receivers is firstly investigated. Morphological and microstructural characterizations by XRD, SEM and EBSD demonstrate the formation of polycrystalline AlN coatings with a faceted surface morphology and a columnar structure. On molybdenum-based alloys (TZM), the higher deposition temperature (1200 °C) lead to a preferential orientation of $(11\bar{2}2)$. Such $(11\bar{2}2)$-textured microstructures, however, enable fast diffusion of oxygen through short-circuits between AlN crystallites, and therefore a loss of protection of the substrate. On Fecralloy and APMT substrates, the AlN coatings are deposited at 1100 °C. The surface morphology and microstructure of AlN coatings are identical on these two substrates. Studies shown that the evolution of microstructure and preferred orientation(s) are a function of N/Al ratios. These studies show that the increase in the N/Al ratio leads to an increase of supersaturation, and thus to a decrease of grain size. At a low degree of supersaturation (N/Al<5), the semi-polar crystalline plane $(10\bar{1}2)$ is preferentially grown. At a high degree of supersaturation (N/Al>5), the $(11\bar{2}2)$ orientation is favored.

The oxidation properties of AlN coatings on Fecralloy and APMT have been characterized in the temperature range of 800-1100 °C. The cyclic oxidation of AlN coated samples follows a linear kinetics in this temperature range. Very thin oxide scales mainly composed of alumina are grown between 800 and 900 °C. The lifetime of 40 μm coatings can be a few years. For a temperature of 1100 °C, the lifetime of the coating depends on its thickness, about 500 h for a 45 μm coating. The grown alumina layer is porous. Such a microstructure enables fast diffusion of oxygen through the alumina layer and the rate-limiting reaction takes place at the Al_2O_3/AlN interface. This confirms the linear kinetics. Afterwards, AlN coating is completely converted to Al_2O_3 and the oxidation proceeds in the substrate.

For daily thermal cycle conditions, the oxide layers remain adherent even after consumption of the entire coating. However, residual stresses in AlN coatings at ambient temperature rapidly increase, and finally approach to their compressive strength, whereas stresses in the grown alumina layer gradually decreases, and are far from its compressive strength.

To further investigate the stress evolution within the coating(s)/substrate system during the cyclic oxidation, an analytical model is proposed. The model takes into account intrinsic CVD growth stress in the coating(s), operating conditions, creep relaxation and oxide scale growth process. Special analyses were made for a TZM coated with 60 μm AlN on both sides. The model reveals that the transformation of AlN to Al_2O_3 significantly affects the system symmetry, and thus alters the stress evolution. A high heat flux can result in a large stress gradient within the system, while a high working temperature of the heat transfer fluid ($\geq$ 1000 °C) facilitates the cracking and/or delamination of oxide scales during the cooling stage. The selection of slow-creeping coating and substrate materials leads to a nearly elastic evolution of stresses in the coatings and substrate. To reduce stresses in the coatings at high temperature, the intrinsic growth stress induced by CVD should be carefully controlled. The thermal mismatches between the oxide, coating(s) and substrate should be reduced as much as possible for the selection of materials. The choice of a material having a smaller thermal expansion (than the oxide) as the substrate will lead to a tensile residual stress in the oxide at ambient temperature, which is considered to cause cracking and spallation of the oxide scale. The model discussed in this thesis can be used to complete the criteria for the selection of materials for their use in solar receivers and can also help to find out their optimal operating conditions.

Moreover, the proposed model can be extended and used in other high temperature applications where high temperature, aggressive environment is coupled with mechanical loading to predict the stress evolution within the coating system, such as thermal-barrier coatings, and to estimate their lifetime. Optical properties of the stacks AlN/Fecralloy and AlN/APMT showed a significant solar absorptivity in the solar spectrum and a α/ε ratio close to 1. However, the development of the alumina scale leads to a degradation of the absorptivity. Therefore, it is not recommended to use alumina-forming materials as solar receiver materials. New measurements of optical and thermal properties, as well as durability at high temperature are needed to complete the evaluation of the AlN coating. The results in this thesis show that this coating is not the ideal material for CSP receivers working in air at temperature higher than 1000 °C. However, it is an efficient barrier on metals for the deposition of others ceramic coatings like SiC on high temperature alloys. The oxidation-resistant SiC/AlN coatings lead to higher absorptivity while maintaining an interesting solar spectral selectivity. However, the stresses generated in the coatings during cyclic oxidation lead to the formation of macro-cracks and delamination of the SiC/AlN coatings. A careful control of the coating-substrate interface should be made to avoid the cracking and/or delamination.

In summary, in this study, the potential of AlN and/or SiC coatings as alternative coating materials for solar receivers has been investigated. An analytical

model is proposed to simulate the stress evolution within the coating(s)/substrate system and complete the selection of materials. The SiC/AlN coatings seem to be promising materials for solar receivers operating at temperatures higher than 1000 °C.

Perspectives

This thesis has proposed a coating(s)/substrate system adapted to solar receivers operating at high temperature ($\geq$ 1000 °C) to improve the performance of concentrating solar power (CSP) plants. To confirm the potentiality of AlN/SiC coatings in solar receivers at temperatures above 1000 °C, some issues and questions need to be addressed in the future work:

Aluminization and/or silicidation of molybdenum-based substrate

Refractory-based alloys are promising substrate materials for their excellent thermal and mechanical properties. Moreover, their thermal expansion coefficients are close to that of AlN and SiC coatings. However, their processing technique and/or the cutting can lead to 'laminated' porosity, which may give rise to a catastrophic loss of protection during high temperature oxidation. Adequate surface coatings on these substrates are necessary prior the deposition of AlN to provide a first protection. Aluminization and/or silicidation of the substrates by CVD are proposed as alternative methods to address this issue in a further study.

Effect of microstructure of AlN coatings on their oxidation kinetics

As only few researches focus on the oxidation kinetics of AlN coatings or thin films, the relationship between the microstructure of AlN coatings and their oxidation kinetics is not yet fully understood. Casaux et al. [201] suggested that the oxidation of c-axis textured AlN coatings have better oxidation resistance. The oxidation resistance of AlN is a function of the total area formed by orthogonal projection of (0001) planes. Therefore, in a future work, the effect of microstructure of AlN coatings on their oxidation resistance should be investigated.

Development of the proposed analytical model

Despite the good agreement between numerical and experimental results, a list of recommendations for future researches for the development of the analytical model proposed in this thesis is given:

(1) delamination and/or spallation of the oxide scale should be taken into account in the model since tensile stress developed during the cooling stage can cause failure of the oxide;

(2) the interaction between oxygen diffusion, stress and creep relaxation can be introduced in the model to further extend its application;

(3) in this work, the oxidation temperature of AlN is assumed to be constant to simplify the calculations. However, the oxidation rate of AlN is strongly dependent on the temperature. When the thickness of the alumina layer is high, this assumption is no longer accurate. Time-dependent oxidation temperature should be further employed in the model.

Optimization and further characterizations of SiC coatings

The SiC coatings are deposited at a high degree of supersaturation in this thesis. Thus, their deposition conditions are needed to be further optimized. Moreover, in spite of the great interest shown by SiC coatings in their use for solar receivers able to meet the requirement of future CSP plants, new measurement of the optical properties of SiC coatings after long-term oxidation (> 100 h) and their durability during daily operation are needed to complete the evaluation of this coating.

Selection of substrate materials

Through the analyses in this thesis, the criteria of selection of materials can be further developed. Indeed, as previously mentioned, if the thermal expansion coefficient of the substrate is smaller than the coating(s) and/or oxide scale, tensile stress will be induced in the coating(s) and/or oxide scale. This is considered to cause cracking and/or delamination of coating(s) and/or oxide during the cooling stage. Nevertheless, the larger the mismatches of thermal expansion coefficients between the substrate, coating(s) and oxide, the larger the thermal stresses will be generated. The choice of material having slightly higher thermal expansion coefficient (than the coating(s) and oxide) as substrate can help to avoid the cracking and spallation of coating(s) and oxide.

The recently developed heating element, Kanthal Super ER (a molybdenum aluminosilicide ($Mo(Si,Al)_2$)-based composite) combines the good thermal and mechanical properties of molybdenum-based alloys and good oxidation resistance of alumina-forming materials. It also has a modest thermal expansion coefficient ($\sim 8\times10^{-6}$ K^{-1}), which is close to that of AlN (4.5×10^{-6} K^{-1}) and SiC (4×10^{-6} K^{-1}). It is therefore proposed as a promising substrate material in future studies. MAX phase materials like Ti_2AlC are also worth investigating for the same reason.

Résumé

Un système solaire à concentration consiste à produire de l'électricité à l'aide de systèmes optiques concentrateurs couplés à des systèmes récepteurs. Il permet de convertir la puissance rayonnée en puissance thermique puis en puissance électrique (Figure R.1). Contrairement aux installations solaires photovoltaïques dont le produit est directement l'électricité, les technologies solaires thermodynamiques génèrent de la chaleur. Le fluide chauffé ayant une certaine inertie thermique (capacité à stocker de la chaleur), la production d'électricité thermodynamique est donc moins 'saccadée' que la production d'électricité photovoltaïque. De surcroît, des systèmes de stockage dynamique de la chaleur peuvent être intégrés aux installations, prolongeant la génération d'électricité jusqu'à plusieurs heures après la disparition des rayonnements solaires. Afin de rendre cette filière plus compétitive, un des axes d'amélioration pour la technologie à tour est de concevoir des récepteurs capables de tolérer des températures de 1000 °C tout en conservant leur intégrité structurale et fonctionnelle. Des matériaux standards tels que les aciers inoxydables possèdent une bonne tenue mécanique ainsi qu'une forte résistance à la corrosion, mais leur température de service est généralement limitée à 600 °C. Des métaux réfractaires résistent à des températures de l'ordre de 2200 °C mais sont sujets aux problèmes d'oxydation à haute température. Des alliages de nickel à haute teneur en chrome peuvent être utilisés pour les récepteurs solaires fonctionnant à des températures de l'ordre de 700-800 °C. Les céramiques denses ou poreuses sont les matériaux les plus appropriés pour des températures supérieures à 800 °C. Des températures de 1200 °C peuvent être atteintes avec des céramiques SiSiC et 1500 °C avec des céramiques SiC. Mais l'inconvénient majeur est leur fragilité mécanique. Ainsi, les matériaux idéaux pour un récepteur solaire à températures supérieures à 1000 °C doivent être capable de résister à des sollicitations extrêmes telles que l'oxydation cyclique tout en conservant une stabilité mécanique (bonne résistance au fluage et à la fracture, faible coefficient dilatation thermique), en transmettant efficacement la chaleur (conductivité thermique élevée et), et en absorbant l'énergie solaire (sélectivité spectrale définie).

L'objectif de cette thèse est de concevoir un système composé (1) d'un alliage métallique choisi pour ses bonnes propriétés mécaniques et thermiques, (2) un revêtement externe conférant les propriétés de surface requises (sélectivité spectrale, résistance à l'oxydation) et (3) de couches intermédiaires entre le revêtement externe et le matériau métallique assurant la compatibilité chimique et mécanique de l'ensemble (Figure R.2). Le démonstrateur réalisé devra pouvoir résister à plusieurs cycles thermiques en conditions extrêmes (sous air,

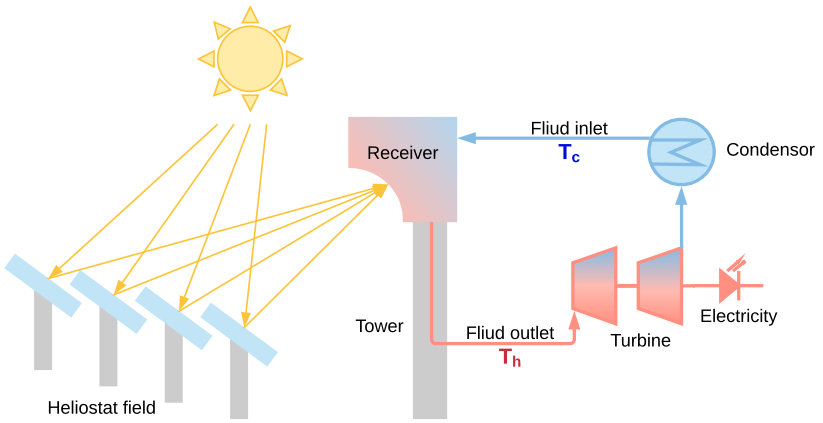

Figure R.1 Schéma des technologies solaires à concentration.

T≥1000 °C).

Le nitrure d'aluminium (AlN) et le carbure de silicium (SiC) sont choisis comme revêtements pour leur conductivité thermique élevée, faible coefficient de dilatation thermique, stabilité à haute température et capacité à développer d'oxydes stables à haute température. Deux types d'alliages sont choisis comme substrats : (1) des alliages métalliques réfractaires pour leur bonne conductivité thermique et bonne résistance au fluage et à la fracture et (2) des alliages FeCrAl (Fecralloy et Kanthal APMT) pour leur capacité à développer des couches d'alumine stable à haute température et de simplifier la caractérisation de la durée de vie des revêtements. La méthodologie suivie dans cette thèse consiste à (1) déposer un revêtement par dépôt chimique en phase vapeur à haute température (HTCVD), (2) caractériser la microstructure, la résistance à l'oxydation, la durabilité et les propriétés optiques des revêtements et (3) étudier l'évolution des contraintes dans le système revêtement(s)/substrat au cours de son fonctionnement.

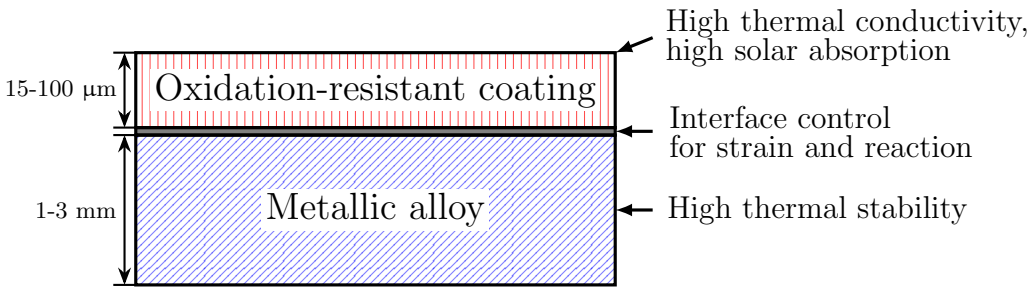

Figure R.2 Schéma des empilements de matériaux pour les récepteurs solaires.

Les analyses morphologiques et microstructurales des revêtements d'AlN sont réalisées par DRX, MEB et EBSD. Les revêtements sont polycristallins et présentent une microstructure colonnaire. Sur les alliages à base de molybdène (TZM), la température de dépôt élevée (1200 °C) conduit à une orientation préférentielle ($11\bar{2}2$) (Figure R.3). Une telle texture permet une diffusion rapide

de l'oxygène par les joints de grains, et donc une dégradation rapide à haute température.

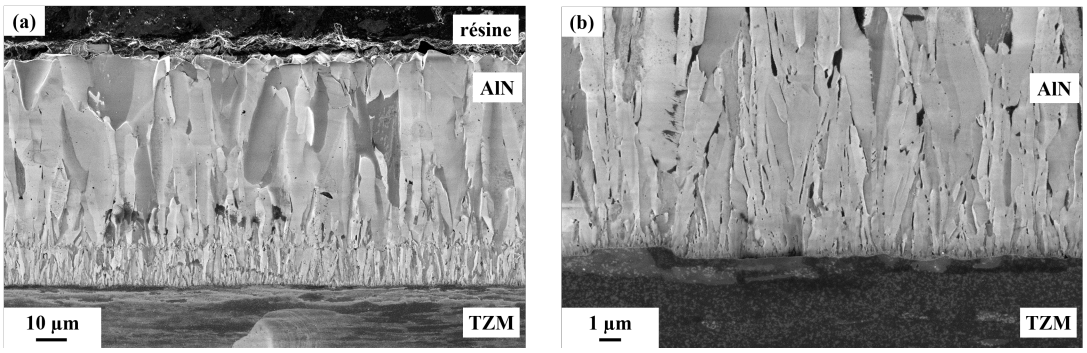

Figure R.3 (a) Exemple de texture sur les revêtements déposés sur TZM et (b) une grande magnification de (a) à l'interface AlN/TZM.

Sur les alliages Fecralloy et APMT, les revêtements d'AlN sont déposés à 1100 °C. La morphologie de surface et la microstructure des revêtements sont identiques sur ces deux substrats (Figure R.4). Des études ont montré que l'évolution de la microstructure et de l'orientation préférentielle dépendent fortement du rapport N/Al (rapport $NH_3/AlCl_3$ en phase gazeuse). Les études montrent que plus le rapport N/Al est élevé, plus la sursaturation est importante. L'augmentation de la sursaturation entraîne une diminution de la taille des grains de revêtements d'AlN. A un faible degré de sursaturation (N/Al<5), le revêtement est dense et le plan semi-polaire $(10\bar{1}2)$ est favorisé. A un degré élevé de sursaturation (N/Al>5), les joints de grains immobiles sont formés par la coalescence des petits îlots initiales avec des rapports surface/volume élevés. La croissance compétitive suivant la coalescence conduit à une sélection incomplète de l'orientation, donc à une couche faiblement texturée.

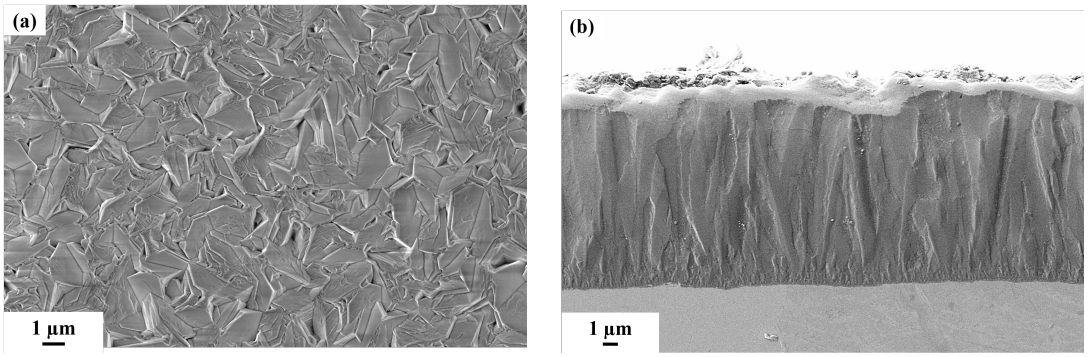

Figure R.4 Exemple de texture sur les revêtements déposés sur acier: (a) la morphologie de surface et (b) la microstructure.

L'oxydation des revêtements d'AlN sur Fecralloy et APMT a été étudiée à des températures variant entre 800 et 1100 °C. Une cinétique d'oxydation linéaire a été mesurée dans cette gamme de température. Des couches très fines composées

principalement d'alumine sont analysées entre 800 et 900 °C. La durée de vie des revêtements de 45 μm peut être de quelques années. Pour la température de 1100 °C, la durée de vie du revêtement dépend de son épaisseur, environ 500 h pour un revêtement de 45 μm (Figure R.5).

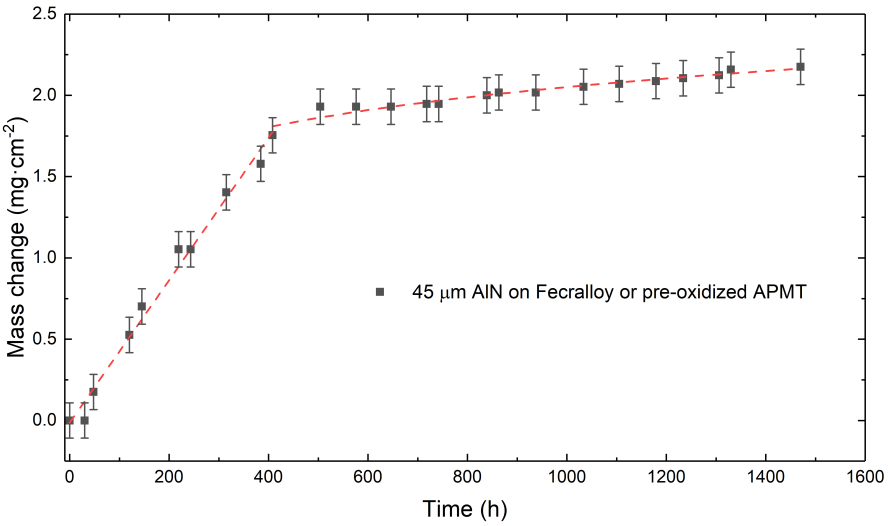

Figure R.5 Cinétique d'oxydation d'une couche de 45 μm d'AlN sur Fecralloy (ou APMT).

La cinétique d'oxydation linéaire est le résultat de la croissance d'une couche d'alumine poreuse (Figure R.6) conduisant à une diffusion rapide de l'oxygène à travers la couche d'alumine. La réaction limitante se produit ainsi à l'interface alumine/AlN. Ensuite, le revêtement d'AlN est entièrement converti en alumine. L'oxydation se poursuit dans le substrat. Les couches d'alumine restent adhérentes en conditions cycliques même après la consommation totale du revêtement. De plus, les contraintes résiduelles dans ces couches diminuent progressivement et sont loin de la résistance à la compression de l'alumine. Par contre, les contraintes résiduelles dans les revêtements augmentent rapidement et s'approchent de leur résistance à la compression.

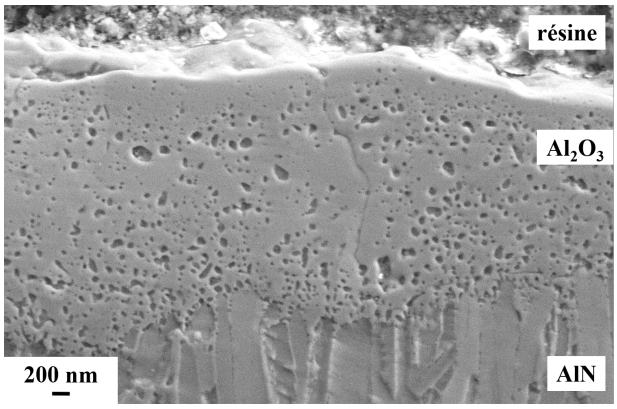

Figure R.6 Mise en évidence de la porosité de la couche d'alumine formée au cours de l'oxydation.

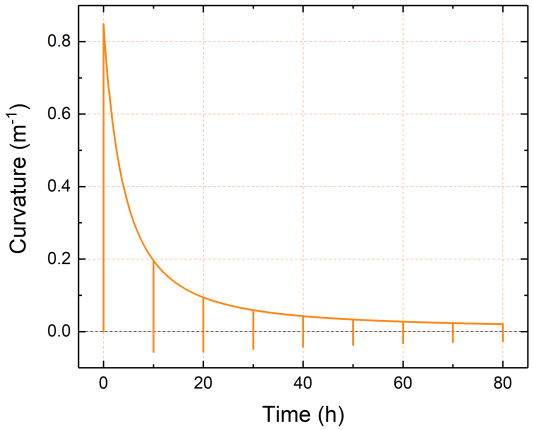

(a) Courbure

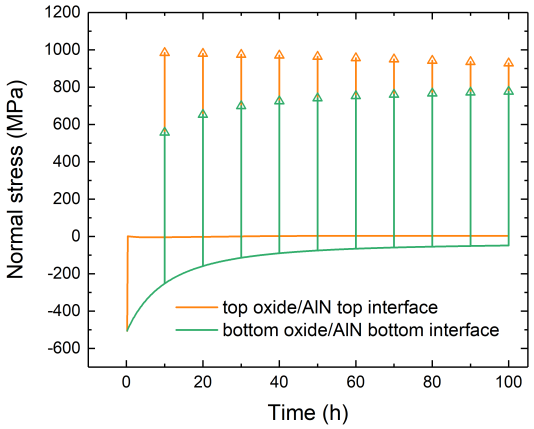

(b) Contrainte dans l'oxyde à l'interface oxyde/AlN

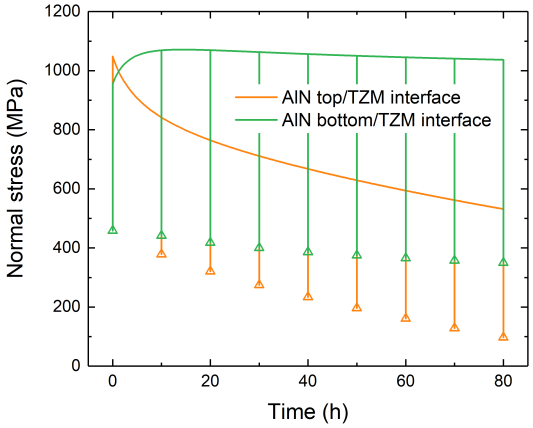

(c) Contrainte dans l'AlN à l'interface AlN/substrat

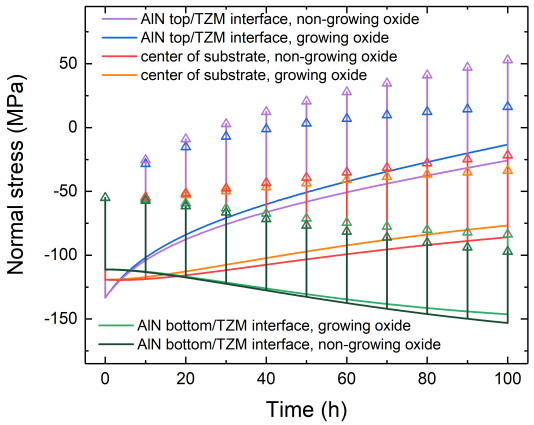

(d) Contrainte dans le substrat

Figure R.7 Mise en évidence des contraintes dans le système revêtement/substrat: (a) évolution de courbure du système, et évolution des contraintes (b) à l'interface oxyde/AlN (dans l'oxyde), (c) à l'interface AlN/substrat (dans la couche d'AlN) et (d) dans le substrat; les triangles représentent la courbure et/ou les contraintes à température ambiante.

Un modèle analytique est développé pour étudier en détail l'évolution des contraintes dans le système revêtement(s)/substrat au cours de l'oxydation cyclique. Les contraintes de croissance du revêtement, les conditions thermiques de fonctionnement d'un récepteur solaire, la relaxation par fluage du matériau à haute température et l'oxydation sont pris en compte dans le modèle. Les résultats montrent que la transformation d'AlN en alumine affecte de manière significative la symétrie du système et ainsi modifie l'évolution des contraintes (Figure R.7). Un flux de chaleur élevé imposé peut entraîner un gradient de contrainte important dans le système, tandis qu'une température de fluide caloporteur élevée facilite la relaxation des contraintes dans la couche d'alumine à haute température et l'accumulation des contraintes pendent le refroidissement. Les matériaux possédant une bonne résistance de fluage permettent d'obtenir une évolution des contraintes quasi-élastique dans le système. Pour réduire les contraintes dans les revêtements à haute température, les contraintes de croissance dans les revêtements, induites pendent le dépôt CVD, doivent être contrôlées. Les différences de coefficients de dilatation thermiques entre l'oxyde, le(s) revêtement(s) et le substrat doivent être minimisées. Le choix d'un substrat ayant une dilatation thermique inférieure (à celle de l'oxyde) entraîne une contrainte résiduelle de traction dans l'oxyde à la température ambiante. Ceci est considéré comme une cause de fissuration et d'écaillement de la couche d'oxyde. Le modèle présenté dans cette thèse peut être utilisé pour compléter les critères de sélection des matériaux et peut également aider à déterminer leurs conditions de fonctionnement optimales. De plus, ce modèle peut être étendu et utilisé pour d'autres applications à haute température pour prédire l'évolution des contraintes dans le système de revêtement(s)/substrat en cours d'utilisation et pour estimer leur durée de vie.

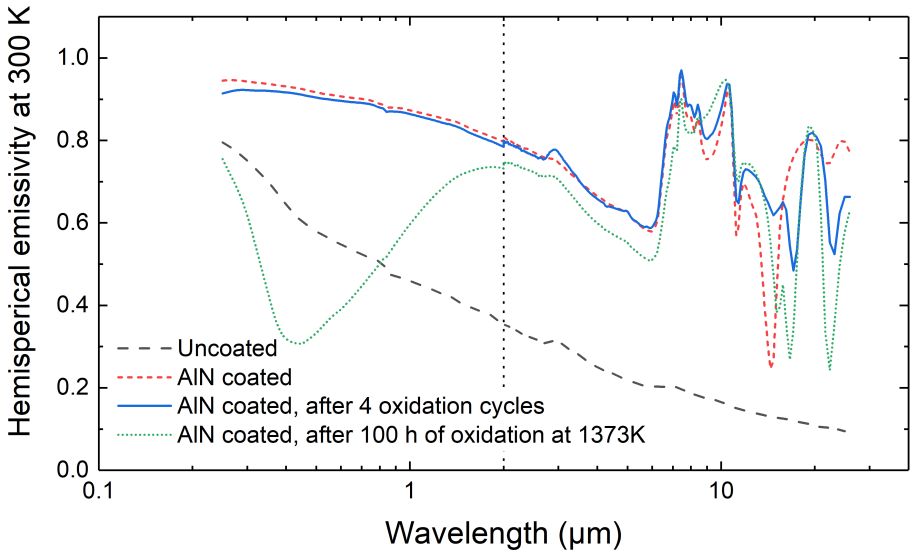

Figure R.8 Emissivité hémisphérique spectrale à 300 K des échantillons d'APMT revêtu d'AlN (45 μm) et oxydé.

Les revêtements d'AlN augmentent l'absorptivité solaire des substrats avec un rapport absorptivité/émissivité supérieur à 1. La croissance d'alumine au

cours de l'oxydation entraîne une dégradation de l'absorptivité (Figure R.8). Par conséquent, ce revêtement formant de l'alumine, l'une des meilleures barrières à haute température, n'est pas un candidat idéal pour les récepteurs solaires fonctionnant sous l'air à une température supérieure à 1000 °C. De nouvelles mesures des propriétés optiques et thermiques, ainsi que des propriétés à haute température sont nécessaires pour compléter l'évaluation de ces revêtements. Toutefois, ces revêtements sont parmi les rares matériaux (hors oxydes) qui ne réagissent pas avec les matériaux métalliques. Ils peuvent utilisés comme barrière de diffusion sur les alliages pour le dépôt d'autres revêtements céramiques comme le SiC. Notre étude montre que les bicouches revêtement SiC/AlN augmentent l'absorptivité d'une manière significative en conservant une sélectivité spectrale solaire intéressant. Cependant, les contraintes générées dans les revêtements pendent l'oxydation cyclique conduisent à la formation de macro-fissures et à la délamination des revêtements SiC/AlN. Un contrôle prudent de l'interface revêtement/substrat doit être effectué pour éviter les fissures et la délamination.

En conclusion, la possibilité d'utiliser des revêtements d'AlN pour les récepteurs solaires fonctionnant à haute température ($\geq$1000 °C) a été étudiée. L'objectif de l'efficacité de ces revêtements à plus de 1000 °C n'a pu être démontré. Ils peuvent par contre être utilisés comme barrière de diffusion sur les matériaux métalliques pour permettre la croissance d'autres céramiques conductrices thermiquement telles que le carbure de silicium. Un modèle analytique est proposé pour simuler l'évolution des contraintes dans le système revêtement(s)/substrat, et peut être utilisé pour compléter la sélection des matériaux. Les revêtements SiC/AlN optimisent l'absorptivité du substrat, et peuvent être soumis à des conditions d'utilisation extrêmes.

References

[1] Philibert, C. *Solar Energy Perspectives*; Organisation for Economic Co-operation and Development/International Energy Agency (OECD/IEA), 2011.

[2] Turchi, C. Supercritical CO_2 power cycles: Next-Gen Power for CSP? SunShot CSP Summit and Integration Workshop. 2016.

[3] Chacartegui, R.; Sánchez, D.; Muñoz, J.; Sánchez, T. Alternative ORC bottoming cycles for combined cycle power plants. *Applied Energy* **2009**, *86*, 2162 – 2170.

[4] Siefert, J. A.; Libby, C.; Shingledecker, J. Concentrating solar power (CSP) power cycle improvements through application of advanced materials. *AIP Conference Proceedings* **2016**, *1734*, 070030.

[5] Chordia, L.; Portnoff, M. A.; Green, E. *High temperature heat exchanger design and fabrication for systems with large pressure differentials*; 2017.

[6] Swindeman, R. W. *A review & assessment of current operating conditions allowable stresses in ASME Section III subsection NH*; 2009.

[7] Slack, G. A.; Tanzilli, R.; Pohl, R.; Vandersande, J. The intrinsic thermal conductivity of AIN. *Journal of Physics and Chemistry of Solids* **1987**, *48*, 641 – 647.

[8] Slack, G. A. Thermal conductivity of pure and impure silicon, silicon carbide, and diamond. *Journal of Applied Physics* **1964**, *35*, 3460 – 3466.

[9] Reeber, R. R.; Wang, K. Lattice Parameters and Thermal Expansion of Important Semiconductors and Their Substrates. *MRS Proceedings* **2000**, *622*, T6.35.1.

[10] Su, J.; Boichot, R.; Blanquet, E.; Mercier, F.; Pons, M. Chemical vapor deposition of titanium nitride thin films: kinetics and experiments. *CrystEngComm* **2019**, *21*, 3974 – 3981.

[11] Freund, L. B.; Suresh, S. *Thin Film Materials: Stress, Defect Formation and Surface Evolution*; Cambridge University Press, 2004.

[12] Van der Drift, A. Evolutionary selection, a principle governing growth orientation in vapour-deposited layers. *Philips Res. Rep* **1967**, *22*, 267.

[13] Wu, B.; Bai, J.; Tassev, V.; Nakarmi, M. L.; Sun, W.; Huang, X.; Dudley, M.; Zhang, H.; Bliss, D.; Lin, J., et al. Stress evolution during the early stages of AlN vapor growth. Materials Research Society Symposium Proceedings. 2006; p 653.

[14] Stevenson, A.; Jones, A.; Raghavan, S. Characterization of particle dispersion and volume fraction in alumina-filled epoxy nanocomposites using photo-stimulated luminescence spectroscopy. *Polymer journal* **2011**, *43*, 923.

[15] Claudel, A.; Blanquet, E.; Chaussende, D.; Boichot, R.; Martin, R.; Mank, H.; Crisci, A.; Doisneau, B.; Chaudouet, P.; Coindeau, S., et al. Growth and Characterization of Thick Polycrystalline AlN Layers by HTCVD. *Journal of The Electrochemical Society* **2011**, *158*, H328 – H332.

[16] Quadakkers, W. J.; Bongartz, K. The prediction of breakaway oxidation for alumina forming ODS alloys using oxidation diagrams. *Materials and Corrosion* **1994**, *45*, 232 – 241.

[17] Dollet, A.; Casaux, Y.; Matecki, M.; Rodriguez-Clemente, R. Chemical vapour deposition of polycrystalline AlN films from $AlCl_3$–NH_3 mixtures: II — surface morphology and mechanisms of preferential orientation at low-pressure. *Thin Solid Films* **2002**, *406*, 118 – 131.

[18] Meyers, M. A.; Chawla, K. K. *Mechanical Behavior of Materials*, second edition ed.; Cambtidge University Press, 2009.

[19] Clarke, D. The lateral growth strain accompanying the formation of a thermally grown oxide. *Acta Materialia* **2003**, *51*, 1393 – 1407.

[20] Romero, M.; Buck, R.; Pacheco, J. E. An update on solar central receiver systems, projects, and technologies. *Journal of Solar Energy Engineering* **2002**, *124*, 98 – 108.

[21] Ahmadi, M. H.; Ghazvini, M.; Sadeghzadeh, M.; Alhuyi Nazari, M.; Kumar, R.; Naeimi, A.; Ming, T. Solar power technology for electricity generation: A critical review. *Energy Science & Engineering* **2018**, *6*, 340 – 361.

[22] Tian, Y.; Zhao, C. A review of solar collectors and thermal energy storage in solar thermal applications. *Applied Energy* **2013**, *104*, 538 – 553.

[23] SolarReserve, Crescent Dunes Solar Energy Project. `https://www.solarreserve.com/en/global-projects/csp/crescent-dunes`.

[24] Alexopoulos, S.; Hoffschmidt, B. Advances in solar tower technology. *Wiley Interdisciplinary Reviews: Energy and Environment* **2016**, *6*, e217.

[25] National Renewable Energy Laboratory (NREL), Concentrating Solar Power Projects. `https://solarpaces.nrel.gov/`.

[26] Hennecke, K.; Schwarzbözl, P.; Koll, G.; Beuter, M.; Hoffschmidt, B.; Göttsche, J.; Hartz, T. The solar power tower Jülich — A solar thermal power plant for test and demonstration of air receiver technology. Proceedings of ISES World Congress 2007 (Vol. I – Vol. V). Berlin, Heidelberg, 2009; pp 1749 – 1753.

[27] Zhu, G.; Libby, C. Review and future perspective of central receiver design and performance. *AIP Conference Proceedings* **2017**, *1850*, 030052.

[28] Ho, C. K.; Iverson, B. D. Review of high-temperature central receiver designs for concentrating solar power. *Renewable and Sustainable Energy Reviews* **2014**, *29*, 835 – 846.

[29] Ho, C. K. Advances in central receivers for concentrating solar applications. *Solar Energy* **2017**, *152*, 38 – 56, Progress in Solar Energy Special Issue: Concentrating Solar Power (CSP).

[30] Behar, O.; Khellaf, A.; Mohammedi, K. A review of studies on central receiver solar thermal power plants. *Renewable and Sustainable Energy Reviews* **2013**, *23*, 12 – 39.

[31] Turchi, C. S.; Ma, Z.; Neises, T. W.; Wagner, M. J. Thermodynamic study of advanced supercritical carbon dioxide power cycles for concentrating solar power systems. *Journal of Solar Energy Engineering* **2013**, *135*, 041007.

[32] Sarvghad, M.; Maher, S. D.; Collard, D.; Tassan, M.; Will, G.; Steinberg, T. A. Materials compatibility for the next generation of concentrated solar power plants. *Energy Storage Materials* **2018**, *14*, 179 – 198.

[33] He, J.; Clarke, D. R. Determination of the Piezospectroscopic Coefficients for Chromium-Doped Sapphire. *Journal of the American Ceramic Society* **1995**, *78*, 1347 – 1353.

[34] Vasudévan, A.; Petrovic, J. A comparative overview of molybdenum disilicide composites. *Materials Science and Engineering: A* **1992**, *155*, 1 – 17, Proceedings of the First High Temperature Structural Silicides Workshop.

[35] Ayers, J. E.; Kujofsa, T.; Rago, P.; Raphael, J. *Heteroepitaxy of semiconductors: theory, growth, and characterization*; CRC press, 2016.

[36] Yim, W. M.; Paff, R. J. Thermal expansion of AlN, sapphire, and silicon. *Journal of Applied Physics* **1974**, *45*, 1456 – 1457.

[37] Levinshtein, M. E.; Rumyantsev, S. L.; Shur, M. S. *Properties of Advanced Semiconductor Materials: GaN, AIN, InN, BN, SiC, SiGe*; John Wiley & Sons, 2001.

[38] Vasudev, A.; More, K.; Ailey-Trent, K.; Davis, R. Kinetics and mechanisms of high-temperature creep in polycrystalline aluminum nitride. *Journal of Materials Research* **1993**, *8*, 1101 – 1108.

[39] Plansee, Propertities of Molybdeum. `https://www.plansee.com/en/materials/molybdenum.html`.

[40] Maag, W.; Mattson, W. *Experimental biaxial creep data for tantalum, molybdenum, and alloys T-111, TZM, and TZC*; 1971.

[41] Shackelford, J. F.; Alexander, W. *CRC Materials Science and Engineering Handbook*, third edition ed.; CRC press LLC, 2001.

[42] Kalogirou, S. A. In *Solar Energy Engineering*; Kalogirou, S. A., Ed.; Academic Press: Boston, 2009; pp 521 – 552.

[43] Richter, C.; Teske, S.; Short, R. In *Concentrating solar power — Global outlook 2009*; Short, R., Writer, T., Eds.; Greenpeace International, European Solar Thermal Electricity Association (ESTELA) and SolarPACES, 2009.

[44] Lovegrove, K., Stein, W., Eds. *Concentrating Solar Power Technology: Principles, Developments and Applications*; Woodhead Publishing, 2012.

[45] Lata, J. M.; Rodríguez, M.; de Lara, M. Á. High flux central receivers of molten salts for the new generation of commercial stand-alone solar power plants. *Journal of Solar Energy Engineering* **2008**, *130*, 021002.

[46] Dunham, M. T.; Iverson, B. D. High-efficiency thermodynamic power cycles for concentrated solar power systems. *Renewable and Sustainable Energy Reviews* **2014**, *30*, 758 – 770.

[47] Schwarzbözl, P.; Buck, R.; Sugarmen, C.; Ring, A.; Crespo, M. J. M.; Altwegg, P.; Enrile, J. Solar gas turbine systems: Design, cost and perspectives. *Solar Energy* **2006**, *80*, 1231 – 1240, Solar Power and Chemical Energy Systems (SolarPACES'04).

[48] Heller, P.; Pfänder, M.; Denk, T.; Tellez, F.; Valverde, A.; Fernandez, J.; Ring, A. Test and evaluation of a solar powered gas turbine system. *Solar Energy* **2006**, *80*, 1225 – 1230, Solar Power and Chemical Energy Systems (SolarPACES'04).

[49] Poživil, P.; Aga, V.; Zagorskiy, A.; Steinfeld, A. A pressurized air receiver for solar-driven gas turbines. *Energy Procedia* **2014**, *49*, 498 – 503, Proceedings of the SolarPACES 2013 International Conference.

[50] Barigozzi, G.; Bonetti, G.; Franchini, G.; Perdichizzi, A.; Ravelli, S. Thermal performance prediction of a solar hybrid gas turbine. *Solar Energy* **2012**, *86*, 2116 – 2127.

[51] Buck, R.; Giuliano, S.; Uhlig, R. In *Advances in Concentrating Solar Thermal Research and Technology*; Blanco, M. J., Santigosa, L. R., Eds.; Woodhead Publishing Series in Energy; Woodhead Publishing, 2017; pp 353 – 382.

[52] CNRS-PROMES, PEGASE, Production d'Electricité par turbine à GAz et énergie SolairE. `https://www.promes.cnrs.fr/index.php?page=pegase-accueil`.

[53] Grange, B. Modélisation et dimensionnement d'un récepteur solaire à air pressurisé pour le projet PEGASE. PhDthesis, Université de Perpignan, 2012.

[54] Kretzschmar, H.; Gauché, P. Hybrid pressurized air receiver for the SUNSPOT cycle. 1st South African Solar Energy Conference (SASEC). 2012; pp 21 – 23.

[55] Ho, C. K.; Mahoney, A. R.; Ambrosini, A.; Bencomo, M.; Hall, A.; Lambert, T. N. Characterization of Pyromark 2500 paint for high-temperature solar receivers. *Journal of Solar Energy Engineering* **2014**, *136*, 014502.

[56] Abe, F. Research and development of heat-resistant materials for advanced USC power plants with steam temperatures of 700 °C and above. *Engineering* **2015**, *1*, 211 – 224.

[57] Viswanathan, R.; Henry, J. F.; Tanzosh, J.; Stanko, G.; Shingledecker, J.; Vitalis, B.; Purgert, R. U.S. program on materials technology for ultra-supercritical coal power plants. *Journal of Materials Engineering and Performance* **2005**, *14*, 281 – 292.

[58] Bradshaw, R. W.; Dawson, D.; De la Rosa, W.; Gilbert, R.; Goods, S.; Hale, M.; Jacobs, P.; Jones, S. A.; Kolb, G. J.; Pacheco, J. E.; Prairie, M. R.; Reilly, H. E.; Showalter, S. K.; Vant-Hull, L. L. *Final test and evaluation results from the solar two project*; 2002.

[59] Kolb, G. J. *An evaluation of possible next-generation high-temperature molten-salt power towers*; 2011.

[60] Shingledecker, J. P.; Siefert, J. A. Age hardenable nickel-based alloy developments and research for new high temperature power cycles. Proceedings of the 9th International Symposium on Superalloy 718 & Derivatives: Energy, Aerospace, and Industrial Applications. Cham, 2018; pp 3 – 22.

[61] Ortega, J.; Khivsara, S.; Christian, J.; Ho, C.; Yellowhair, J.; Dutta, P. Coupled modeling of a directly heated tubular solar receiver for supercritical carbon dioxide Brayton cycle: Optical and thermal-fluid evaluation. *Applied Thermal Engineering* **2016**, *109*, 970 – 978, Special Issue: Solar Energy Research Institute for India and the United States (SERIIUS) – Concentrated Solar Power.

[62] Ortega, J.; Khivsara, S.; Christian, J.; Ho, C.; Dutta, P. Coupled modeling of a directly heated tubular solar receiver for supercritical carbon dioxide Brayton cycle: Structural and creep-fatigue evaluation. *Applied Thermal*

Engineering **2016**, *109*, 979 – 987, Special Issue: Solar Energy Research Institute for India and the United States (SERIIUS) – Concentrated Solar Power.

[63] Li, Q.; de Tourville, N. G.; Yadroitsev, I.; Yuan, X.; Flamant, G. Micro-channel pressurized-air solar receiver based on compact heat exchanger concept. *Solar Energy* **2013**, *91*, 186 – 195.

[64] Moon, J.; Kim, T. K.; VanSaders, B.; Choi, C.; Liu, Z.; Jin, S.; Chen, R. Black oxide nanoparticles as durable solar absorbing material for high-temperature concentrating solar power system. *Solar Energy Materials and Solar Cells* **2015**, *134*, 417 – 424.

[65] Boubault, A.; Claudet, B.; Faugeroux, O.; Olalde, G. Accelerated aging of a solar absorber material subjected to highly concentrated solar flux. *Energy Procedia* **2014**, *49*, 1673 – 1681, Proceedings of the SolarPACES 2013 International Conference.

[66] Boubault, A.; Claudet, B.; Faugeroux, O.; Olalde, G. Aging of solar absorber materials under highly concentrated solar fluxes. *Solar Energy Materials and Solar Cells* **2014**, *123*, 211 – 219.

[67] Setien, E.; Fernández-Reche, J.; Álvarez-de Lara, M.; Ariza, M. J. Experimental system for long term aging of highly irradiated tube type receivers. *Solar Energy* **2014**, *105*, 303 – 313.

[68] Mehos, M.; Turchi, C.; Vidal, J.; Wagner, M.; Ma, Z.; Ho, C.; Kolb, W.; Andraka, C.; Kruizenga, A. *Concentrating solar power Gen3 demonstration roadmap*; 2017.

[69] Sakthivel, T.; Laha, K.; Nandagopal, M.; Chandravathi, K.; Parameswaran, P.; Selvi, S. P.; Mathew, M.; Mannan, S. K. Effect of temperature and strain rate on serrated flow behaviour of Hastelloy X. *Materials Science and Engineering: A* **2012**, *534*, 580 – 587.

[70] Special Metals, Inconel® alloy 625LCF. Under "Products" at www.specialmetals.com.

[71] Special Metals, Inconel® alloy 740H. Under "Products" at www.specialmetals.com.

[72] Special Metals, Inconel® alloy 800H/800HT®. Under "Products" at www.specialmetals.com.

[73] Falcone, P. *A handbook for solar central receiver design*; 1986.

[74] Boiler,; Pressure Vessel Code, A. Section I—Rules for construction of power boilers and Section II—Materials. *American Society of Mechanical Engineeers, New York, USA* **2007**,

[75] Rojas-Morín, A.; Fernández-Reche, J. Estimate of thermal fatigue lifetime for the Inconel 625LCF plate while exposed to concentrated solar radiation. *Revista de Metalurgia* **2011**, *47*, 112 – 125.

[76] Olivares, R. I.; Stein, W.; Marvig, P. Thermogravimetric study of oxidation-resistant alloys for high-temperature solar receivers. *JOM* **2013**, *65*, 1660 – 1669.

[77] Ávila Marín, A. L. Volumetric receivers in solar thermal power plants with central receiver system technology: A review. *Solar Energy* **2011**, *85*, 891 – 910.

[78] Chavez, J. M.; Chaza, C. Testing of a porous ceramic absorber for a volumetric air receiver. *Solar Energy Materials* **1991**, *24*, 172 – 181.

[79] Karni, J.; Kribus, A.; Doron, P.; Rubin, R.; Fiterman, A.; Sagie, D. The DIAPR: a high-pressure, high-temperature solar receiver. *Journal of solar energy engineering* **1997**, *119*, 74 – 78.

[80] Kribus, A.; Doron, P.; Rubin, R.; Reuven, R.; Taragan, E.; Duchan, S.; Karni, J. Performance of the directly-irradiated annular pressurized receiver (DIAPR) operating at 20 bar and 1200 °C. *Journal of Solar Energy Engineering* **2001**, *123*, 10 – 17.

[81] Fend, T.; Robert-Pitz-Paal,; Reutter, O.; Bauer, J.; Hoffschmidt, B. Two novel high-porosity materials as volumetric receivers for concentrated solar radiation. *Solar Energy Materials and Solar Cells* **2004**, *84*, 291 – 304, International Solar Energy Society World Congress 2003.

[82] Agrafiotis, C. C.; Mavroidis, I.; Konstandopoulos, A. G.; Hoffschmidt, B.; Stobbe, P.; Romero, M.; Fernandez-Quero, V. Evaluation of porous silicon carbide monolithic honeycombs as volumetric receivers/collectors of concentrated solar radiation. *Solar Energy Materials and Solar Cells* **2007**, *91*, 474 – 488.

[83] Capeillère, J.; Toutant, A.; Olalde, G.; Boubault, A. Thermomechanical behavior of a plate ceramic solar receiver irradiated by concentrated sunlight. *Solar Energy* **2014**, *110*, 174 – 187.

[84] Leray, C.; Ferriere, A.; Toutant, A.; Olalde, G.; Peroy, J.-Y.; Chéreau, P.; Ferrato, M. Design and proof of concept of an innovative very high temperature ceramic solar absorber. *AIP Conference Proceedings* **2017**, *1850*, 030032.

[85] Leray, C. Study of the thermomechanical behavior of a ceramic solar absorber submitted to high solar flux. PhDthesis, Université de Perpignan, 2017.

[86] Sani, E.; Mercatelli, L.; Francini, F.; Sans, J.-L.; Sciti, D. Ultra-refractory ceramics for high-temperature solar absorbers. *Scripta Materialia* **2011**, *65*, 775 – 778.

[87] Caccia, M. et al. Ceramic–metal composites for heat exchangers in concentrated solar power plants. *Nature* **2018**, *562*, 406 – 409.

[88] Sani, E.; Mercatelli, L.; Sansoni, P.; Silvestroni, L.; Sciti, D. Spectrally selective ultra-high temperature ceramic absorbers for high-temperature solar plants. *Journal of Renewable and Sustainable Energy* **2012**, *4*, 033104.

[89] Sani, E.; Mercatelli, L.; Fontani, D.; Sans, J.-L.; Sciti, D. Hafnium and tantalum carbides for high temperature solar receivers. *Journal of Renewable and Sustainable Energy* **2011**, *3*, 063107.

[90] Kennedy, C. E. *Review of mid- to high-temperature solar selective absorber Materials*; 2002.

[91] Wuchina, E.; Opila, E.; Opeka, M.; Fahrenholtz, W.; G. Talmy, I. UHTCs: Ultra-High Temperature Ceramic Materials for Extreme Environment Applications. *Electrochemical Society Interface* **2007**, *16*, 30–36.

[92] Fahrenholtz, W. G.; Hilmas, G. E.; Talmy, I. G.; Zaykoski, J. A. Refractory diborides of zirconium and hafnium. *Journal of the American Ceramic Society* **2007**, *90*, 1347 – 1364.

[93] Opeka, M. M.; Talmy, I. G.; Zaykoski, J. A. Oxidation-based materials selection for 2000 °C + hypersonic aerosurfaces: Theoretical considerations and historical experience. *Journal of Materials Science* **2004**, *39*, 5887 – 5904.

[94] Silvestroni, L.; Kleebe, H.-J.; Fahrenholtz, W. G.; Watts, J. Super-strong materials for temperatures exceeding 2000 °C. *Scientific Reports* **2017**, *7*, 40730.

[95] Harrington, G. J. K.; Hilmas, G. E. In *Ultra-High Temperature Ceramics*; Fahrenholtz, W. G., Wuchina, E. J., Lee, W. E., Zhou, Y., Eds.; John Wiley & Sons, Ltd, 2014; pp 197 – 235.

[96] Sciti, D.; Silvestroni, L.; Mercatelli, L.; Sans, J.-L.; Sani, E. Suitability of ultra-refractory diboride ceramics as absorbers for solar energy applications. *Solar Energy Materials and Solar Cells* **2013**, *109*, 8 – 16.

[97] Sciti, D.; Silvestroni, L.; Sans, J.-L.; Mercatelli, L.; Meucci, M.; Sani, E. Tantalum diboride-based ceramics for bulk solar absorbers. *Solar Energy Materials and Solar Cells* **2014**, *130*, 208 – 216.

[98] Mercatelli, L.; Sani, E.; Jafrancesco, D.; Sansoni, P.; Fontani, D.; Meucci, M.; Coraggia, S.; Marconi, L.; Sans, J.-L.; Beche, E.; Silvestroni, L.; Sciti, D. Ultra-refractory diboride ceramics for solar plant receivers. *Energy Procedia* **2014**, *49*, 468 – 477, Proceedings of the SolarPACES 2013 International Conference.

[99] Sani, E.; Mercatelli, L.; Meucci, M.; Silvestroni, L.; Balbo, A.; Sciti, D. Process and composition dependence of optical properties of zirconium, hafnium and tantalum borides for solar receiver applications. *Solar Energy Materials and Solar Cells* **2016**, *155*, 368 – 377.

[100] Musa, C.; Licheri, R.; Orrù, R.; Cao, G.; Balbo, A.; Zanotto, F.; Mercatelli, L.; Sani, E. Optical characterization of hafnium boride and hafnium carbide-based ceramics for solar energy receivers. *Solar Energy* **2018**, *169*, 111 – 119.

[101] Silvestroni, L.; Sciti, D.; Zoli, L.; Balbo, A.; Zanotto, F.; Orrù, R.; Licheri, R.; Musa, C.; Mercatelli, L.; Sani, E. An overview of ultra-refractory ceramics for thermodynamic solar energy generation at high temperature. *Renewable Energy* **2019**, *133*, 1257 – 1267.

[102] Sarwar, J.; Shrouf, T.; Srinivasa, A.; Gao, H.; Radovic, M.; Kakosimos, K. Characterization of thermal performance, flux transmission performance and optical properties of MAX phase materials under concentrated solar irradiation. *Solar Energy Materials and Solar Cells* **2018**, *182*, 76 – 91.

[103] Granqvist, C. G. Solar energy materials. *Advanced Materials* **2003**, *15*, 1789 – 1803.

[104] López-Herraiz, M.; Fernández, A. B.; Martinez, N.; Gallas, M. Effect of the optical properties of the coating of a concentrated solar power central receiver on its thermal efficiency. *Solar Energy Materials and Solar Cells* **2017**, *159*, 66 – 72.

[105] Zhang, K.; Hao, L.; Du, M.; Mi, J.; Wang, J.-N.; Meng, J.-P. A review on thermal stability and high temperature induced ageing mechanisms of solar absorber coatings. *Renewable and Sustainable Energy Reviews* **2017**, *67*, 1282 – 1299.

[106] Gray, M.; Tirawat, R.; Kessinger, K.; Ndione, P. High temperature performance of high-efficiency, multi-layer solar selective coatings for tower applications. *Energy Procedia* **2015**, *69*, 398 – 404, International Conference on Concentrating Solar Power and Chemical Energy Systems, SolarPACES 2014.

[107] Selvakumar, N.; Barshilia, H. C. Review of physical vapor deposited (PVD) spectrally selective coatings for mid- and high-temperature solar thermal applications. *Solar Energy Materials and Solar Cells* **2012**, *98*, 1 – 23.

[108] Esposito, S.; Antonaia, A.; Addonizio, M.; Aprea, S. Fabrication and optimisation of highly efficient cermet-based spectrally selective coatings for high operating temperature. *Thin Solid Films* **2009**, *517*, 6000 – 6006.

[109] Antonaia, A.; Castaldo, A.; Addonizio, M.; Esposito, S. Stability of W-Al_2O_3 cermet based solar coating for receiver tube operating at high temperature. *Solar Energy Materials and Solar Cells* **2010**, *94*, 1604 – 1611.

[110] Zhang, Q.-C. Recent progress in high-temperature solar selective coatings. *Solar Energy Materials and Solar Cells* **2000**, *62*, 63 – 74.

[111] Zhang, Q.-C.; Zhao, K.; Zhang, B.-C.; Wang, L.-F.; Shen, Z.-L.; Lu, D.-Q.; Xie, D.-L.; Zhou, Z.-J.; Li, B.-F. A cylindrical magnetron sputtering system for depositing metal–aluminium nitride cermet solar coatings onto batches of tubes. *Journal of Vacuum Science & Technology A* **1998**, *16*, 628–632.

[112] Morris, D.; López-Delgado, A.; Padilla, I.; Muñoz-Morris, M. Selection of high temperature materials for concentrated solar power systems: Property maps and experiments. *Solar Energy* **2015**, *112*, 246 – 258.

[113] Burlafinger, K.; Vetter, A.; Brabec, C. J. Maximizing concentrated solar power (CSP) plant overall efficiencies by using spectral selective absorbers at optimal operation temperatures. *Solar Energy* **2015**, *120*, 428 – 438.

[114] Ogata, T. Creep-fatigue damage and life prediction of alloy steels. *Materials at High Temperatures* **2010**, *27*, 11 – 19.

[115] Davis, J. *ASM Specialty Handbook: Heat-Resistant Materials*; ASM International, 1997.

[116] Ashby, M. F.; Abel, C. A.; Goulette, M. J.; Cottrell, A. H.; Webster, G. A.; Cahn, R. W.; Evans, A. G.; McLean, M. Materials selection to resist creep. *Philosophical Transactions of the Royal Society of London. Series A: Physical and Engineering Sciences* **1995**, *351*, 451 – 468.

[117] Chou, T. C.; Joshi, A. High temperature interfacial reactions of SiC with metals. *Journal of Vacuum Science & Technology A* **1991**, *9*, 1525 – 1534.

[118] Heard, H. C.; Cline, C. F. Mechanical behaviour of polycrystalline BeO, Al_2O_3 and AlN at high pressure. *Journal of Materials Science* **1980**, *15*, 1889 – 1897.

[119] Subhash, G.; Ravichandran, G. Mechanical behaviour of a hot pressed aluminum nitride under uniaxial compression. *Journal of Materials Science* **1998**, *33*, 1933 – 1939.

[120] Cheng, Q.; Yang, P.; Zhang, Z. Radiative properties of ceramic Al_2O_3, AlN, and Si_3N_4 I.Experiments. *International Journal of Thermophysics* **2016**, *37*, 62.

[121] Sani, E.; Mercatelli, L.; Jafrancesco, D.; Sans, J. L.; Sciti, D. Ultra-high temperature ceramics for solar receivers: spectral and high-temperature emittance characterization. *Journal of the European Optical Society - Rapid publications* **2012**, *7*.

[122] de Faoite, D.; Browne, D. J.; Chang-Díaz, F. R.; Stanton, K. T. A review of the processing, composition, and temperature-dependent mechanical and thermal properties of dielectric technical ceramics. *Journal of Materials Science* **2012**, *47*, 4211 – 4235.

[123] Lavrenko, V.; Alexeev, A. Oxidation of sintered aluminium nitride. *Ceramics International* **1983**, *9*, 80 – 82.

[124] Katnani, A. D.; Papathomas, K. I. Kinetics and initial stages of oxidation of aluminum nitride: Thermogravimetric analysis and X-ray photoelectron spectroscopy study. *Journal of Vacuum Science & Technology A* **1987**, *5*, 1335 – 1340.

[125] Sato, T.; Haryu, K.; Endo, T.; Shimada, M. High temperature oxidation of hot-pressed aluminium nitride by water vapour. *Journal of Materials Science* **1987**, *22*, 2277 – 2280.

[126] Suryanarayana, D. Oxidation Kinetics of Aluminum Nitride. *Journal of the American Ceramic Society* **1990**, *73*, 1108 – 1110.

[127] Bellosi, A.; Landi, E.; Tampieri, A. Oxidation behavior of aluminum nitride. *Journal of Materials Research* **1993**, *8*, 565 – 572.

[128] Kim, H.-E.; J. Moorhead, A. Oxidation Behavior and Flexural Strength of Aluminum Nitride Exposed to Air at Elevated Temperatures. *Journal of the American Ceramic Society* **1994**, *77*, 1037 – 1041.

[129] Robinson, D.; Dieckmann, R. Oxidation of aluminium nitride substrates. *Journal of Materials Science* **1994**, *29*, 1949 – 1957.

[130] Osborne, E. W.; Norton, M. G. Oxidation of aluminium nitride. *Journal of Materials Science* **1999**, *33*, 3859 – 3865.

[131] Brown, A. L.; Norton, M. G. Oxidation kinetics of AlN powder. *Journal of Materials Science Letters* **1998**, *17*, 1519 – 1522.

[132] Opila, E.; Humphrey, D.; Oda, K.; Jacobson, N.; Yoshio, T. The oxidation of AlN in dry and wet oxygen. Proceedings of the Symposium on High Temperature Corrosion and Materials Chemistry. 1998; p 430.

[133] Tseng, W. J.; Tsai, C.-J.; Fu, S.-L. Oxidation, microstructure and metallization of aluminum nitride substrates. *Journal of Materials Science: Materials in Electronics* **2000**, *11*, 131 – 138.

[134] Gu, Z.; Edgar, J. H.; Speakman, S. A.; Blom, D.; Perrin, J.; Chaudhuri, J. Thermal oxidation of polycrystalline and single crystalline aluminum nitride wafers. *Journal of Electronic Materials* **2005**, *34*, 1271 – 1279.

[135] mei Hou, X.; sheng Yue, C.; Singh, A. K.; Zhang, M.; Chou, K.-C. Morphological development and oxidation mechanisms of aluminum nitride whiskers. *Journal of Solid State Chemistry* **2010**, *183*, 963 – 968.

[136] Hou, X.; Wang, E.; Liu, Y.; Chou, K.-C. The effect of water vapor and temperature on the reaction behavior of AlN powder at 1273 K to 1423 K. *Metallurgical and Materials Transactions A* **2015**, *46*, 1621 – 1627.

[137] Korbutowicz, R.; Zakrzewski, A.; Rac-Rumijowska, O.; Stafiniak, A.; Vincze, A. Oxidation rates of aluminium nitride thin films: Effect of composition of the atmosphere. *Journal of Materials Science: Materials in Electronics* **2017**, *28*, 13937 – 13949.

[138] Cao, C.; Feng, Y.; Qiu, T.; Yang, J.; Li, X.; Liang, T.; Li, J. Effects of isothermal annealing on the oxidation behavior, mechanical and thermal properties of AlN ceramics. *Ceramics International* **2017**, *43*, 9334 – 9342.

[139] Yeh, C.-T.; Tuan, W.-H. Oxidation mechanism of aluminum nitride revisited. *Journal of Advanced Ceramics* **2017**, *6*, 27 – 32.

[140] Lin, C.-Y.; Lu, F.-H. Oxidation behavior of AlN films at high temperature under controlled atmosphere. *Journal of the European Ceramic Society* **2008**, *28*, 691 – 698.

[141] Azema, N.; Durand, J.; Berjoan, R.; Dupuy, C.; Cot, L. Oxidation stages of aluminium nitride thin films obtained by plasma-enhanced chemical vapour deposition (PECVD). *Journal of the European Ceramic Society* **1991**, *8*, 291 – 298.

[142] Wang, F.; Zhang, R.; Xiu, X. Q.; Lu, D. Q.; Gu, S. L.; Shen, B.; Shi, Y.; Zheng, Y. D. Study of dry oxidation of aluminum nitride on Si(111) substrate grown by metalorganic chemical vapor deposition. *Surface Review and Letters* **2003**, *10*, 625 – 628.

[143] Chowdhury, E. A.; Kolodzey, J.; Olowolafe, J. O.; Qiu, G.; Katulka, G.; Hits, D.; Dashiell, M.; van der Weide, D.; Swann, C. P.; Unruh, K. M. Thermally oxidized AlN thin films for device insulators. *Applied Physics Letters* **1997**, *70*, 2732 – 2734.

[144] Labatut, C.; Kharchi, D.; Aspar, B.; Sibieude, F.; Armas, B. An in-situ study of the oxidation of AlN layers fabricated by LPCVD using X-ray diffraction. *Journal of the European Ceramic Society* **1994**, *13*, 339 – 344.

[145] Ansart, F.; Ganda, H.; Saporte, R.; Traverse, J. Study of the oxidation of aluminium nitride coatings at high temperature. *Thin Solid Films* **1995**, *260*, 38 – 46.

[146] Ashby, M. F.; Cebon, D. Materials selection in mechanical design. *Journal de Physique IV* **1993**, *03*, C7–1–C7–9.

[147] Ashby, M. Multi-objective optimization in material design and selection. *Acta Materialia* **2000**, *48*, 359 – 369.

[148] Cebon, D.; Ashby, N. Materials selection for precision instruments. *Measurement Science and Technology* **1994**, *5*, 296 – 306.

[149] Seiler, P.; Bäker, M.; Rösler, J. Multi-scale failure mechanisms of thermal barrier coating systems. *Computational Materials Science* **2013**, *80*, 27 – 34, Recent Advances in Computational Mechanics of Materials.

[150] Mortazavi, N.; Geers, C.; Esmaily, M.; Babic, V.; Sattari, M.; Lindgren, K.; Malmberg, P.; Jönsson, B.; Halvarsson, M.; Svensson, J., et al. Interplay of water and reactive elements in oxidation of alumina-forming alloys. *Nature materials* **2018**, *17*, 610.

[151] Naumenko, D.; Pint, B. A.; Quadakkers, W. J. Current Thoughts on Reactive Element Effects in Alumina-Forming Systems: In Memory of John Stringer. *Oxidation of Metals* **2016**, *86*, 1 – 43.

[152] Dryepondt, S.; Turan, J.; Leonard, D.; Pint, B. A. Long-Term Oxidation Testing and Lifetime Modeling of Cast and ODS FeCrAl Alloys. *Oxidation of Metals* **2017**, *87*, 215 – 248.

[153] Jönsson, B.; Lu, Q.; Chandrasekaran, D.; Berglund, R.; Rave, F. Oxidation and Creep Limited Lifetime of Kanthal APMT®, a Dispersion Strengthened FeCrAlMo Alloy Designed for Strength and Oxidation Resistance at High Temperatures. *Oxidation of Metals* **2013**, *79*, 29 – 39.

[154] Houngniou, C.; Chevalier, S.; Larpin, J. P. High-Temperature-Oxidation Behavior of Iron–Aluminide Diffusion Coatings. *Oxidation of Metals* **2006**, *65*, 409 – 439.

[155] Berthomé, G.; N'Dah, E.; Wouters, Y.; Galerie, A. Temperature dependence of metastable alumina formation during thermal oxidation of FeCrAl foils. *Materials and Corrosion* **2005**, *56*, 389 – 392.

[156] Blocher, J. M. Structure/property/process relationships in chemical vapor deposition CVD. *Journal of Vacuum Science and Technology* **1974**, *11*, 680 – 686.

[157] Thompson, C. V. Structure Evolution During Processing of Polycrystalline Films. *Annual Review of Materials Science* **2000**, *30*, 159 – 190.

[158] Jones, R. L. In *Metallurgical and Ceramic Protective Coatings*; Stern, K. H., Ed.; Springer Netherlands: Dordrecht, 1996; pp 194 – 235.

[159] Chen, G. In *Thermal Barrier Coatings*; Xu, H., Guo, H., Eds.; Woodhead Publishing Series in Metals and Surface Engineering; Woodhead Publishing, 2011; pp 243 – 262.

[160] Pangarov, N. On the crystal orientation of electrodeposited metals. *Electrochimica Acta* **1964**, *9*, 721 – 726.

[161] García, J.; Pinto, H.; Ramos-Moore, E.; Espinoza, C.; Östby, J.; Coelho, R. In-situ high temperature stress analysis of Ti(C,N) coatings on functionally graded cemented carbides by energy dispersive synchrotron X-ray diffraction. *International Journal of Refractory Metals and Hard Materials* **2016**, *56*, 27 – 34.

[162] Kuball, M. Raman spectroscopy of GaN, AlGaN and AlN for process and growth monitoring/control. *Surface and Interface Analysis* **2001**, *31*, 987 – 999.

[163] Yang, S.; Miyagawa, R.; Miyake, H.; Hiramatsu, K.; Harima, H. Raman Scattering Spectroscopy of Residual Stresses in Epitaxial AlN Films. *Applied Physics Express* **2011**, *4*, 031001.

[164] Shillington, E.; Clarke, D. Spalling failure of a thermal barrier coating associated with aluminum depletion in the bond-coat. *Acta Materialia* **1999**, *47*, 1297 – 1305.

[165] Christensen, R. J.; Lipkin, D. M.; Clarke, D. R.; Murphy, K. Nondestructive evaluation of the oxidation stresses through thermal barrier coatings using Cr3+ piezospectroscopy. *Applied Physics Letters* **1996**, *69*, 3754 – 3756.

[166] Lipkin, D. M.; Clarke, D. R. Measurement of the stress in oxide scales formed by oxidation of alumina-forming alloys. *Oxidation of Metals* **1996**, *45*, 267 – 280.

[167] Yeh, C.-T.; Tuan, W.-H. Pre-oxidation of AlN substrates for subsequent metallization. *Journal of Materials Science: Materials in Electronics* **2015**, *26*, 5910 – 5916.

[168] Schuster, J. C.; Nowotny, H. Phase relationships in the ternary systems (V, Cr, Mo, W, Mn, Re)-Al-N. *Journal of Materials Science* **1985**, *20*, 2787 – 2793.

[169] Boichot, R.; Coudurier, N.; Mercier, F.; Claudel, A.; Baccar, N.; Milet, A.; Blanquet, E.; Pons, M. CFD modeling of the high-temperature HVPE growth of aluminum nitride layers on c-plane sapphire: from theoretical chemistry to process evaluation. *Theoretical Chemistry Accounts* **2013**, *133*, 1419.

[170] Boichot, R.; Coudurier, N.; Mercier, F.; Lay, S.; Crisci, A.; Coindeau, S.; Claudel, A.; Blanquet, E.; Pons, M. Epitaxial growth of AlN on c-plane sapphire by High Temperature Hydride Vapor Phase Epitaxy: Influence of the gas phase N/Al ratio and low temperature protective layer. *Surface and Coatings Technology* **2013**, *237*, 118 – 125, Proceedings of the 40th International Conference on Metallurgical Coatings and Thin Films (ICMCTF).

[171] Pons, M.; Boichot, R.; Coudurier, N.; Claudel, A.; Blanquet, E.; Lay, S.; Mercier, F.; Pique, D. High temperature chemical vapor deposition of aluminum nitride, growth and evaluation. *Surface and Coatings Technology* **2013**, *230*, 111 – 118, 19th European Conference on Chemical Vapor Deposition (EuroCVD19), Varna, Bulgaria, 1st - 6th September 2013.

[172] Balaji, M.; Claudel, A.; Fellmann, V.; Gélard, I.; Blanquet, E.; Boichot, R.; Pierret, A.; Attal-Trétout, B.; Crisci, A.; Coindeau, S.; Roussel, H.; Pique, D.; Baskar, K.; Pons, M. Effects of AlN nucleation layers on the growth of AlN films using high temperature hydride vapor phase epitaxy. *Journal of Alloys and Compounds* **2012**, *526*, 103 – 109.

[173] Boichot, R.; Claudel, A.; Baccar, N.; Milet, A.; Blanquet, E.; Pons, M. Epitaxial and polycrystalline growth of AlN by high temperature CVD: Experimental results and simulation. *Surface and Coatings Technology* **2010**, *205*, 1294 – 1301, ICMCTF 2010 Special Issue.

[174] Claudel, A.; Blanquet, E.; Chaussende, D.; Audier, M.; Pique, D.; Pons, M. Thermodynamic and experimental investigations on the growth of thick aluminum nitride layers by high temperature CVD. *Journal of Crystal Growth* **2009**, *311*, 3371 – 3379.

[175] Isselé, H. Mechanical characterization and modeling of thin films for processing of microelectronic devices - application to the fied of 3D integration. PhDthesis, Université de Grenoble, 2014.

[176] Feng, X.; Huang, Y.; Rosakis, A. On the Stoney formula for a thin film/substrate system with nonuniform substrate thickness. *Journal of Applied Mechanics* **2007**, *74*, 1276 – 1281.

[177] Vanhumbeeck, J.-F. In situ monitoring of the internal stress evolution during titanium thin film anodising. PhDthesis, 2009.

[178] Luo, Q.; Jones, A. High-precision determination of residual stress of polycrystalline coatings using optimised XRD-sin$^2\psi$ technique. *Surface and Coatings Technology* **2010**, *205*, 1403 – 1408, ICMCTF 2010 Special Issue.

[179] Raghavan, S.; Redwing, J. M. In situ stress measurements during the MOCVD growth of AlN buffer layers on (111) Si substrates. *Journal of Crystal Growth* **2004**, *261*, 294 – 300, Proceedings of the 11th Biennial (US) Workshop on Organometallic Vapor Phase Epitaxy (OMVPE).

[180] Boichot, R.; Chen, D.; Mercier, F.; Baillet, F.; Giusti, G.; Coughlan, T.; Chubarov, M.; Pons, M. Epitaxial Growth of AlN on (0001) Sapphire: Assessment of HVPE Process by a Design of Experiments Approach. *Coatings* **2017**, *7*.

[181] Gan, B. K.; Bilek, M. M. M.; McKenzie, D. R.; Taylor, M. B.; McCulloch, D. G. Effect of intrinsic stress on preferred orientation in AlN thin films. *Journal of Applied Physics* **2004**, *95*, 2130 – 2134.

[182] Raghavan, S.; Redwing, J. M. Intrinsic stresses in AlN layers grown by metal organic chemical vapor deposition on (0001) sapphire and (111) Si substrates. *Journal of Applied Physics* **2004**, *96*, 2995 – 3003.

[183] Chakraborty, S.; Banerjee, S.; Sharma, I.; Suri, A. Development of silicide coating over molybdenum based refractory alloy and its characterization. *Journal of Nuclear Materials* **2010**, *403*, 152 – 159.

[184] Majumdar, S. Formation of MoSi2 and Al doped MoSi2 coatings on molybdenum base TZM (Mo–0.5Ti–0.1Zr–0.02C) alloy. *Surface and Coatings Technology* **2012**, *206*, 3393 – 3398.

[185] Park, J.; Kim, J. M.; Lee, S.; Park, J. S. Oxidation behaviors of the aluminide coated TZM alloy via pack cementation. *The Physics of Metals and Metallography* **2014**, *115*, 1351 – 1355.

[186] Majumdar, S.; Sharma, I.; Raveendra, S.; Samajdar, I.; Bhargava, P. In situ chemical vapour co-deposition of Al and Si to form diffusion coatings on TZM. *Materials Science and Engineering: A* **2008**, *492*, 211 – 217.

[187] Claudel, A.; Blanquet, E.; Chaussende, D.; Boichot, R.; Doisneau, B.; Berthomé, G.; Crisci, A.; Mank, H.; Moisson, C.; Pique, D.; Pons, M. Investigation on AlN epitaxial growth and related etching phenomenon at high temperature using high temperature chemical vapor deposition process. *Journal of Crystal Growth* **2011**, *335*, 17 – 24.

[188] Claudel, A. et al. Influence of the V/III ratio in the gas phase on thin epitaxial AlN layers grown on (0001) sapphire by high temperature hydride vapor phase epitaxy. *Thin Solid Films* **2014**, *573*, 140 – 147.

[189] Harris, G. X. Quantitative measurement of preferred orientation in rolled uranium bars. *The London, Edinburgh, and Dublin Philosophical Magazine and Journal of Science* **1952**, *43*, 113 – 123.

[190] Kumar, M.; Kumar, A.; Abhyankar, A. C. Influence of Texture Coefficient on Surface Morphology and Sensing Properties of W-Doped Nanocrystalline Tin Oxide Thin Films. *ACS Applied Materials & Interfaces* **2015**, *7*, 3571–3580, PMID: 25603393.

[191] Jönsson, B.; Westerlund, A. Oxidation Comparison of Alumina-Forming and Chromia-Forming Commercial Alloys at 1100 and 1200 °. *Oxidation of Metals* **2017**, *88*, 315 – 326.

[192] Jönsson, B.; Berglund, R.; Magnusson, J.; Henning, P.; Hättestrand, M. High temperature properties of a new powder metallurgical FeCrAl alloy. Materials Science Forum. 2004; pp 455 – 462.

[193] Engkvist, J.; Canovic, S.; Hellström, K.; Järdnäs, A.; Svensson, J.-E.; Johansson, L.-G.; Olsson, M.; Halvarsson, M. Alumina Scale Formation on a Powder Metallurgical FeCrAl Alloy (Kanthal APMT) at 900–1100 °C in Dry O_2 and in O_2 + H_2O. *Oxidation of Metals* **2010**, *73*, 233 – 253.

[194] Young, D. J.; Naumenko, D.; Niewolak, L.; Wessel, E.; Singheiser, L.; Quadakkers, W. J. Oxidation kinetics of Y-doped FeCrAl-alloys in low and high pO2 gases. *Materials and Corrosion* **2010**, *61*, 838 – 844.

[195] Naumenko, D.; Gleeson, B.; Wessel, E.; Singheiser, L.; Quadakkers, W. Correlation between the Microstructure, Growth Mechanism, and Growth Kinetics of Alumina Scales on a FeCrAlY Alloy. *Metallurgical and Materials Transactions A* **2007**, *38*, 2974 – 2983.

[196] Hellström, K.; Israelsson, N.; Mortazavi, N.; Canovic, S.; Halvarsson, M.; Svensson, J.-E.; Johansson, L.-G. Oxidation of a Dispersion-Strengthened Powder Metallurgical FeCrAl Alloy in the Presence of O2 at 1100 °C: The Influence of Water Vapour. *Oxidation of Metals* **2015**, *83*, 533 – 558.

[197] Dimyati, A.; Penkalla, H.; Untoro, P.; Naumenko, D.; Quadakkers, W.; Mayer, J. High-Temperature Oxidation of FeCrAl Alloys: The Effect of Mg Incorporation into the Alumina Scale: Dedicated to Professor Dr. Dr. hc Manfred Rühle on the Occasion of his 65th Birthday. *Zeitschrift für Metallkunde* **2003**, *94*, 180 – 187.

[198] Lee, J. W.; Radu, I.; Alexe, M. Oxidation behavior of AlN substrate at low temperature. *Journal of Materials Science: Materials in Electronics* **2002**, *13*, 131 – 137.

[199] Hou, X.-M.; Chou, K.-C. Quantitative interpretation of the parabolic and nonparabolic oxidation behavior of nitride ceramic. *Journal of the European Ceramic Society* **2009**, *29*, 517 – 523.

[200] Itoh, H.; Kato, M.; Sugiyama, K. Oxidation Resistance of AlN Coated Graphite Prepared by Plasma Enhanced CVD. *Journal of the Ceramic Association, Japan* **1986**, *94*, 145 – 150.

[201] Casaux, Y.; Dollet, A.; Sibieude, F.; Berjoan, R. Influence de l'orientation cristalline sur la résistance à l'oxydation de revêtements de AIN: étude in-situ par diffractométrie X. *Le Journal de Physique IV* **1998**, *8*, Pr5 – 249.

[202] Hsueh, C. Thermal stresses in elastic multilayer systems. *Thin Solid Films* **2002**, *418*, 182 – 188.

[203] Hsueh, C.-H. Modeling of elastic deformation of multilayers due to residual stresses and external bending. *Journal of Applied Physics* **2002**, *91*, 9652 – 9656.

[204] Hsueh, C.-H.; Lee, S.; Lin, H.-Y. Analyses of mode I edge delamination by thermal stresses in multilayer systems. *Composites Part B: Engineering* **2006**, *37*, 1 – 9.

[205] Hsueh, C.; Lee, S.; Chuang, T. J. An alternative method of solving multilayer bending problems. *Journal of Applied Mechanics, Transactions, American Society of Mechanical Engineers* **2003**, *70*, 151 – 153.

[206] Limarga, A. M.; Wilkinson, D. S. A model for the effect of creep deformation and intrinsic growth stress on oxide/nitride scale growth rates with application to the nitridation of $\gamma - TiAl$. *Materials Science and Engineering: A* **2006**, *415*, 94 – 103.

[207] Limarga, A. M.; Wilkinson, D. S. Modeling the interaction between creep deformation and scale growth process. *Acta Materialia* **2007**, *55*, 189 – 201.

[208] Evans, H. E. Stress effects in high temperature oxidation of metals. *International Materials Reviews* **1995**, *40*, 1–40.

[209] Zhang, X. C.; Xu, B. S.; Wang, H. D.; Wu, Y. X. Residual stress relaxation in the film/substrate system due to creep deformation. *Journal of Applied Physics* **2007**, *101*, 083530.

[210] Chen, Q.-Q.; Xuan, F.-Z.; Tu, S.-T. Residual stress analysis in the film/substrate system with the effect of creep deformation. *Journal of Applied Physics* **2009**, *106*, 033512.

[211] Dong, X.; Feng, X.; Hwang, K.-C. Oxidation stress evolution and relaxation of oxide film/metal substrate system. *Journal of Applied Physics* **2012**, *112*, 023502.

[212] Li, B.; Fan, X.; Zhou, K.; Wang, T. A semi-analytical model for predicting stress evolution in multilayer coating systems during thermal cycling. *International Journal of Mechanical Sciences* **2018**, *135*, 31 – 42.

[213] Padture, N. P.; Gell, M.; Jordan, E. H. Thermal Barrier Coatings for Gas-Turbine Engine Applications. *Science* **2002**, *296*, 280 – 284.

[214] Abe, F. In *Structural Alloys for Power Plants*; Shirzadi, A., Jackson, S., Eds.; Woodhead Publishing Series in Energy; Woodhead Publishing, 2014; pp 250 – 293.

[215] Kassner, M. In *Fundamentals of Creep in Metals and Alloys*, second edition ed.; Kassner, M. E., Ed.; Elsevier: Amsterdam, 2008; pp 9 – 93.

[216] Norton, F. H. *The creep of steel at high temperatures*; McGraw-Hill Book Company, Incorporated, 1929.

[217] Clarke, D. R. Stress generation during high-temperature oxidation of metallic alloys. *Current Opinion in Solid State and Materials Science* **2002**, *6*, 237 – 244.

[218] Rhines, F. N.; Wolf, J. S. The role of oxide microstructure and growth stresses in the high-temperature scaling of nickel. *Metallurgical Transactions* **1970**, *1*, 1701 – 1710.

[219] Chou, K.-C. A Kinetic Model for Oxidation of Si–Al–O–N Materials. *Journal of the American Ceramic Society* **2006**, *89*, 1568 – 1576.

[220] Hou, X.; Chou, K.-C. Investigation of isothermal oxidation of AlN ceramics using different kinetic model. *Corrosion Science* **2009**, *51*, 556 – 561.

[221] Jou, Z. C.; Virkar, A. V. High-Temperature Creep and Cavitation of Polycrystalline Aluminum Nitride. *Journal of the American Ceramic Society* **1990**, *73*, 1928 – 1935.

[222] Porter, J.; Blumenthal, W.; Evans, A. Overview 14 Creep fracture in ceramic polycrystals—I. creep cavitation effects in polycrystalline alumina. *Acta Metallurgica* **1981**, *29*, 1899 – 1906.

[223] Kanthal, Propertities of APMT. `https://www.kanthal.com/en/products/material-datasheets/tube/kanthal-apmt/`.

[224] Field, K. G.; Snead, M. A.; Yamamoto, Y.; Terrani, K. A. *Handbook on the Material Properties of FeCrAl Alloys for Nuclear Power Production Applications (FY18 Version: Revision 1)*; 2018.

Appendices

Annex 1: Material properties for the selection of substrates

Table A.1.1 Thermal, elastic and mechanical parameters used in determination of Fracture Resistance (FR), Creep Resistance (CR) and thermal shock resistance (ΔT) for a wide range of high temperature materials.

Material	**Fracture toughness** ($\mathbf{MPa{\cdot}m^{-\frac{1}{2}}}$)	**Young's modulus (GPa)**	**Thermal conductivity** ($\mathbf{W{\cdot}m^{-1}{\cdot}K^{-1}}$)	**Creep strength (MPa)**	**Thermal expansion coefficient** ($\mathbf{\times 10^{-6}\ K^{-1}}$)
Tungsten, commercial purity, R07004, annealed	120-150	340-350	170-175	110-120	4.2-4.4
Tungsten-copper alloy, Elkonite 50W3	120-150	270-338	80-100	110-120	5.7-6.3
Tungsten-Ni-Cu alloy, CMW 1000	120-150	270-282	90-98	110-120	5.2-5.7
Tungsten-Ni-Fe alloy, CMW 3000	120-150	310-360	72-80	110-120	4.3-4.9
Tungsten-Ni-Mo-Fe alloy, Anviloy 1150	120-150	331-338	70-90	110-120	5.2-5.7
Tungsten-rhenium alloy, wire	120-150	338-352	100-115	110-120	4.8-5.2
Ti-40%SiC(f), Ti-15V-3Sn-3Cr-3Al/40%SiC	25-29	192-200	29-40	200	6.5-6.8
Tantalum-W-Hf alloy, T-111	120-150	195-205	40.3-43.7	724	5.8-6
Tantalum-W-Hf alloy, T-222	120-150	195-205	30-55	585	5-6.5
Carbon steel SA216, cast, anneald	116-129	198-209	58-62.8	120	11.2-11.8
ET-45	50	160	11	50	16
Low alloy steel, AISI 4140 steel, normalized	68-107	208-216	42-48	120	11.5-13.5
Stainless Fe-Cr Steel	50-100	200	15-25	30	10-20
Niobium-Hf-Ti alloy, Alloy C-103, cold rolled	95-135	82-92	40-44	74	7.8-8.4
Niobium-Mo-V alloy, Alloy B-66	120-150	100-110	40-60	157	8.3-8.7
Inconel 625, annealed	190-211	205-216	9.9-10.7	30	12.8-13.4

Material	**Fracture toughness** ($\mathbf{MPa \cdot m^{-\frac{1}{2}}}$)	**Young's modulus (GPa)**	**Thermal conductivity** ($\mathbf{W \cdot m^{-1} \cdot K^{-1}}$)	**Creep strength (MPa)**	**Thermal expansion coefficient** ($\mathbf{\times 10^{-6}\ K^{-1}}$)
Inconel 718, solution treated	244-271	253	11.6-12.6	700	12.8-13.4
Ni superalloys	50-150	180	15-75	150	10-15
Ni3Al	50	180	30	100	12
Nickel-magnetic alloy, 45Ni-3Mo-Fe, soft	167-185	200-240	32-45	230	6-14.5
Nickel-magnetic alloy, 45Ni-Fe, Alloy 1, soft (annealed)	215-239	200-210	35-43	230	6-8
Nickel-magnetic alloy, 78.5Ni-Fe, soft	205-228	200-240	32-45	240	6-14.5
Mo Silicide, Mo2Si3-Al2O3	6.5	370	19	300-1000	7.5
Mo Silicide, Mo5Si3	2.5	320	19	50	8.5
Mo Silicide, Mo5SiB2	1.5	370	27	300	7.5
Mo Silicide, MoSi2-SiC	3	300-440	40	50	8.5
Mo Silicide, Mo-Si-B	5-12	250	75	300-1000	7.75
Molybdenum, Alloy 363, TZM	30-50	305-325	129-147	30-300	4.7-5.5
Fe-20Al	40	145	18	10	20
Fe-20Al-5Cr	40	135	18	20	20
Fe-35Al	40	165	18	20	22
Fe-40Al	30	180	16	40	30
Kanthal	50	200	20	20	15
Kanthal AF	50	130	26	1.7	15
Kanthal APM	50	130	26	2	15
Kanthal APMT	50	130	27	10.9	14.7

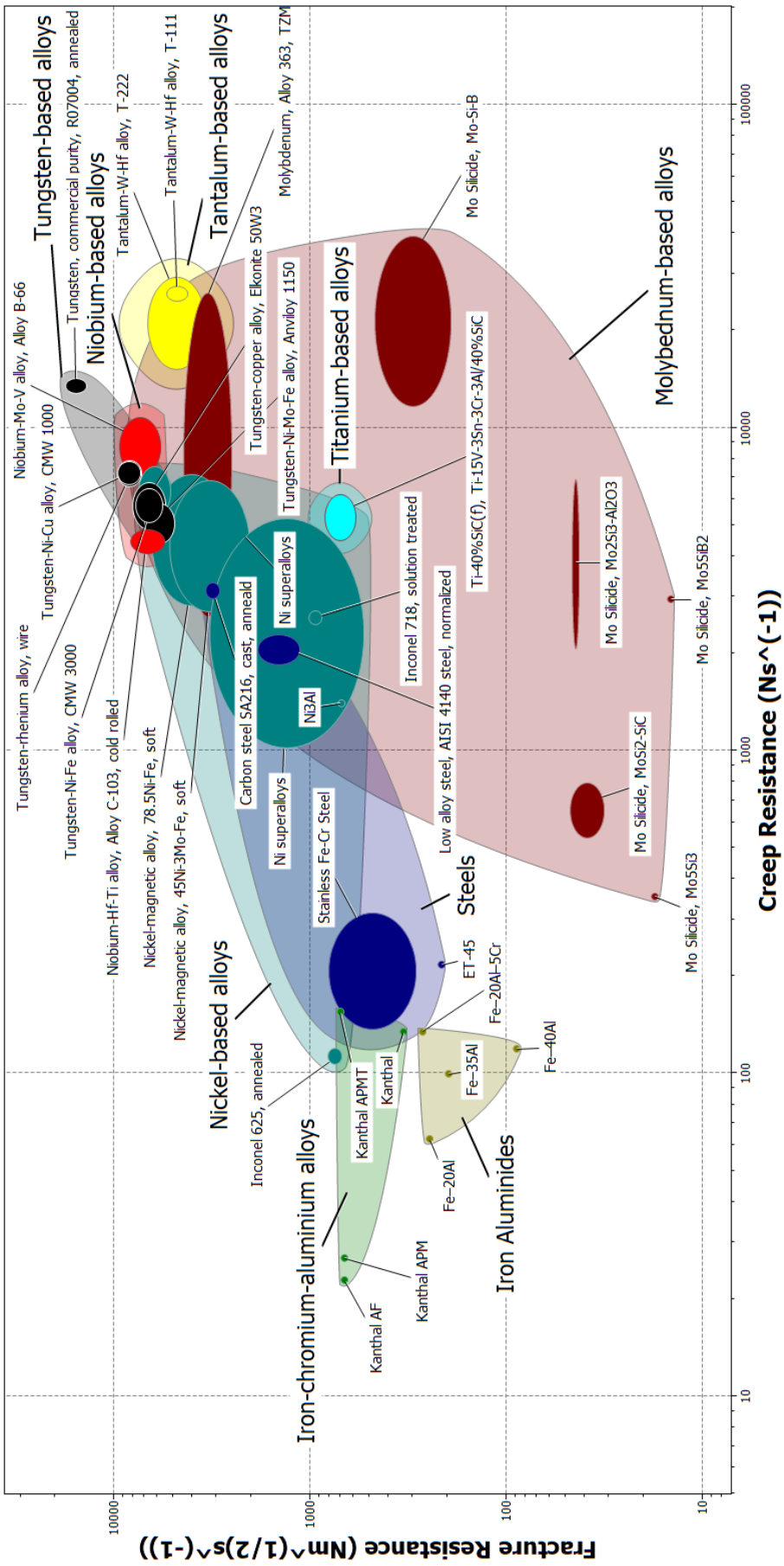

Figure A.1.1 Property map showing the resistance of materials to fracture versus its resistance to creep.

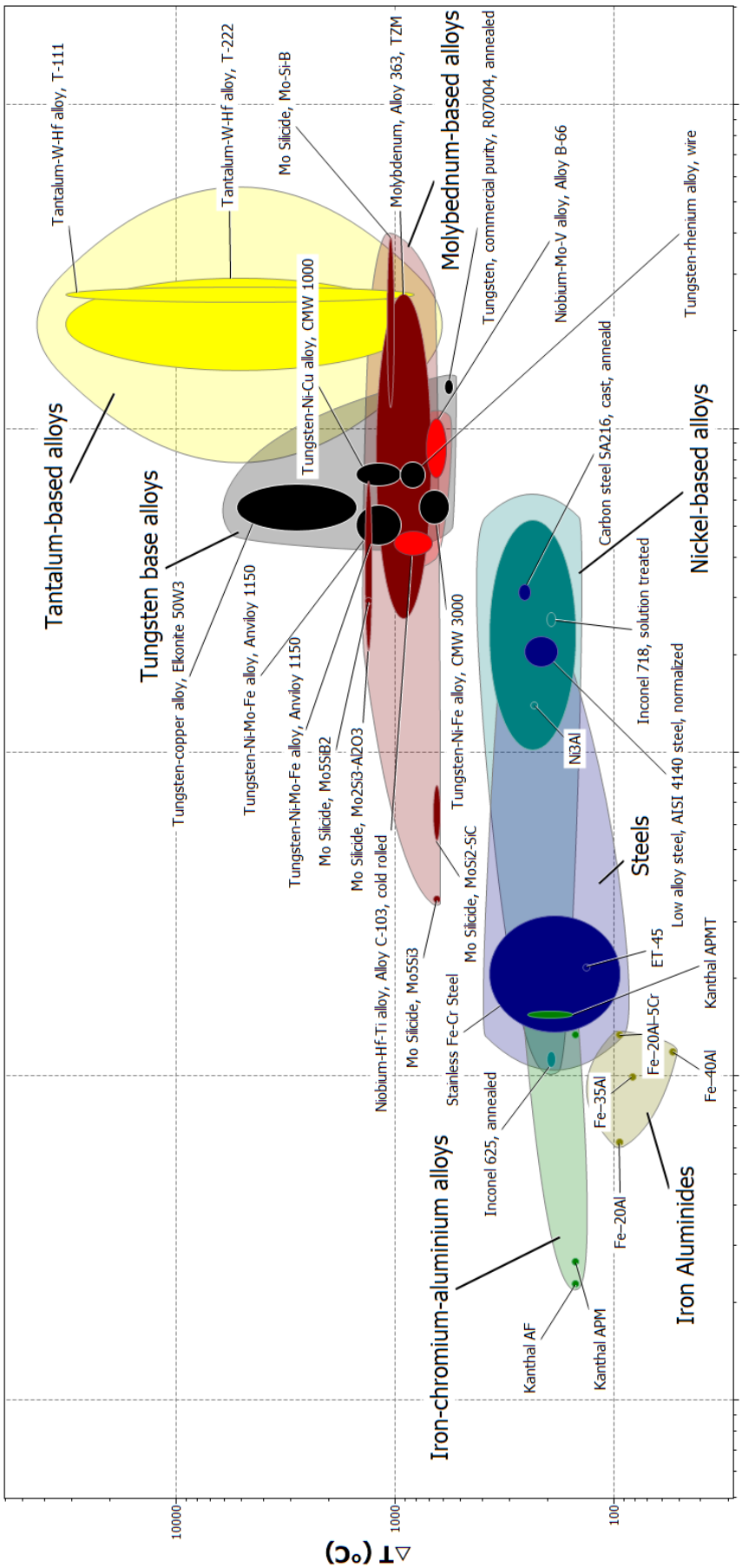

Figure A.1.2 Property map showing the resistance of materials to the spallation of AlN coating versus its resistance to creep.

Annex 2: Pole figure analysis

Figure A.2.1 presents the pole figures of AlN coating deposited at a N/Al ratio of 3 for $(10\bar{1}2)$, $(10\bar{1}3)$ and $(20\bar{1}3)$) orientations. The high index (red color) indicates that three orientations are well aligned with the A1 axis which is perpendicular to the substrate surface. AlN grains are preferred to grow along the $(10\bar{1}2)$, $(10\bar{1}3)$ and $(20\bar{1}3)$) orientations.

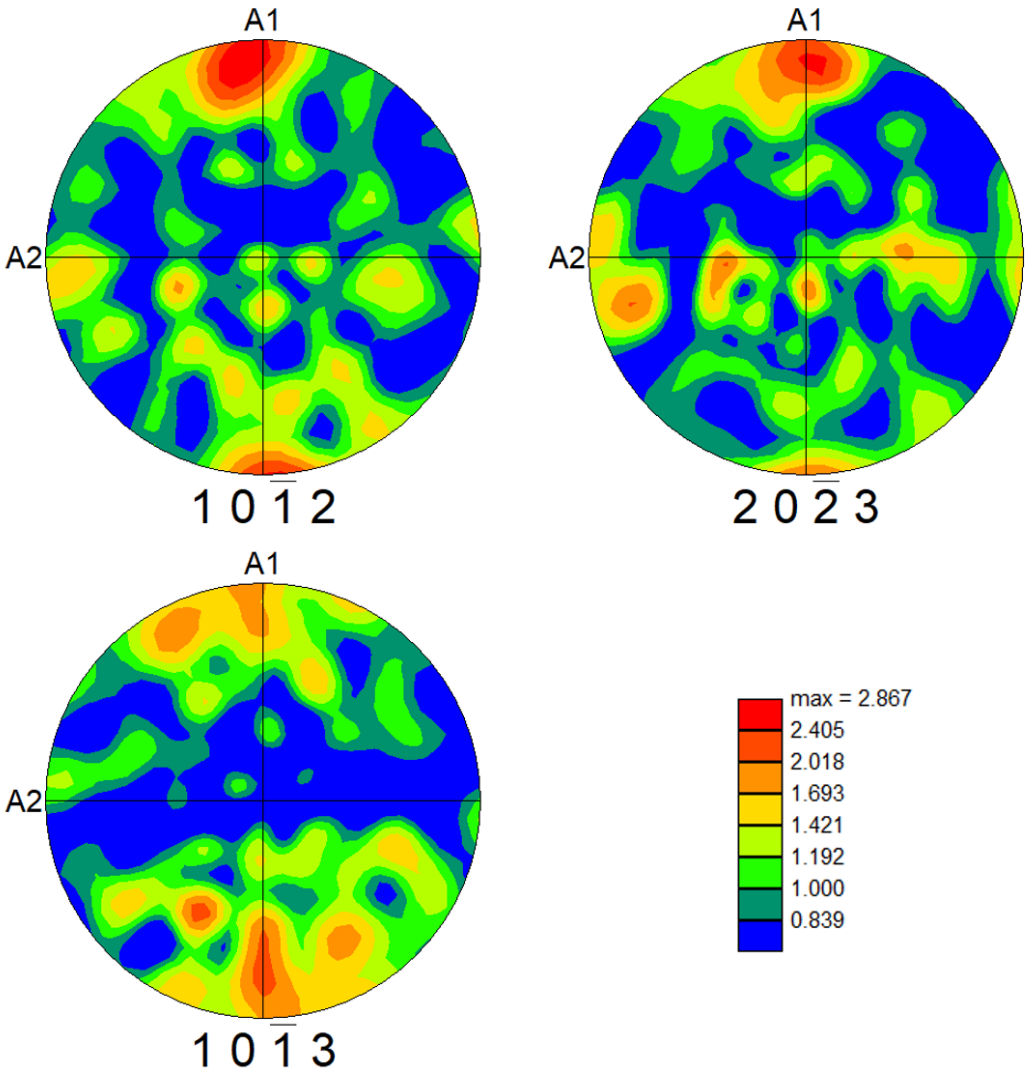

Figure A.2.1 Pole figures of coated system deposited at N/Al=3 (Figure 3.11(e) and (j)) for $(10\bar{1}2)$, $(10\bar{1}3)$ and $(20\bar{1}3)$) orientations; the A1 axis is perpendicular to the substrate surface.

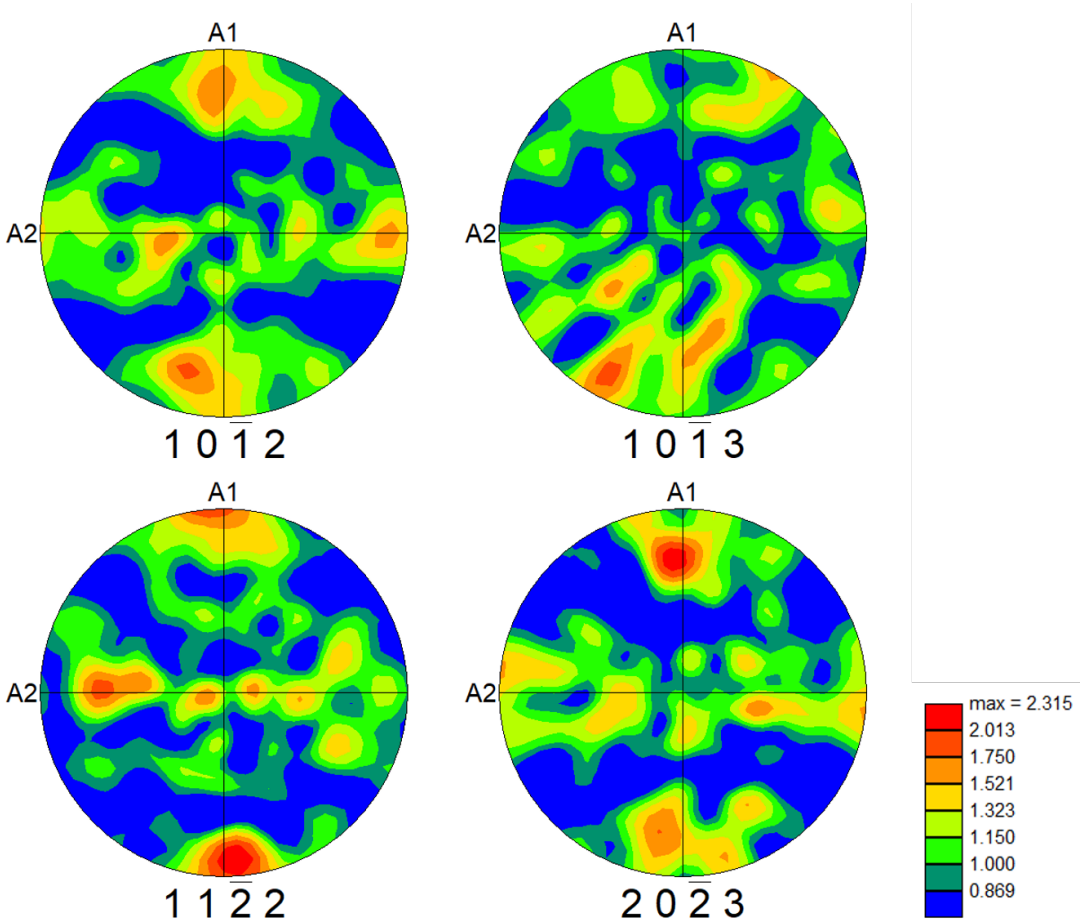

Figure A.2.2 Pole figures of coated system deposited at N/Al=11.25 (Figure 3.11(d) and (i)) for $(10\bar{1}2)$, $(10\bar{1}3)$, $(20\bar{1}3)$, and $(11\bar{2}2)$) orientations; the A1 axis is perpendicular to the substrate surface.

For AlN coating deposited at a higher N/Al ratio (N/Al=11.25), pole figures in Figure A.2.2 reveal that the $(11\bar{2}2)$ orientation is well aligned with the A1 axis, while the $(10\bar{1}2)$ and $(20\bar{1}3)$) orientations are. These findings correspond to the smaller texture coefficients calculated by XRD of the $(10\bar{1}2)$ and $(20\bar{1}3)$) orientations. The $(10\bar{1}3)$ orientation seems to be less preferred according to the pole figure.

Annex 3: Material properties for modeling

Table A.3.1 Material properties of AlN and TZM for the benchmark with FEA [7, 35–41].

Properties	**AlN**	**TZM**
Thickness, t (mm)	0.06	1
Young's modulus, E (GPa)	340	320
Poisson's ratio, ν	0.21	0.3
Thermal conductivity, k ($W{\cdot}m^{-1}{\cdot}K^{-1}$)	30	103.5
Thermal expansion coefficient, α_{th} ($10^{-6}{\cdot}{}^{\circ}K^{-1}$)	$4.5{\times}10^{-6}$	$5.2{\times}10^{-6}$
Creep exponent, n	1	3.03
Creep prefactor, A ($MPa^{-n}{\cdot}s^{-1}$)	$2.928{\times}10^{10}$	$1.796{\times}10^{3}$
Creep activation energy, Q_{cr} ($J{\cdot}mol^{-1}$)	$5.860{\times}10^{5}$	$4.810{\times}10^{5}$
Volume per Al ion, Ω (m^3)	$2.091{\times}10^{-29}$	/

Table A.3.2 Input parameters for the benchmark with FEA.

Parameters	**Values**	**Remark**
Deposition temperature, T_{growth} (°C)	1200	The system is initially stress-free at T_{growth}
Ambient temperature, T_{amb} (°C)	25	
Number of thermal cycles	10	Figure 4.7
High temperature duration in each cycle	10 h	Figure 4.7
Heating and cooling periods in each cycle	Assumed to be less than 1 min	Figure 4.7
Heat flux, $\overrightarrow{q}$ ($MW{\cdot}m^2$)	-10	Not realistic value, chosen to clarify the stress evolution during thermal cycling
Creep behavior of materials	Implicit Norton creep equation	TBOPT=10

Table A.3.3 Material properties of Al_2O_3 used in the complete model.

Properties	**Values**	**Reference**
Young's modulus, E (GPa)	379	[211]
Poisson's ratio ν	0.25	[211]
Thermal conductivity, k ($W{\cdot}m^{-1}{\cdot}K^{-1}$)	10	
Thermal expansion coefficient, α_{th} ($10^{-6}{\cdot}{}^{\circ}C^{-1}$)	fifth-order fitting	[9]
A_0 ($10^{-6}{\cdot}{}^{\circ}C^{-1}$)	5.077	
A_1 ($10^{-6}{\cdot}{}^{\circ}C^{-2}$)	1.432×10^{-2}	
A_2 ($10^{-6}{\cdot}{}^{\circ}C^{-3}$)	-2.305×10^{-5}	
A_3 ($10^{-6}{\cdot}{}^{\circ}C^{-4}$)	2.064×10^{-8}	
A_4 ($10^{-6}{\cdot}{}^{\circ}C^{-5}$)	-8.839×10^{-12}	
A_5 ($10^{-6}{\cdot}{}^{\circ}C^{-6}$)	1.425×10^{-15}	
Creep exponent, n	1.65	[222]
Creep prefactor, A ($MPa^{-n}{\cdot}s^{-1}$)	6.472×10^{6}	[222]
Creep activation energy, Q_{cr} ($J{\cdot}mol^{-1}$)	4.600×10^{5}	[222]
Oxidation kinetics	linear	Experiment
Oxidation pre-exponential factor, k_0 ($mg{\cdot}cm^{-2}{\cdot}h^{-1}$)	35.92	Experiment
Oxidation activation energy, E_a($J{\cdot}mol^{-1}$)	9.732×10^{4}	Experiment
Volume per Al ion, Ω (m^3)	2.132×10^{-29}	[41]

Table A.3.4 Material properties of APMT used in the model.

Properties	**Values**	**Reference**
Young's modulus, E (GPa)	220	[223]
Poisson's ratio, ν	0.3	[223]
Thermal conductivity, k ($W{\cdot}m^{-1}{\cdot}K^{-1}$)	27	[223]
Thermal expansion coefficient, α_{th} ($10^{-6}{\cdot}{}^{\circ}C^{-1}$)	fifth-order fitting	[223, 224]
A_0 ($10^{-6}{\cdot}{}^{\circ}C^{-1}$)	10.768	
A_1 ($10^{-6}{\cdot}{}^{\circ}C^{-2}$)	4.059×10^{-3}	
A_2 ($10^{-6}{\cdot}{}^{\circ}C^{-3}$)	-5.860×10^{-8}	
A_3 ($10^{-6}{\cdot}{}^{\circ}C^{-4}$)	-6.174×10^{-9}	
A_4 ($10^{-6}{\cdot}{}^{\circ}C^{-5}$)	1.065×10^{-11}	
A_5 ($10^{-6}{\cdot}{}^{\circ}C^{-6}$)	4.569×10^{-15}	
Creep exponent, n	4.98	[149]
Creep prefactor, A ($MPa^{-n}{\cdot}s^{-1}$)	78.978	[149]
Creep activation energy, Q_{cr} ($J{\cdot}mol^{-1}$)	4.530×10^{5}	[149]
Oxidation kinetics	parabolic	[211]
Oxidation constant, k_p ($m^2{\cdot}s^{-1}$)	2.366×10^{-17}	[211]
lateral growth strain rate constant	4.250×10^{4}	[211]

Annex 4: Finite element model

In the present study, the sequential field-coupling is employed to analyze the stress field assuming that the stress field in a structure depends on the temperature field in that structure, but the reverse is not significant. In such thermal-stress analysis, the nodal temperatures calculated from an uncoupled heat transfer analysis are applied as 'body force' loads in the subsequent stress/deformation analysis. The geometry is meshed with two dimensional eight-node biquadratic elements to avoid problems related to material incompressibility. The element types are Plane 77 in thermal analysis and Plane 183 in stress analysis. A structured grid is employed with a mesh size of 0.1 mm in the length (x) direction and of 0.01 mm in the thickness (z) direction. The symmetric boundary condition is applied at the left edge of the model to remove the horizontal displacement, as illustrated in Figure A.4.1. The node at the bottom of the symmetric axis is fixed to constraint the displacement along the z direction.

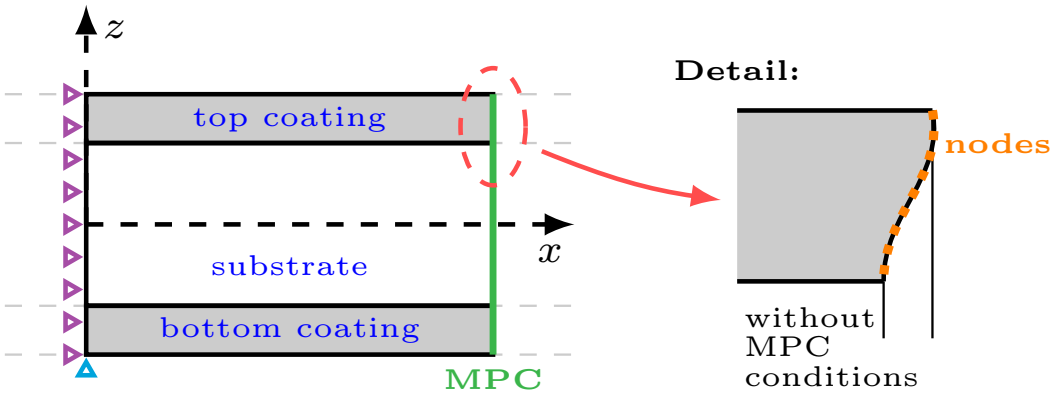

Figure A.4.1 Schematic representation of a part of the system; boundary conditions are employed in the finite element model: violet triangles represent symmetric boundary condition and the cyan one show the constraint of vertical displacement; MPC conditions applied at the righ edge to force nodes move along a straight line.

The slider type multi-point constrain (MPC) is applied on the right edge using the MPC184 slider element in ANSYS (KEYOPT(1)=3). The utilization of MPC allows to connect different nodes and their degrees of freedom together. In this work, the system is considered as an infinite plate. It is desirable to constrain the nodes on the free edge (right edge) to remain in a straight line, but allow the deformation and movement of nodes along this line as well as the change in length of the line. As shown in Figure A.4.1, a portion of the system is modeled.

In theory, any cross-section should remain straight and normal to the mid-surface of the system. Without MPC or other boundary conditions, nodes on the right edge are free to deflect. It is not accurate to simulate the part of the system not included in the analysis.

Figure A.4.2 shows the normal stress contour (σ_x) before thermal cycling (after deposition, at T_{amb}), with and without the utilization of MPC boundary condition on the right edge, respectively. As shown in Figures 2(b) and 2(c), the free deflection of nodes in the region close to the right edge leads to stress relaxation along the length direction in both coating and substrate. There also exists a stress gradient along the z direction with stress concentration at the coating/substrate interface. As presented above, the slider type MPC restrains the right edge to deform as a straight line. Figure 2(a) shows a uniform stress distribution in both coating and substrate, which is consistent with thin plate theory. It is therefore confident to use the MPC boundary condition for the benchmarking.

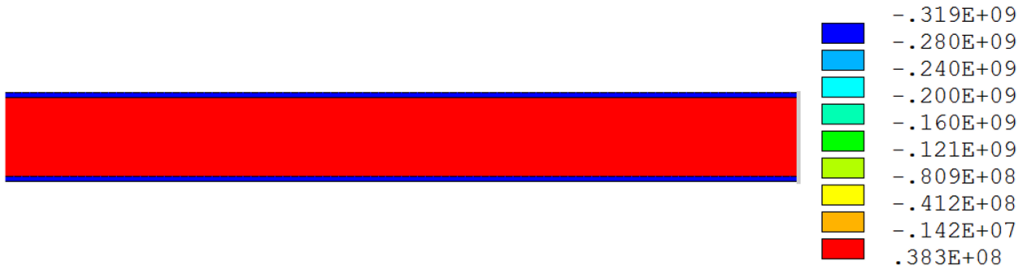

(a) Stress field after deposition, with MPC boundary condition

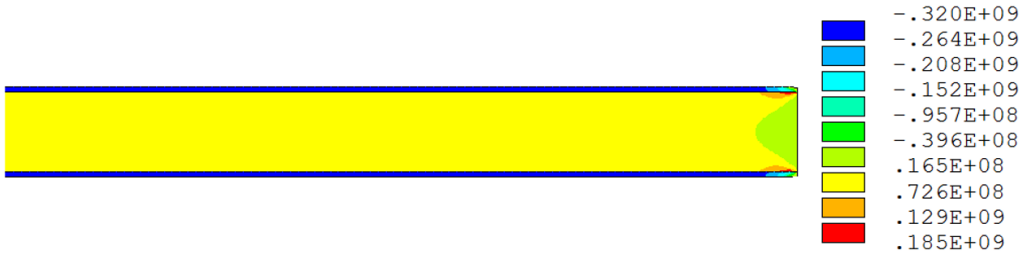

(b) Stress field after deposition, without MPC boundary condition

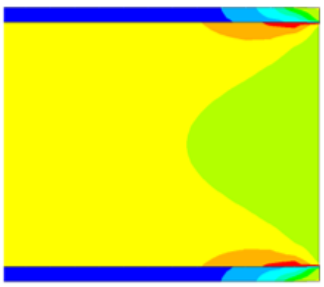

(c) High magnification of (b) at the right edge, for clarity

Figure A.4.2 Normal stress field calculated by FEA after deposition at T_{amb}: (a) with MPC boundary condition applied at the right edge; (b) without the use of MPC boundary condition and (c) a high magnification of (b) at the right edge.

Multilayer coatings based on aluminum nitride coatings for receivers in concentrated solar power technology

There is an increasing interest for concentrated solar power (CSP) systems which can work at temperatures higher than 1000 °C to optimize efficiency. One of the challenges is to design the receiver that will be heated at high temperature in air. Compared to coatings in gas turbine engine, the coating(s)/substrate system must have a high thermal conductivity to ensure a good heat transfer to the fluid. Aluminum nitride (AlN) coating, deposited by chemical vapor deposition at 1100-1200 °C at a growth rate of 10-50 $\mu m \cdot h^{-1}$, is selected for its high thermal conductivity, low thermal expansion coefficient, high temperature stability and its ability to develop stable alumina scales above 1000 °C. Molybdenum-based alloys are selected as substrate materials for their excellent thermal and mechanical properties. The alumina-forming iron-based alloys are also chosen as model substrates to reduce the influencing parameters in real-life receivers and to study the potential of these coatings. Accelerated cyclic oxidation tests and emissivity measurements allow the evaluation of AlN coatings as materials for high temperature CSP receivers. The multilayered systems exhibit low degradation after hundreds of thermal cycles at 800 °C in air and can support higher temperatures (1100 °C) for 100 to 500 h depending on the coating thickness. Nevertheless, the fast cyclic oxidation in solar furnace leads to cracks through the coatings. An analytical model is developed to study the stress evolution within the coating(s)/substrate system. Calculated results are in good agreement with experimental data. The measurements of the optical properties reveal a decrease of absorptivity after oxidation for AlN coatings, but a significant increase of absorptivity when SiC coating is added as a top layer.

Key words : Aluminum nitride, chemical vapor deposition, coatings, concentrated solar power plants, oxidation, simulation

Revêtements multicouches à base de nitrure d'aluminium pour les récepteurs des systèmes solaires à concentration

Il y a un intérêt croissant pour les systèmes d'énergie solaire concentrée (CSP) qui peuvent fonctionner à des températures supérieures à 1000 °C afin d'optimiser leur efficacité. L'un des défis consiste à définir un matériau récepteur qui sera soumis à un chauffage à haute température dans l'air. Contrairement aux revêtements utilisés dans les turbines à gaz, le ou les systèmes revêtement(s)/substrat doivent avoir une conductivité thermique élevée pour assurer un transfert thermique optimal vers le fluide. Les revêtements de nitrure d'aluminium (AlN), déposés par dépôt chimique en phase vapeur à 1100-1200 °C à une vitesse de croissance de 10-50 $\mu m \cdot h^{-1}$, sont choisis pour leur conductivité thermique élevée, leur faible coefficient de dilatation thermique, leur stabilité thermique élevée et leur capacité à développer des couches stables d'alumine au-dessus de 1000 °C. Les alliages à base de molybdène sont choisis comme substrat pour leurs excellentes propriétés thermiques et mécaniques. Les alliages à base de fer formant des couches d'alumine sont également choisis comme substrats modèles pour étudier le potentiel de ces revêtements et réduire le nombre de paramètres lors de l'oxydation. Des tests accélérés d'oxydation cyclique et des mesures d'émissivité permettent d'évaluer les revêtements AlN comme matériaux pour les récepteurs CSP haute température. Les systèmes multicouches présentent une faible dégradation après des centaines de cycles thermiques à 800 °C dans l'air et peuvent supporter des températures plus élevées (1100 °C) pendant 100 à 500 h selon l'épaisseur du revêtement. Néanmoins, l'oxydation cyclique rapide dans les fours solaires conduit à des fissures dans les revêtements. Un modèle analytique est développé pour étudier l'évolution des contraintes dans le(s) système(s) revêtement(s)/substrat. Les résultats calculés sont en bon accord avec les données expérimentales. Les mesures des propriétés optiques révèlent une diminution de l'absorptivité après oxydation pour les revêtements AlN, mais une augmentation significative de l'absorptivité lorsque un revêtement de SiC est ajouté comme couche de finition.

Mots clés : Nitrure d'aluminium, dépôt chimique en phase vapeur, revêtements, centrale solaire thermodynamique, oxydation, simulation